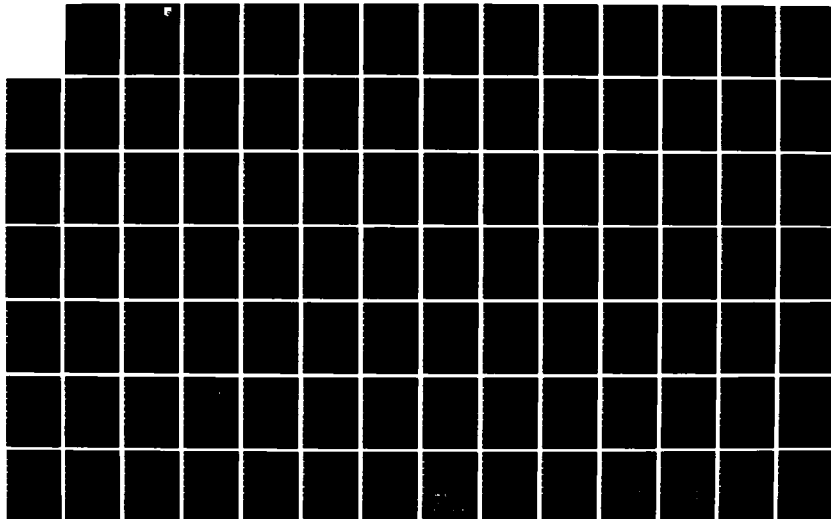
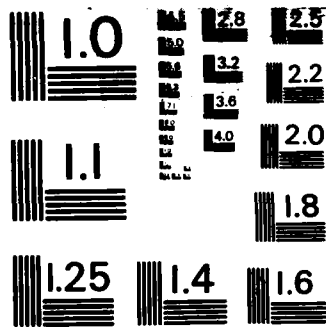


AD-A139 931 VIBRATION CONTROL OF SPACE STRUCTURES VCOSS A: HIGH AND 1/3
LOW-AUTHORITY HAR. (U) LOCKHEED MISSILES AND SPACE CO
INC SUNNYVALE CA J N AUBRUN ET AL. JUL 83 LMSC-D883019
UNCLASSIFIED AFWAL-TR-83-3074 F33615-81-C-3220 F/G 20/11 NL

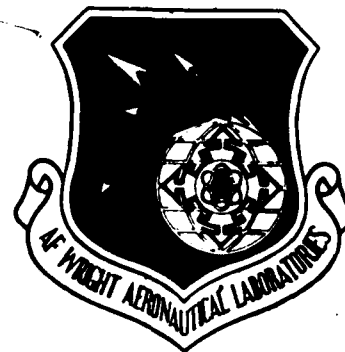




MICROCOPY RESOLUTION TEST CHART
NATIONAL BUREAU OF STANDARDS-1963-A

AD A139931

AFWAL-TR-83-3074



Vibration Control of Space Structures VCOSS A: High and Low-Authority Hardware Implementations

Lockheed Missiles & Space Company, Inc.
1111 Lockheed Way
Sunnyvale, California 94086

July 1983

Final Report Period

Approved for public release, distribution unlimited

APR 11 1984

DTIC FILE COPY

Flight Dynamics Laboratory
Air Force Wright Aeronautical Laboratories
Air Force Systems Command
Wright-Patterson Air Force Base, Ohio 45433

84

04

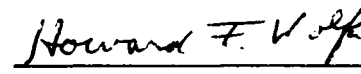
NOTICE

When Government drawings, specifications, or other data are used for any purpose other than in connection with a definitely related Government procurement operation, the United States Government thereby incurs no responsibility nor any obligation whatsoever; and the fact that the government may have formulated, furnished, or in any way supplied the said drawings, specifications, or other data, is not to be regarded by implication or otherwise as in any manner licensing the holder or any other person or corporation, or conveying any rights or permission to manufacture, use, or sell any patented invention that may in any way be related thereto.

This technical report has been reviewed and is approved for publication.




JEROME PEARSON, Technical Manager
Engineering Technology Group



HOWARD F. WOLFE, Acting Chief
Structural Vibration Branch

FOR THE COMMANDER:



JAMES J. OLSEN
Assistant for Research & Technology
Structures & Dynamics Division

"If your address has changed, if you wish to be removed from our mailing list, or if the addressee is no longer employed by your organization please notify AFWAL/FIBG, W-P AFB, OH 45433 to help maintain a current mailing list".

Copies of this report should not be returned unless return is required by security considerations, contractual obligations, or notice on a specific document.

UNCLASSIFIED

SECURITY CLASSIFICATION OF THIS PAGE (When Data Entered)

REPORT DOCUMENTATION PAGE		READ INSTRUCTIONS BEFORE COMPLETING FORM
1. REPORT NUMBER AFWAL-TR-83-3074	2. GOVT ACCESSION NO. AD-A139931	3. RECIPIENT'S CATALOG NUMBER
4. TITLE (and Subtitle) Vibration Control of Space Structures (VCOSS) VCOSS A: High- and Low-Authority Hardware Implementations		5. TYPE OF REPORT & PERIOD COVERED FINAL REPORT 15 Sep 1981 - 15 April 1983
		6. PERFORMING ORG. REPORT NUMBER LMSC-D883019
7. AUTHOR(s) J. N. Aubrun, C. Z. Gregory (ISI), M. G. Lyons (ISI), R. L. Kosut (ISI), A. A. Woods, Jr.		8. CONTRACT OR GRANT NUMBER(s) F33615-81-C-3220
9. PERFORMING ORGANIZATION NAME AND ADDRESS Integrated Systems, Inc. 151 University Avenue, Palo Alto, CA 94301 Lockheed Missiles & Space Co., Box 504, Sunnyvale		10. PROGRAM ELEMENT, PROJECT, TASK AREA & WORK UNIT NUMBERS P. E. 62201F Project 2401 Task 240104 CA W.U. 24010415
11. CONTROLLING OFFICE NAME AND ADDRESS Flight Dynamics Laboratory (AFWAL/FIBG) Air Force Wright Aeronautical Laboratories Wright-Patterson AFB OH 45433		12. REPORT DATE July 1983
14. MONITORING AGENCY NAME & ADDRESS (if different from Controlling Office)		13. NUMBER OF PAGES 228
		15. SECURITY CLASS. (of this report) UNCLASSIFIED
16. DISTRIBUTION STATEMENT (of this Report) Approved for public release; distribution unlimited.		15a. DECLASSIFICATION/DOWNGRADING SCHEDULE N/A
17. DISTRIBUTION STATEMENT (of the abstract entered in Block 20, if different from Report) CSDL (Charles Stark Draper Lab.) no. 2		
18. SUPPLEMENTARY NOTES AFWAL Project Manager: Jerome Pearson		
19. KEY WORDS (Continue on reverse side if necessary and identify by block number) <u>Cosati Codes</u> 22 02 SPACECRAFT 20 11 SOLID MECHANICS, VIBRATION 20 06 OPTICS 17 09 RADAR ANTENNA 09 02 COMPUTERS 15 03 SURVEILLANCE SYSTEMS 13 13 STRUCTURAL ENGINEERING 09 05 FEEDBACK AMPLIFIERS, SERVO MECHANISMS		
20. ABSTRACT (Continue on reverse side if necessary and identify by block number) The report considers some hardware aspects of large space structure control implementations. Hardware and system performance requirements are overviewed, principally in the context of vibration suppression. Analytical models based on soft and stiff versions of CSDL #2 structure are used to evaluate vibration suppression performance for actively controlled and passive structures. The effects of hardware bandwidth limitations and system modeling errors are evaluated for the active controls case. It is shown that hardware bandwidth		


DD FORM 1 JAN 73 1473 EDITION OF 1 NOV 65 IS OBSOLETE

UNCLASSIFIED
SECURITY CLASSIFICATION OF THIS PAGE (When Data Entered)

UNCLASSIFIED

SECURITY CLASSIFICATION OF THIS PAGE(When Data Entered)

(cont)

limitations do not pose significant control or sign problems. The basic elements for a hardware demonstration program to evaluate these results is given. 

UNCLASSIFIED

SECURITY CLASSIFICATION OF THIS PAGE(When Data Entered)

FOREWORD

This report was prepared by the Lockheed Missiles and Space Company Integrated Systems, Inc. The work was done under Contract F33615-81-C-3220 for the Air Force Wright Aeronautical Laboratories, Flight Dynamics Laboratory, Wright-Patterson Air Force Base, Ohio. The research was conducted under Project 2401 and Task 240104, "Vibration Prediction and Control, Measurement and Analysis"; and was partially funded by the Defense Advanced Research Projects Agency. The Air Force technical monitor was Jerome Pearson (AFWAL/FIBG).



Accession Fee	
NTIS GRA&I	
DTIC TAB	
Unannounced	
Justification	
By	
Distribution /	
Availability Codes	
Avail and/or	
Dist	Spec
A-1	

CONTENTS

Section		Page
I	CONTROL HARDWARE ASSESSMENT	1
	1. Disturbance Source and Performance Metric Characterization	1
	2. Hardware Requirements Assessment	5
	3. Existing/Proposed Hardware Devices	10
	4. Required Hardware Development	12
II	SYSTEM DESIGN	13
	1. Overall Control System Design	13
	2. Actuator Selection and Modeling	18
	3. Sensor Selection and Modeling	34
	4. Signal Processing	39
III	MODEL INTEGRATION	47
	1. VCOSS Model Description	47
	2. Actuator/Sensor Locations and Types	61
	3. Open-Loop System Evaluation for Control Design	64
	4. Control Designs	82
	"Cautious" Controller	113
	5. Impact of Disturbance Model Changes	107
	6. Low Frequency Actuator Limitations	113
	7. Effects of Actuator Dynamics	125
	8. Sensor Modeling Effects	162
	9. Effects of General Actuator/Sensor Modeling Errors	165
	10. Results Comparison for Stiffness Designs	177
	11. Conclusions	179

CONTENTS (CONT.)

REFERENCES 181

Appendix

A REDUCTION OF LARGE FLEXIBLE SPACECRAFT
MODELS USING INTERNAL BALANCING THEORY A-1

B CHARLES START DRAPER LABORATORY -
REFERENCE DATA B-1

LIST OF ILLUSTRATIONS

Figure		Page
1	Disturbance Factors	2
2	Disturbance Power Spectral Density	6
3	General Overview of Damping Devices Domain of Operation	9
4	System Design Methodology	15
5	Classification Matrix of Actuators for Vibration Control and Generic Examples	19
6	Inertial Actuators Range of Operation	20
7	Typical Region of Operation of CMG's	21
8	Typical Region of Operation of a Proof-Mass Actuator	24
9	CMG Sizing	26
10	PPM Actuator Dynamics Model	27
11	PPM Actuator Design-Performance Region	30
12	PPM Actuator Design Curves	32
13	Typical Inertial-Grade Accelerometer Noise PSD	35
14	Wordlength Effect on Coefficient Perturbation and Stability	43
15	Minimum Number of Bits for Stable Control Computations	44
16	Deleted	
17	An Architecture for High-Speed Control	46
18	VCOSS Model Draper Labs Model #2, Revision #3	48
19	VCOSS Finite-Element Model	49
20	Modified Mirror Models	52
21	VCOSS Optical System	55

LIST OF ILLUSTRATIONS (CONT)

Figure		Page
22	VCOSS Evaluation Model Frequency vs. Mode Number	67
23	PSD of Disturbance to LOS _x	68
24	PSD of Disturbance to LOS _y	69
25	Integrated PSD of Disturbance to Total LOS	70
26	Integrated PSD of Disturbance to LOS _x	71
27	Integrated PSD of Disturbance to LOS _y	72
28	Open-Loop Modal Analysis	76
29	Controllability/LOS Levels for Actuators 1, 2, and 3	79
30	Controllability/LOS Levels for Actuators 4, 5, and 6	80
31	Controllability/LOS Levels for Actuators 7, 8, and 9	81
32	10-Mode Control Design Selection	83
33	// VCOSS (+) Open-Loop Spectrum, (X) Closed-Loop Spectrum, 26th Order	87
34	// VCOSS Closed-Loop Evaluation	88
35	// VCOSS (+) Open-Loop Spectrum, (X) Closed-Loop Spectrum, 26th Order	89
36	// VCOSS (+) Open-Loop Spectrum, (X) Closed-Loop Spectrum, 26th Order	90
37	Closed-Loop Modal Costs for 10-Mode Controller	92
38	Mode-Selection for 14-Mode Reduced Model	93
39	(+) Open-Loop Spectrum, (X) Closed-Loop Spectrum, 34th Order	97
40	(+) Open-Loop Spectrum, (X) Closed-Loop Spectrum, 34th Order	98
41	(+) Open-Loop Spectrum, (+) Closed-Loop Spectrum, 34th Order	99
42	VCOSS Open-Loop (Open) and Closed-Loop (Shaded) Modal Costs for 34th Order Controller	100
43	(+) Open-Loop Spectrum, (X) Closed-Loop Spectrum, HAC/LAC	102

LIST OF ILLUSTRATIONS (CONT)

Figure		Page
44	(+) Open-Loop Spectrum, (X) Closed-Loop Spectrum, HAC/LAC	103
45	(+) Open-Loop Spectrum, (X) Closed-Loop Spectrum, HAC/LAC	104
46	VCOSS/PPM Actuator Power Requirements	115
47	VCOSS/PPM Actuator Power Requirements	116
48	VCOSS/PPM Actuator Power Requirements	117
49	VCOSS/PPM Actuator Power Requirements	118
50	Actuator Sizing	122
51	Low-Frequency PPM Design	124
52	Frequency Response of Active and Passive Dampers	126
53	Open-Loop Modal Analysis of 34-Mode Model	128
54	Open-Loop Frequencies of 34-Mode Evaluation Model and Design Model	129
55	Full Closed-Loop Spectrum (X=HAC, O=HAC/LAC)	134
56	Full Closed-Loop System: X=HAC, O=HAC/LAC (Expanded Scale)	135
57	Open-Loop Modal Coordinate "Component Costs" with Corrected Disturbance	137
58	Open-Loop Modal Coordinate "Component Costs" with Corrected Disturbance - Expanded Scale	138
59	Full Closed-Loop Spectrum: X=HAC, O=HAC/LAC, *=Locus as First-Order Rolloff Decreases	140
60	Effect of First-Order Actuator Rolloff Upon Mode 31	141
61	Effect of First-Order Actuator Rolloff Upon Mode 32	142
63	Effect of First-Order Rolloff Upon Mode 34: O=HAC/LAC, + = Open Loop	144
64	Performance Degradation Due to First-Order Actuator Rolloff	146
65	Effect of 2nd-Order Actuator Dynamics Upon LAC	150

LIST OF ILLUSTRATIONS (CONT)

Figure		Page
66	Effect of 2nd-Order Actuator Dynamics Upon Mode 34	151
67	Effect of 2nd-Order Actuator Dynamics Upon Mode 33	152
68	Effect of 2nd-Order Actuator Dynamics Upon Mode 32	153
69	Effect of 2nd-Order Rolloff Upon HAC/LAC: X=HAC, O=HAC/LAC, * = Locus as Rolloff Frequency Decreases	155
70	Effect of 2nd-Order Rolloff Upon HAC/LAC: Mode 31	156
71	Effect of 2nd-Order Rolloff Upon HAC/LAC: Mode 32	157
72	Effect of 2nd-Order Rolloff Upon HAC/LAC: Mode 33	158
73	Effect of 2nd-Order Rolloff Upon HAC/LAC: Mode 34	159
74	Performance Degradation Due to 2nd-Order Actuator Rolloff	161
75	Accelerometer Noise Models	163
76	Block Diagram of Controlled Spacecraft	167
77	Stability Margin (Actuator Bandwidth 3.7 Hz)	175
78	Performance Margin 10% Degradation (Actuator Bandwidth 160 Hz)	176

LIST OF ABBREVIATIONS

CMG	Control Moment Gyro
CSDL	Charles Stark Draper Laboratory
DOF	Degrees of Freedom
HAC	High Authority Control
LAC	Low Authority Control
LOS	Line of Sight
LQG	Linear Quadratic Gaussian
LSS	Large Space Structures
PPM	Pivoted Proof Mass
PSD	Power Spectral Density
PZT	Piezoelectric Type
RAM	Random Access Memory
RMS	Root Mean Square
RRI	Riverside Research Institute
RSS	Root Sum Square
SASS	Six-Axis Space Sensor
TAARA	Three-Axis Angular Rate and Acceleration
VCSS	Vibration Control of Space Structures

LIST OF TABLES

Table		Page
1	Sensor Types and Applications	7
2	Actuator Types and Applications	9
3	Characteristic Parameters of Prototype PPM Actuator	29
4	Inertial Grade Space Accelerometers	36
5	Steady-State LQG Controller Form	41
6	Eigenvalue Perturbation and Stability Condition	43
7	Minimum Number of Bits to Ensure Controller Stability	44
8	Deleted	
9	Changes in Lumped Masses	50
10	Mirror Unrestrained Degrees of Freedom	53
11	VCOSS Mass Matrix Comparison	56
12	VCOSS Modal Frequency Comparison (Hz)	57
13	Line-of-Sight (LOS) Equations	58
14	Results of Line-of-Sight (LOS)	60
15	Modal Rankings Suggested by the Analysis	77
16	Closed-Loop Control Spectrum of 10-Mode Model	85
17	Closed-Loop Filter Spectrum for 10-Mode Model	86
18	Closed-Loop Control Spectrum for 14-Mode Model	94
19	Closed-Loop Filter Spectrum for 14-Mode Model	95

LIST OF TABLES (Cont)

Table		Page
20	Stochastic Performance Analysis of VCOSS Controllers	105
21	Individual Actuator RMS Effort for Each Controller (N)	106
22	Normalized Stochastic Performance Analysis of VCOSS Controllers - 6 Independent Disturbances	108
23	Stochastic Performance of VCOSS Controllers - 2 Independent Disturbances	110
24	RSS Actuator Effort - 2 Independent Disturbances	111
25	Normalized Stochastic Performance of VCOSS Controllers - 2 Independent Disturbances	112
26	Corrected Actuator Effort (N)	114
27	Actuator Sizing	119
28	Actuator Sizing	121
29	Frequencies of 10-Mode Design Model	130
30	Control Design Spectrum	132
31	Filter Design Spectrum	131
32	34-Mode Performance Evaluation	136
33	Full Closed-Loop LAC Spectrum	149
34	34-Mode Performance Evaluation	164
35	Stability and Performance Robustness Margins	171
36	Passive System Response to Complete PSD	178
37	Rev 03 Closed-Loop Performance Without Discrete Frequency Power Spectra	178

SECTION I

CONTROL HARDWARE ASSESSMENT

1. DISTURBANCE SOURCE AND PERFORMANCE METRIC CHARACTERIZATION

Typical high performance large flexible spacecraft of the type which have motivated this study are subject to a wide range of disturbance loads characterized in Fig. 1. The selection of control architectures and, subsequently, sensor/actuator, and processor hardware depends strongly on the precise form of the system performance metric, the vehicle structural characteristics, and the relative disturbance levels. Without these descriptions, hardware selection is not possible. Many performance metrics may be selected, depending on mission requirements, including line-of-sight, wavefront, structural amplitude, and rigid body pointing errors. For the systems of interest in the VCOSS program, only steady-state dynamic line-of-sight (LOS) errors will be considered. This type of error will form the basis for evaluating benefits of control-configured spacecraft design. Limiting the performance metric in this way widens the choices in actuator and sensor selection by eliminating any direct need to measure or control rigid body modes or absolute motion with respect to inertial space. Static LOS offsets due to shape and alignment errors are generally controlled with specialized actuator/sensor systems that operate near DC; actuator/sensor placement is governed by spatial frequency error and optical alignment requirements which are not generally compatible with controllability/observability measures for dynamic system modes. Thus, it is usually the case that dynamic error suppression systems must be synthesized separately from (static) figure control systems and the distinction between static and dynamic figure control should be clearly made in any discussion.

DISTURBANCE FACTORS

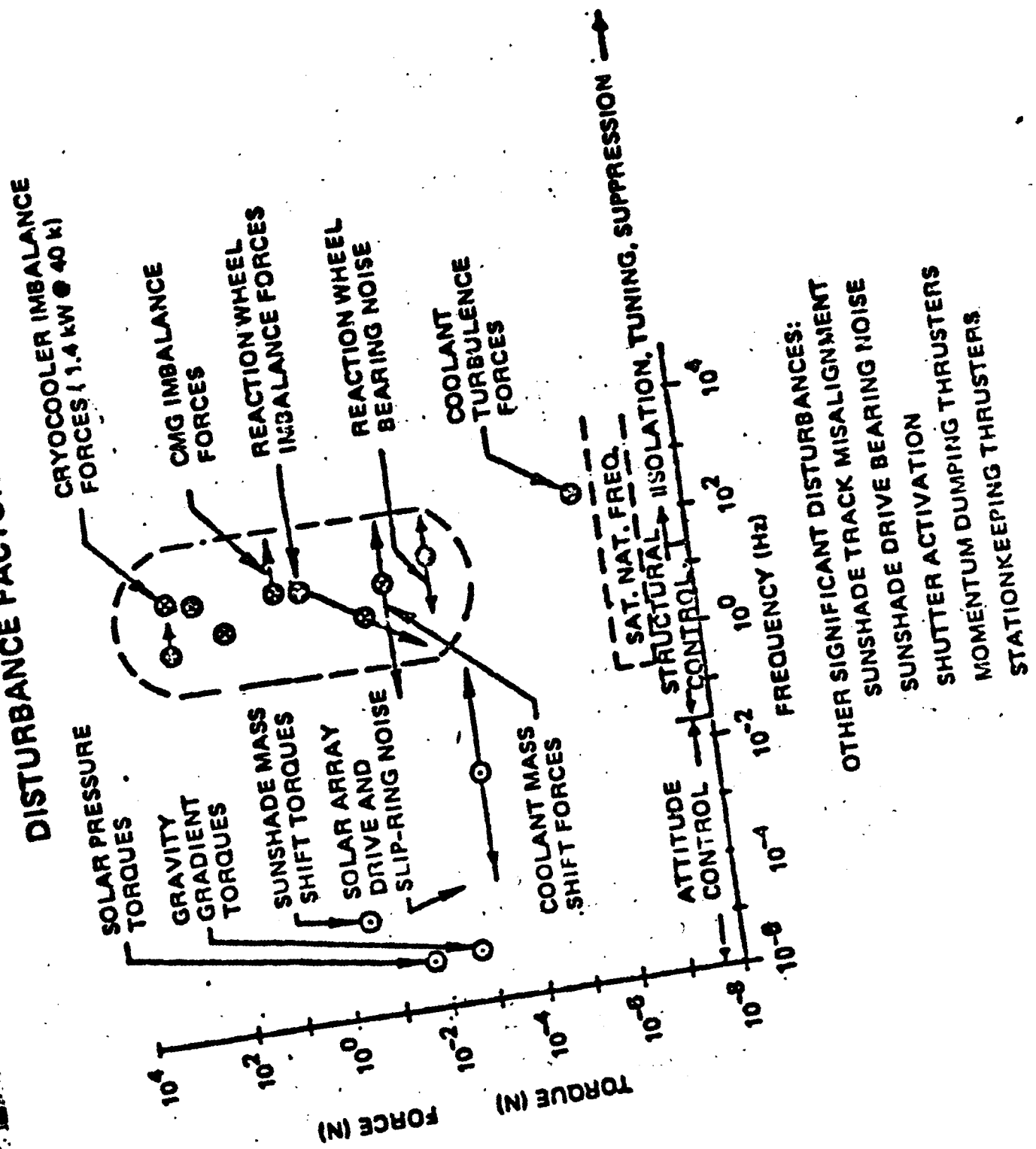


Figure 1. Disturbance Factors

With these ideas in the background, it is now possible to qualitatively evaluate the effects of the disturbances in Fig. 1. For structures in the 30m size range, significant modes below 0.1 Hz are unlikely. Thus, orbit rate based disturbances induced by gravity-gradient torques, magnetic dipole moments, and solar pressure effects all look like static input loads to a "stiff" structure and will be compensated by static figure and alignment subsystems. These disturbances are spectrally separated from those which interact with the vehicle dynamics and, thus, they do not influence requirements for dynamic error suppression systems (i.e., these disturbances will be ignored in this study). The only possible exception to this scenario will be thermal and solar pressure transients during solar eclipse with the earth. For certain applications these inputs will influence the required modal damping in the lower frequency modes. Usually, however, stabilization of the attitude control system places similar damping requirements on these modes so that transient settling at low frequencies is generally not treated as a separate design problem.

Vibration sources which excite structural modes may then be considered to originate on-board the spacecraft in the form of cryo-cooler pumps, CMG rotors, reaction wheels, coolant systems, and reaction jets. Roughness in digital controllers used to implement stability augmentation and disturbance rejection systems may also produce unwanted modal excitation. Momentum storage devices and pumps generally produce narrow-band excitation at multiple frequencies corresponding to rotor and bearing retainer motion. Coolant flow, reaction jet operation, and combustion processes usually produce a wide-band uncorrelated noise. The exact force levels these types of excitation produce depend on types and sizes of devices; in many cases, supporting data for broad-band disturbance levels is non-existent. Meaningful evaluation of structural response must then depend on point design solutions along with assumptions of system linearity. For optical

systems, some questions regarding non-linearity of joints in the micro-vibration region have been raised which have yet to be resolved via ground or flight experiments (necessary to remove the 1g pre-load). For the present evaluations these questions will be put aside.

These considerations can be invoked to create a strawman disturbance spectrum (developed by Riverside Research Institute (RRI) and Charles Stark Draper Laboratory (CSDL) shown in Fig. 2. Draper Model Number Two had two sine disturbances--one at 10N and 10 Hz on the top of the truss and one at 5 Hz and 20N on the aft body. Because of the discrete nature of the disturbances the control system synthesis addressed only part of a realistic disturbance rejection design problem. In addition, the disturbances were oriented along the stiff axis of the structure. To avoid these problems a new model for the disturbances is proposed in Fig. 2. The flat Power Spectral Density (PSD) was selected so that disturbances occurred across the many modes. The level selected was chosen on the basis of supplying as much disturbance energy to the system as the original two discrete systems supplied if a damping ratio of 0.002 was assumed. The 15 Hz rolloff was selected to include more modes than before and to extend disturbances out into the area called the Low Authority Control (LAC) region. The $1/f^2$ rolloff was specified to ease the total bandwidth and keep the problem in hand. The three discrete frequencies are selected to represent motors, etc. The 10 and 20 Hz frequencies were selected to present the problem of control of frequencies at multiples of each other. The 8 Hz frequency was selected to provide a beat frequency against the 10 Hz frequency that was in the structural control bandwidth. The ± 1 Hz on the 8 Hz frequency was to insure a mode would be directly excited by a sine source. Since non-linear elements are not included in the models, frequency mixing will not be an issue here.

The controls problem posed in the VCOSS study is the active rejection of this disturbance (Fig. 2) as measured by a line-of-sight performance metric. Other measures could be used, such as wave front error, which would alter the form of the synthesized control systems. These issues are discussed later in Section 3 on model integration. For now, the assumptions under which actuator/sensor hardware is to be selected are summarized as follows:

- (1) rigid body motions are controlled by other systems
- (2) static figure control is ignored
- (3) only system dynamic line-of-sight error (tilt) is to be controlled.

These restrictions now permit some definite selections to be made.

2. HARDWARE REQUIREMENTS ASSESSMENT

In this section we attempt to specify the kinds of hardware necessary to address the problem discussed above. In subsection 3, generic requirements are examined with respect to what is actually available.

a. Sensor Systems

Sensors for vibration measurement may be classified into inertial measurement and relative measurement categories. The first category includes accelerometers and instrument gyros while the second includes all optical angular and distance measuring devices. Additional sensors to measure point source disturbances may also be required. Sensor types must be matched to performance requirements, control architectures, and mission constraints. Some of these considerations are listed in Table 1.

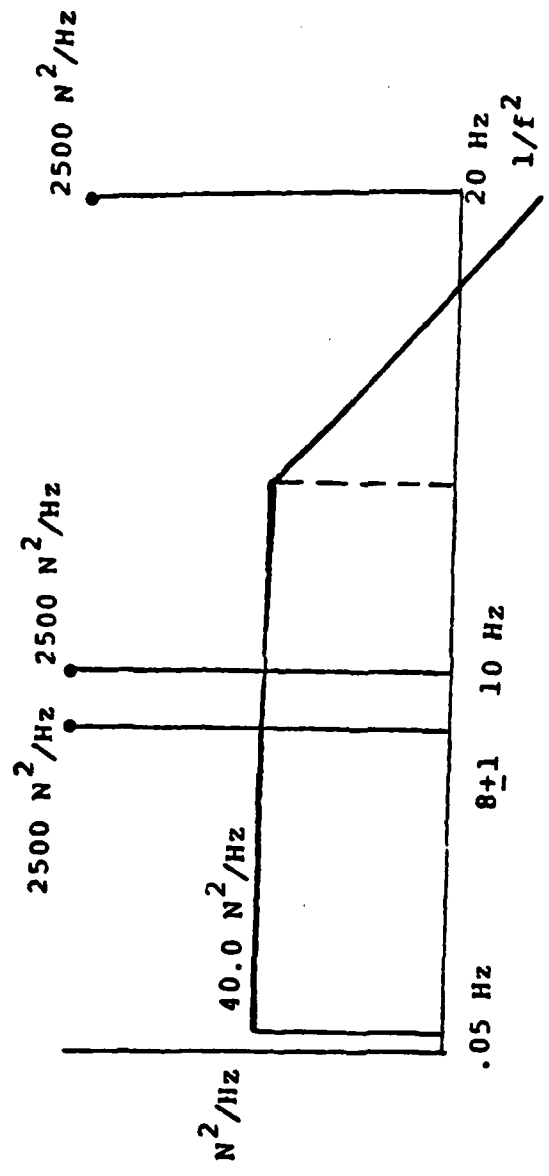


Figure 2. Disturbance Power Spectral Density (PSD)

TABLE 1 SENSOR TYPES AND APPLICATIONS

Sensor Type	Measurement Class	Applicable Control Architecture	Comments
Accelerometer	Inertial	Co-located/ non-colocated state feed- back	Servo-type useful $>$ 0.2 Hz in micro- vibration region
Rate gyros	Inertial	Co-located/ non-colocated state feed- back	Very high cost for micro-vibration applications
Load cells	Relative- strain- guage type	Vibration load, actuator force measurement	Temperature sensitivity/reliability problems
Laser angular systems	Relative	Non-colocated state feed- back*	*Colocated mechaniza- tions possible with base motion compen- sation
Laser phase systems	↓	↓	
Multi- color interfer- ometers	Absolute distance/ non-inertial	Shape control	Bandwidth limited for real-time control for scanning systems

Colocated systems, where actuators and sensors must have coincident effector/sensor axes and locations, are most easily mechanized using inertial measurement instruments or optical systems with inertial base motion compensation. For some applications, it has been demonstrated experimentally that optical angular measurement can provide colocated measurement over a limited frequency range (1). Optical systems inherently provide the widest bandwidth (down to DC) sensing and the best signal-to-noise ratio of any system. The measurements are inherently non-colocated, however, and computation of the measurement matrix is usually complex. System constraints may also not permit deployment of such sensors on certain parts of the spacecraft.

b. Actuator Systems

Actuators which produce constant forces and moments are necessary for attitude control but not for vibration control. Thus, additional actuators capable of producing only oscillating loads may be considered for the VCOSS application. A representative list is shown in Table 2 organized along the lines of the previous sensor table.

The range of controllable structural amplitudes as a function of actuator type is illustrated in Fig. 3. Requirements imposed by the current VCOSS strawman configuration and disturbances limit actuator selection to a subset of those illustrated in the table. Rejection of sinusoidal and broadband disturbance to produce a "quiet" structure may require actuator effectiveness over a 30 Hz bandwidth with linear well-defined response characteristics. Reaction wheels and reaction jets are generally not capable of this type of response. Member dampers, which impose forces and moments on points in the structure are generally bandwidth limited by the additional structure necessary to interconnect two nodes. This also makes actuator modeling more difficult. It appears at present that such devices are more suitable for low-frequency shape control.

TABLE 2 ACTUATOR TYPES AND APPLICATIONS

Actuator Type	Actuator Loads	Applicable Control Architecture	Comments
Proof-mass	Inertial, AC only	Colocated/non-colocated state feedback	Microvibration control > 1 Hz, possible non-linear behavior
CMG	Inertial, limited DC torque	Attitude control, non-colocated state feedback*	*Most common use, high bandwidth torque unavailable with current designs, very high torque possible
Reaction wheel	Inertial, limited DC torque	↓	Low bandwidth ~ 1 Hz, low torque, difficult vibration isolation
Member damper	Intra-structural loads (to DC)	Non-colocated state feedback	Complex control distribution matrix, complex actuator dynamics, usable for static shape control
Reaction jet	Inertial to DC	Attitude control, colocated/non-colocated state feedback	Inherent vibration sources, principal use in maneuvering, and large amplitude control

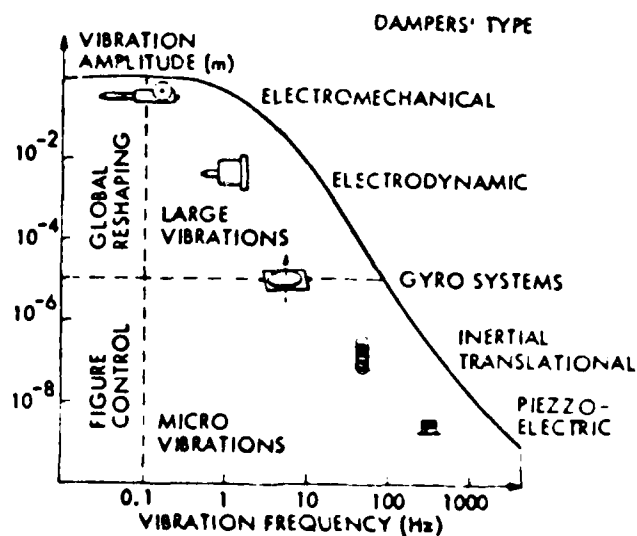


Figure 3. General Overview of Damping Devices' Domain of Operation

3. EXISTING/PROPOSED HARDWARE DEVICES

The kinds of hardware shown in subsection 2 represent either specialized applications of existing devices or entirely new devices, most of which have never been tested. In spacecraft system design, measurement of surface modal deflections, and control of dynamic mode shapes and amplitudes have not historically been of interest. Hardware development has not been specifically directed toward such applications. Consequently, few directly usable devices exist. Paper studies, prototype development, and modification of existing hardware have occurred, nonetheless, and some of this work was reported to DARPA by CSDL and LMSC in a joint briefing in late 1980. Very little new work exists to date, and an overview of this device survey is now presented as representative of current thinking in the hardware development area and as a basis for the device models suggested in the next section.

The state of the art in inertial instrument design is quite advanced and devices which are now flight qualified or which could be flight qualified are presented in Appendix B. The list of usable servo-type accelerometers is reasonably long and instruments similar to the Bell XI are listed also in Section II. Piezo-electric type accelerometers do not currently perform well enough for the VCOSS application because of their high noise level and poor low frequency performance. Two new instruments, derived from existing CSDL hardware, the Three-Axis Angular Rate & Acceleration (TAARA) and Six-Axis Space Sensor (SASS) sensors, provide three axis angular measurement and integrated angular and translational measurement respectively in a single instrument. Such devices can be colocated with a cluster of Control Moment Gyro (CMG) actuators and/or proof-mass drivers. The characteristics of these devices are described in Appendix B. A new low-cost accelerometer using a flexible substrate chip technology may have possible applications to VCOSS if sensitivity and signal-to-noise can be improved from current levels. Prototype devices do show some promise as indicated in the tables.

The use of optical systems to measure structural deflections was originally motivated by use of multi-color interferometers to compute figure error on large surfaces (such as mirrors). Absolute figure measurement is unnecessary for dynamic figure error suppression but some form of high-bandwidth microvibration relative velocity and position measurement will be needed for some applications. Stand-off measurement capability offered by these systems is, however, difficult to use because the effective measurement matrix usually reflects base motion of the sensor as well as motion of the desired structural components. In some instances, an accurate measurement matrix can be constructed, in others, base motion may be restrained inertially (active or passive), and for some applications, base motion reference can be provided. The inertially stabilized retro-reflectors shown in the charts accomplish this last objective by providing a reference surface against which other vibration measurements from the optics are compared. This allows colocated measurement and control if the actuators are located at the surface measurement sites.

A representative 10 channel microphase optical system is then described, built out to the prototype test stage, which might be used in conjunction with such stabilized retro-reflectors.

Actuators usable for VCROSS systems are essentially all in the early development stage. The basic proof-mass driver using electrodynamic motor technology, is illustrated. A proposed high-bandwidth CMG which uses electrodynamic gimbal torquers and suspension components to isolate high frequency rotor vibration from the controlled structure is also sketched. No prototypes of this device currently exist. The last item illustrated is a sketch of a member damper concept using either piezoelectric or electrodynamic drivers. It must be emphasized that such devices have only been tested in the form of external actuators used to maneuver test specimens and have not actually been used as intra-structural "dampers". Small piezoelectric actuators have been used as intrastructural dampers by R. L. Forward at Hughes.

4. REQUIRED HARDWARE DEVELOPMENT

Actuators which appear most promising for vibration control include proof-mass (linear, inertial force) and control moment gyro types. (These devices provide band-limited, inertial structural loads.) Characteristics and sizing of these devices will be discussed in the next section. Proof-mass devices exist only as laboratory test articles and must be developed into flight qualified hardware. CMG flight hardware has been limited to low-bandwidth attitude control actuators which can control low frequency bending but which are inadequate to affect broad band noise. In addition to current designs, new high-bandwidth prototype designs need to be brought to the ground test stage of development.

Accelerometers are now highly developed and the servo types can yield nano-g resolution above 0.5 Hz. Optical systems and instruments are well-developed but use on Large Space Structures (LSS) will be very case dependent and sensitive to specific geometry. System level tests are needed to bring such instruments into wide-spread use at the ground test level before configuring them for subsequent flight tests.

The hardware illustrated in the previous section represents recent thinking by CSDL, LMSC, Integrated Systems, and other industry practitioners. Many of these devices are in the pre-development or early development stage. Successful deployment of LSS type systems in the next 5 to 10 years will depend on the rigorous development of these and other devices.

In Section II the system design aspects of an LSS vibration control design are explained, including hardware selection and placement methodology. Basic models for selected hardware are described.

SECTION II

SYSTEM DESIGN

1. OVERALL CONTROL SYSTEM DESIGN

a. Introduction

This section will attempt to define a rational procedure to specify active vibration control devices and integrate them in the design of a control configured space structure, given certain performance requirements in the presence of on-board or environmental disturbances. However, because of the present scarcity of applicable actuators and sensors and technological limitations, it is expected that some trade-off studies will always have to be made between actuator/sensor performance and system performance. It is not unusual that a small relaxation of mission requirements could yield a significant decrease in the required performance for the hardware and make the system much more realizable. Thus the procedure described here should be envisioned more as a guide-line or as one step in a more complex iterative process.

The second problem encountered in the design of a Vibration Controlled Space Structure is that the starting point is not well defined in practice. Although it would seem that the overall design of the spacecraft should be started as a whole, i.e., including the control system (the so-called Control Configured Spacecraft), it is more usual that the structural elements are first defined and then control systems are built around them. This second approach is considered in this report, especially in view of the specific application to the model spacecraft developed by CSDL discussed in Section III.

b. System Design Main Steps

The overall process is sketched in Figure 4. Once the physical structure of the spacecraft has been designed to satisfy more or less the mission requirements, a structural (finite-element, FEM) model is usually obtained. From this FEM model, the mathematical model for the disturbances, and the various performance metrics definitions, a state-space model is obtained which will be the basis of the open-loop analyses.

These analyses constitute a very important step because it is from them that actuator and sensor selection can proceed. Various methods are used for this selection (discussed later) and they result in the definition of the location of the actuator, the type of actuation (force, torque, bending moments, etc.) and the direction of the effort. Similar results obtain for the sensors.

At this point the set of actuators and sensors are still conceptual, with ideal characteristics. From this set, and the original spacecraft model, the system's model is derived to which control synthesis techniques are applied.

The definition of the control laws and their subsequent evaluation furnish information concerning the control effort and the sensing sensitivity which generate requirements for the actuators and sensors to be designed. If these requirements are easy to meet, the process could stop there. In practice, as was stated earlier, many iterations may be required. A strong driver for this iterative process is that the physical actuator (or sensor) has non-ideal characteristics (limited bandwidth, nonlinear behavior, noise) which need to be modeled and evaluated for their impact upon the total system performance.

This last process of actuator design could vary from just selecting an "off-the-shelf" item to designing an entirely new actuator or sensor.

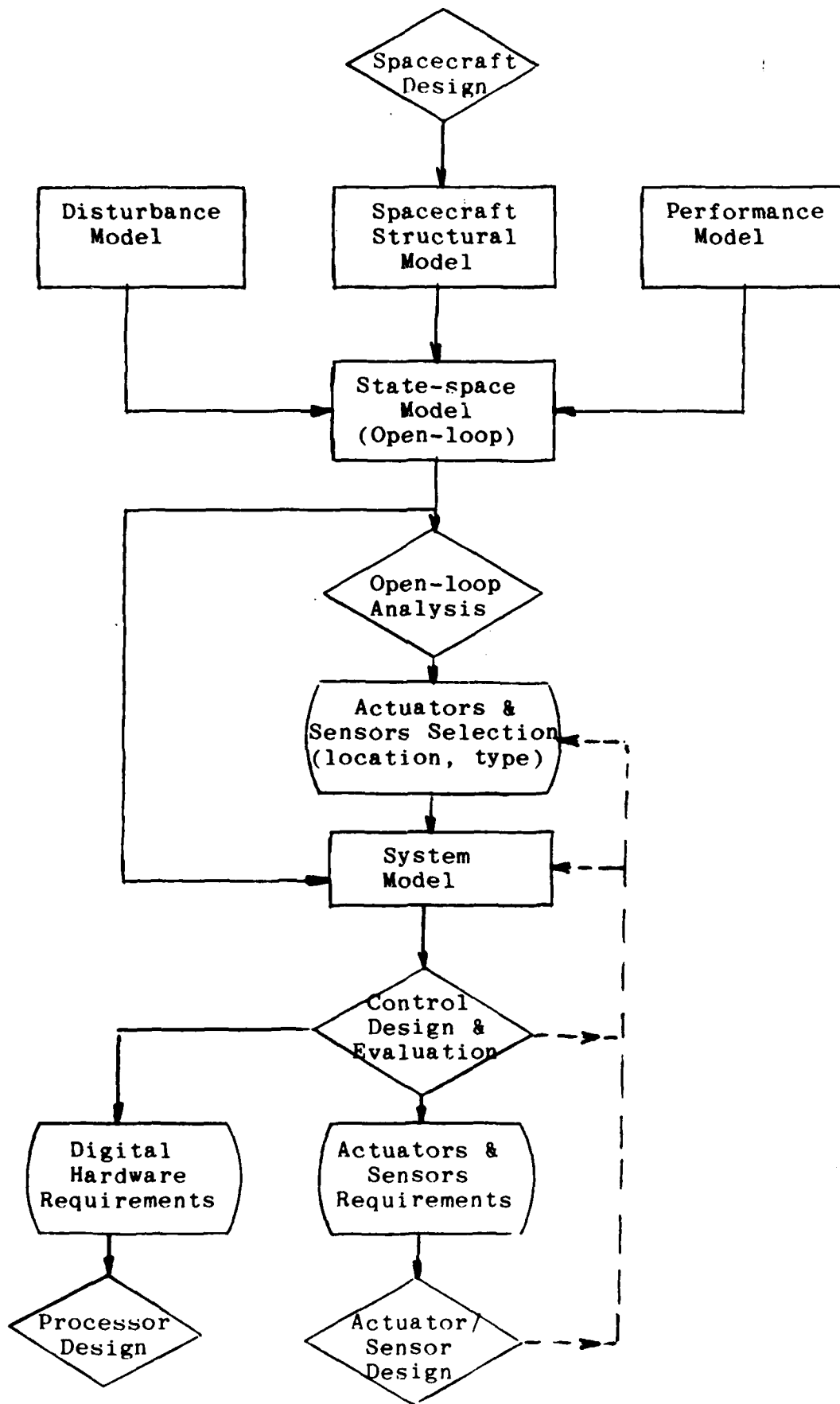


Figure 4. System Design Methodology

Finally, the control design leads also to requirements for the digital (and analog) hardware which in turn drive the choice or design of the microprocessors and electronic compensators.

c. Actuator Selection

The actuator selection process is generally dependent upon the type of performance which is sought. In general, the first step is to "look" at the structure when it is being excited open-loop, and determine what degrees of freedom are moving the most and what are those which are the most responsible for the degradation of the performance. This "look" can be either graphical (movies, computer graphics, displays, etc.) or merely mathematical in nature (controllability maps, etc.). In any case it must be done with a keen sense of the physics of the problem, commonly known as engineering judgment. For instance, in an optical system, the line-of-sight (LOS) error will be a direct function of the motion of a certain critical degrees-of-freedom (dof) of the structure. This relationship is termed the performance metric. If the problem is to stabilize the LOS, the actuators should be placed on the corresponding nodes and act in the direction of the excited dof's. This method leads to far more superior results than stuffing the structure with actuators at all the places which seem to be moving. Certainly the latter will ensure a reduction of the vibration, but will require a tremendous amount of power and, because it was not tailored to the specific problem, the actual LOS performance may not be as good. However, if the full surface of a mirror is to be kept within optical tolerances, the same performance metric method, used for the LOS, may indicate the need for many actuators on that surface.

The more serious question concerns the possibility of further reducing the number of the actuators. Despite the theoretical result from optimal control stating that if all the modes of interest are controllable with one actuator (this just implies that those modes do not have a vibration node at the exact

location of the actuator) then only one actuator is enough to do the job, there are several other considerations which will mandate the use of somewhat more "redundant" set. Between the extremes of one actuator for the whole system and as many actuators as there are degrees of freedom, the optimal number cannot yet be determined by a push-button technique but rather by trials, errors and trade-off studies.

In summary, location will be determined by the performance metric (i.e., at the nodes which have a direct influence on the performance), while the type will depend upon the kind of motions involved. Displacements will call for force actuators, rotations for torque actuators (corresponding to proof-mass actuators or CMG's for instance). But again, because of the necessary redundancy and non-unique solution, there is no hard-line choice in general but only trade-offs at the system's level, and the initial decision may be modified on the basis of the next step of the process, where requirements are defined in terms of power, bandwidth, etc.

d. Sensor Selection

Now that the control system has been given muscle, the sensing system must be selected so that the loop could eventually be closed. Sensor selection is more difficult than its actuator counterpart, because it is related to what the "error signal" is going to be, which is part of the control design.

Thus, although the chart of Fig. 4 shows this process appearing after the open-loop analyses, the dotted line coming from the control design is very important. From open-loop considerations, one may, as for the actuators, place sensors where the motion is maximum and choose the type which will measure either the local displacements or local rotations. In an optimal control design, the goal is to obtain a good estimate for the

state vector, and observability is the criterion. However, in some special cases, specific sensors are sought. For instance, in the case of on-board sinusoidal disturbance, where frequency-shaping techniques play an essential role in the control design, it is important to measure the LOS error, because it is a direct input to the control system. Certainly the LOS error can be estimated--reconstructed from nodal motions measurements--but it is very advantageous to obtain it from a focal plane image processor, for instance, or any other direct means.

The most immediately applicable sensors are the accelerometers and the angular and linear optical sensors. The first give inertial measurements and are straightforward, but the optical sensors give only relative indications and thus their implementation is less obvious because it involves differential motions between parts of the structure. With optical sensors, the idea of a decentralized colocated system has to be abandoned or generalized to bi-located systems which do not lend themselves to simple analytical or practical methods of selection. The process of selection is much more case dependent and has a greater element of arbitrariness.

In summary, location and type of sensors are determined from both open-loop simulations and preconceived ideas on the control system itself, and, like actuators, will depend on the type of performance sought.

2. Actuator Selection and Modeling

Structural actuators can be classified to reflect the duality between translation/force and rotation/torque, as well as the criterion which distinguishes where the reaction forces or torques are transmitted. If these reactions are transmitted back into the structure, the actuators are intrastructural, while if they are transmitted to inertial space, the actuators are inertial. The corresponding classification matrix, with some generic examples, are shown in Figure 5.

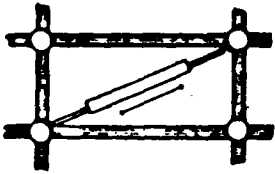

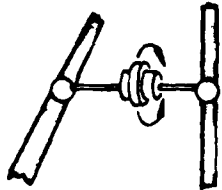

	INTERSTRUCTURAL DAMPERS	INERTIAL DAMPERS
TRANSLATION/FORCE	 <p>TRANSLATIONAL MEMBER DAMPER</p>	 <p>TRANSLATIONAL INERTIAL DAMPER (SOLENOID ACTUATED "PROOF MASS") A: INTEGRATED ACCELEROMETER FOR RATE FEEDBACK</p>
ROTATION/TORQUE	 <p>ROTATIONAL MEMBER DAMPER</p>	 <p>V-CMG DAMPER OR Y-CMG DAMPER</p> <p>ROTATIONAL INERTIAL DAMPER (MOTOR DRIVEN GEARALS, REQUIRES ANGULAR θ RATE SENSOR)</p>

Figure 5. Classification Matrix of Actuators for Vibration Control and Generic Examples

A general property of inertial actuators is their inability to transmit structural vibration energy from one part of the structure to another, as can occur when several intrastructural member dampers are used simultaneously. Nevertheless, non-inertial dampers (other than member dampers) may be required for very low frequencies or global reshaping (e.g., curvature control), rather than just for vibration suppression.

Low frequency and large amplitudes are preferably handled by intrastructural actuators, while lower amplitudes and higher frequencies will use inertial devices. Vibration control actuators have a very typical range of operations as shown in Fig. 6.

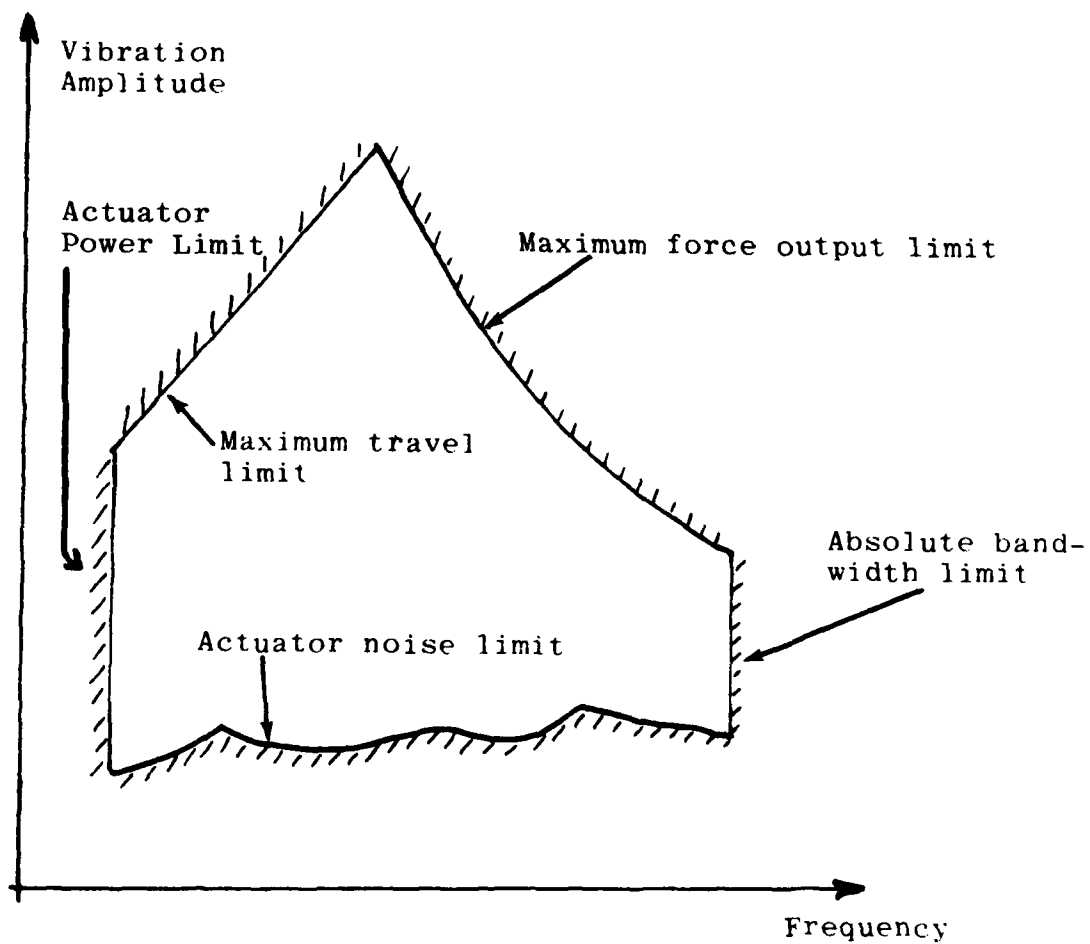


Figure 6. Inertial Actuators Range of Operation

The main design drivers are the travel and force limits. The shape of the travel limit boundary depends upon the type of actuator considered and leads to various types of optimization. Figures 7 and 8 show typical curves for CMG and Pivoted Proof-Mass (PPM) actuators respectively. In the case of the CMGs, two more constraints were considered, the maximum gimbal rate ($\dot{\sigma}_{\max}$) and power dissipation (p_{\max}). The output force limit is expressed in terms of the maximum gimbal acceleration ($\ddot{\sigma}_{\max}$) that the gimbal motor can produce.

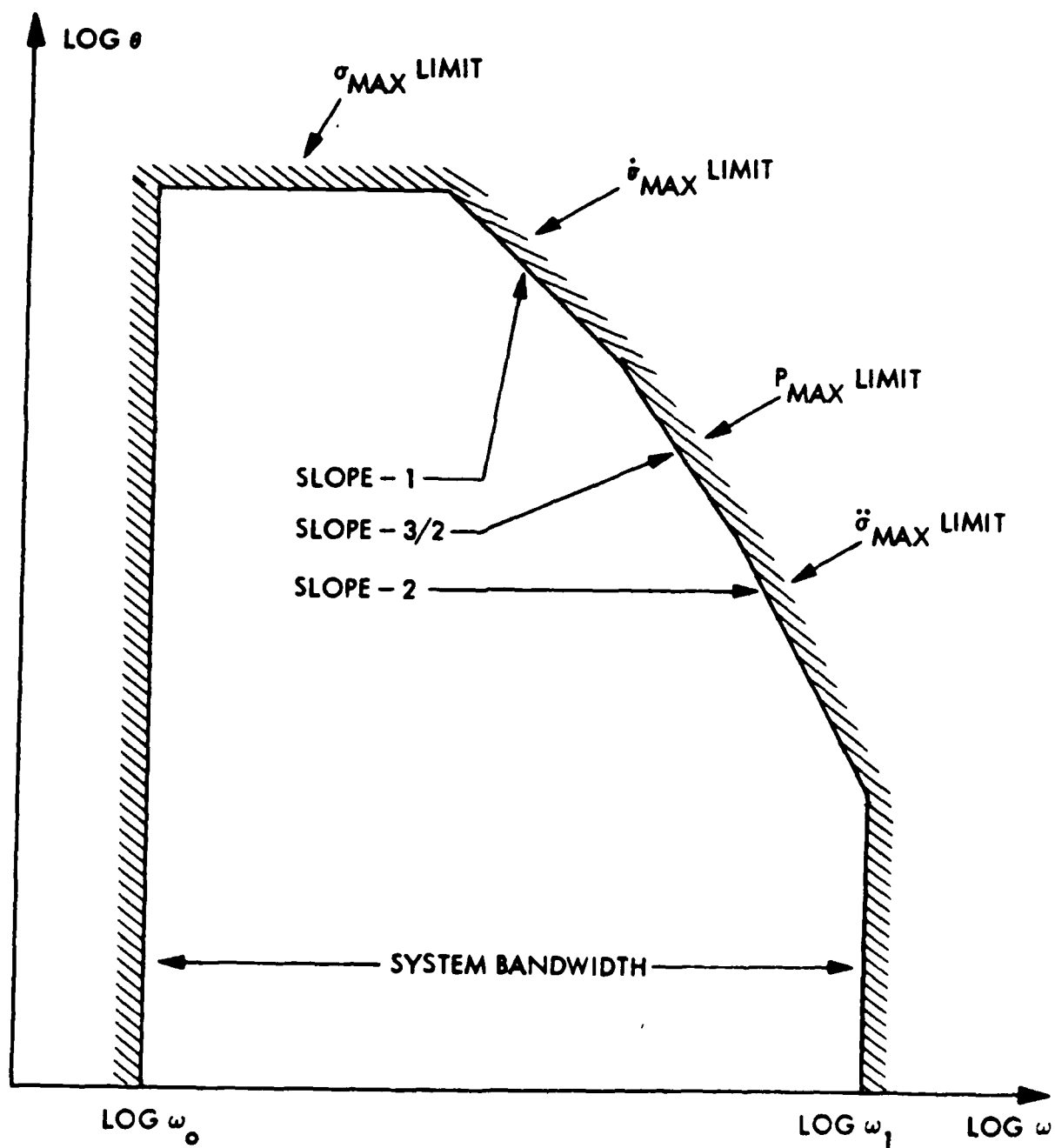


Figure 7. Typical Region of Operation of CMGs

The boundaries of Fig. 8 are derived from the CMG dynamic equations and the equations describing the structural dynamics.

For the purposes of illustration, it is convenient to use a simple example. The linearized equations of motion for a single mode controlled by a single CMG are as follows:

$$J\ddot{\sigma} = K(\dot{\sigma}_c - \dot{\sigma}) + H\dot{\theta} \quad (1)$$

$$\ddot{\theta} + 2\zeta_n \omega_n \dot{\theta} + \omega_n^2 \theta = \phi_n H \dot{\sigma} \quad (2)$$

where θ is the local rotation angle associated with the mode and σ is the CMG gimbal angle; J and H are, respectively, the transverse moment of inertia and angular momentum of the CMG; K is the servo loop gain and σ_c the commanded rate; $\omega_n, \zeta_n,$ and ϕ_n are, respectively, the frequency, damping ratio, and influence coefficient of the mode.

Within the bandwidth of the CMG actuator, $\dot{\sigma}_c = \dot{\sigma}$, and for $\omega = \omega_n$, equation (2) leads to the relation

$$\dot{\theta} = \frac{\phi_n H}{2\zeta_n \omega_n} \dot{\sigma} \quad (3)$$

The various hardware constraints can now be expressed in terms of inequalities involving ω and θ . For instance:

$$\dot{\sigma} < \dot{\sigma}_{\max} \Rightarrow \theta < \frac{\phi_n H}{2\zeta_n \omega_n} \frac{\dot{\sigma}_{\max}}{\omega}$$

$$\ddot{\sigma} < \ddot{\sigma}_{\max} \Rightarrow \theta < \left(\frac{\phi_n H}{2\zeta_n \omega_n} \right) \frac{\ddot{\sigma}_{\max}}{\omega^2}, \text{ etc.}$$

Similar equations may be derived for proof-mass actuators, but in this case instead of a torque ($H\dot{\sigma}$), the actuator produces a force equal to $m\ddot{x}$, where m is the mass of the proof-mass and x its displacement. Equation (3) now has the form:

$$\delta = \frac{\phi_n m}{2\zeta_n \omega_n} \ddot{x}$$

where δ is the local displacement of the structure (where the actuator is attached). Thus the boundaries shown in Fig. 8. Absolute bandwidth is determined from the electrical properties of the system (e.g., AC coupling, windings inductance, etc.).

Design (scaling) curves may be obtained from simplified actuator models to help properly size these devices. Examples are derived below for the CMGs and the PPMs.

a. CMGs

The model equations are:

$$J\ddot{\sigma} = T_G \tag{4}$$

$$T_V = H\dot{\sigma} \tag{5}$$

where T_G is the gimbal torque (produced by the gimbal motor) and T_V the torque produced on the vehicle. The latter is limited by the mechanical strength of the rotor, which is directly related to the wheel cross-section at the shaft. If CMGs of different size are considered, assuming that they are geometrically proportional, and letting L be this geometric scaling factor, T_V will then

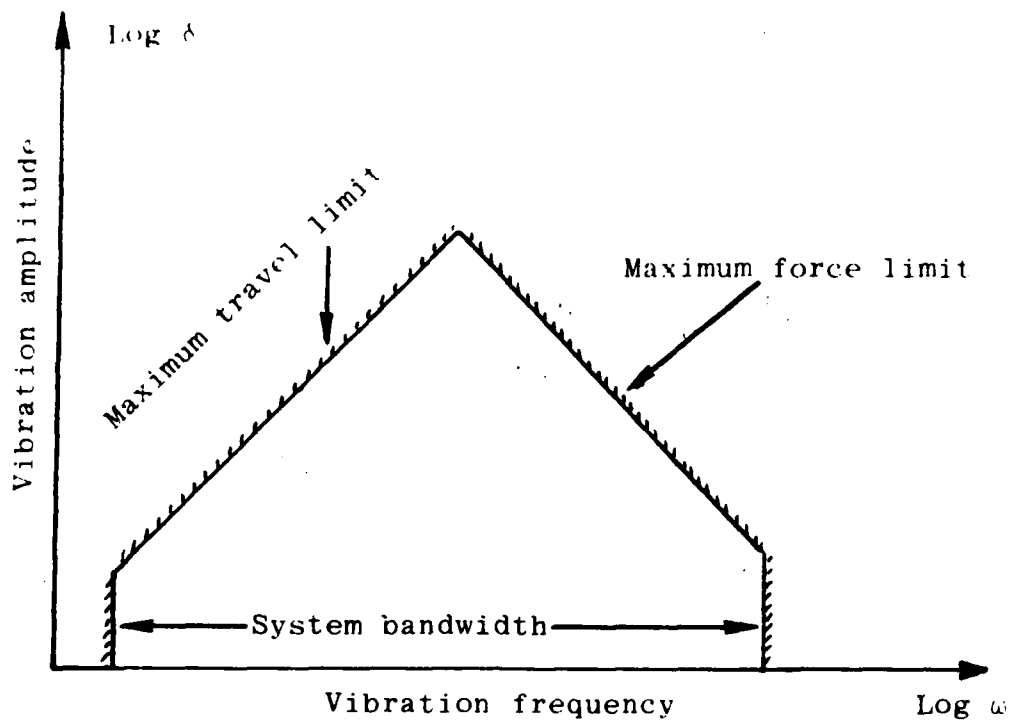


Figure 8. Typical Region of Operation of a Proof-Mass Actuator

vary as L^2 . Similarly the other properties of the CMG may be written in terms of L . Based on simple physical considerations it is possible to establish such scaling factors (the "K" quantities in the following expressions):

$$J = K_J L^5 \text{ (spin inertia)}$$

$$H = K_H L^4 \text{ (momentum)}$$

$$T_V = K_T L^2 \text{ (output torque)}$$

$$T_G = K_G L^2 \text{ (gimbal torque)}$$

Other quantities may be derived from these scaling laws, such as $\dot{\sigma}_{\max}$ or $\ddot{\sigma}_{\max}$ which are more currently used by gyro manufacturers:

$$\dot{\sigma}_{\max} = (K_T/K_H) L^{-2}$$

$$\ddot{\sigma}_{\max} = (K_G/K_J) L^{-3}$$

Assuming that the maximum angular travel σ_{\max} is used, and a sinusoidal excitation, (4) and (5) yield:

$$T_V = H\sigma_{\max}\omega = K_H\sigma_{\max}L^4\omega \leq K_T L^2$$

$$T_G = J\sigma_{\max}\omega^2 = K_J\sigma_{\max}L^5\omega^2 \leq K_G L^2$$

Thus the conditions:

$$L^2\omega \leq (K_T/K_H) \sigma_{\max}$$

$$L^3\omega^2 \leq (K_G/K_J) \sigma_{\max}$$

A nomogram such as the one shown in Fig. 9 may then be used for sizing.

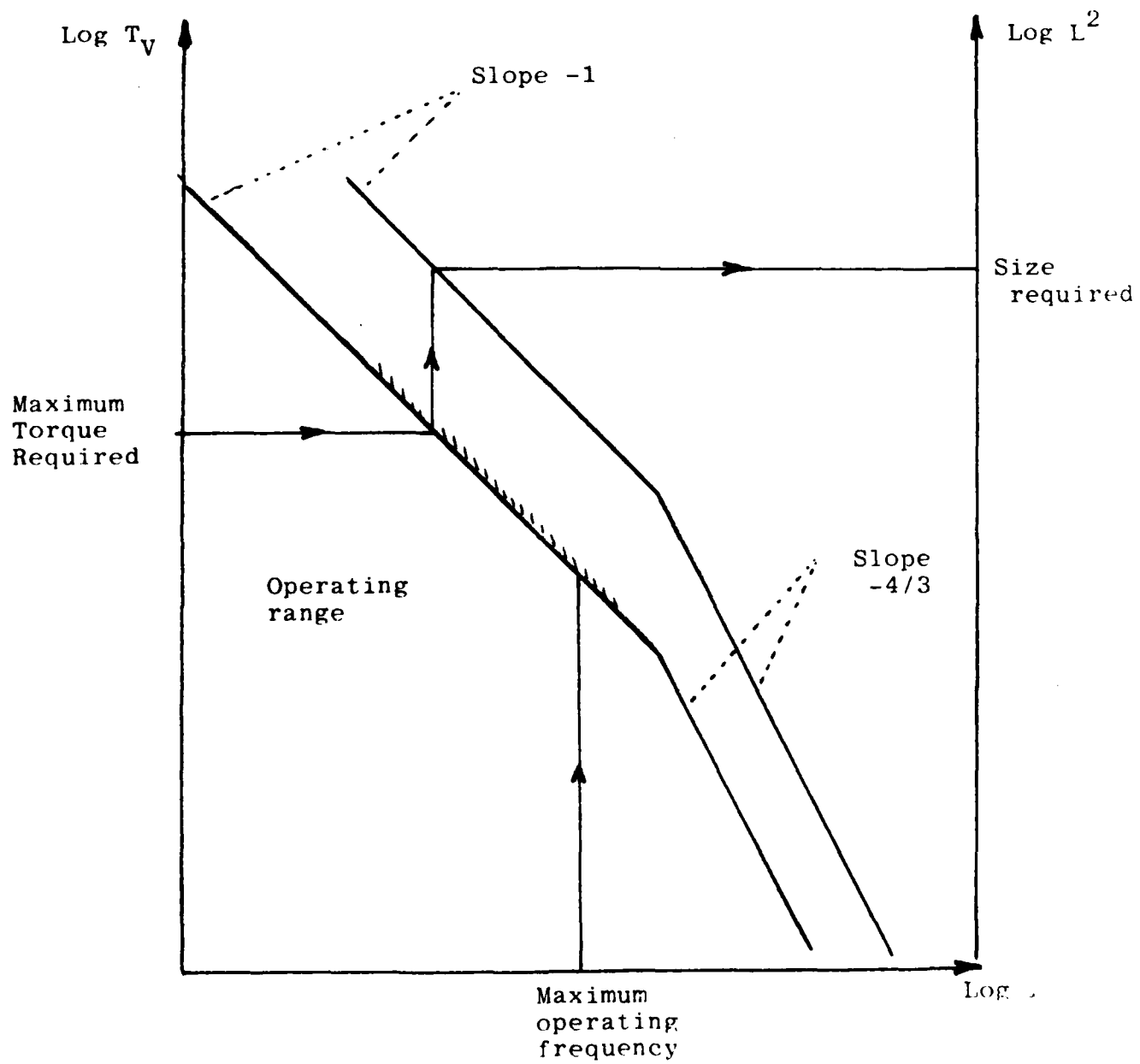


Figure 9. CMG Sizing

b. PPMs

Similar curves may be obtained for the PPMs. The dynamic model shown in Fig. 10 leads to the following linearized equations:

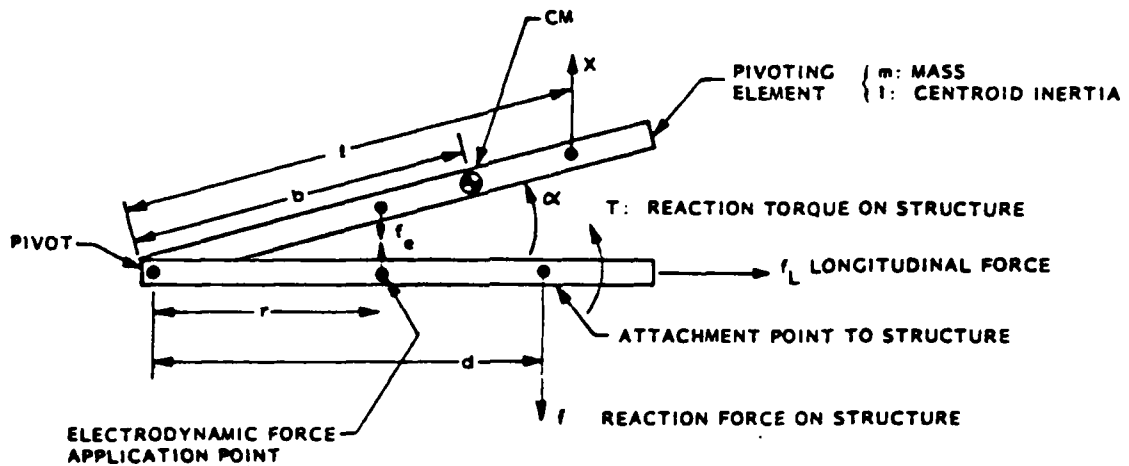


Figure 10. PPM Actuator Dynamics Model

$$f \equiv mb\ddot{\alpha} \quad (6)$$

$$T \equiv (I + mb^2 - mbd)\ddot{\alpha} \quad (7)$$

where

$$\ddot{\alpha} = \frac{rf_e}{I + mb^2} \quad (8)$$

Equation (7) shows that it is possible to have no torque transmitted to the structure by choosing the attachment point at the distance

$$d_0 = (I + mb^2)/mb \quad (9)$$

Varying d above or below this value will change the sign of the output torque as well as its magnitude. The mass of the PPM actuator and its CM may be adjusted by changing the position and mass of a lead piece situated at the distance ℓ from the pivot point.

Let b_o , m_o and I_o be respectively the position of the CM, the mass and the inertia with respect to the pivot of the "unloaded" actuator, and m_1 the mass of the lead piece with which it is loaded. Then

$$\begin{aligned}
 m &= m_o + m_1 \\
 b &= \frac{m_o b_o + m_1 \ell}{m} \\
 I &= mb^2 = I_o + m_1 \ell^2
 \end{aligned}
 \tag{10}$$

and using Eqs. (6) and (8) shows that

$$f/f_e = \frac{1 + m_o b_o / m_1 \ell}{1 + I_o / m_1 \ell^2} \frac{r}{\ell}
 \tag{11}$$

There are two important parameters in the design and use of PPM actuators besides the mass/inertia properties mentioned previously:

- (1) f_{em} = maximum electrodynamic force
- (2) α_m = maximum angular displacement

Since the angular displacement α depends upon the frequency, optimal choices for the design parameters will depend upon the frequency range of application. From the two conditions

$$|f_e| \leq f_{em}$$

$$|\alpha| \leq \alpha_m$$

and Eqs. (6), (10) and (11), two new conditions are found:

$$|f| \leq \frac{1 + m_o b_o / m_1 \ell}{1 + I_o / m_1 \ell^2} \frac{r}{\ell} f_{em} \quad (12)$$

$$|f| \leq (1 + m_o b_o / m_1 \ell) m_1 \ell \omega^2 \theta_m \quad (13)$$

when $\omega/2\pi$ is the frequency of the output force.

These two limits are shown on Fig. 11 as functions of ℓ/r for a prototype PPM actuator whose characteristic parameters are shown in Table 3.

TABLE 3 CHARACTERISTIC PARAMETERS OF PROTOTYPE PPM ACTUATOR

Mass	Geometry	Electrodynamic
$I_o = 1.5 \cdot 10^{-5} \text{ kgm}^2$	$b_o = .016 \text{ m}$	
$m_o = .088 \text{ kg}$	$r = .021 \text{ m}$	$f_{em} = 1 \text{ N}$
	$\theta_m = .067 \text{ rad}$	

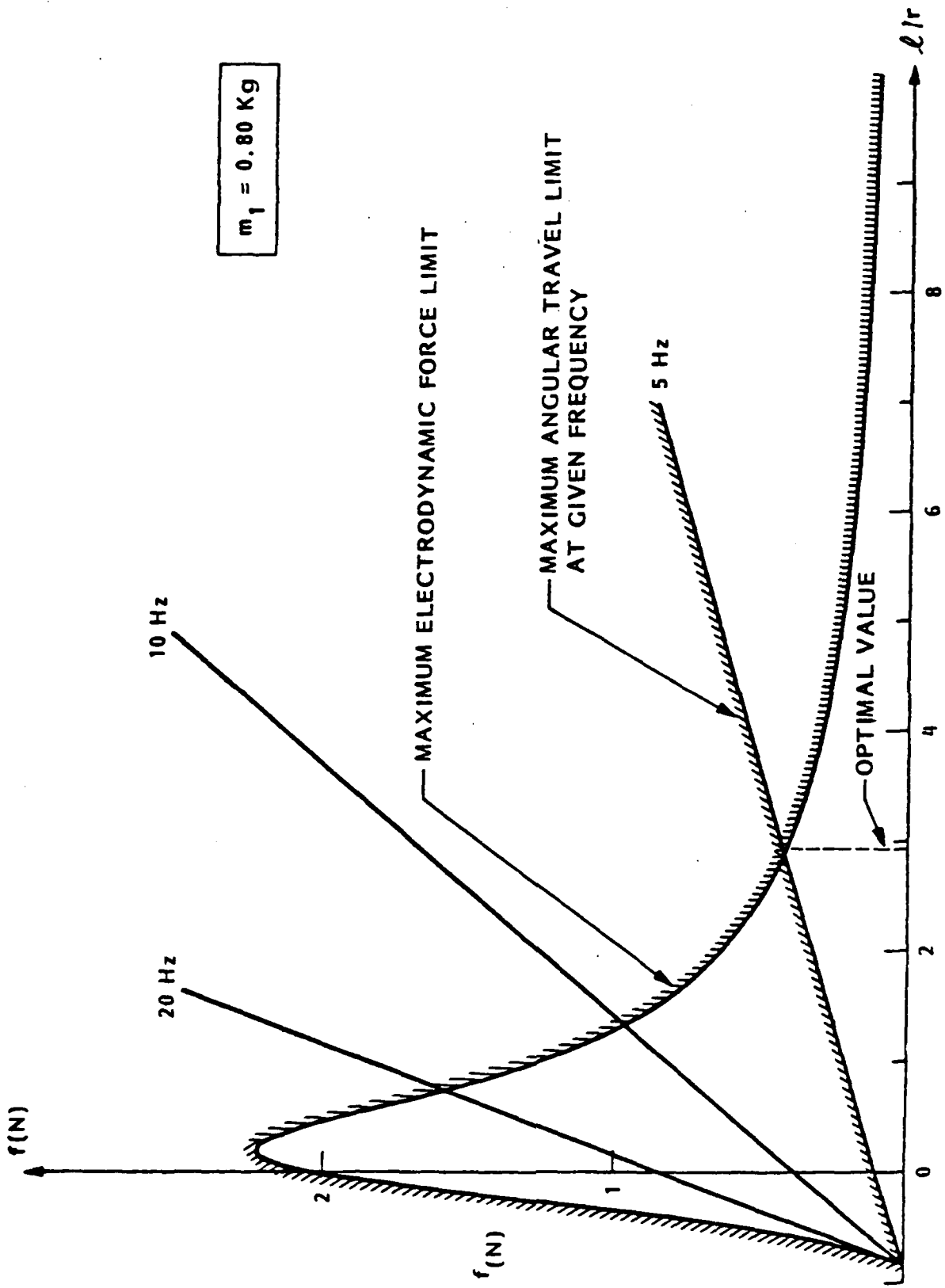


Figure 11. PPM Actuator Design - Performance Region (f, l)

An optimal value for l/r is obtained at the intersection of the two curves. Assuming that this optimal value is always used in the design, it is then possible to proceed with design curves by relating the various parameters to the geometric scaling factor L . Fig. 12 shows a set of such curves for various values of the ratio $x = m_1/m_0$. The value $L = 1$ corresponds to the existing prototype actuator. For desired values of f and ω , a point is chosen on the right vertical axis. Intersecting the corresponding horizontal line with the first set of curves ascending gives values for L . Then the optimal l/r ratio is obtained with the other set of curves (descending).

c. Actuator Models

(1) CMG Model

This model is linear and includes the interaction between the structure and the CMG. Defining the gimbal axis by the unit vector \bar{g} and the nominal position of the momentum vector by the unit vector \bar{h} , the following equations hold:

$$J\ddot{\sigma} = T_g + H\bar{c} \cdot \bar{\omega} \quad (14)$$

$$\bar{T}_V = -\bar{c}\dot{\sigma} \quad (15)$$

where $\bar{c} = \bar{g} \times \bar{h}$ and $\bar{\omega}$ is the local angular rate of the structural element to which the gyro is attached.

(2) PPM Model

This linear model is as follows:

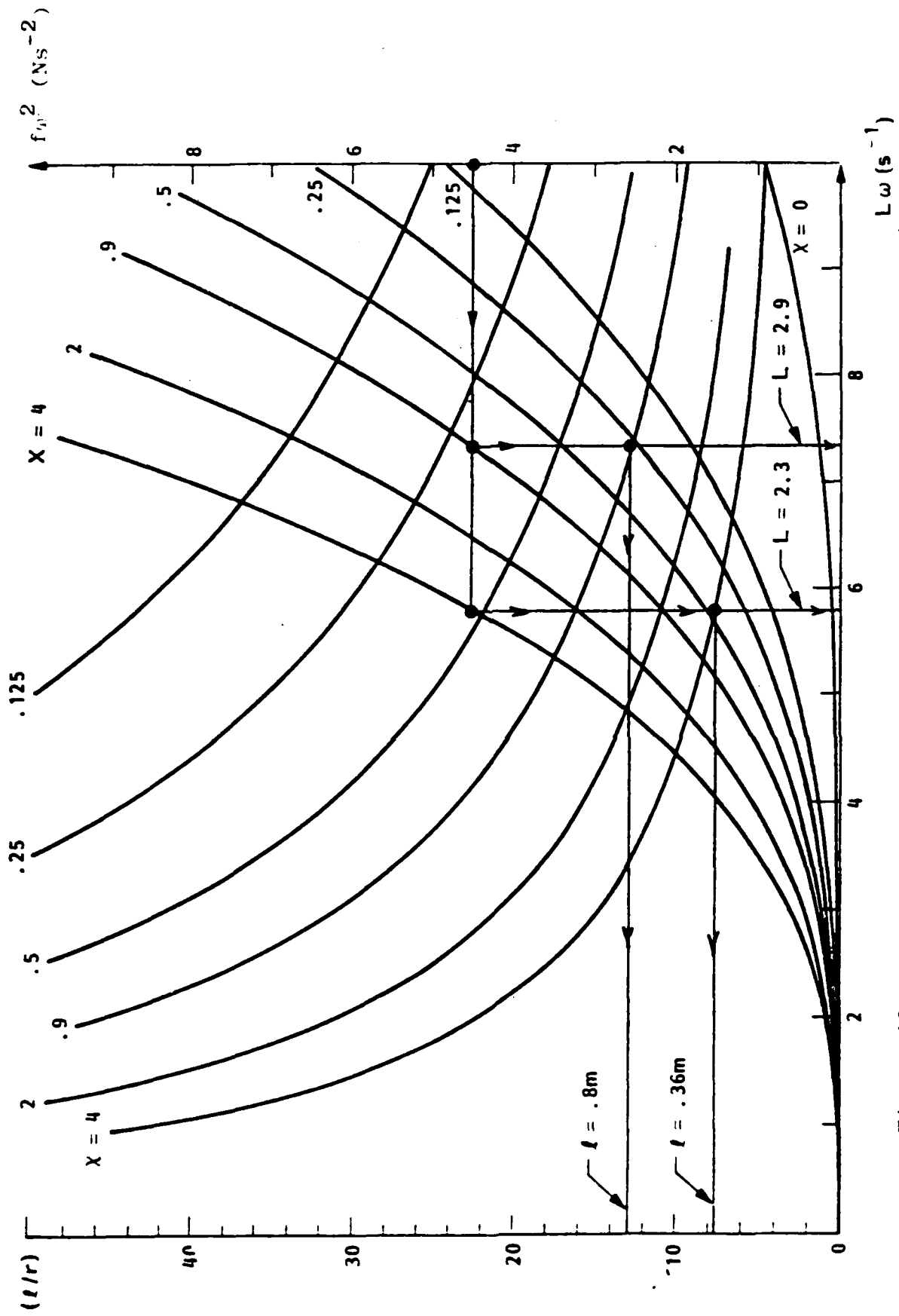


Figure 12. PPM Actuator Design Curves ($x = m_1/m_0$ as a Parameter)

Assuming that the application point is chosen according to Eq. (9) (no torque produced) the PPM equations may be written as:

$$m\ddot{x} + k(x-\delta) = f \quad (16)$$

$$f_v = -f \quad (17)$$

where k is the flex pivot spring constant, x the inertial displacement of the center of mass of the PPM actuator moving arm, δ the local displacement of the structure, and f_v the reaction force seen by the structure; f is related to the electrodynamic force f_e by the equation (11).

3. SENSOR SELECTION AND MODELING

The primary sensors selected for the VCOSS design study are accelerometers. These devices provide the most practical and lowest cost sensing alternative for vibration rejection and are relatively easy to model. Optical systems used outside the laboratory environment will have to deal with complex geometries, base motion compensation, and other issues too complex to model in the present study. Trade studies conducted in Phase II with these basic sensors will provide a foundation for studying more complex mechanizations later in the program.

a. Background

Accelerometers of the piezoelectric type (PZT) have been extensively used for structural modal testing and, recently, for feedback control associated with large space structure stability augmentation. Although PZT mechanizations offer rugged, low-cost instrumentation, high noise PSD at low frequencies may make them unsuitable for LSS control applications. For system identification, where ensemble averaging and advanced signal processing techniques can improve signal-to-noise ratios, the PZT devices may still be adequate, though for real-time control between 0.5 and 10 Hz these devices may be excessively noisy. Inertial grade servo force rebalance and PIGA (pendulus integrating gyro accelerometer) types can provide substantially higher performance at lower frequencies if one to two orders of magnitude cost increase can be justified over the laboratory grade PZT.

b. Typical Inertial Grade Accelerometer Performance

The noise PSD for a generic inertial grade accelerometer is shown in Figure 13. This behavior is representative of all high-performance accelerometers such as the Bell model 7 and others listed in the CSDL data of Table 4. Above 0.5 Hz (3 rad/sec)

the noise spectrum is essentially white with an RMS acceleration resolution on the order of 10^{-8} m/sec². Below 0.5 Hz the response is dominated by 1/f noise down to about 10^{-3} rad/sec. Below this frequency, bias and drift stability issues dominate the performance, which varies from instrument to instrument, and such values are difficult to measure. For LSS control, the region above 0.5 Hz is probably the most practical one.

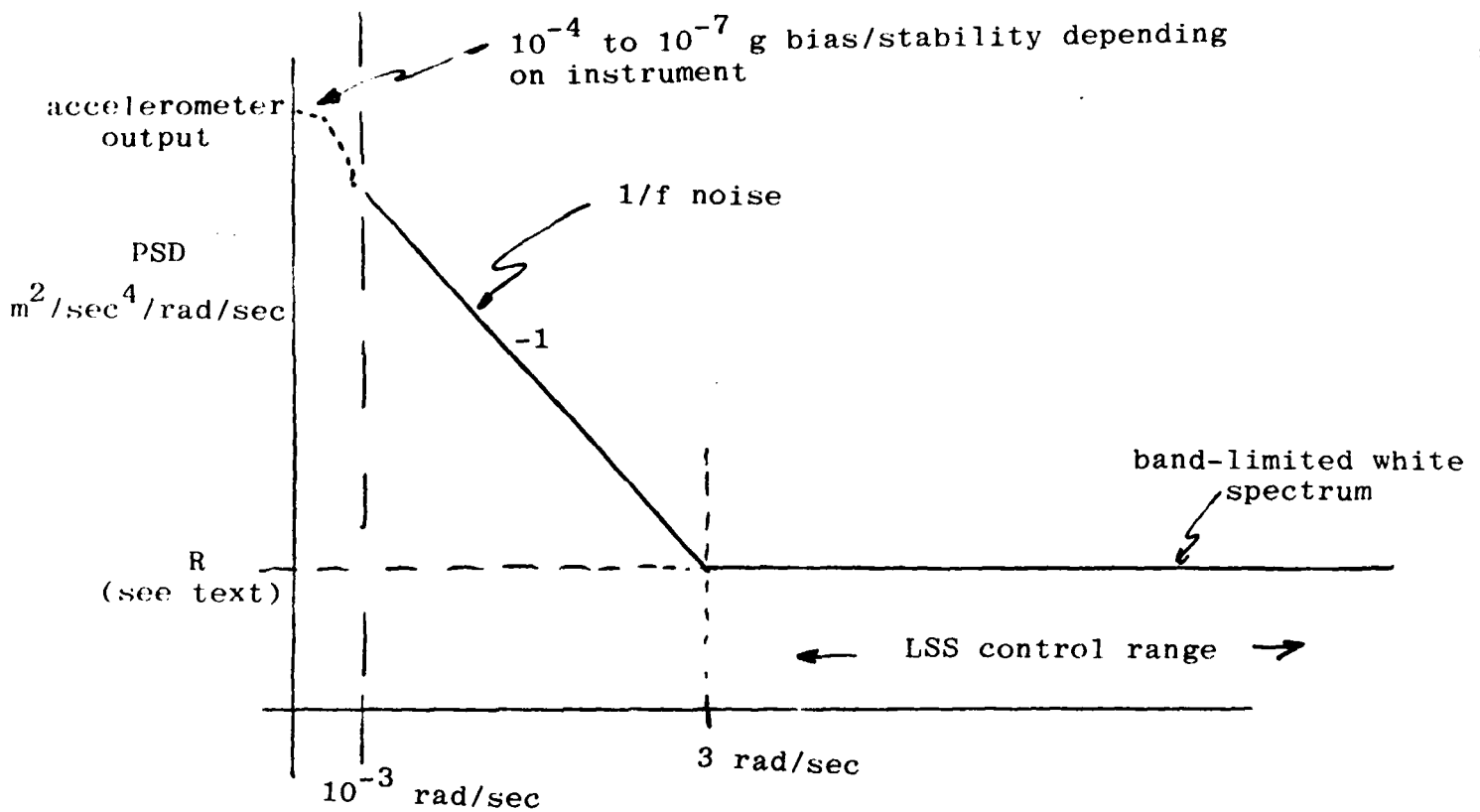


Figure 13. Typical Inertial-grade Accelerometer Noise PSD

TABLE 4 INERTIAL GRADE SPACE ACCELEROMETERS

Manufacturer	Model	Type	Size (In.)	Weight (gm)	Power (W)	Drift	Noise	Bandwidth (Hz)	Applications	Comments
CSDL	10 PICA (Moneywell)	SOOF, floated	2.0 x 3.42	495	2.3	*		~30	Trident II	
CSDL	SP1R (Moneywell)	SOOF, floated	2.8 x 3.4	740		*			MS	
Bell	NI	Pendulous force rebalance	1.425 x 0.9 L = D	48	1.5	0.01 ug 1 h, 10	0.1 ug (0.1-100 Hz) Gradiometer version	40-300		40 Hz at 450 v max 300 Hz at 100 g max
Bell	MESA (Miniature Electrostatic accelerometer)	Electrostatic proof mass rebalance (low g)	3.5 x 3.0 x 0.5	2500	8	NA	NA		Spacecraft	
Kearfott	2401		2 x 1.13 x 1.0	127		7 ug, 1 h	NA	25	DIGS, AHS, IUS, Shuttle, K-70	
Sundstrand	Q Flex	Dry	1.0 x 1.0	80		15 ug 1 h, 10	NA	80	Harpoon Blk 50	
Systron Donner	4841	Servo force balance pendulum	1.5 x 2 x 1.0	200	1.5 peak	2 ug 1 h, 10			Delta, Trident Sub. Lance, Titan III D.	

For the white portion of the spectrum, the spectral intensity, R , is typically (BW denotes bandwidth)

$$\sigma^2 = R(\text{BW})$$

$$(10^{-8} \text{ m/sec}^2)^2 = R (0.1 \text{ rad/sec})$$

$$R = 10^{-15} (\text{m sec}^2)^2 / \text{rad/sec} .$$

Thus, over a 100 rad/sec typical useful operating range for LSS control (above 0.5 Hz), the RMS noise observed is

$$\sigma^2 = [10^{-15} \text{ m/sec}^2 \text{ sec}^{-1}] 100 \text{ rad/sec}$$

$$\sigma = 3 \times 10^{-7} \text{ m/sec}^2 = 30 \text{ ng}$$

Values as low as 0.3 ng may be achievable with instrument modifications and greatly increased costs. Cost of "standard" instruments should range from \$5K to \$15K which probably does not include space qualification and certainly does not include special modifications.

c. Applications

For space structure control including vibration rejection on precision optical surfaces, figure error at near IR is

$$|\Delta y| = \text{Displacement} = \frac{\lambda}{20} = \frac{2.7}{20} \mu\text{m} = 0.135 \mu\text{m} .$$

For sinusoidal deflection of the surface,

$$\Delta y = |\Delta y| e^{j\omega t}$$

$$\begin{aligned} \text{and } |\Delta \ddot{y}| &= \omega^2 |\Delta y| \\ &= (0.135 \mu\text{m}) \omega^2 \end{aligned}$$

at $\omega = 0.5 \text{ Hz}$ (3 rad/sec)

$$|\Delta \ddot{y}| \cong 1 \mu\text{m}/\text{sec}^2 = 0.1 \mu\text{g} = 100 \text{ ng}.$$

Thus, precision optical surfaces should be controllable to $\lambda/20$ tolerances down to 0.5 Hz with a signal to noise ratio of better than 3 to 1 at low frequencies. This S/N improves rapidly, as the frequency squared, at higher frequencies. The degraded signal to noise at low frequency will probably not have a significant impact on system performance due to the overlap between figure control and vibration control systems at low frequency. Figure sensing systems will control deformation below 0.5 Hz using absolute position measurement with $S/N > 10^3$. For non-precision structural deformations, control tolerances can be relaxed by at least an order of magnitude which will yield an $S/N \geq 30$.

d. Preliminary Conclusions

Although microvibration control will be difficult with PZT type instruments, high performance should be attainable with currently available inertial grade accelerometers, especially

those designed for gradiometer applications. Signal processing electronics may require some redesign but noise levels well below 50 ng should be achievable in the frequency range 0.5 - 15 Hz. Commercial versions, possibly already flight qualifiable, should cost between \$5K and \$15K. Ultra-high performance types such as Bell Mesa might cost \$100K/unit. Sensing below 0.5 Hz will be handled by the figure/alignment control system sensor which, typically, will be an optical measurement instrument.

In the frequency range of interest, sensor dynamics are not of any particular concern since actuator dynamics will dominate system behavior much earlier in the spectrum. These devices can be modeled effectively using only bias, scale factor, and white additive measurement noise terms.

4. SIGNAL PROCESSING

Difficulties experienced in VCOSS Phase IA with digital implementation have led to new signal processing architectures to achieve high sample rates for multivariable controllers. New architectures, discussed near the end of this section, will remove sampling rate constraints, but in so doing, raise the issue of filter stability vs. wordlength. These issues are discussed first. The basic signal processing issues for LSS control are:

- Wordlength and algorithm selection for
 - Minimum pole shift (robustness)
 - Mechanization stability
- Sample rate selection
 - Constraints imposed by stability
 - Constraints imposed by architectures
 - Architecture assessment/memory requirements
- Requirement for anti-aliasing filters

- Other investigations
 - Quantization effects and controller roughness
 - Throughput capacity and efficiency
 - Flexibility, fault-tolerance
 - Emulation of large spacecraft model

Some of these issues are discussed below.

a. Multivariable Flight Control

Multivariable control methods have been highly successful for designing complex control systems for multi-input/multi-output systems. To apply multivariable control methods to flight control, the spacecraft is generally represented by the equations of Table 3.

Multivariable control design is based on the quadratic cost functional shown in the table which produces the closed-loop feedback control law.

When the state x is not measured, x must be estimated from sensor outputs using the Kalman filter also shown in the table.

In the steady-state, the control and filter gains are constant and can be solved off-line for C and K . C and K can then be used to compute u and x in real time. Therefore, the real time calculations required to implement a steady-state multivariable controller are given in Table 3.

The real time implementation can be performed by analog or digital circuits. However, the digital implementation is often more flexible since it can be easily modified.

TABLE 5 STEADY-STATE IQG CONTROLLER FORM

MULTIVARIABLE CONTROLLER EQUATIONS

<u>State and Measurement Equations:</u>	$\dot{\bar{x}} = F\bar{x} + G\bar{u} + w$	
	$y = H\bar{x} + v$	
<u>Control Design:</u>	$J = \int_0^T (\bar{x}^T A \bar{x} + \bar{u}^T B \bar{u}) dt$	penalty functional
	$\bar{u} = C\bar{x}$	control structure
	$SF + F^T S + A - SGB^{-1}G^T S = 0$	steady-state control gains
	$C = -B^{-1}G^T S$	
<u>Filter Design:</u>	$J = \int_0^T (w^T Q w + v^T R v) dt$	noise covariances (weightings)
	$\dot{\hat{x}} = F\hat{x} + G\bar{u} + Kv$	filter structure
	$v = y - H\hat{x}$	
	$FP + PF^T + Q - PH^T R^{-1} HP = 0$	steady-state filter gains
	$K = PH^T R^{-1}$	

Kalman Filter: $\hat{x}_{k+1} = \phi \hat{x}_k + \Gamma u_k + K(v_k - H \hat{x}_k)$

Control Law: $u_k = -C \hat{x}_k$

where ϕ and Γ are discrete versions of F and G .

• Implementation Equation

$$\begin{pmatrix} \hat{x}_{k+1} \\ u_k \end{pmatrix} = \underbrace{\begin{bmatrix} F_{11} & F_{12} \\ F_{21} & F_{22} \end{bmatrix}}_{\text{control design matrix}} \begin{pmatrix} \hat{x}_k \\ v_k \end{pmatrix}$$

where $F_{11} = \phi - KH - \Gamma C$, $F_{12} = K$, $F_{21} =$ and $F_{22} = \Gamma$

By examining the steady-state controller equations it is clear that only matrix-vector multiplication is required for implementation. The matrix elements, which are constant in the steady-state designs, can be stored in memory for each flight condition. These observations form the basis for the architecture described later.

b. Stability Analysis

Because of modeling uncertainties, it is important to examine the margin of stability associated with the computations. Figure 14 gives a geometric interpretation of a stability margin in the z -plane. $|z|$ represents the magnitude of poles of $H(z)$ and $|\Delta z|$ is the distance from $|z|$ to the edge of the unit circle. The magnitude of $|\Delta z|$ is dependent on a number of factors such as modeling uncertainties and finite wordlength considerations. From an analysis viewpoint, it is convenient to lump these considerations into a perturbation of F_{11} and analyze the stability of the eigenvalues of $F_{11} + \Delta F_{11}$.

If F_{11} is perturbed to $F_{11} + \Delta F_{11}$, then the corresponding change in the eigenvalues of F_{11} , can be estimated from the formula shown in Table 6.

c. Wordlength Considerations

The formula in Table 7 represents an effective numerical test for rapidly determining the minimum number of bits required to implement a given digital flight control law. The magnitude of the maximum eigenvalue of F_{11} is the parameter which defines the margin of stability. The equation was evaluated for different values of λ_{\max} and n . The results are shown in Figure 15. Note that the number of bits required for stability increases substantially as $\lambda_{\max} + 1$ and as n increases.

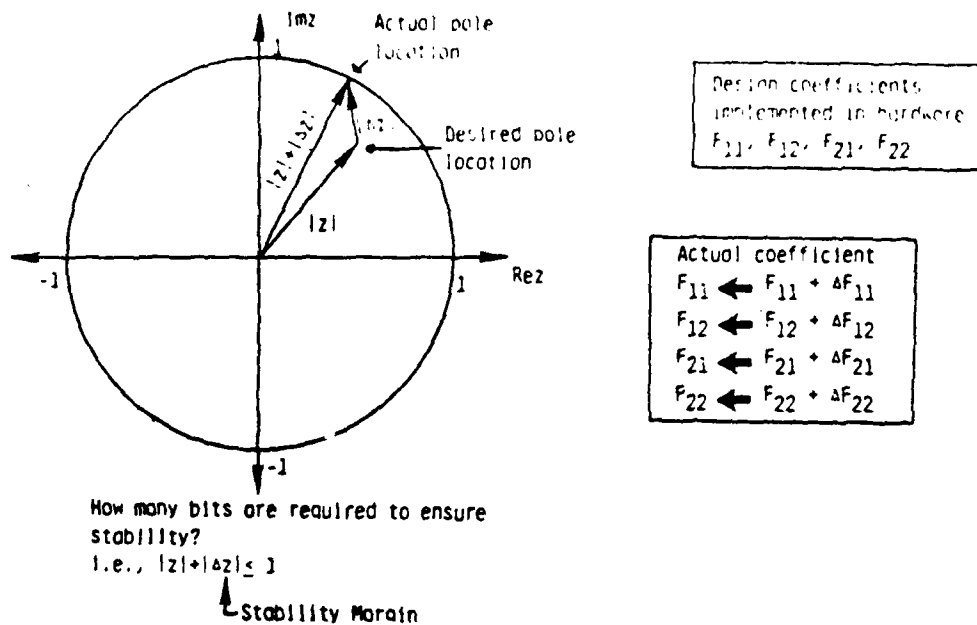


Figure 14. Wordlength Effect on Coefficient Perturbation and Stability

Table 6. EIGENVALUE PERTURBATION AND STABILITY CONDITION

For the discrete controller

$$\hat{x}_{k+1} = F_{11} \hat{x}_k + F_{12} y_k$$

$$u_k = F_{21} \hat{x}_k$$

If $F_{11} = F_{11} + \Delta F_{11}$, then the change in the eigenvalues of F_{11} are given by Jacobi's formula:

$$\Delta \lambda_i = v_i^T \Delta F_{11} u_i \quad i = 1, 2, \dots, n$$

where u and v are the right and left eigenvectors, respectively, of F_{11} and $v_i^T u_i = 1$.

For stability in z-plane,

$$|\lambda_j + \Delta \lambda_j| \leq |\lambda_j| + |v_j^T \Delta F_{11} u_j| \leq 1$$

$$|v_j^T \Delta F_{11} u_j| \leq 1 - |\lambda_j|$$

Stability Margin

TABLE 7 MINIMUM NUMBER OF BITS TO ENSURE CONTROLLER STABILITY

• Perturbation in F_{11}

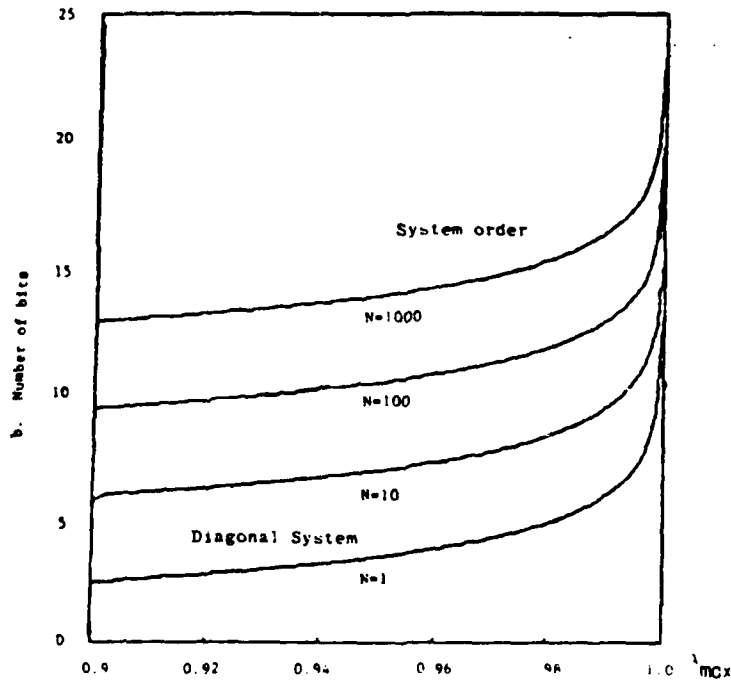
$$F_{11} = F_{11} + \Delta F_{11} \text{ where } \|\Delta F_{11}\|_{\infty} \leq \frac{m}{2} 2^{-b}$$

where b is the number of bits, and n is the system order

• Stable Control Computations Require

$$b = \left\lceil -(1 + \log_2 ((1 - \lambda_{\max})/n)) \right\rceil \geq 0$$

$$\text{where } \lambda_{\max} = \max_{1 \leq i \leq n} |\lambda_i|$$



16-bits are adequate for most problems

Figure 15. Minimum Number of Bits for Stable Control Computations

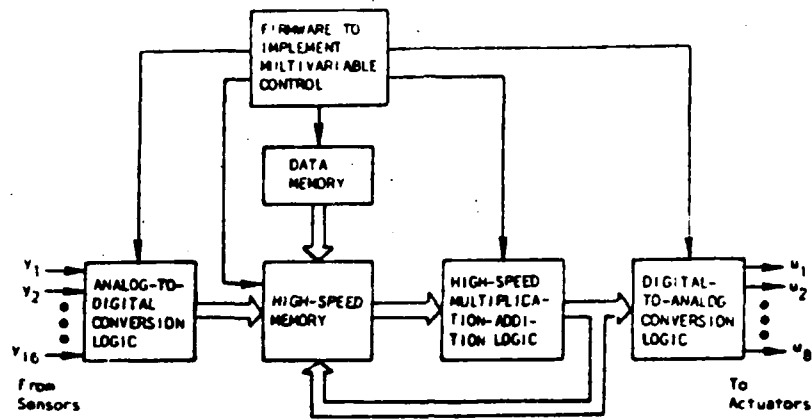
** Table 8 and Figure 16 DELETED **

This formula represents an effective numerical test for rapidly determining the minimum number of bits required to implement a given digital flight control law. The magnitude of the maximum eigenvalues of F_{11} is the parameter which defines the margin of stability $= 1 - \lambda_{\max} = \Delta\lambda$. The equation was evaluated for different values of λ_{\max} and n . The results are shown in Figure 15. Note that the number of bits required for stability increases substantially as $\lambda_{\max} \rightarrow 1$ and as n increases. Because λ_{\max} is directly related to the sampling rate ($1/\Delta\tau$), Figure 15 indicates, therefore, that at high sampling rates, a large number of bits are needed to keep the computations stable. Since the improvement in stability is marginal beyond 16 bits, a 16 bit arithmetic processor is used.

d. Architecture of the Controller

The architecture of the processor is centered around a high-speed matrix-vector multiplier (see Figure 17). The control design matrix elements are stored in data memory and then downloaded into a high-speed RAM. The analog measurement data are converted to digital form by a high-speed, 12-bit, A/D converter. The results are stored in a high-speed RAM along with the state estimates. The control law is then evaluated by multiplying the control-design matrix by the state estimates and measured data in RAM. A high-speed, 16-bit hardware multiplier/adder performs the matrix multiplications and additions required. All addresses for the RAMs and hardware multiplier/adders are generated by the firmware. The digital controls are then sent to a 12-bit D/A converter. The D/A converts the digital controls to analog signals which are stored in sample-and-hold circuitry. Once the controls have been updated, the controls are simultaneously sent to the actuators.

In phase II of the VCOSS program, digital emulations like the illustration above will be used to assess signal processing hardware effects on the CSDL #2 system.



Architecture has been optimized for control/
filtering computations.

Figure 17. An Architecture for High-Speed Control

SECTION III

MODEL INTEGRATION

1. VCOSS MODEL DESCRIPTION

This section describes the evolution of the VCOSS systems model from the original CSDL data. Development of complex control design and evaluation models has historically been a team effort involving many validation processes to assure that structural data and performance matrices correctly represent the physics of the problem. This model development process has been followed for VCOSS and some of the modeling revisions are discussed now. This validation process is essential to the synthesis of meaningful and physically implementable controls and to the accurate assessment of control system/vehicle performance.

The structural model used for the VCOSS control design is the Charles Stark Draper Laboratory (CSDL) model #2 (revision #3) (Figures 18 and 19). Model #2 was described in CSDL report C-5437 dated September 1981 (ref. 7) and revision #3 was described in CSDL memo entitled "VCOSS Design Model and Disturbances" dated November 12, 1981 (ref. 8).

Listed here (in items 1a - h) are additional points of information that are needed to create the VCOSS revision #3 model which are not covered by either of the aforementioned CSDL documents.

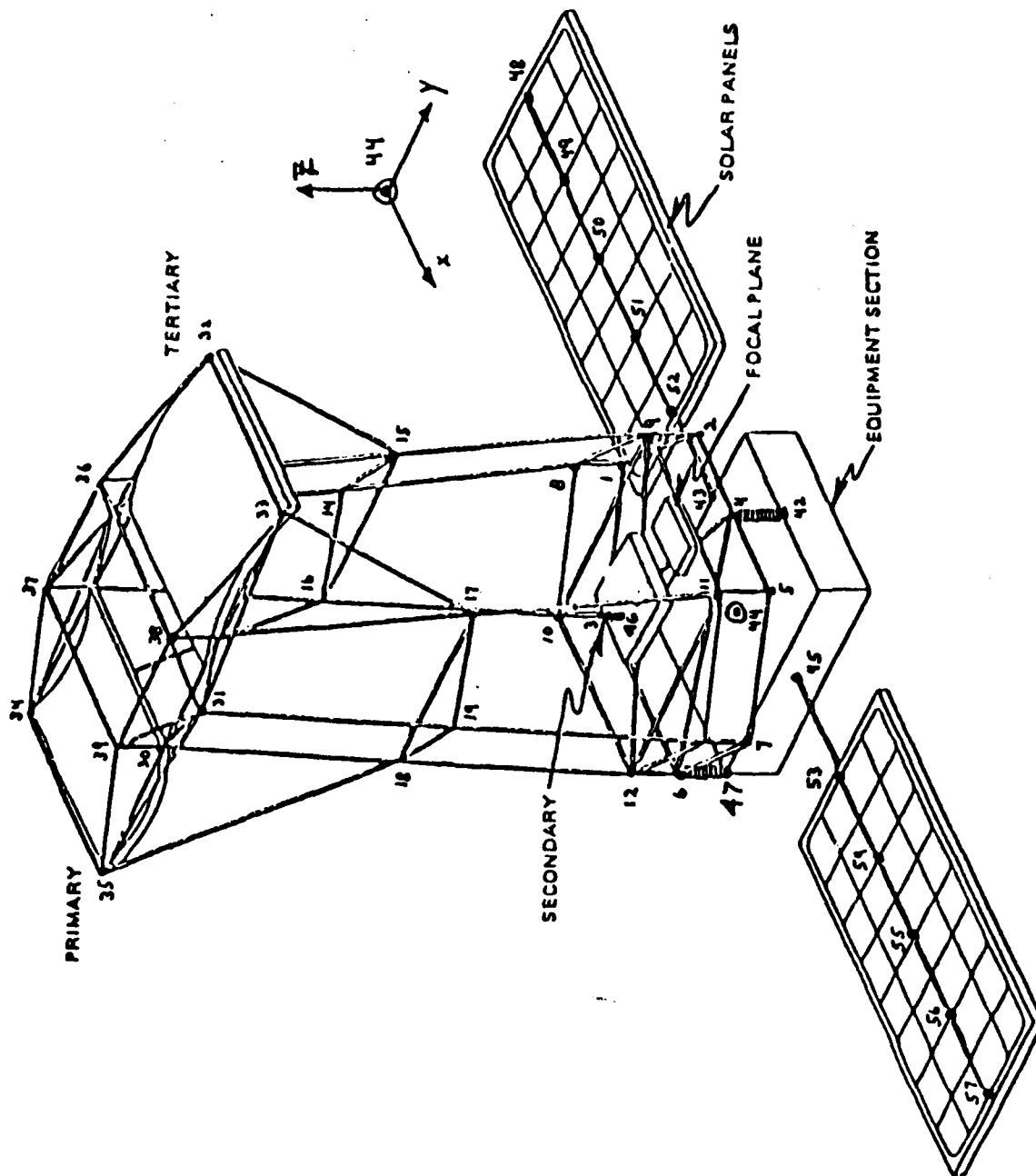
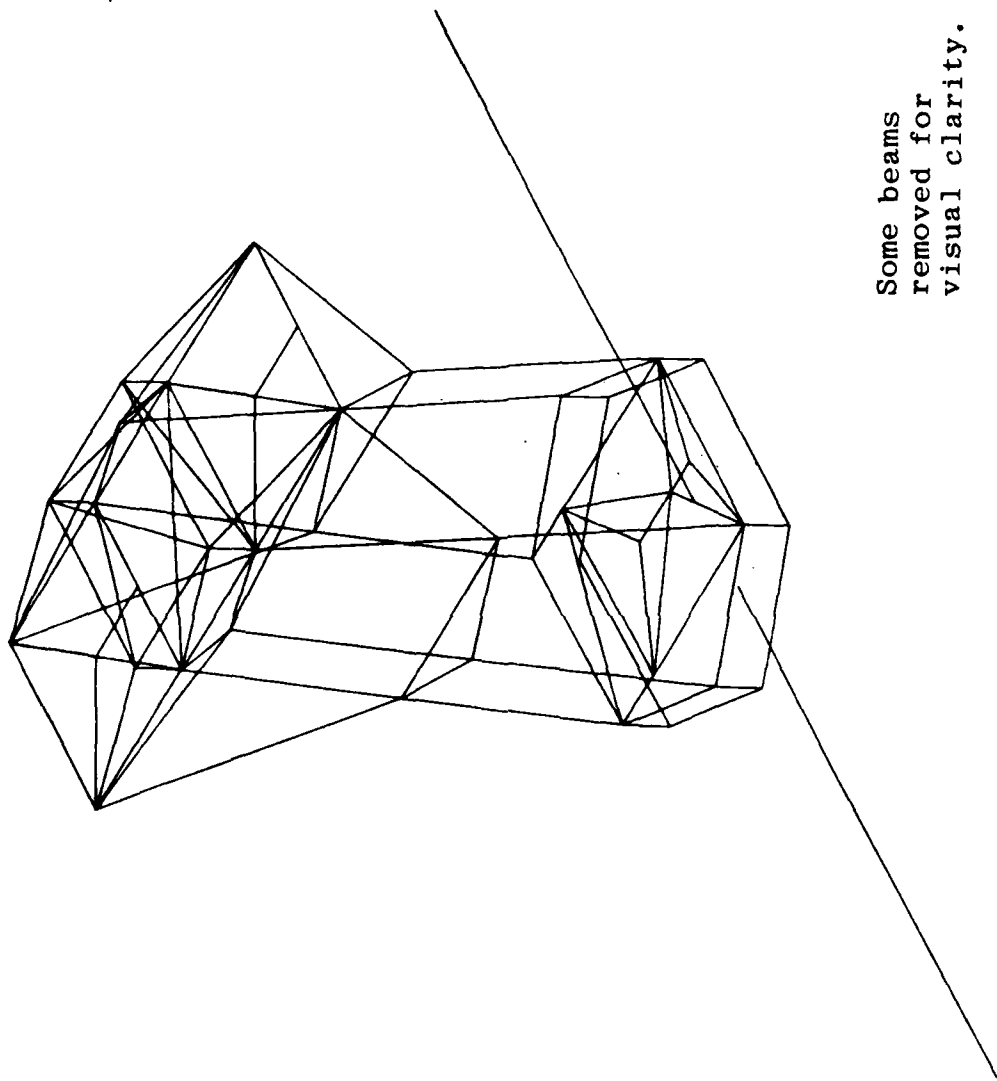
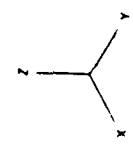


Figure 18. VCOSS Model
 Draper Labs Model #2 Revision #3



Some beams
removed for
visual clarity.

Figure 19. VCOSS Finite-Element Model



a. CSDL model #2 (ref. 7) had lumped masses to provide the total mass distribution. The VCOSS model (ref. 8) uses both lumped masses and structural member weights to define the total mass distribution. The mass changes needed for reference 7 model to become reference 8 model are shown in Table 9. Essentially, these changes represent changes in the mirrors and their supports.

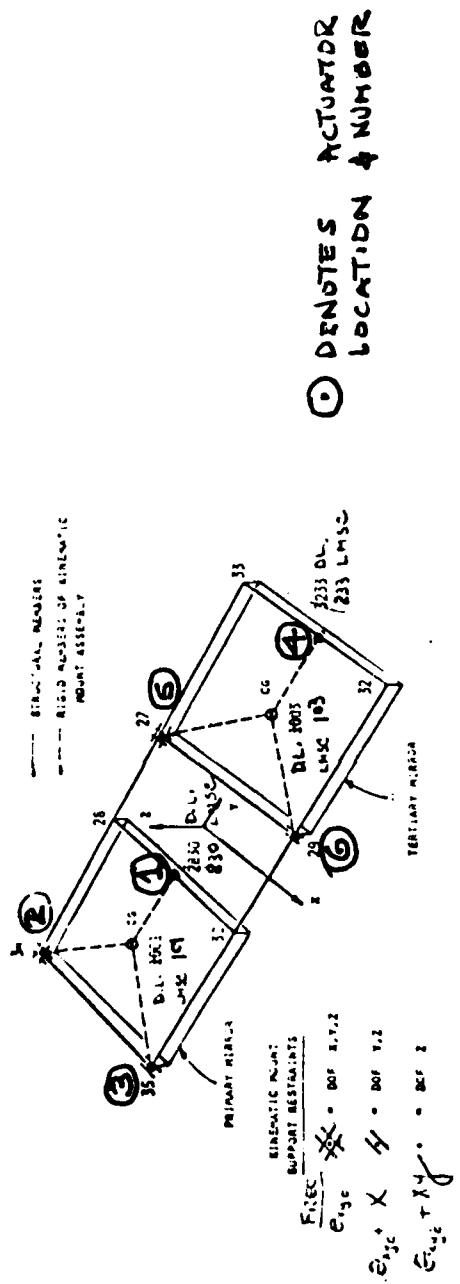
TABLE 9 CHANGES IN LUMPED MASSES

Node Number	Translation (x,y,z) Mass (kg.)	($\theta_x, \theta_y, \theta_z$) Rotation Mass (kg-M ²)
27	69.5	
28	6.74	
29	69.5	
30	6.74	
32	6.74	
33	6.74	
34	69.5	
35	69.5	
9	67.4	
10	67.4	
11	67.4	
12	67.4	
44	3500.	20611,10500, 28777
48	81.91	270
50	163.82	540
52	73.82	270
53	73.82	270
55	163.82	540
57	81.91	270

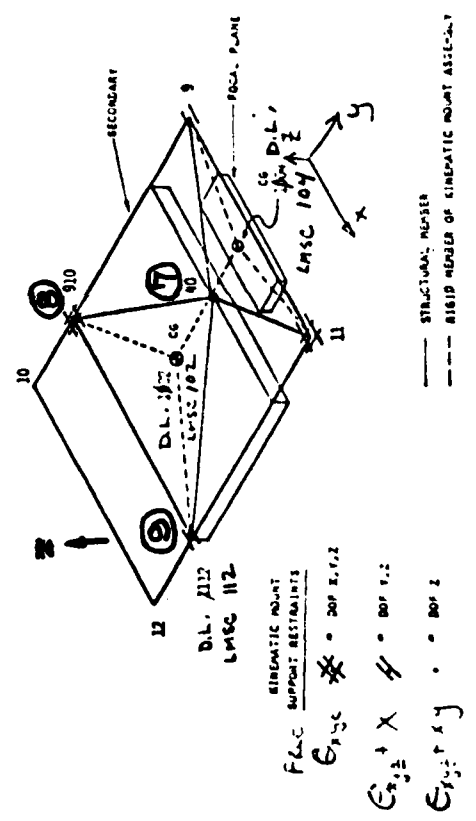
*For ref. 7 to become ref. 8 model.

**Masses lumped at nodes 14, 15, 16, 17, 18, 19 were removed.

- b. Material properties now include a value of $\rho = 1720 \text{ kg/m}^3$ (ref. 8) for all beam members except the tubular truss members #116 and #185 which use a value of $\rho = 2579.701 \text{ kg/m}^3$ (ref. 8).
- c. The value of torsional inertia (J) for the beam members is equal to twice the bending moment of inertia ($J = 2I$).
- d. The equipment section was separated 30 centimeters from the truss structure. This means that node numbers 43, 44, 45, 48, 49, 50, 51, 52, 53, 54, 55, 56, 57 have a z coordinate of -1.30 m.
- e. The changes listed in reference 8 for the structural beams were listed by beam member numbers rather than by the node numbers for the ends of the beam.
- f. Section properties were shown in reference 8 for each of the beam members. Many of the same section properties were repeated for different beam members. In order to make a concise section property table, a unique set of these section properties (20 in all) was constructed and assigned section numbers for each beam member to reference more efficiently.
- g. The new mirror models (Figure 20) described in reference 8 assume that each surface is a planar rigid body which is connected to the support structure by kinematic mounts which decouple elastic motion. The CSDL NASTRAN model uses rigid body kinematic equations to relate the motions of the mirror center of mass to its support restraints. The restraint conditions are shown on the sketches for each mirror model in that memo. LMSC ASTRO model uses very stiff massless tubes (outer diameter = 1 M, inner diameter = .9 M) to connect the mirror center of mass to its support points. Guyan reduction was used on these beam element stiffness matrices to eliminate the mirror support degrees of freedom which are not attached to the backup structure.



Modified Primary and Tertiary Mirror Models



Modified Secondary and Focal Plane Mirror Models

Figure 20. Modified Mirror Models

The unattached d.o.f. which provide a "free" motion for the mirrors are listed below.

TABLE 10 MIRROR UNRESTRAINED DEGREES OF FREEDOM

Mirror	Node	Unrestrained Degrees of Freedom
PRIMARY	34	$\theta_x, \theta_y, \theta_z$
	35	x & $\theta_x, \theta_y, \theta_z$
	2830	x, y & $\theta_x, \theta_y, \theta_z$
TERTIARY	27	$\theta_x, \theta_y, \theta_z$
	29	x & $\theta_x, \theta_y, \theta_z$
	3233	x, y & $\theta_x, \theta_y, \theta_z$
SECONDARY	910	$\theta_x, \theta_y, \theta_z$
	1112	x & $\theta_x, \theta_y, \theta_z$
	40	x, y & $\theta_x, \theta_y, \theta_z$
FOCAL PLANE	11	$\theta_x, \theta_y, \theta_z$
	9	x & $\theta_x, \theta_y, \theta_z$
	40	x, y & $\theta_x, \theta_y, \theta_z$

h. The LOS error model from ref. 7 was updated to produce the correct line-of-sight equations for the VCOSS model. These equations use the restrained degrees of freedom of the primary, tertiary, and focal plane surfaces (Fig. 21) together with the six degrees of freedom of the secondary mirror center of mass. The CSDL NASTRAN NODE 100 DOF #1 represents the LOSX, DOF #2 represents the LOSY and DOF #3 represents the DEFOCUS. The DEFOCUS in the NASTRAN results was corrected due to an incorrect model coordinate for node 40, i.e., node 40 (x,y,z) coordinates of (0,5.0,2.) should have been coordinates of (0,2.5,2.). This error was on the LOS error model only and did not affect the NASTRAN structural model mode shapes (see Table 13).

i. The equipment section was modeled by CSDL in NASTRAN using rigid body equations to connect node 44 to nodes 42, 45, 47, 46, 43. This section was modeled by LMSC in ASTRO using very stiff massless tubes (outer diameter = 1M, inner diameter = 0.9M) to connect node 44 to nodes 42, 45, 47, 46, 43. In addition, these tubes were used around the perimeter of the equipment section to provide more rigidity by connecting nodes 41-45-47-46-43-42.

j. All degrees of freedom were retained and used in the modal analysis by CSDL. Only the degrees of freedom which had masses assigned to them were retained and used in the modal analysis by LMSC. The massless degrees of freedom (DOF) were reduced out of the stiffness matrix using Guyan reduction. This was done on the massless DOF because they have no dynamic effect and reducing them produces a smaller "STATICALLY EQUIVALENT" stiffness matrix which can be numerically manipulated with much greater speed.

k. The Mass Matrix for the VCOSS model at coordinates (0,0,0) is shown (Table 11) for both LMSC and Draper models and the results are in excellent agreement. This verifies all of the model coordinates and mass distribution.

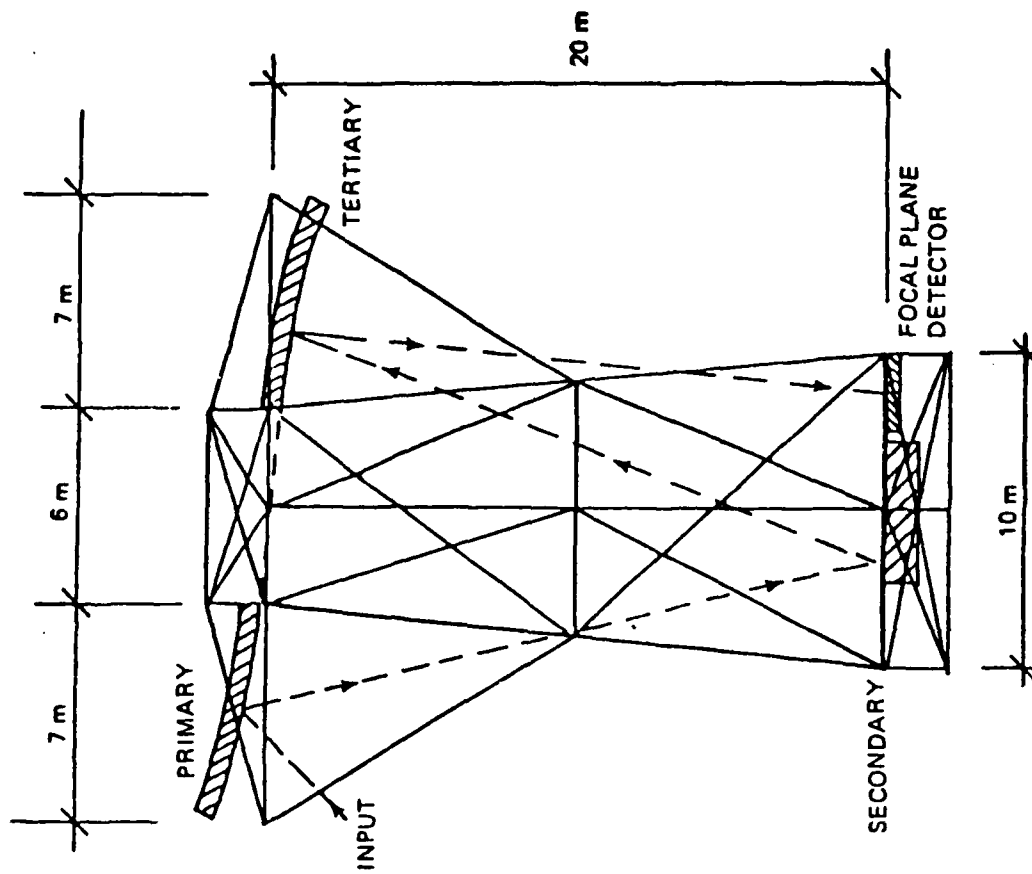


Figure 21. VCOSS Optical System

Table 11. VCOSS MASS MATRIX COMPARISON

LMSC MODEL AT (0,0,0)
MASS MATRIX

	x	y	z	θ_x	θ_y	θ_z
8,963.6						
0	8,963.6					
0	0	8,963.6				
0	-62,664.	-2,151.4	1,614,000.			
62,664.	0	0	-166.73	1,680,500		
2,151.4	0	0	-.36	-40,458.	443,930.	

MASS UNITS
x,y,z in kg.
 $\theta_x, \theta_y, \theta_z$ in kgm^2

CENTER OF GRAVITY
(0, -.24, 6.99) meters

DRAPER MODEL AT (0,0,0)
MASS MATRIX

	x	y	z	θ_x	θ_y	θ_z
8,963.6						
0	8,963.6					
0	0	8,963.6				
0	-62,664	-2,151.4	1,614,000.			
62,664.	0	0	-166.73	1,680,500		
2,151.4	0	0	-.36	-40,458	443,926	

Table 12. VCOSS MODAL FREQUENCY COMPARISON (Hz)

MODE			MODE		
#	LMSC	DRAPER	#	LMSC	DRAPER
1	-0.0534	0.0000010	38	10.25	10.34
2	-0.0462	0.0000084	39	10.51	10.52
3	-0.0290	0.0000031	40	11.48	11.55
4	-0.0269	0.0000038	41	11.65	11.65
5	-0.0215	0.0000047	42	11.65	11.65
6	-0.0154	0.0000048	43	11.65	11.65
7	0.1131	0.1140	44	11.66	11.66
8	0.1469	0.1469	45	11.74	11.84
9	0.1490	0.1496	46	13.34	13.50
10	0.1741	0.1752	47	14.10	14.19
11	0.4549	0.4554	48	14.89	15.03
12	0.5568	0.5573	49	16.51	16.74
13	0.5953	0.5962	50	17.14	17.32
14	0.6131	0.6148	51	17.51	17.61
15	0.6351	0.6363	52	17.77	17.77
16	0.6403	0.6416	53	17.77	17.77
17	0.8151	0.8151	54	17.77	17.77
18	0.8160	0.8162	55	17.78	17.78
19	0.8235	0.8235	56	21.08	21.32
20	0.9152	0.9156	57	21.66	21.68
21	0.9703	0.9720	58	22.02	22.16
22	1.158	1.159	59	23.47	23.89
23	1.551	1.551	60	23.89	23.94
24	1.773	1.773	61	24.35	24.56
25	2.250	2.250	62	24.48	24.66
26	2.254	2.254	63	25.46	25.69
27	3.434	3.434	64	25.94	26.11
28	3.452	3.452	65	26.44	26.79
29	3.957	3.957	66	28.12	28.41
30	3.986	3.987	67	28.72	29.02
31	4.051	4.052	68	31.85	32.38
32	4.337	4.338	69	32.55	33.11
33	6.550	6.563	70	33.21	33.56
34	8.057	8.065	71	35.03	35.37
35	8.434	8.453	72	36.06	36.60
36	8.840	8.854	73	38.76	39.44
37	8.991	9.010	74	39.90	40.17
			75	40.04	40.63

Table 13. LINE-OF-SIGHT (LOS) EQUATIONS

$$[LOS] = [A][B][C][O]$$

- [A] ~ RELATES TRANSLATIONAL DEFOCUS TERMS TO LOS ERROR
- [B] ~ RELATES MIRROR VERTEX MOTION TO TRANSLATIONAL DEFOCUS
- [C] ~ RELATES MOTION OF MODEL NODES TO MIRROR VERTEX MOTION
- [O] ~ MODE SHAPES CORRESPONDING TO MODEL NODES

MODEL		LOSX	LOSZ	DEFOCUS
DOF				
PRIMARY MIRROR (LMSC-830-z)	34-x	.00000	-.37106-01	.00000
	34-y	-.18553-01	-.46382-01	.00000
	34-z	-.14286+00	-.25000+00	-.19124-01
	35-y	-.18553-01	.46382-01	.00000
	35-z	-.14286+00	.25000+00	-.19124-01
	2830-z	.28571+00	.00000	.12749+00
SECONDARY MIRROR (LMSC-102)	1002-x	.00000	.16131+00	.00000
	1002-y	.80657-01	-.60493-01	.00000
	1002-z	-.35489+00	-.62106+00	.77803+00
	1002-θx	.80657-01	.60493-01	.00000
	1002-θy	-.35489+00	.62106+00	.77803+00
	1002-θz	.70978+00	.00000	-.46682+00
TERTIARY MIRROR (LMSC-323-z)	27-x	.00000	.00000	.00000
	27-y	.00000	.00000	.00000
	27-z	.00000	.00000	-.17849+00
	29-y	-.34842+01	.00000	.00000
	29-z	.00000	.34842+01	.00000
	3233-z	.00000	.00000	.00000
FOCAL PLANE	11-x	.00000	-.12421+00	.00000
	11-y	-.62104-01	-.77630-01	.00000
	11-z	.00000	.00000	.50000+00
	9-y	-.62104-01	.77630-01	.00000
	9-z	.00000	.00000	.50000+00
	40-z	.00000	.00000	-.20000+01

$$[A][B][C] =$$

A normal modes analysis of the VCOSS finite-element model was performed using the ASTRO finite element program. The resulting list of frequencies up to 40 Hz have been tabulated (Table 12). The LMSC model was created with the ASTRO computer program for the following reasons:

a. Was used as a verification check on the CSDL model. This procedure enabled CSDL and LMSC to eliminate certain discrepancies and inconsistencies in the original model and to converge to a final version that was considered as a baseline. The minor remaining numerical differences between the two models are inconsequential as far as the control studies are concerned.

b. LMSC Model interfaces with other LMSC control analysis programs.

c. LMSC Model can produce 16mm movies to observe modal sine sweeps and LOS jitter on ray traces from mirrors.

Comparisons between Draper and LMSC models show very good agreement with minor differences arising from different modeling techniques used for "rigid" body substructures and numerical round-off caused by matrix reduction.

The performance of this system is measured by the ability to maintain line-of-sight (LOS) and defocus within specified tolerances. The results of the LOS for sixty-nine modes (elastic mode numbers 7-75 renumbered as mode numbers 1-69) are tabulated for each mode to show LOS-x, LOS-y, and defocus for the optical axis (Table 14).

Table 14. RESULTS OF LINE-OF-SIGHT (LOS)

MODE #	LMSC		MODE #	LMSC		DEFOCUS
	LOSX	LOS Y		LOS X	LOS Y	
1	55502-05	19323-03	36	10675-04	12317-04	98550-05
2	56490-05	32578-06	37	33748-04	83754-05	29728-04
3	15107-03	15643-05	38	44407-04	25436-05	39458-04
4	40876-05	12085-03	39	25532-01	33401-01	23513-01
5	13188-04	75369-05	40	31360-01	65084-02	21344-01
6	64483-06	76299-03	41	39317-01	21260-02	53986-01
7	88721-03	20997-05	42	70429-02	25152-01	74497-02
8	37158-05	55967-03	43	11459-02	90756-03	51010-01
9	22686-03	69043-05	44	23018-02	10030-01	38297-02
10	19773-04	88394-04	45	13747-01	42675-04	75793-02
11	40513-04	12497-05	46	74124-06	27208-06	85668-06
12	10236-03	77104-06	47	26672-06	38966-05	20770-07
13	30173-07	37804-07	48	51987-06	34343-06	23440-05
14	34239-04	46210-05	49	46008-06	37278-05	39136-07
15	10528-04	44263-03	50	39782-01	48859-03	36910-01
16	25707-06	28350-02	51	24660-06	78405-06	67907-06
17	21953-04	20125-01	52	16533-04	23353-01	46623-02
18	47062-04	85415-03	53	14946-01	39415-02	64432-01
19	26352-08	23219-07	54	11250-04	23242-04	30897-04
20	33563-05	63821-07	55	27008-02	33284-02	74632-02
21	73988-09	36164-07	56	93998-02	12045-02	16095-01
22	55335-05	21788-06	57	75560-02	10426-01	10605-02
23	73450-05	12714-06	58	22751-01	28721-03	12611-01
24	21015-05	42665-06	59	28677-01	43823-02	26972-01
25	80087-06	39650-04	60	23649-01	10787-01	27195-01
26	19915-06	13447-03	61	88149-03	38599-02	21137-02
27	21788-01	58223-04	62	37997-02	12426-01	13613-02
28	12582-02	12999-01	63	62007-02	14561-02	24688-01
29	14982-02	17078-02	64	49441-04	51452-02	22282-01
30	26180-03	82333-03	65	45043-03	48380-02	18033-02
31	14296-01	25088-02	66	27124-02	52011-03	10013-01
32	14089-02	17802-01	67	51552-02	13817-02	19597-01
33	14169-02	88858-02	68	11105-02	29086-02	89462-03
34	17419-01	42084-01	69	16744-03	42712-03	88898-03
35	13040-05	66471-05				

Elastic modes 7-75
renumbered here as
modes 1-69

2. ACTUATOR/SENSOR LOCATIONS AND TYPES

Selection of actuator/sensor types and locations is a necessary first step in the actual process of control design. Before this selection can be made, certain ground rules must be established which loosely define the control objectives and, thus, partially motivate the hardware selection. For the VCOSS system, as well as for many others, these ground rules or design assumptions play a crucial role in determining system performance, viz., these assumptions are far more important than selection of control design algorithms because they set physical constraints on achievable performance. For this study, the principal guidelines are: (1) vibration sources cannot be isolated, (2) actuator/sensor dynamics must fall in the bandwidth of the evaluation model, (3) control design models must use no more than 50% of the evaluation model modes, and (4) more than one type of control system will be required (at the system level). These assumptions very substantially impact achievable performance. The first assumption means that active vibration isolation, an important subject, will not be studied now. The study objective here is structural control; vibration isolation does not raise the LSS control design issues (and hardware limitations) like robustness, spillover insensitivity, etc., and is therefore considered to be a separate design exercise.

The second assumption means that, for example, very high bandwidth actuators may not be either feasible or desirable and the effects of such limitations will be investigated and not ignored. The third assumption is critical with respect to rejection of broadband noise in a structure. Since so many modes are excited, large evaluation models are necessary to evaluate system performance. It is not practical (and perhaps not even possible) to identify large portions of such models. Thus, practical control design must be based on realistic subsets; this sharply limits closed-loop performance from many orders-of-magnitude reduction

factors to factors on the order of 100. Very high performance against broadband noise will require active isolation of the disturbance directly, when allowed by system design constraints.

The last assumption strongly influences interpretation of results. In particular, the VCOSS structure exhibits low-frequency bending near 0.1 Hz. Distortion of LOS performance this close to DC (zero frequency) will be controlled by mirror/optical train alignment systems which may use member/actuator devices. In the analytical work below only one type of actuator dynamics was studied to more closely conform to program resources. Since controls power is necessary over a broad range of frequencies, multiple actuator types will be necessary for real systems, and several different actuator models will have to be included in the design. These complexities are left to future work.

These guidelines were introduced and agreed upon during the first TD meeting review at AFWAL on June 16, 1982 and reaffirmed in the second TD meeting on March 8, 1983. It is important to understand the reasons for these guidelines. For the CSDL #2 problem considered in this study, isolation of the vibration sources obviates any need to control structural modes because no other disturbance loads are considered. (This is not the case in a real system). Structural control solutions which use all, or nearly all, of the evaluation model as a basis for control design, can produce any performance level desired (assuming sufficiently good sensors and activators). It is unfortunate, in this case, that the broadband noise spectrum effectively excites the entire evaluation model. This means that high performance, near the specification limit, cannot be achieved without isolation.

Without these assumptions on isolation and synthesis models, structural control performance evaluations are meaningless for the VCOSS/CSDL problem. It was also agreed that the rigid body modes

would be eliminated from the control design exercises. This means that all very low frequency control mechanizations (rigid body sensing, surface figure sensing, and alignment) are eliminated from consideration (since they all interact), i.e., low frequency control cannot be studied with the rigid body modes deleted.

For the baseline VCOSS control system implementation, analysis of the line-of-sight performance indicates that linear proof-mass actuators installed to control mirror tilt will directly influence the desired performance metric and provide adequate modal control. The actuator locations are shown in Fig. 20. Each driver acts in the z-direction which gives x and y tilt plus defocus control. Colocated accelerometers are placed at each proof-mass actuator location. Thus, the baseline system provides 9 colocated actuators and sensors plus a focal plane processor/alignment system output which provides a direct measurement of LOS error. All LAC mechanizations require the colocated sensor outputs while high authority control (HAC) and adaptive systems require the focal plane sensor to evaluate the performance metric. Note that the actuators are mounted to structural nodes and not directly to the mirrors.

In phase II, some of these actuators are removed to evaluate fault tolerance and redundancy requirements.

3. OPEN-LOOP SYSTEM EVALUATION FOR CONTROL DESIGN

a. Linear First-Order Evaluation Model

A linear VCOSS evaluation model is formed by taking the first 54 structural modes and transforming to a 108th order linear system. Six disturbance inputs are used: one each in the x, y, and z directions at each disturbance location. The disturbance is modeled as six independent colored noise sources having the PSD given in Figure 2. The resulting linear evaluation model is:

$$\begin{bmatrix} \dot{x} \\ \dot{v} \end{bmatrix} = \begin{bmatrix} F & D \\ 0 & E \end{bmatrix} \begin{bmatrix} x \\ v \end{bmatrix} + \begin{bmatrix} G \\ 0 \end{bmatrix} u + \begin{bmatrix} 0 \\ I \end{bmatrix} w \quad (18)$$

$$w \sim n(0, W) \quad (19)$$

$$z = [M \ 0] \begin{bmatrix} x \\ v \end{bmatrix} \quad (\text{LOS}) \quad (20)$$

$$y = [G^T \ 0] \begin{bmatrix} x \\ v \end{bmatrix} \quad (\text{sensors}) \quad (21)$$

where

$$\Xi = -30\pi I \text{ sec}^{-1}$$

$$W = 36000\pi^2 I N^2 / \text{sec}$$

$$E \{v v^T\} = 600\pi I N^2 \text{-sec}$$

This gives a 114th order linear evaluation model.

Open-loop frequencies for this model are plotted in Figure 22 (disregarding the noise states). Significant frequency "clustering" of the modes is evident. The effect of the colored noise, as seen through the line-of-sight, is shown in Figures 23 through 27 which give the PSD and integrated PSD for each LOS component. The LOSy level is an order of magnitude higher than that of LOSx. The dominant modal contributions are below 2 Hz for LOSy and below 1 Hz for LOSx. The modal properties of the disturbance are evaluated in detail later.

The computation of these curves was done on the digital computer and based on the following procedure. The closed-loop system equations are represented by:

$$\begin{aligned} \dot{x} &= Fc x + D1\omega1 + D2\omega2 & (22) \\ \text{LOSx} &= Hx x \\ \text{LOSy} &= Hy x \end{aligned}$$

where x is the state vector, $\omega1$ and $\omega2$ the disturbance inputs, and Fc , $D1$, $D2$, Hx and Hy constant coefficient matrices. These equations can be used to define the transfer functions between disturbances and LOS errors. For instance

$$\text{LOSx}/\omega1 = Hx (j\omega I - Fc) D1 \triangleq Tx1 (\omega) \quad (23)$$

the PSD of LOSx is then obtained by:

$$\text{PSD}_x(\omega) = |\text{Tx}_1(\omega)|^2 |w(\omega)|^2 + |\text{Tx}_2(\omega)|^2 |w(\omega)|^2 \quad (24)$$

where $|w(\omega)|^2$ represents the disturbance PSD as defined in Section I, Figure 2. (w_1 and w_2 have some PSD and are uncorrelated). The LMSC analysis software computed the transfer functions Tx_1 , Tx_2 , Ty_1 , Ty_2 and the expression which was plotted as a function of frequency the total LOS error is given by

$$\text{LOS}^2 = \text{LOS}_x^2 + \text{LOS}_y^2$$

thus the total PSD was obtained by simply summing PSD_x and PSD_y . Finally, the integrated value was computed by the integral

$$S(\omega) = \frac{1}{\pi} \int_0^{\omega} \text{PSD}(\omega) d\omega \quad (25)$$

(Note that the total RMS error is simply $\sqrt{S(\infty)}$)

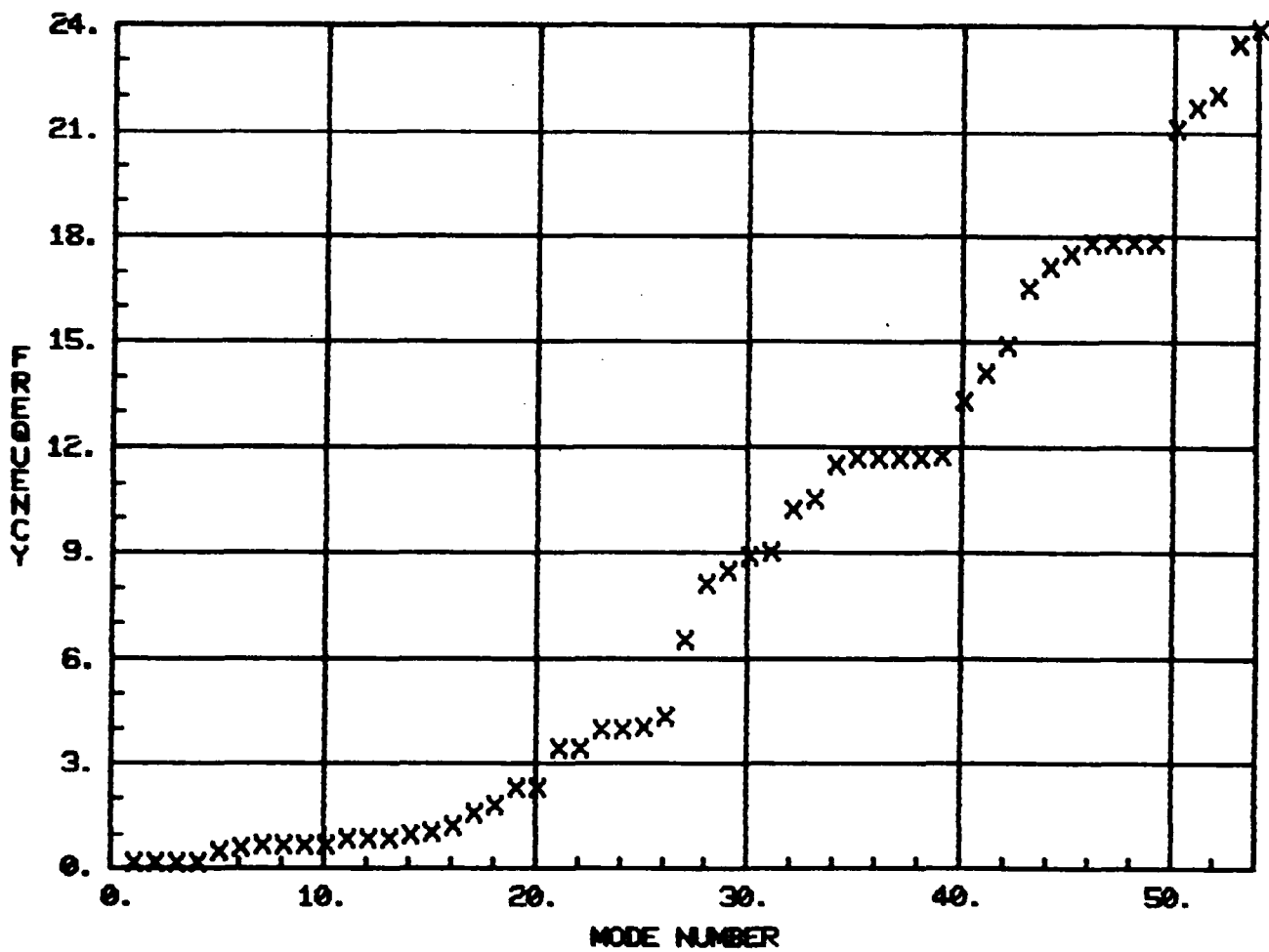


Figure 22. VCOSS Evaluation Model Frequency vs. Mode Number

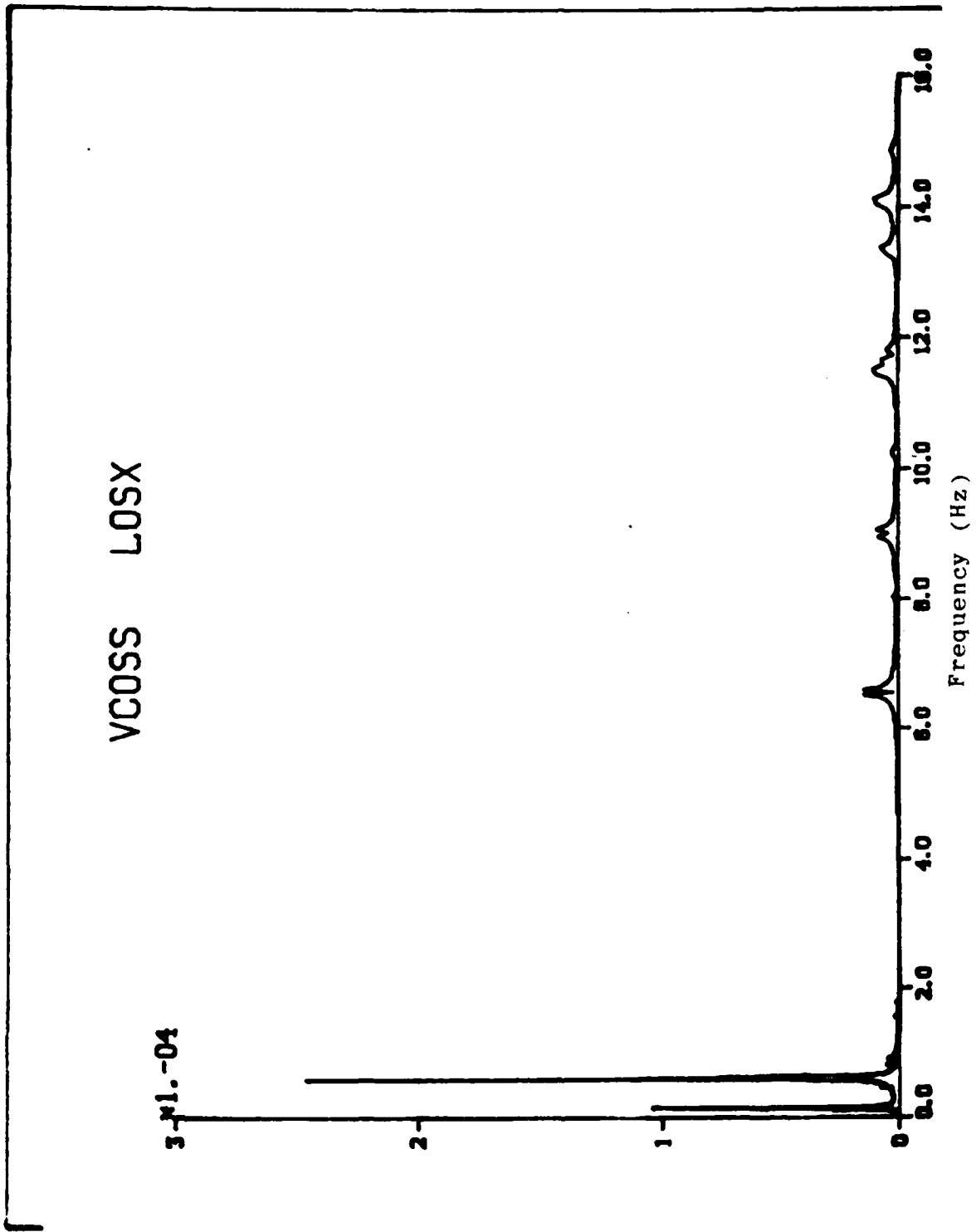


Figure 23. PSD of Disturbance to LOSx

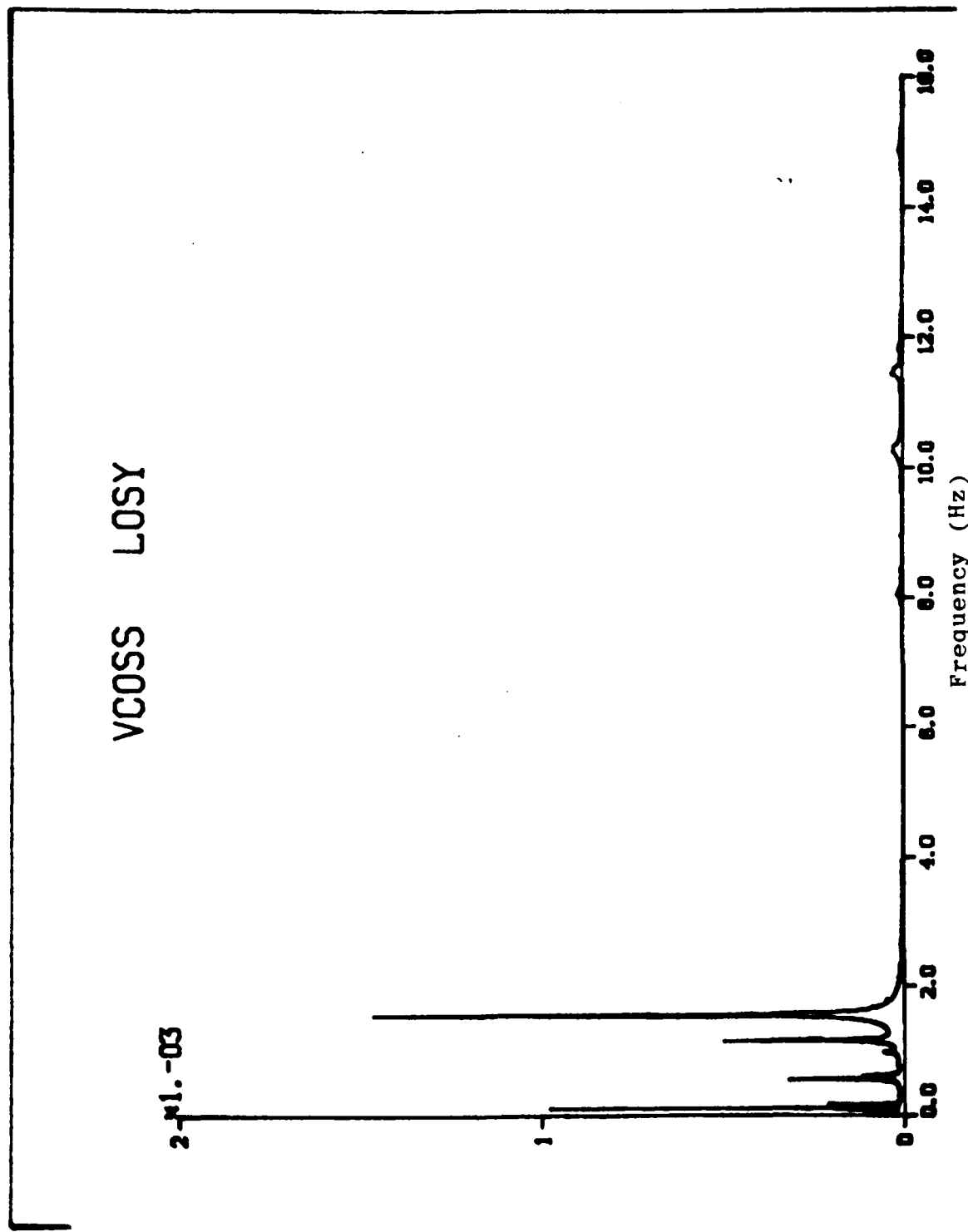


Figure 24. PSD of Disturbance to LOSy

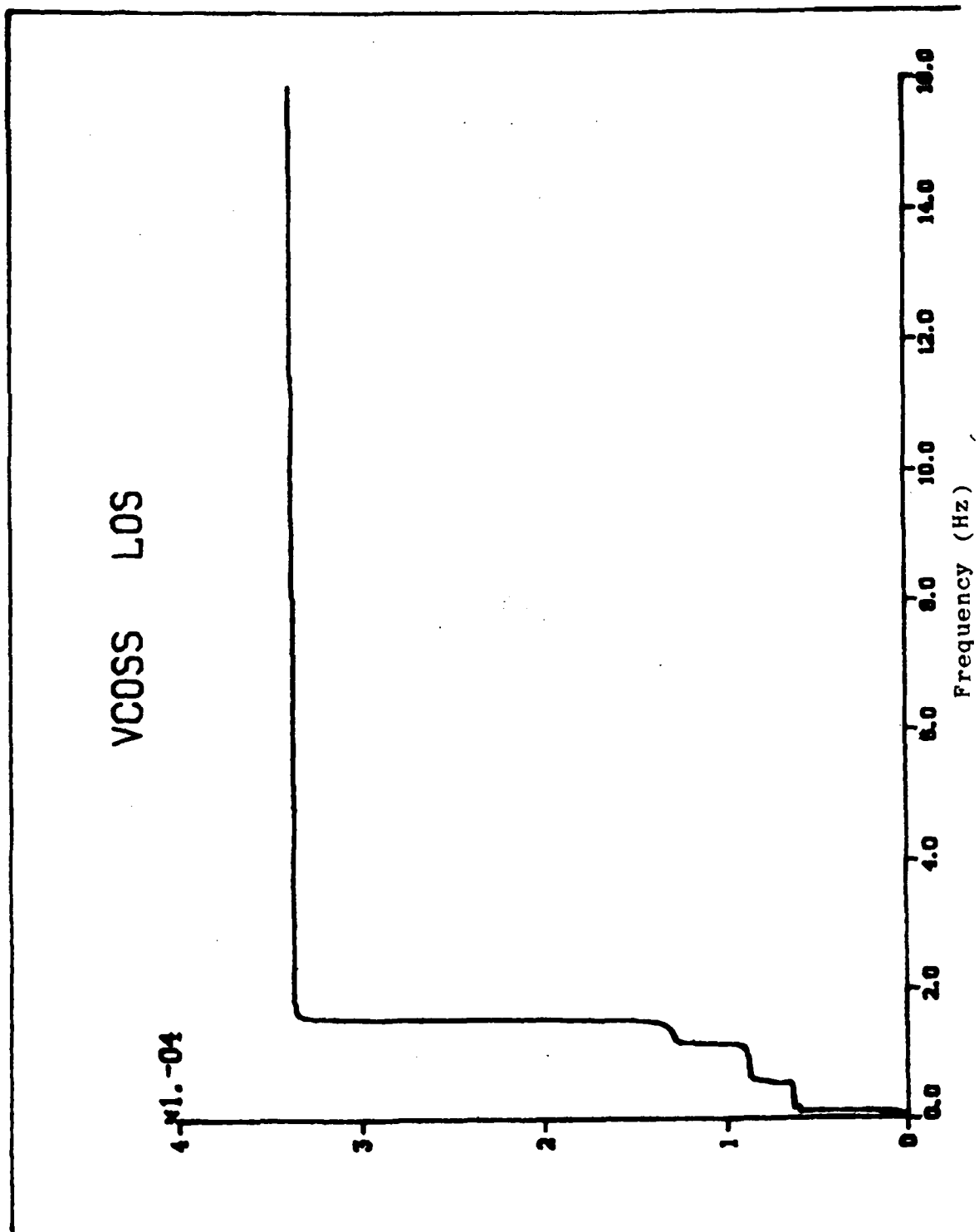


Figure 25. Integrated PSD of Disturbance to Total LOS

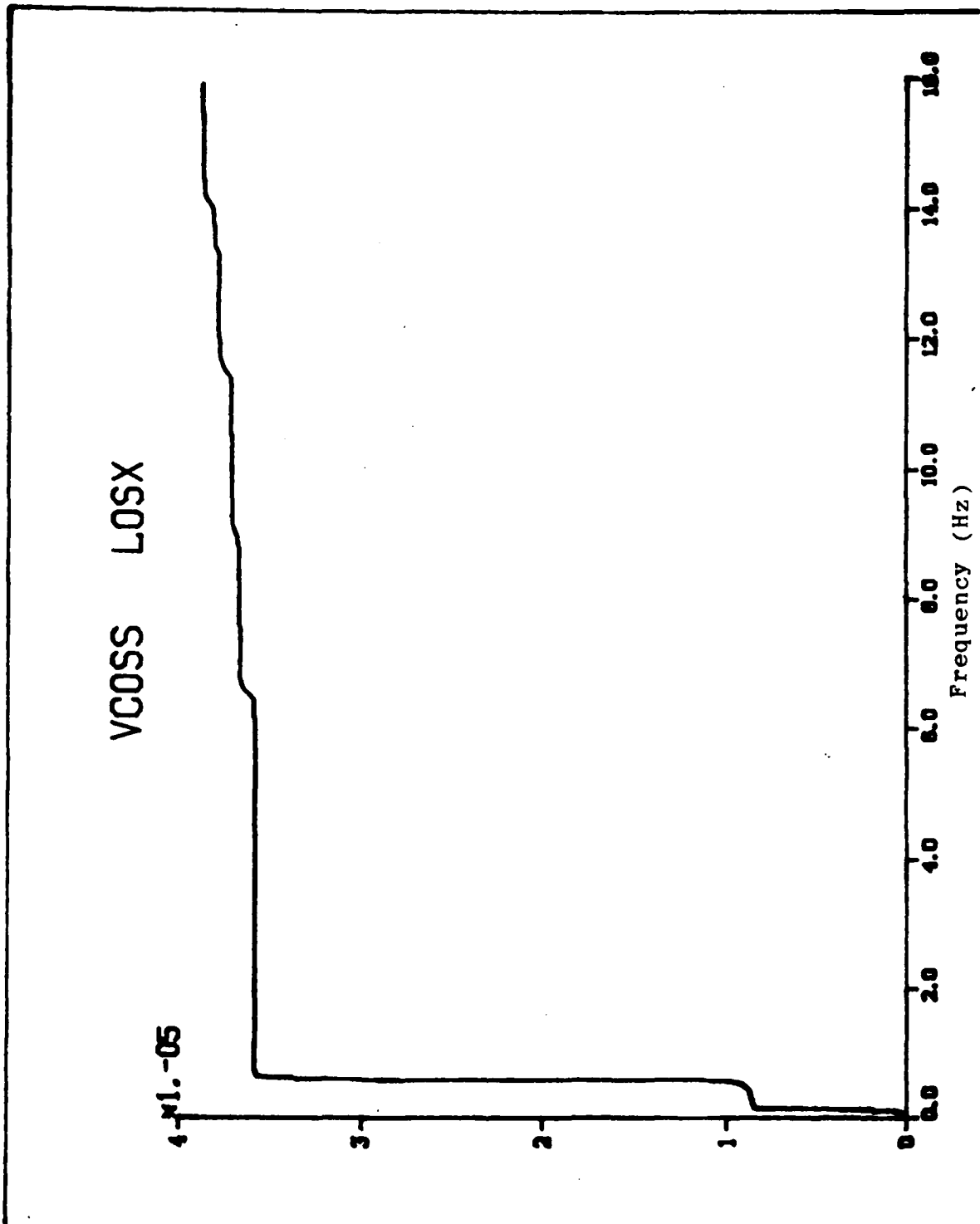


Figure 26. Integrated PSD of Disturbance to LOSx

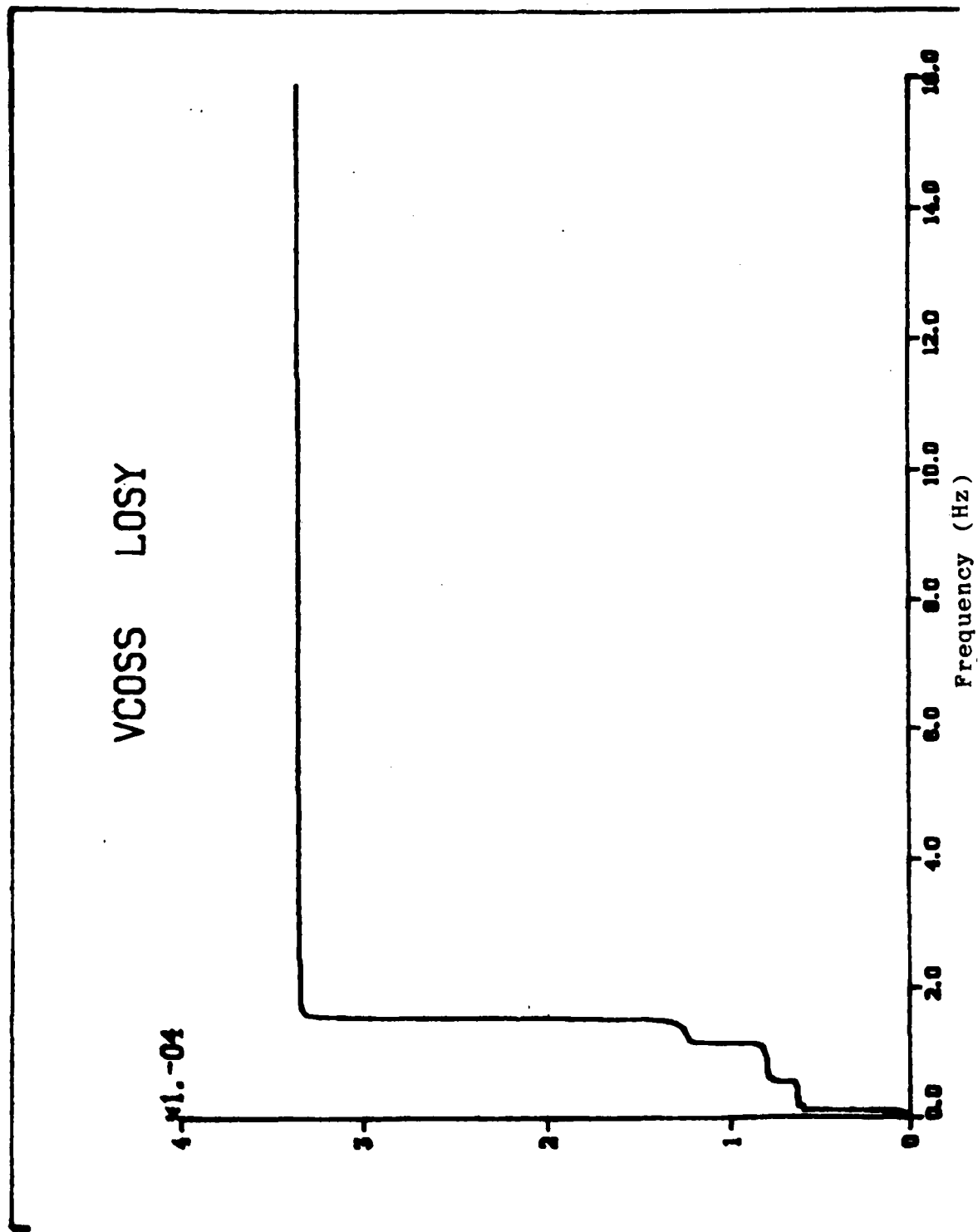


Figure 27. Integrated PSD of Disturbance to LOSy

b. Modal-Analysis for Mode Selection-Theory

The size of the model and uncertainty in the high-frequency modes makes model-reduction necessary for control design. Although a 114th order controller poses no numerical difficulties, high-frequency feedback based upon poorly modeled modes is undesirable. Several criteria for mode selection are used. To account for model uncertainty at high-frequency, it is assumed that the model is unreliable above 6 Hz. In other words, the first 25% of the 24 Hz bandwidth is considered accurate enough for control design. This is an ad hoc limit.

(1) Internal Balancing

To determine the most important modes for control design, many criteria must be considered including controllability, disturbability, observability in performance, and observability in the measurements. Any mode which is highly controllable, observable, and disturbable must clearly be included in the design model; however highly controllable-but-unobservable modes, for example, are difficult to judge. Moore (Ref. 1) has developed an "internal balancing" approach whereby asymptotically stable linear models are transformed to an essentially unique coordinate representation for which controllability and observability rankings are identical. The definition of internally balanced coordinates follows:

- Def. An asymptotically stable model $\begin{cases} \dot{x} = Ax + Bu \\ y = Cx \end{cases}$ is

Internally balanced over $(0, \infty)$ IFF

$$\int_0^{\infty} e^{At} B B^T e^{-A^T t} dt = \int_0^{\infty} e^{A^T t} C^T C e^{-At} dt = \sum^2$$

where $\sum^2 = \text{diag} \left\{ \sigma_1^2 \quad \sigma_1^2 \quad \dots \quad \sigma_n^2 \right\}$ and $i > j \Rightarrow \sigma_i^2 \geq \sigma_j^2$ (26)

Notice that the balanced representation is such that the controllability Gramian and observability Gramian are equal and diagonal. The σ_i 's are termed "second-order modes."

In general, the required transformation "scrambles" the original coordinate system such that the physical meaning of the states is lost.

However, for lightly damped structural models with decoupled dynamics, the internally balanced coordinate representation is approximately equal to a scaled representation of the modal states. Thus it is possible to write approximate formulae for the $\{\sigma_i^2\}$ in terms of the original model. Three modal rankings are considered:

- disturbance inputs to LOS
- actuator inputs to LOS
- actuator inputs to sensor outputs

For a linear first order differential model of the form:

$$\dot{\mathbf{x}} = \begin{bmatrix} -2\zeta_1\omega_1 & -\omega_1^2 & & 0 \\ 1 & 0 & & \\ \hline & & -2\zeta_2\omega_2 & -\omega_2^2 \\ & 0 & 1 & 0 \\ \hline & & & \ddots \\ & & & \ddots \\ & & & \ddots \end{bmatrix} \mathbf{x} + \begin{bmatrix} g_1 \\ 0 \\ \hline g_2 \\ 0 \\ \hline \vdots \\ \vdots \\ \vdots \end{bmatrix} \mathbf{u} + \begin{bmatrix} d_1 \\ 0 \\ \hline d_2 \\ 0 \\ \hline \vdots \\ \vdots \\ \vdots \end{bmatrix} \mathbf{v} \quad (27)$$

$$y = [g_1^T \ 0 \ g_2^T \ 0 \ \dots] x \quad (\text{sensors}) \quad (28)$$

$$z_1 = [0 \ m_1 \ 0 \ m_2 \ \dots] x \quad (\text{LOS}) \quad (29)$$

The approximate second order modes are given by (see Appendix A)

- Controllability - Sensors: $\sigma_i^2 = \frac{g_i g_i^T}{4\zeta_i \omega_i} \quad (30)$

- Controllability - LOS: $\sigma_i^2 = \frac{[(g_i g_i^T)(m_i^T m_i)]^{1/2}}{4\zeta_i \omega_i^2} \quad (31)$

- Disturbability - LOS: $\sigma_i^2 = \frac{[(d_i d_i^T)(m_i^T m_i)]^{1/2}}{4\zeta_i \omega_i^2} \quad (32)$

A detailed discussion of the application of internal balancing theory to lightly-damped structural models is provided in Appendix A.

(2) "Modal Cost" [2]

The "modal costs" for a linear-quadratic-gaussian system are simply the diagonal elements of the cost matrix C given by

$$\dot{x} = Fx + Dw \quad (33)$$

$$z = Mx \quad (34)$$

$$\begin{aligned} J &= \lim_{t \rightarrow \infty} E \{z^T z\} \\ &= \text{tr } M^T M \{E[xx^T]\} \\ &= \text{tr } C \end{aligned} \quad (35)$$

These numbers give an indication of the relative contributions of each mode to the total cost. Although mathematically less precise than the second-order modes (e.g., modal costs can be negative), modal cost analysis gives an inexpensive method of ranking which can also be used for closed-loop analysis where the low-damping property no longer holds.

c. Modal Analysis of VCOSS Mode

Using the approximation equations (30) through (32) the approximate second-order modes are computed for the VCOSS evaluation model. Open-loop modal costs are computed using the colored-noise disturbance. Here the absolute values of the modal costs are used. The RMS second-order modes and modal costs are plotted versus mode number in Fig. 28. Immediately evident is the clustering of these modal phenomena. The disturbance effect as seen through the line-of-sight is constrained to clusters of modes as is the ability to measure and control the model. The coincidence of the controllable clusters and disturbable clusters indicates a favorable actuator/sensor configuration for the problem. Table 15 gives the quantitative modal ranking prescribed by each method.

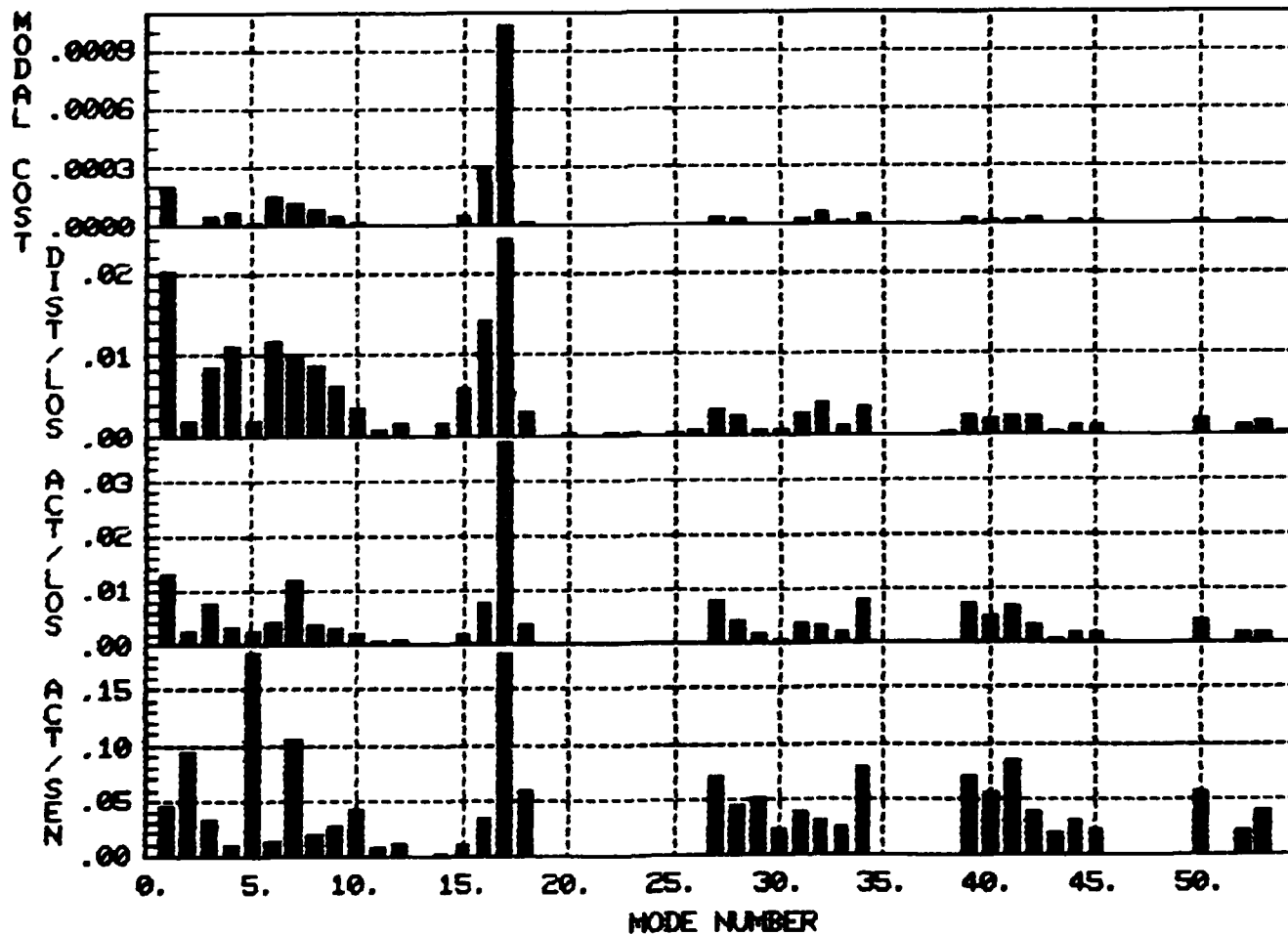


Figure 28. Open-Loop Modal Analysis

Table 15 MODAL RANKINGS SUGGESTED BY THE ANALYSIS

DIST/LOS		ACT/LOS		ACT/SEN		MODAL COST	
Mode	σ_i	Mode	σ_i	Mode	σ_i	Mode	$\mu_i^{1/2}$
17	0.0242	17	0.0366	5	0.1836	17	0.0010
1	0.0202	1	0.0130	17	0.1813	16	0.0003
16	0.0141	7	0.0119	7	0.1037	1	0.0002
6	0.0116	34	0.0081	2	0.0941	6	0.0001
4	0.0110	27	0.0080	41	0.0831	7	0.0001
7	0.0099	3	0.0078	34	0.0786	8	0.0001
8	0.0085	16	0.0074	27	0.0702	4	0.0001
3	0.0084	39	0.0072	39	0.0700	32	0.0001
9	0.0059	41	0.0066	18	0.0582	15	0.0000
15	0.0056	40	0.0051	50	0.0570	34	0.0000
32	0.0038	6	0.0042	40	0.0564	9	0.0000
34	0.0034	28	0.0042	29	0.0510	3	0.0000
10	0.0033	50	0.0041	1	0.0466	27	0.0000
27	0.0032	18	0.0039	28	0.0426	39	0.0000
18	0.0028	8	0.0038	10	0.0417	31	0.0000
31	0.0025	31	0.0038	53	0.0401	28	0.0000
39	0.0024	32	0.0034	31	0.0379	42	0.0000
28	0.0024	42	0.0034	42	0.0367	41	0.0000

(1) Actuator Influence

To lend further insight into the actuator/LOS relationship, the approximate second-order modes were computed for each actuator with respect to the line-of-sight and are plotted in Figs. 29, 30, and 31. Actuators 2, 3, 5, 6, 8, and 9, have very similar profiles to each other and to the total; while actuators 1, 4, and 7 appear to have little LOS authority. Thus in a magnitude sense it appears that the number of actuators required to control the LOS can be reduced to as few as 3 (one for each mirror), although the consequent loss in low authority control (LAC) authority and the increased force requirement might make this reduction desirable.

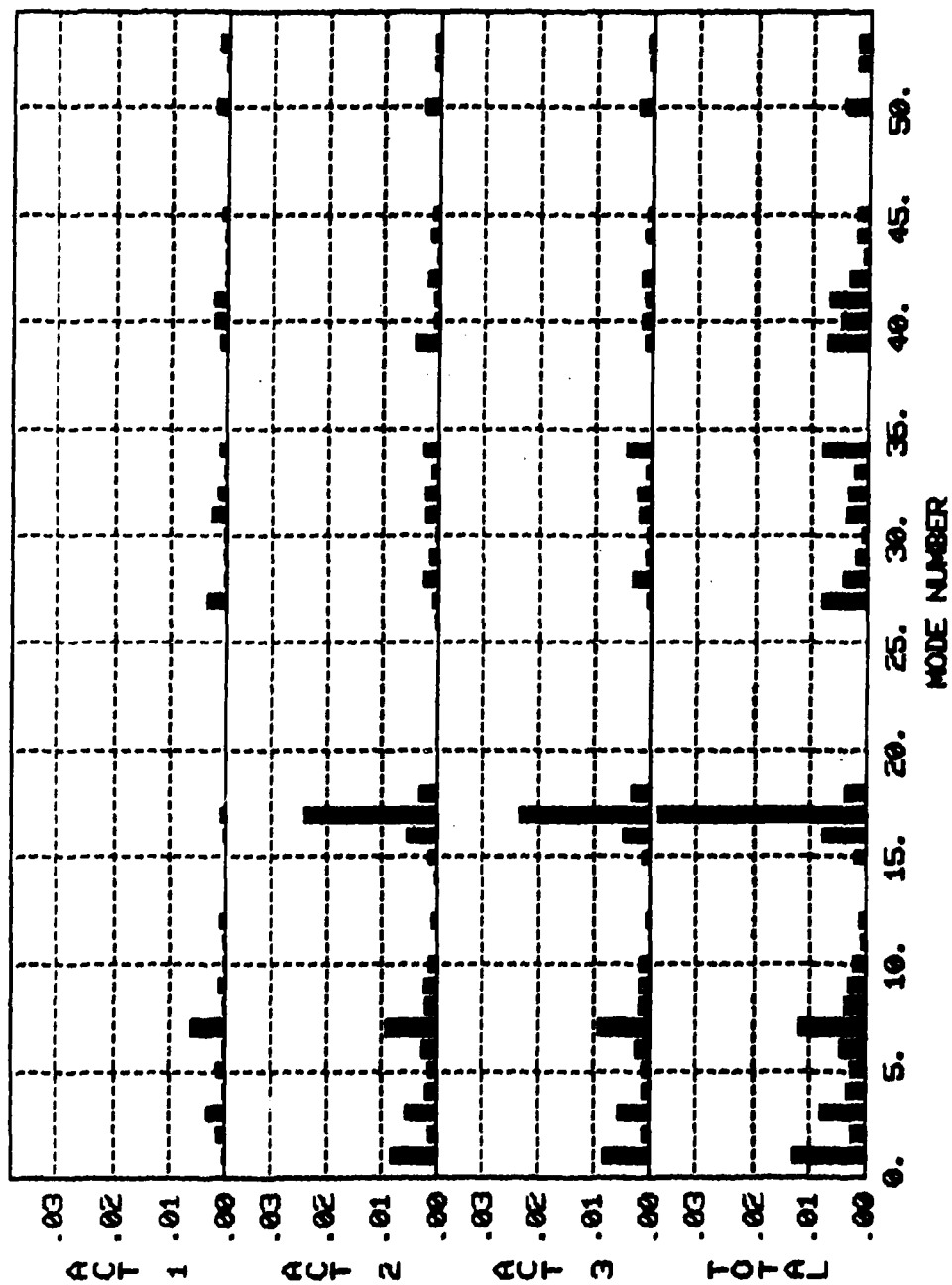


Figure 29. Controllability/LOS Levels for Actuators 1, 2, and 3

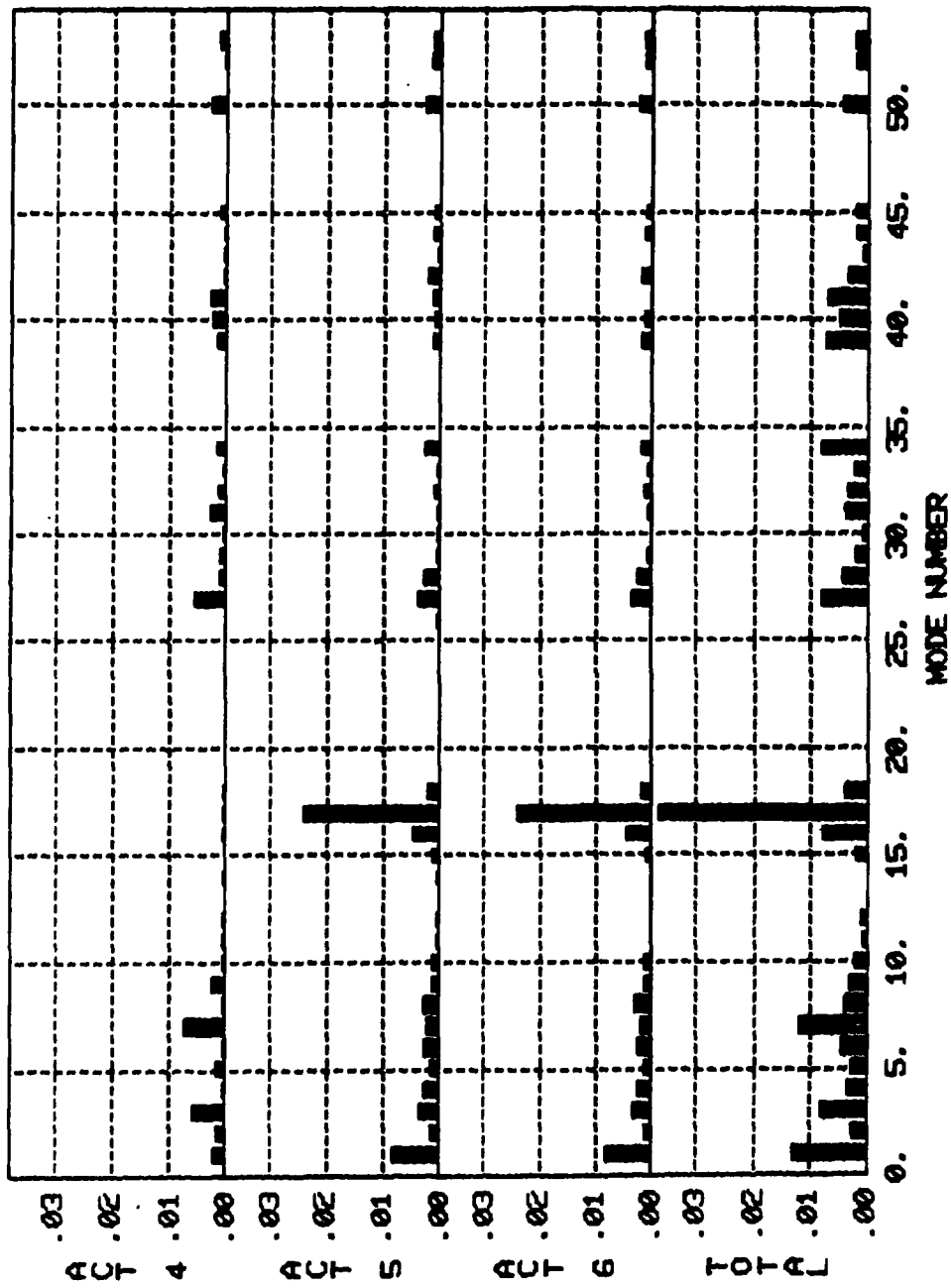


Figure 30. Controllability/LOS Levels for Actuators 4, 5, and 6

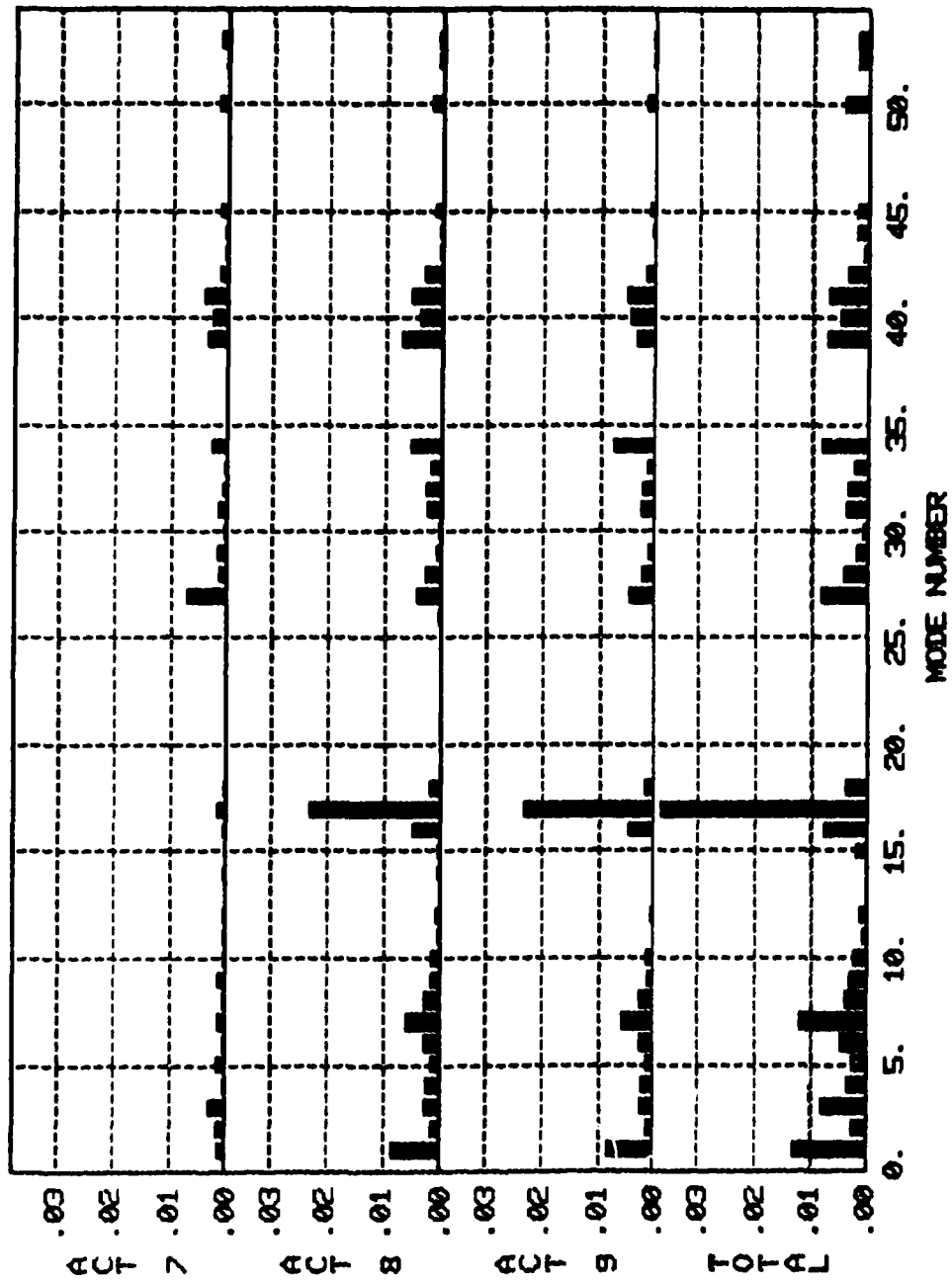


Figure 31. Controllability/LOS Levels for Actuators 7, 8, and 9

4. CONTROL DESIGNS

Three controllers are designed and analyzed for the VCOSS model. The first uses 10 low-frequency modes from the model and relatively low gains, i.e., a cautious design. Based upon closed loop analysis of this controller, four additional modes are selected and a second controller is designed. The bandwidth of this controller is allowed to expand into an adjacent "dead zone" of the model under the assumption that the insensitive modes cannot cause spillover. A low authority control is designed and added to the hi-gain controller to give the third design. Full closed loop modal and stochastic analyses are presented.

a. "Cautious" Controller

(1) Mode selection

Using the modal analyses of Fig. 28, a 10-mode design model is selected. These modes are shown in Table 15, which gives the quantitative modal rankings implied by each method. The first 10 "most disturbable" modes with respect to LOS were used for the design. Figure 32 shows the modal selections. Inspection of the second column shows that several controllable modes have been omitted in the design model bandwidth. It is reasonable to expect that any undesirable effects of the controller will be related to these modes.

(2) Control design

The 10-mode structural design model transforms into a 26th order linear design model (including the disturbance).

Using standard linear quadratic gaussian (LQG) techniques, a state-feedback control is found which minimizes

$$J = \lim_{t \rightarrow \infty} E\{z_R^T z_R + bu_R^T u_R\} \quad (36)$$

AD-A139 931

VIBRATION CONTROL OF SPACE STRUCTURES VCOSS A: HIGH AND
LOW-AUTHORITY HAR. (U) LOCKHEED MISSILES AND SPACE CO
INC SUNNYVALE CA J N AUBRUN ET AL. JUL 83 LMSC-D883019

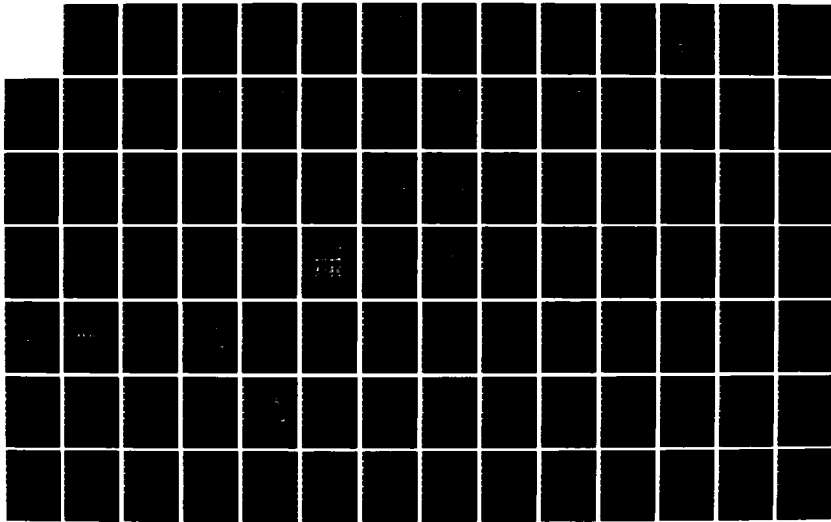
2/3

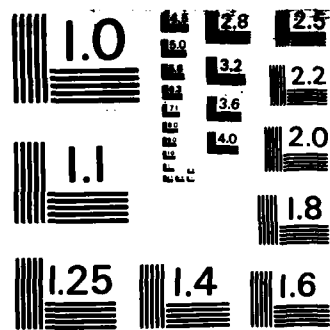
UNCLASSIFIED

AFWAL-TR-83-3074 F33615-81-C-3220

F/G 20/11

NL





MICROCOPY RESOLUTION TEST CHART
NATIONAL BUREAU OF STANDARDS-1963-A

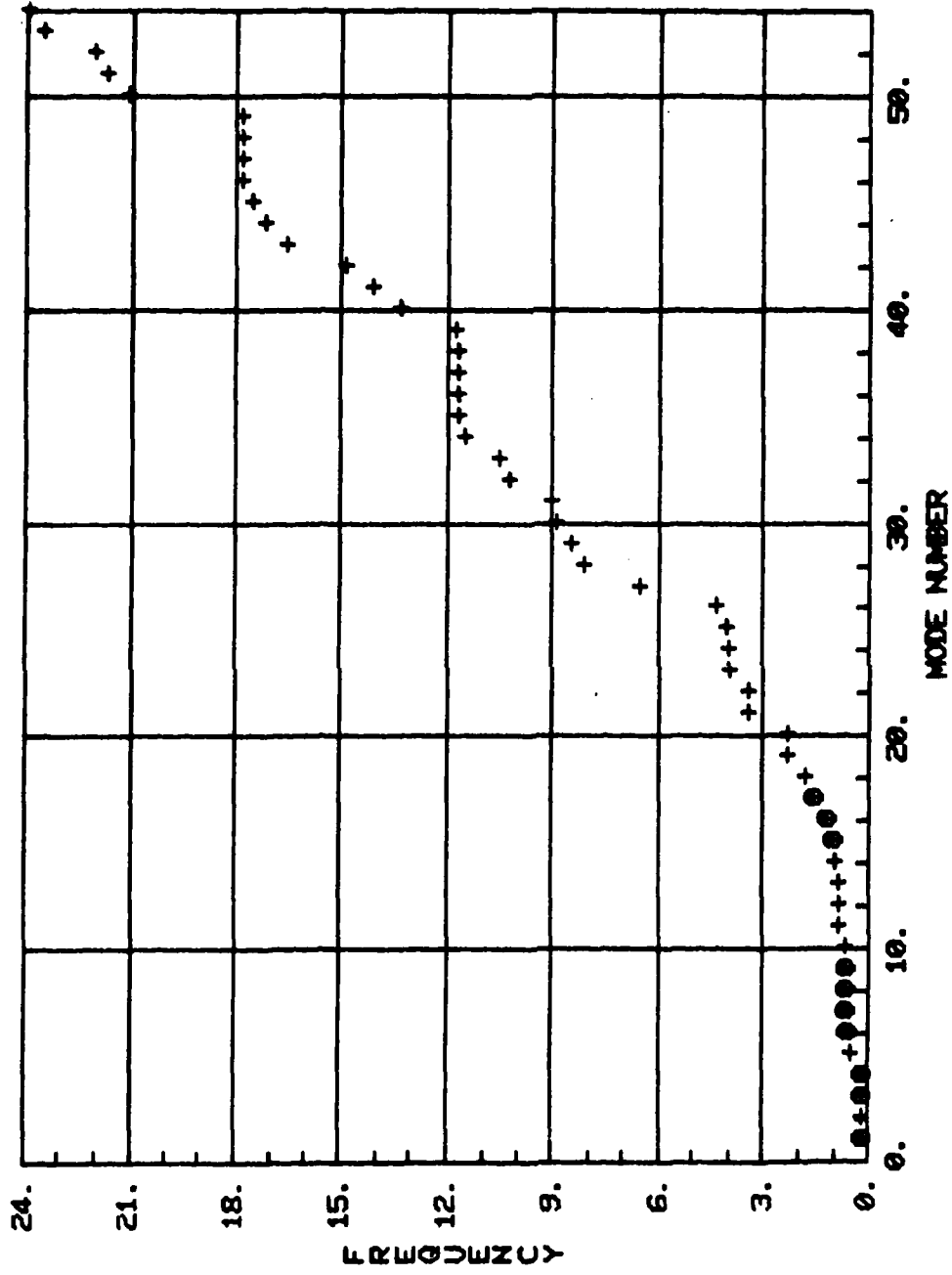


Figure 32. 10-Mode Control Design Selection

where z_R is the LOS output of the reduced model. Several values of b were tried until a reasonable closed-loop bandwidth was obtained using $b = 10^{-11}$. Table 16 shows the resulting closed-loop design spectrum. The significant effect of this control is on modes 17 and 8. The damping on mode 8 is increased by nearly a factor of 100 but the frequency increases by less than one percent. Mode 17 experiences a damping increase of a factor of 20 and the frequency increase is 21%. This is between the frequencies of modes 18 and 19 which are not modeled. Referring again to Fig. 28, modes 19, 20, and 21 are apparently uncontrollable with respect to line of sight as well as sensor placement. Mode 18, however, has some controllability (it ranks 14th out of 54). The control bandwidth is therefore likely to influence mode 18.

Similarly, a standard Kalman filter is found for the design model using the actual disturbance PSD and LOS "measurement noise" of intensity 5×10^{-10} . This choice gives a bandwidth which is roughly equivalent to the control bandwidth. The filter spectrum is shown in Table 17 as is the control. The frequency increase in mode 17 is sufficient to encompass unmodeled mode 18.

(3) Evaluation

The 10-mode controller was implemented with the full 114th order VCOSS model. The closed-loop system is stable. Figures 33 through 36 show the closed-loop and open-loop spectra with varying degrees of magnification about the origin. Four poles, corresponding to modes 2, 5, 10, and 18 move to the right. The spillover in mode 18 is expected since its frequency lies within the controller bandwidth and it is somewhat controllable (see Fig. 28). Modes 2, 5, and 10 are unmodeled modes within the open-loop design model spectrum. Although their modal controllability and disturbability is small, the control and filter gain are sufficient to cause an "in-band" spillover at these frequencies.

Table 16 CLOSED-LOOP CONTROL SPECTRUM OF 10-MODE MODEL

Real part	Imaginary part	Frequency (Hz)	Damping ratio
-4.8001	10.8240	1.8845	.4054
-0.0270	7.3328	1.1671	.0037
-0.0127	6.0956	0.9701	.0021
-0.0115	3.9841	0.6341	.0029
-0.0114	3.8621	0.6147	.0030
-0.2178	3.7528	0.5983	.0579
-0.0114	3.4864	0.5549	.0033
-0.0033	1.0962	0.1745	.0030
-0.0222	0.9388	0.1495	.0237
-0.0203	0.7341	0.1169	.0276

Table 17 CLOSED-LOOP FILTER SPECTRUM OF 10-NODE MODEL

Real part	Imaginary part	Frequency (Hz)	Damping ratio
-5.5453	11.2239	1.9925	.4430
-0.5170	7.3093	1.1662	.0706
-0.0829	6.0898	0.9693	.0136
-0.0654	3.9831	0.6340	.0164
-0.2152	3.9445	0.6287	.0545
-0.4231	3.6162	0.5795	.1162
-0.0944	3.6258	0.5773	.0260
-0.0877	1.0982	0.1753	.0796
-0.0699	0.9299	0.1484	.0750
-0.1559	0.7796	0.1265	.1961

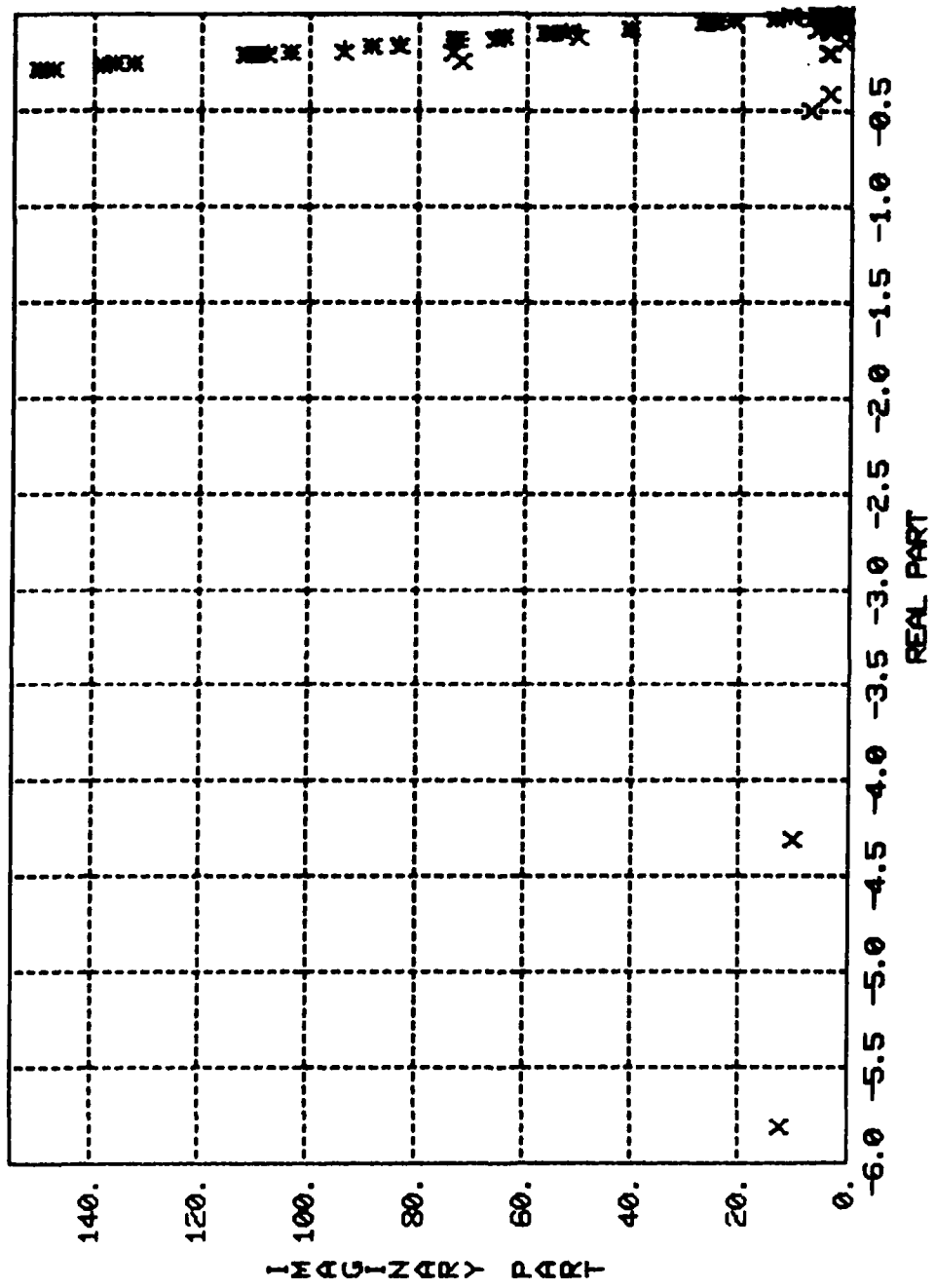


Figure 33. //VCOSS (+) Open-Loop Spectrum, (X) Closed-Loop Spectrum, 26th Order

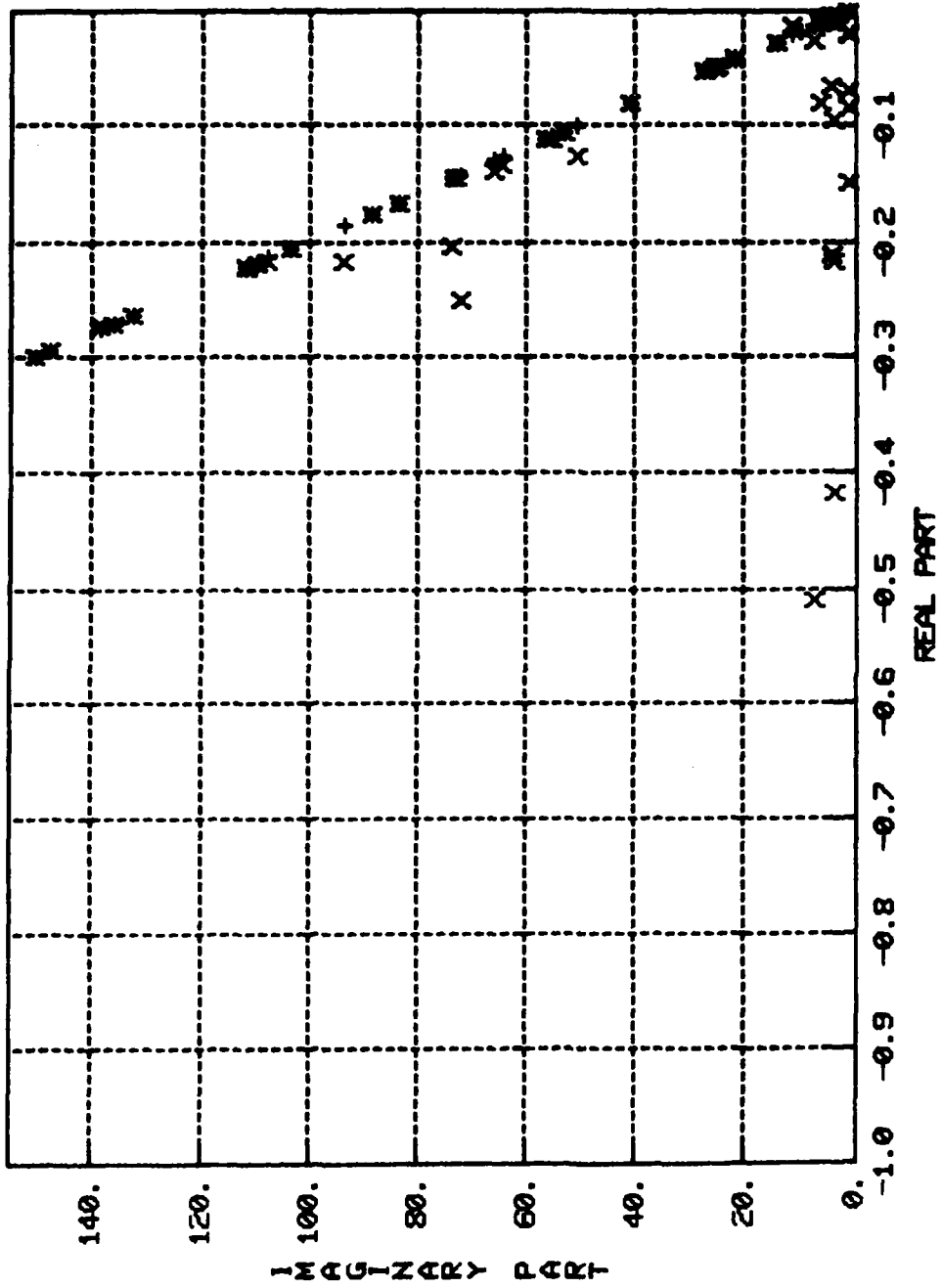


Figure 34. //VCOSS Closed-Loop Evaluation

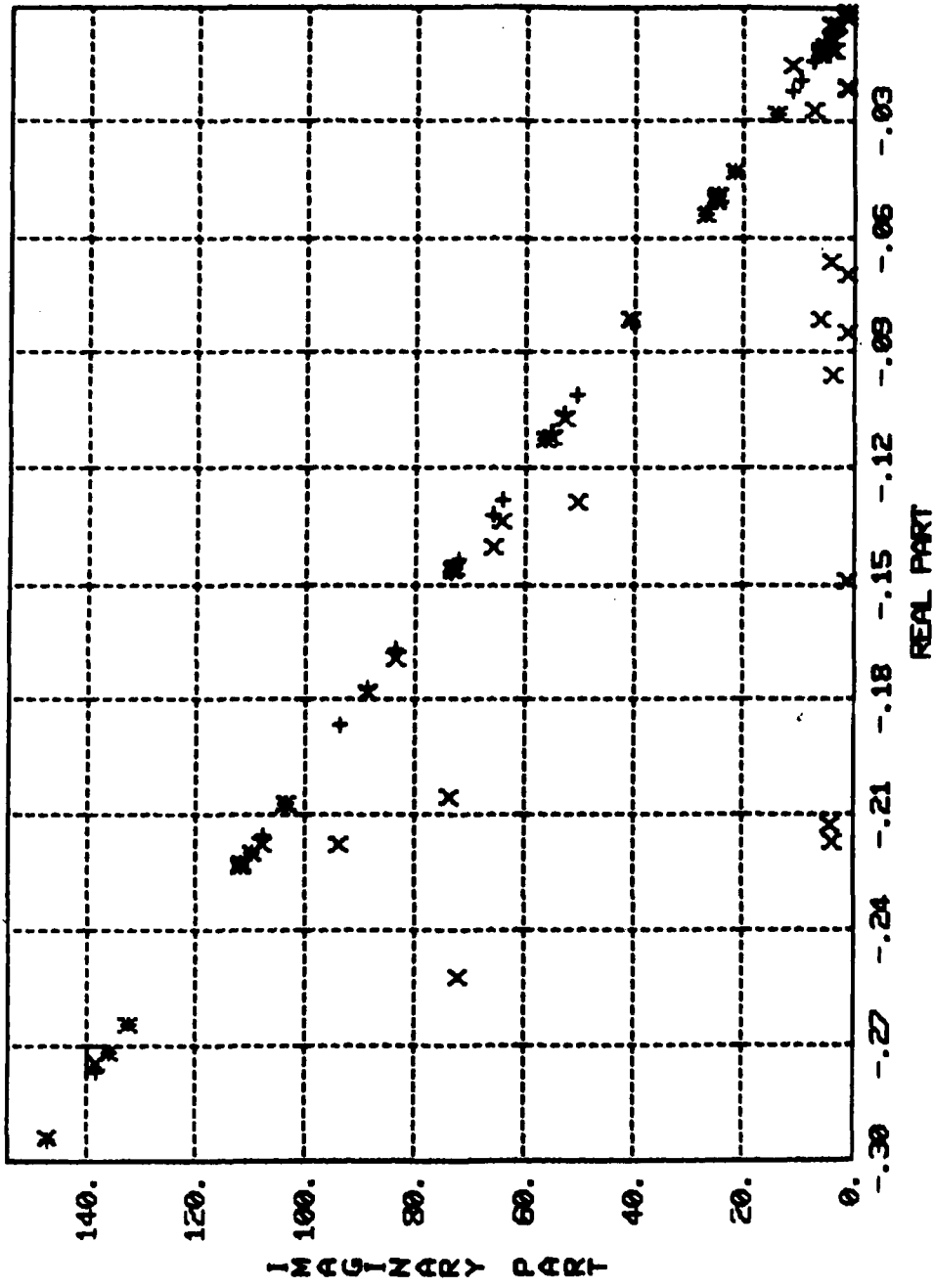


Figure 35. //VCOSS (+) Open-Loop Spectrum, (X) Closed-Loop Spectrum, 26th Order

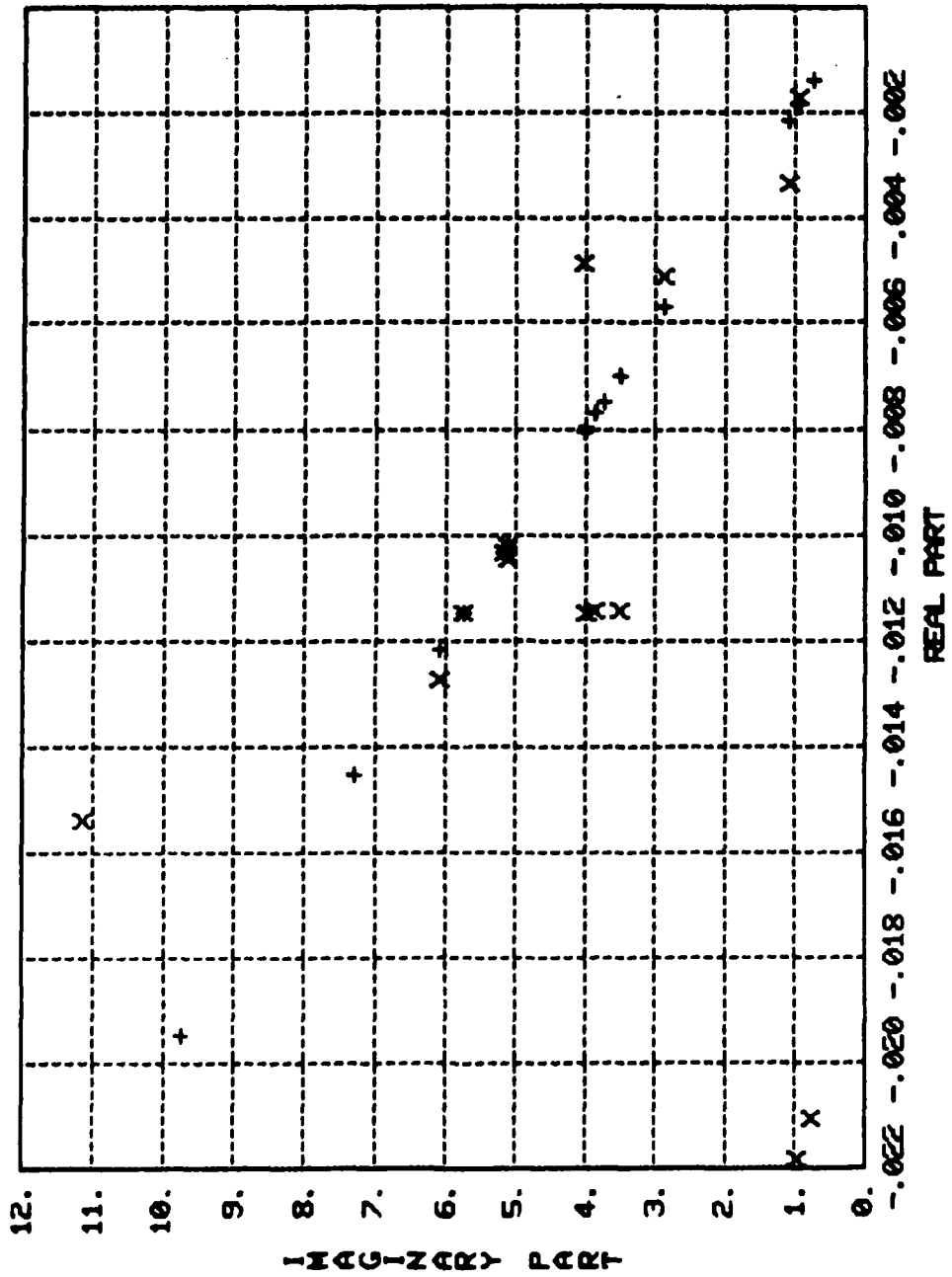


Figure 36. //VCOSS (+) Open-Loop Spectrum, (X) Closed-Loop Spectrum, 26th Order

The stochastic performance with this controller is included in Table 20. Using a total RMS control effort of $12.2N$ the RMS LOS error is reduced to 16% of the open-loop value. The closed-loop (absolute) RMS "modal costs" with this controller are shown in Fig. 37. Notice that the effect is to reduce the disturbance levels significantly in modes 17, 16, and 1; which are the largest open-loop contributors. Also note that the disturbance contribution of the "spillover modes" 2, 5, 10, and 18 does not increase.

b. High-Gain Controller

(1) Mode Selection

The 10-mode controller caused the damping in the unmodeled controllable modes 2, 5, and 10, and "high" frequency mode 18 to decrease. To account for this effect and improve closed-loop performance, these four modes were added to the design model; resulting in a 34th order linear control design model. The 14 modes used are shown in Fig. 38. The in-band unmodeled modes 11 through 14 have very low controllability and are not required. From Fig. 28 it is also evident that modes 19 through 26 are highly insensitive to control and disturbance inputs. This fact is used to justify a closed-loop controller bandwidth extending into this "dead zone."

(2) Control Design

As before, a standard linear LOS regulator and Kalman filter is designed using the 34th order design model. For a control penalty of $5 \times 10^{-12}I$ and "measurement noise" of $5 \times 10^{-11}I$, the resulting controller has bandwidth of 3.5 Hz which is well into the "dead zone." The control and filter design spectra are given in Table 18 and 19, respectively.

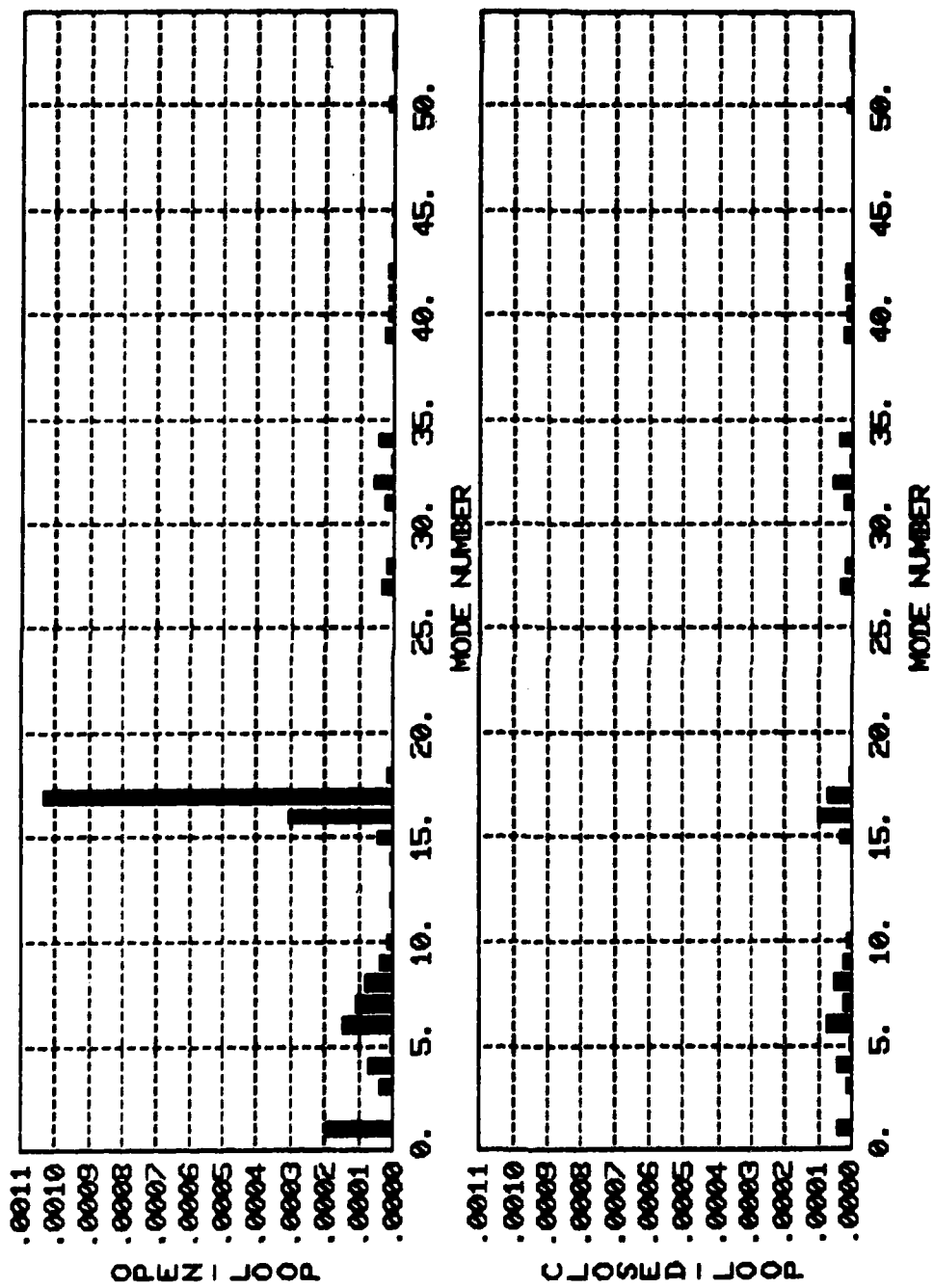


Figure 37. Closed-Loop Modal Costs for 10-Mode Controller

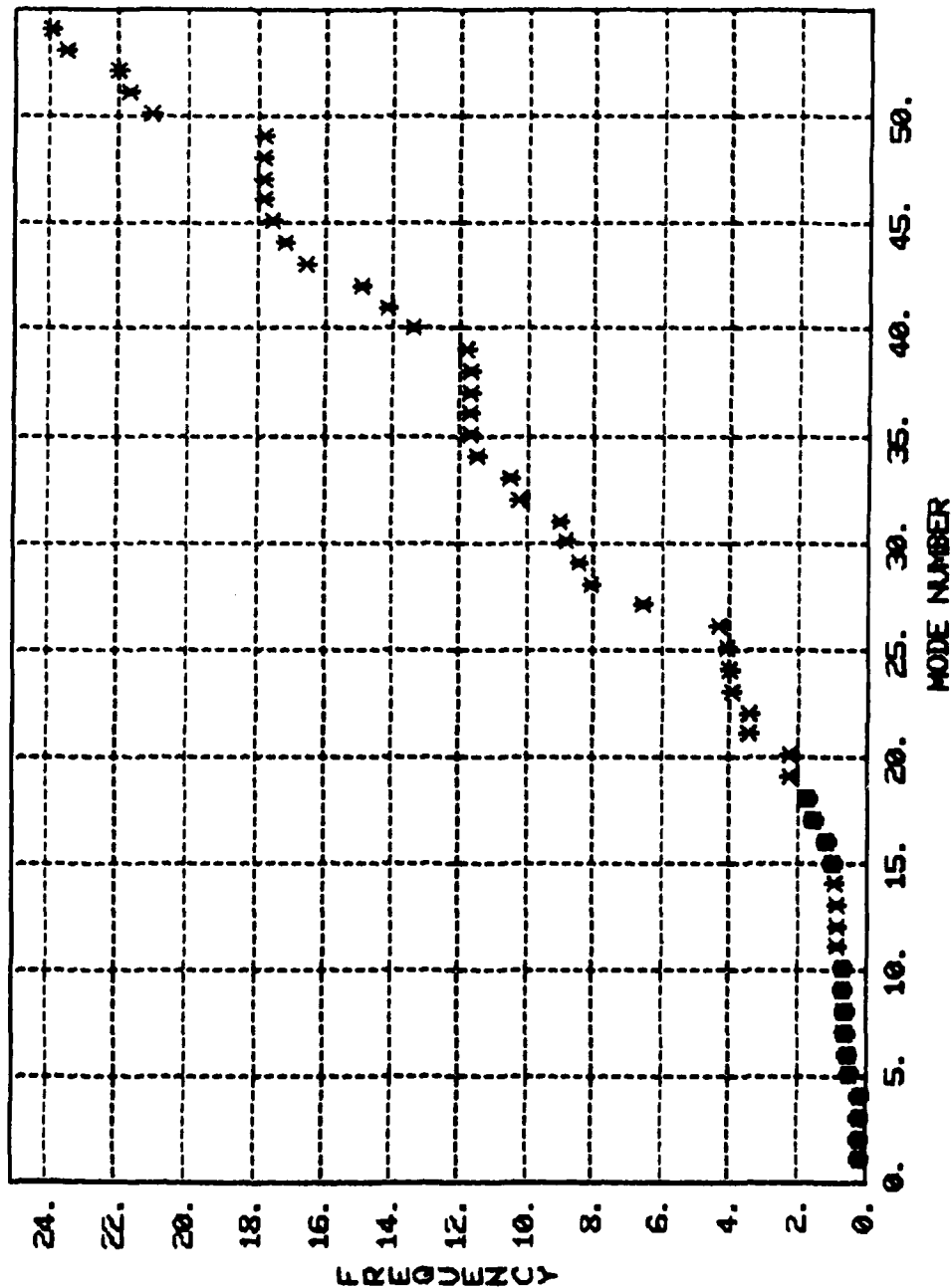


Figure 38. Mode-Selection for 14-Mode Reduced Model

Table 18
 CLOSED-LOOP CONTROL SPECTRUM FOR 14 MODE-MODEL. $b = 5 \times 10^{-12}$

Real Part	Imaginary Part	Frequency (Hz)	Damping Ratio
-13.7611	16.8251	3.4594	0.6331
-13.7611	-16.8251	3.4594	0.6331
-0.0310	11.1483	1.7743	0.0028
-0.0310	-11.1483	1.7743	0.0028
-0.0172	7.3410	1.1684	0.0023
-0.0172	-7.3410	1.1684	0.0023
-0.0129	6.0954	0.9701	0.0021
-0.0129	-6.0954	0.9701	0.0021
-0.9724	3.8742	0.6357	0.2434
-0.9724	-3.8742	0.6357	0.2434
-0.0178	2.8514	0.4538	0.0062
-0.0178	-2.8514	0.4538	0.0062
-0.0077	3.4803	0.5539	0.0022
-0.0077	-3.4803	0.5539	0.0022
-0.0095	3.8664	0.6154	0.0025
-0.0095	-3.8664	0.6154	0.0025
-0.0083	4.0291	0.6413	0.0020
-0.0083	-4.0291	0.6413	0.0020
-0.0097	3.9768	0.6329	0.0024
-0.0097	-3.9768	0.6329	0.0024
-0.0078	0.7501	0.1194	0.0104
-0.0078	-0.7501	0.1194	0.0104
-0.0027	1.0983	0.1748	0.0025
-0.0027	-1.0983	0.1748	0.0025
-0.0747	0.9771	0.1560	0.0762
-0.0747	-0.9771	0.1560	0.0762
-0.0023	0.9227	0.1469	0.0025
-0.0023	-0.9227	0.1469	0.0025

Table 19

CLOSED-LOOP FILTER SPECTRUM FOR 14 MODE-MODEL. $v = 5 \times 10^{-11}$

Real Part	Imaginary Part	Frequency (Hz)	Damping Ratio
-12.3240	15.9457	3.2075	0.6115
-0.0354	11.1465	1.7740	0.0032
-0.0354	-11.1465	1.7740	0.0032
-0.5400	7.3256	1.1691	0.0735
-0.5400	-7.3256	1.1691	0.0735
-0.0906	6.0858	0.9687	0.0149
-0.0906	-6.0858	0.9687	0.0149
-1.0419	3.7793	0.6239	0.2658
-1.0419	-3.7793	0.6239	0.2658
-0.3461	3.9807	0.6359	0.0866
-0.3461	-3.9807	0.6359	0.0866
-0.0222	4.0329	0.6419	0.0055
-0.0222	-4.0329	0.6419	0.0055
-0.0720	3.9663	0.6314	0.0182
-0.0720	-3.9663	0.6314	0.0182
-0.0771	3.6160	0.5756	0.0213
-0.0771	-3.6160	0.5756	0.0213
-0.0143	2.8490	0.4534	0.0050
-0.0143	-2.8490	0.4534	0.0050
-0.1039	1.0994	0.1758	0.0941
-0.1039	-1.0994	0.1758	0.0941
-0.1944	0.7966	0.1305	0.2370
-0.1944	-0.7966	0.1305	0.2370
-0.1713	0.8836	0.1432	0.1903
-0.1713	-0.8836	0.1432	0.1903
-0.0019	0.9227	0.1469	0.0020
-0.0019	-0.9227	0.1469	0.0020

(3) Evaluation

Using the 34th order controller, a closed-loop evaluation with the full VCOSS model was performed. Figures 39 through 41 show the resulting closed-loop spectrum. No "in-band" spillover occurs, since the candidate modes were included in the model. Mode 27 experiences a significant right-shift. It is the closest unmodeled mode to the controller bandwidth having significant controllability (see Fig. 28). Notice that as expected no problems occur in the "dead zone" modes. Higher frequency spillover effects are evident in modes 53, 52, and 31. These are well above the bandwidth of model certainty and cannot be explicitly handled. In the next section a low-authority control is used for the prevention of spillover at unknown high frequencies.

The performance with this controller is included in Table 20. With a total RMS control effort of 29N the RMS LOS error is improved by an order of magnitude. The closed-loop modal costs with this controller are shown in Fig. 42. The modal LOS disturbance contributions are reduced significantly in the controller bandwidth. Note that the modal cost for mode 27 increases slightly over the open-loop.

c. High-Gain Controller with Low-Authority Control

The purpose of low-authority control (LAC) is to add damping to structural modes in the high-frequency uncertainty region. This method is described fully in reference [3] where it was used successfully to eliminate high-frequency spillover. For the nine colocated actuators and sensors of the VCOSS model, a LAC is designed for 4 percent damping in the structural modes.

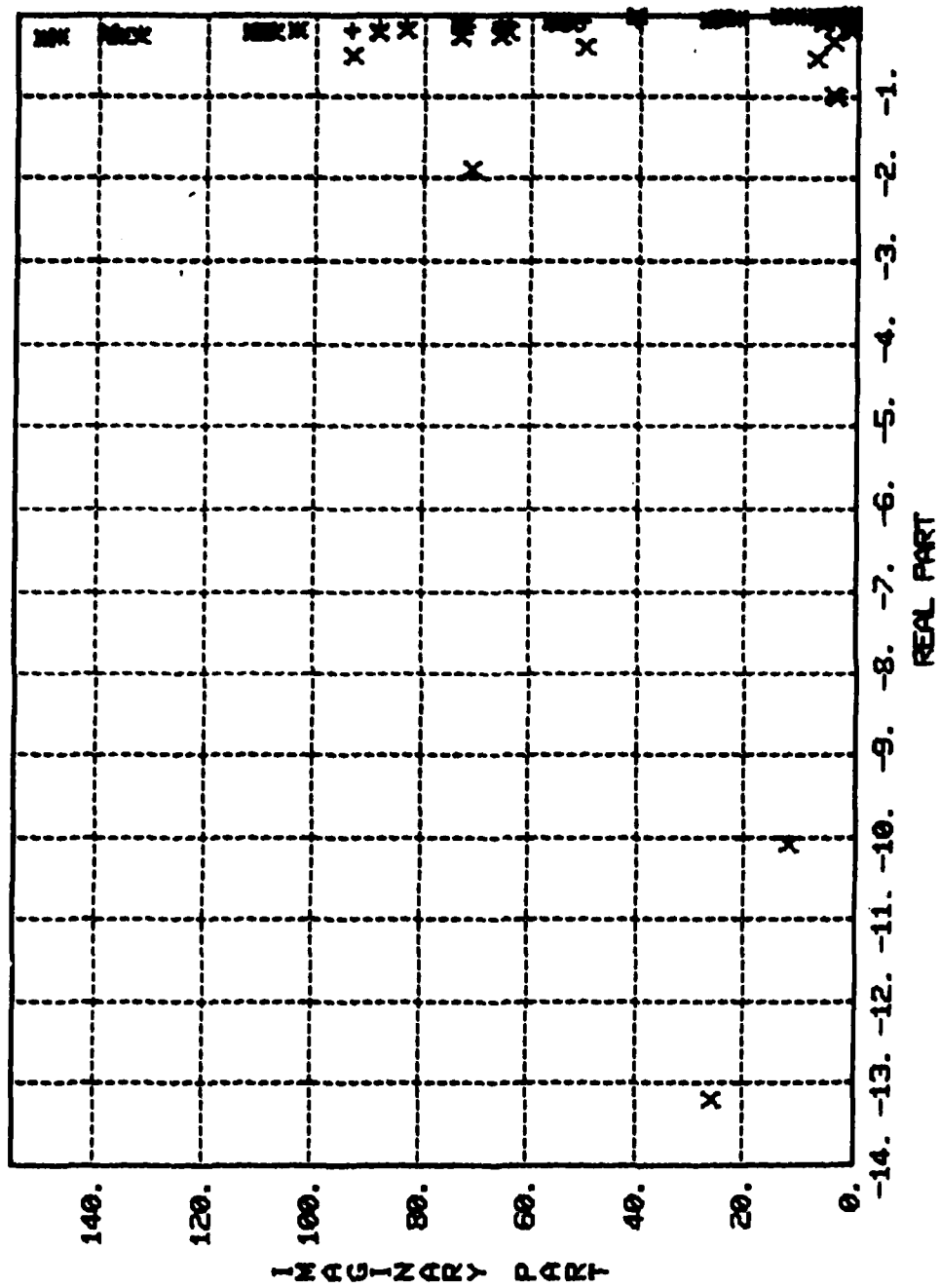


Figure 39. (+) Open-Loop Spectrum, (x) Closed-Loop Spectrum, 34th Order

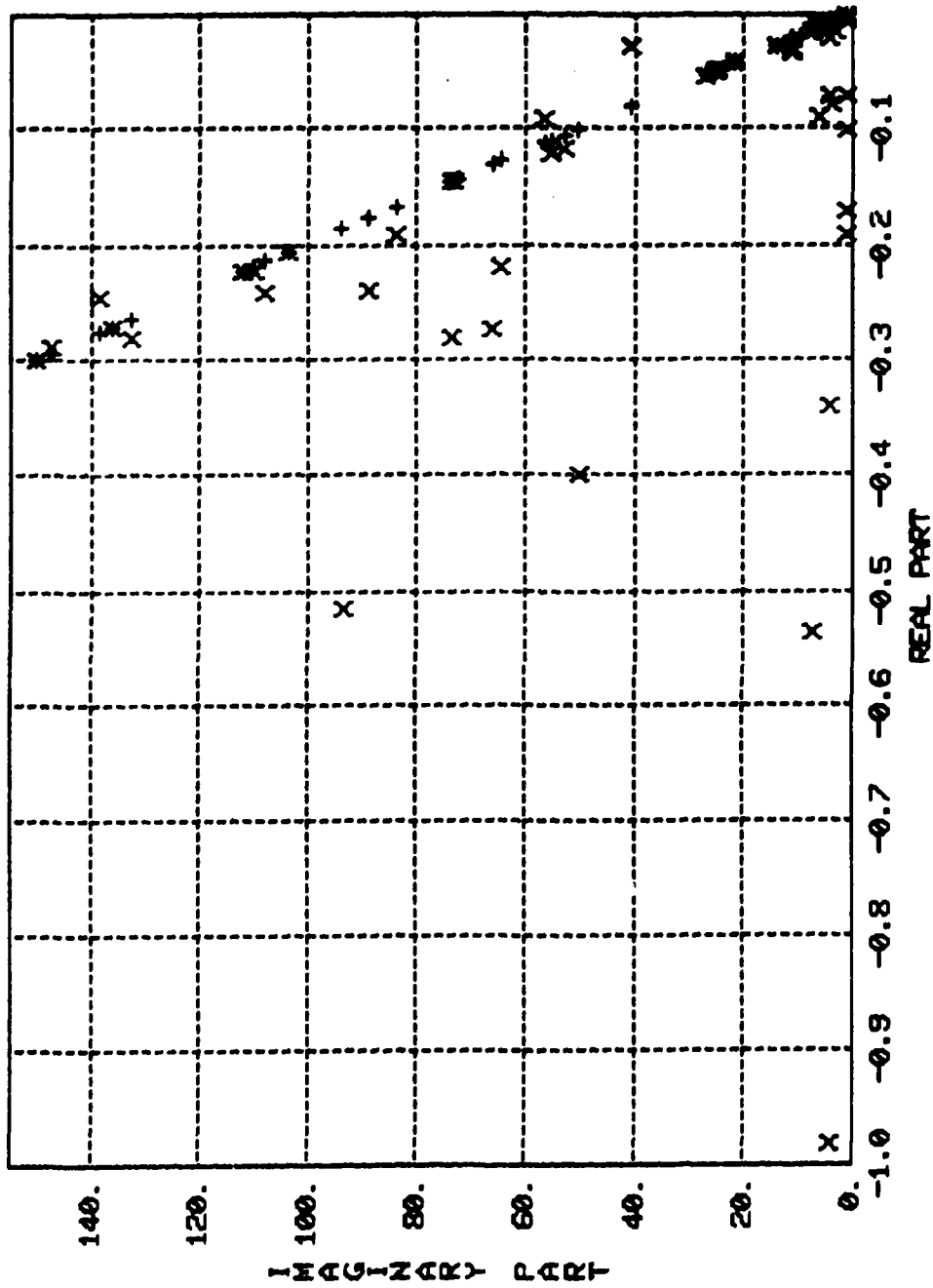


Figure 40. (+) Open-Loop Spectrum, (X) Closed-Loop Spectrum, 34th Order

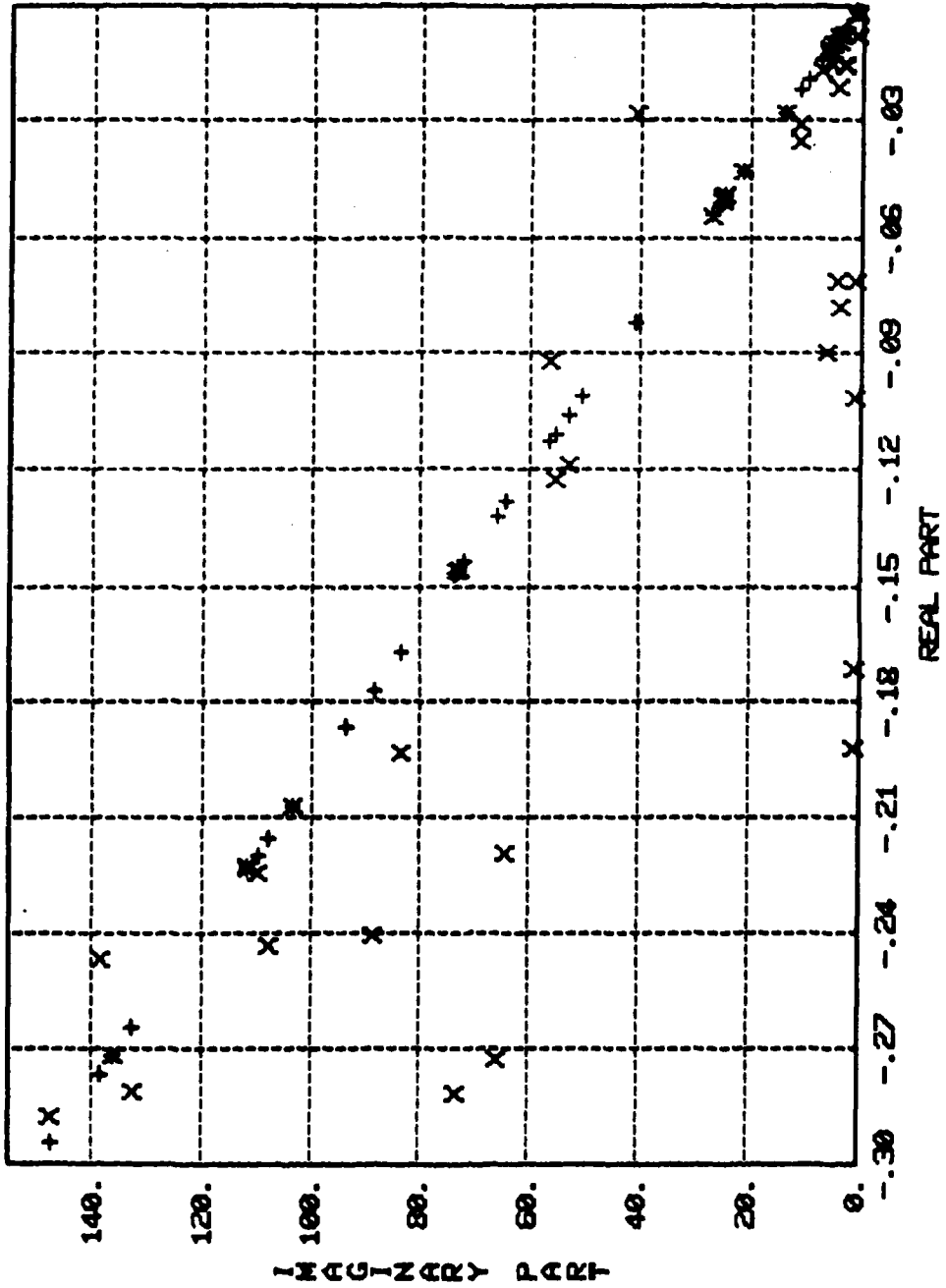


Figure 41. (+) Open-Loop Spectrum, (x) Closed-Loop Spectrum, 34th Order

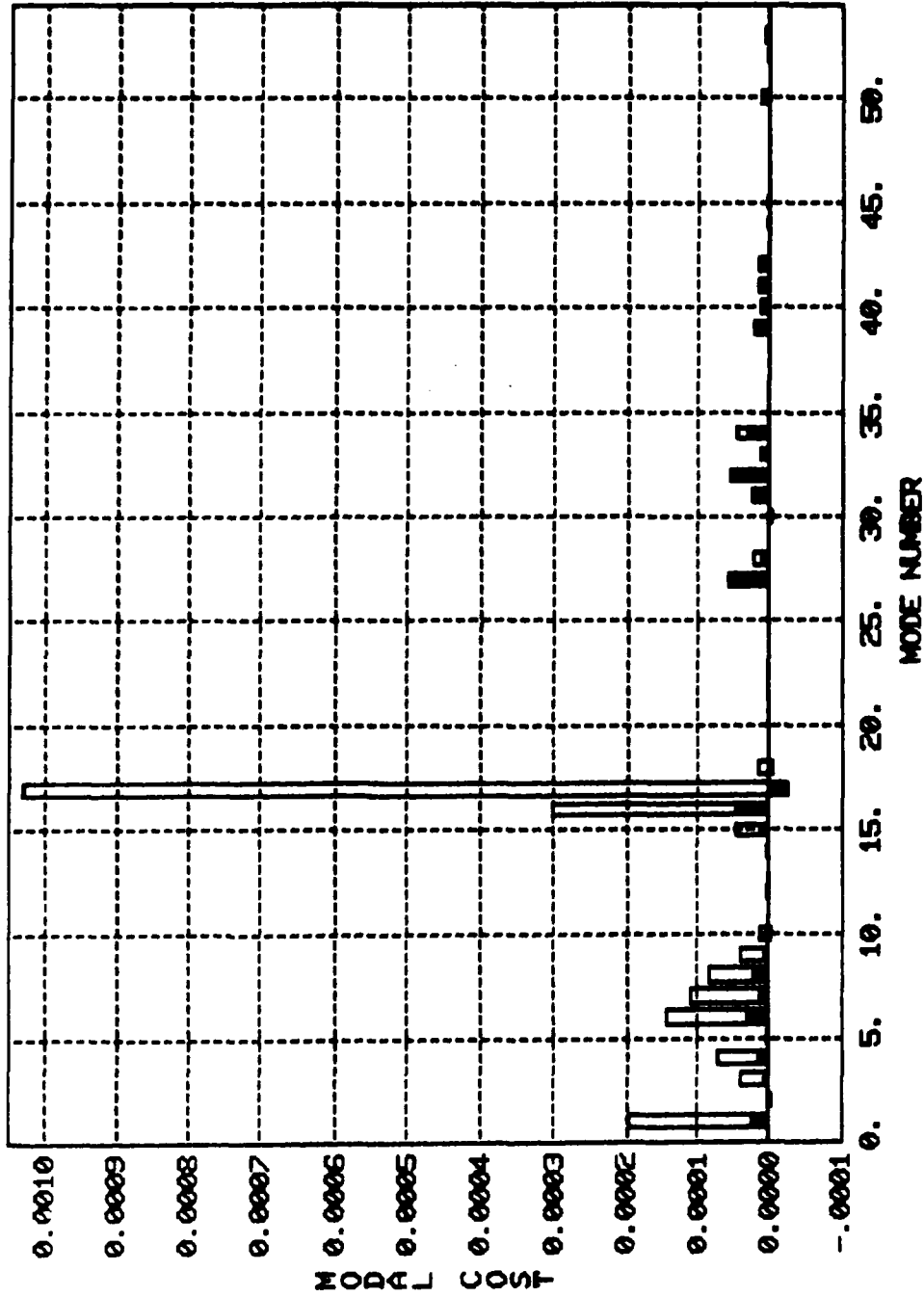


Figure 42. VCOSS Open-Loop (Open) and Closed-Loop (Shaded) Modal Costs for 34th Order Controller

(1) Evaluation

The high-gain controller with low-authority rate feedback was evaluated with the full VCOSS model. The closed-loop spectrum is shown in Figs. 43 through 45. All high-frequency spillover effects appear to be suppressed. The stochastic performance is shown in Table 20, and a breakdown of actuator effort is given in Table 21. There is a 20 percent improvement in the RMS LOS error over the high-gain controller used alone, while the required RMS control effort is reduced to 25N. Apparently, the LAC causes a redistribution of required control effort among the actuators.

One possible reason for this may be found in the sensor-actuator placement. Referring again to Fig. 28, modes 5 and 17 are very significant with respect to sensor-actuator effect. The LQG controls may be working very hard to reduce the stochastic levels in these modes even though the LAC can do so much more cheaply.

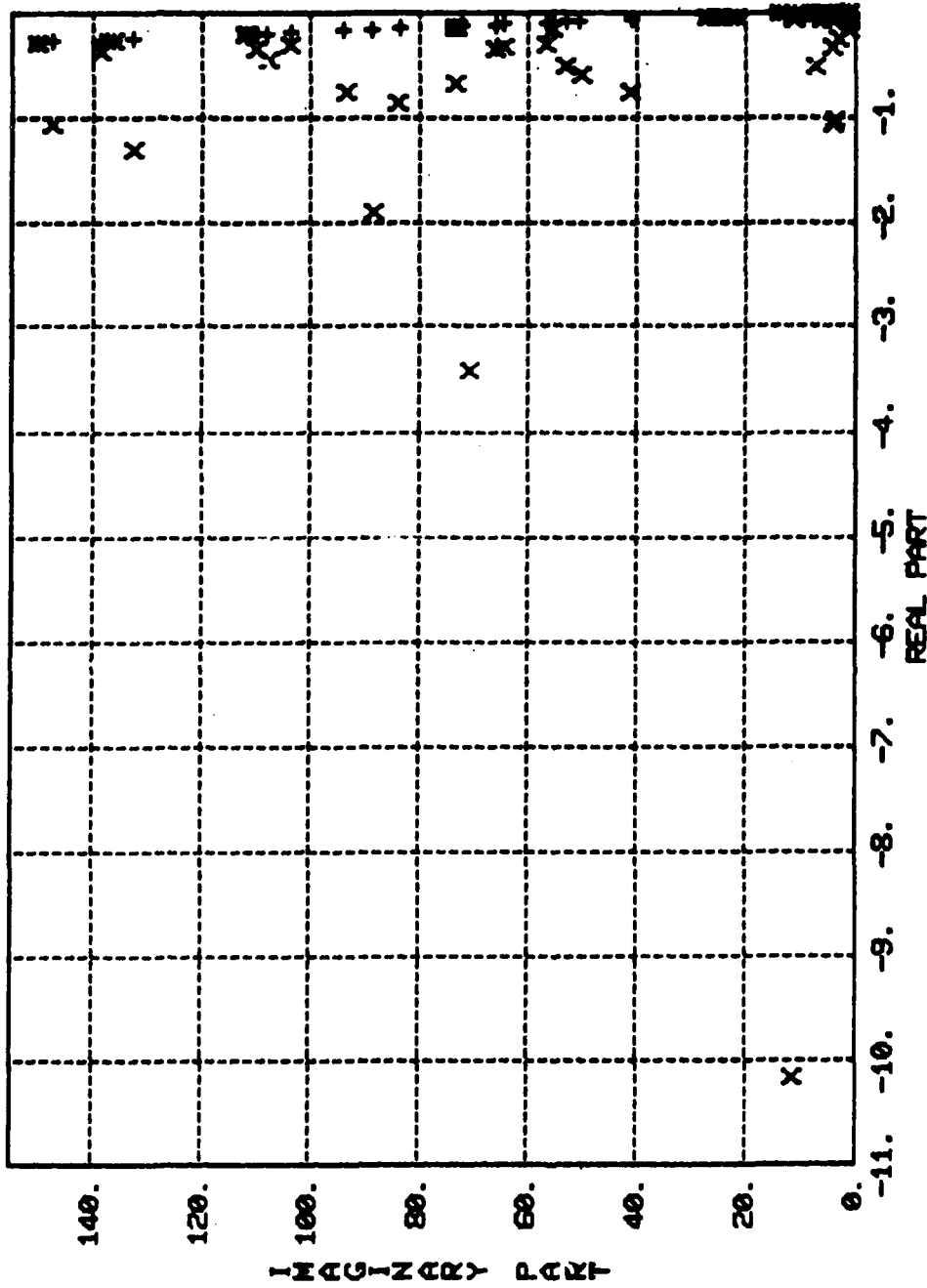


Figure 43. (+) Open-Loop Spectrum, (X) Closed-Loop Spectrum,
HAC/LAC

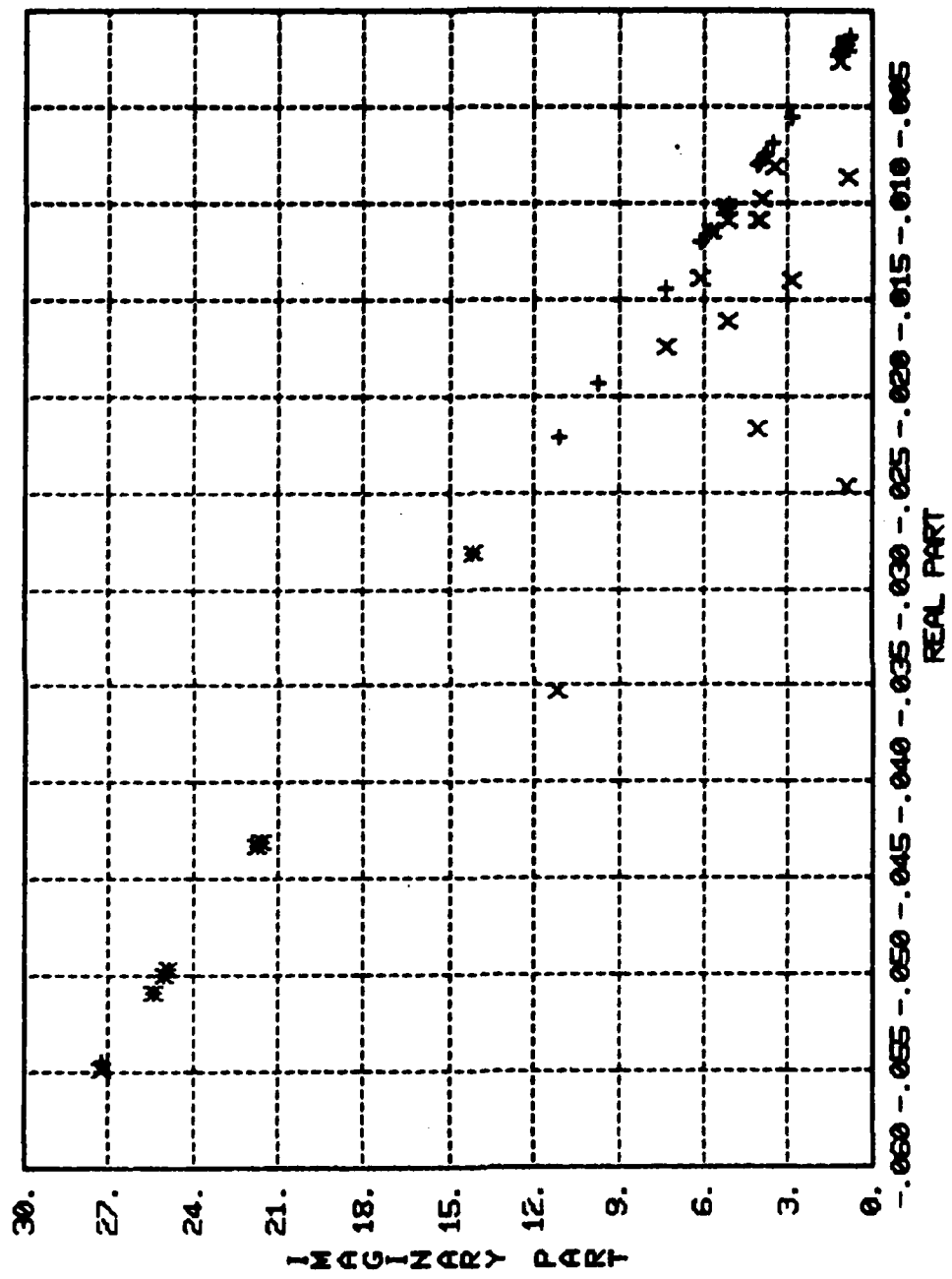


Figure 44. (+) Open-Loop Spectrum, (X) Closed-Loop Spectrum, HAC/LAC

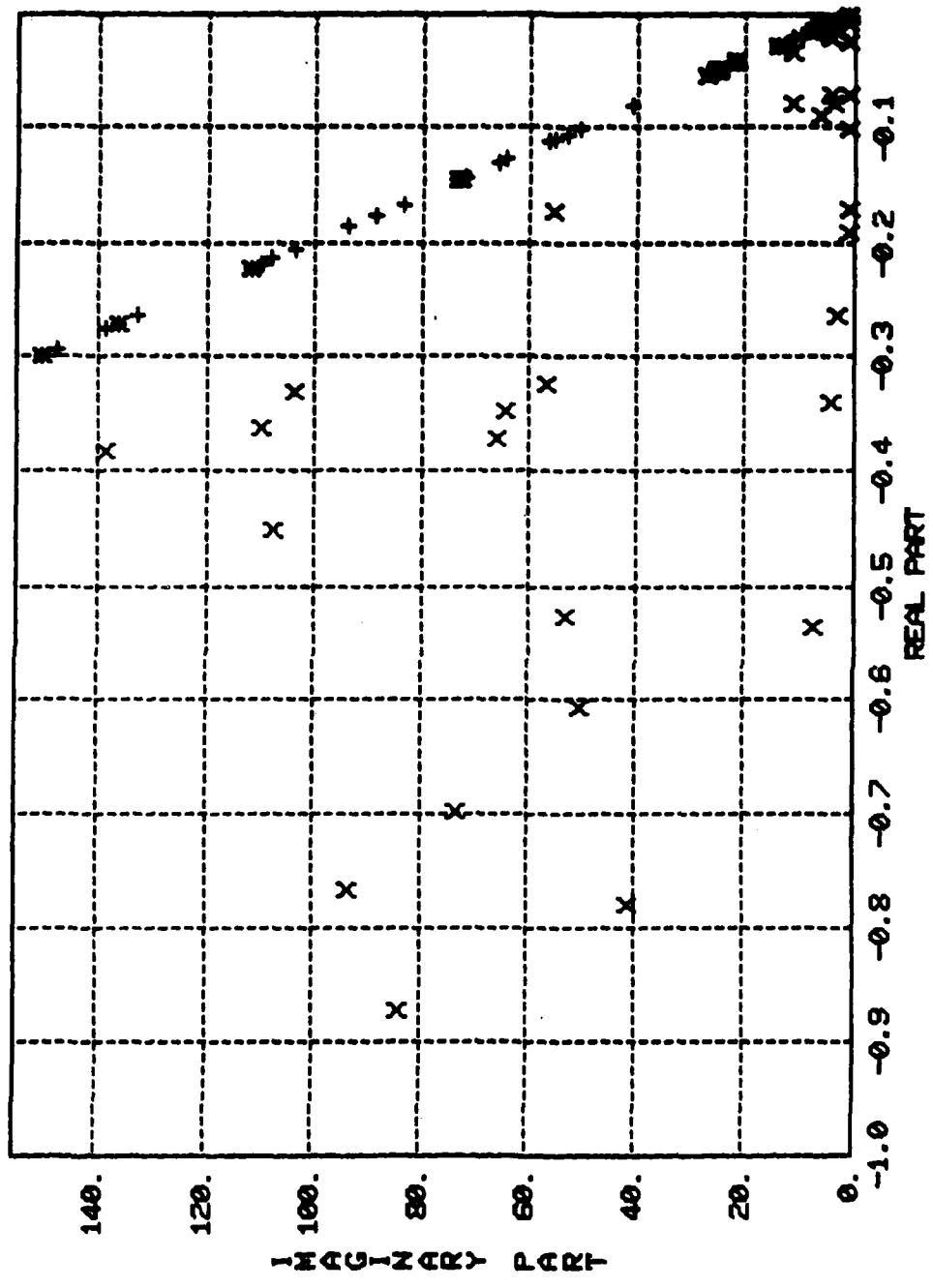


Figure 45. (+) Open-Loop Spectrum, (X) Closed-Loop Spectrum, HAC/LAC

Table 20

STOCHASTIC PERFORMANCE ANALYSIS OF VCROSS CONTROLLERS

	OPEN LOOP	"CAUTIOUS" 10-MODE CONTROL	HIGH GAIN 14-MODE CONTROL	HIGH-GAIN CONTROL WITH LAC
RSS LOS x (μ RAD)	131.7	62.4	69.0	26.4
RSS LOS y (μ RAD)	1109.5	175.9	87.5	75.6
TOTAL RSS LOS (μ RAD)	1117.3	186.6	111.4	80.1
RSS CONTROL EFFORT (N)	0	12.2	28.6	25.3

Table 21

INDIVIDUAL ACTUATOR RMS EFFORT FOR EACH CONTROLLER (N)

Actuator Number	10-Mode Controller	14-Mode Controller	14-Mode Controller with LAC
1	6.1714D-01	1.3286D+00	2.0412
2	5.2332D+00	1.1812D+01	10.1947
3	5.0819D+00	1.1809D+01	10.1013
4	1.0711D+00	2.3408D+00	2.8637
5	4.9265D+00	1.1878D+01	10.4055
6	4.9274D+00	1.1823D+01	10.3886
7	1.9804D-01	5.6409D-01	1.7616
8	4.8079D+00	1.1213D+01	10.2338
9	4.7216D+00	1.1108D+01	10.0071

5. IMPACT OF DISTURBANCE MODEL CHANGES

The preceding analysis presumes six equal and independent colored-noise disturbances -- as modeled by equations (18) to (21). It should be noted that the results obtained may be scaled to give a solution for any 6th order white noise of the form (normal distribution) $w \sim N(0, \bar{w}I)$. This scaling does not affect the relative modal rankings, design model selection, or controller designs. The normalized performance analysis for this form of disturbance is shown in Table 22.

If for computational convenience, the number of disturbances is reduced to two (one along the trisector of the axes at each disturbance location), then the entire solution is affected. The modified disturbance distribution will change the filter gains (as well as the number of noise states in the design model); moreover, the altered open-loop modal rankings of disturbance-to-LOS and disturbance-to-sensors may dictate a different design model selection. Thus, in general, a modified disturbance distribution requires a modified control design. These modifications produce minor changes in controller performance, i.e., this is not a robustness issue.

Table 22

NORMALIZED STOCHASTIC PERFORMANCE ANALYSIS OF VCOSS
CONTROLLERS - 6 INDEPENDENT DISTURBANCES

$\Xi = -30\pi I \text{sec}^{-1}$ $W = \bar{w} I N^2 / \text{sec}$	OPEN LOOP	"CAUTIOUS" 10-MODE CONTROL	HIGH GAIN 14-MODE CONTROL	HIGH GAIN CONTROL WITH LAC
RSS LOS x (μ RAD)	$0.221 \sqrt{\bar{w}}$	$0.105 \sqrt{\bar{w}}$	$0.116 \sqrt{\bar{w}}$	$0.044 \sqrt{\bar{w}}$
RSS LOS y (μ RAD)	$1.861 \sqrt{\bar{w}}$	$0.295 \sqrt{\bar{w}}$	$0.147 \sqrt{\bar{w}}$	$0.127 \sqrt{\bar{w}}$
TOTAL RSS LOS (μ RAD)	$1.874 \sqrt{\bar{w}}$	$0.313 \sqrt{\bar{w}}$	$0.187 \sqrt{\bar{w}}$	$0.134 \sqrt{\bar{w}}$
RSS CONTROL EFFORT (N)	0	$0.021 \sqrt{\bar{w}}$	$0.048 \sqrt{\bar{w}}$	$0.042 \sqrt{\bar{w}}$

To demonstrate the effect of disturbance order reduction upon the 14-mode controller of the previous section, the stochastic performance analysis is repeated using the two-disturbance PSD described in [5]. The results are shown in Tables 23 and 24. Notice that the total RMS LOS reduction is slightly better than that of the six independent disturbance case: a factor of 17 for the former, 13 for the latter. Since closed-loop performance is dominated by truncated-mode response, improvement due to controller redesign will be negligible for this example provided the modal-fidelity ground rules are followed. Therefore, no new design is generated. Table 25 gives the normalized performance analysis for the two-disturbance case where $w \sim N(0, \bar{w}I)$.

Table 23

STOCHASTIC PERFORMANCE OF VCOSS CONTROLLERS - 2
INDEPENDENT DISTURBANCES

	OPEN LOOP	HIGH GAIN 14-MODE CONTROL	HIGH-GAIN CONTROL WITH LAC
RMS LOS x (μ RAD)	77.72	45.82	16.19
RMS LOS y (μ RAD)	968.04	55.33	53.64
TOTAL RMS LOS (μ RAD)	971.16	71.84	56.03
CONTROL EFFORT (N)	0	17.12	16.59

Table 24

RSS ACTUATOR EFFORT - 2 INDEPENDENT DISTURBANCES

ACTUATOR NUMBER	HAC	HAC/LAC
1	1.0307	1.2339
2	7.0623	6.7832
3	7.3079	6.9289
4	1.7503	2.2331
5	7.0328	6.7616
6	6.9560	6.6699
7	0.4196	1.3320
8	6.6080	6.4624
9	6.6393	6.4029
TOTAL RSS	17.1223	16.5913

Table 25

NORMALIZED STOCHASTIC PERFORMANCE OF VCOSS CONTROLLERS -
2 INDEPENDENT DISTURBANCES

$\bar{\epsilon} = -30 \text{ I sec}^{-1}$
 $W = \bar{w} \text{ I N}^2/\text{sec}$

	OPEN LOOP	HIGH GAIN 14-MODE CONTROL	HIGH GAIN CONTROL WITH LAC
RSS LOS x (μ RAD)	$0.184 \sqrt{\bar{w}}$	$0.109 \sqrt{\bar{w}}$	$0.038 \sqrt{\bar{w}}$
RSS LOS y (μ RAD)	$2.297 \sqrt{\bar{w}}$	$0.132 \sqrt{\bar{w}}$	$0.127 \sqrt{\bar{w}}$
TOTAL RSS LOS (μ RAD)	$2.304 \sqrt{\bar{w}}$	$0.170 \sqrt{\bar{w}}$	$0.133 \sqrt{\bar{w}}$
RSS CONTROL EFFORT (N)	0	$0.041 \sqrt{\bar{w}}$	$0.039 \sqrt{\bar{w}}$

6. LOW FREQUENCY ACTUATOR LIMITATIONS

a. Force Requirements

Since the major contributor to the LOS error was shown to be the broadband component of the disturbance PSD, the corresponding control effort is also mainly due to this component. In order to evaluate this control effort, the system was driven with the broadband PSD only and the actuator force PSD was computed for each actuator. The total RMS forces for each of the nine actuators are shown in Table 26.

One may already notice that actuators 1, 4 and 7 require much less force output than the others. This results from the fact that the controllability of the LOS with respect to these three actuators was much less than the other six, and that the optimal controller will tend to use more the most efficient actuators. The evaluation of force requirements is thus narrowed by only considering the actuators with the largest RMS in each group (i.e., primary, secondary and tertiary). Thus, actuators 3, 5 and 8 are selected. The PSDs corresponding to these three actuators are respectively given in Figs. 46, 47 and 48 for frequencies ranging from 0 to 10 rad/sec. As could be expected, the maximum control effort is found at the frequencies of the controlled vibration modes. The force requirements may now be broken down for each frequency, by locally integrating the area under the curve. In Fig. 49 for instance, the scale has been expanded to give a better display of actuator #3 PSD curve around 0.75 rad/sec. Since the energy is very localized, one may separate the requirements at different frequencies. Moreover, since, for sizing purposes, an upper bound is sought, a worst case level of effort table can be built by determining, at each peak frequency, what was the largest effort required among the actuators 3, 5 and 8. Table 27 recapitulates these results. The bandwidth of the curve for

Table 26
CORRECTED ACTUATOR EFFORT (N)

LOCATION	ACTUATOR NUMBER	HAC	HAC/LAC
Primary	1	1.0307	1.2339
	2	7.0623	6.7832
	3	7.3079	6.9289
Secondary	4	1.7503	2.2331
	5	7.0328	6.7616
	6	6.9560	6.6699
Tertiary	7	0.4196	1.3320
	8	6.6080	6.4624
	9	6.6393	6.4029
TOTAL RSS		17.1223	16.5913

ACTUATOR 3 PSD

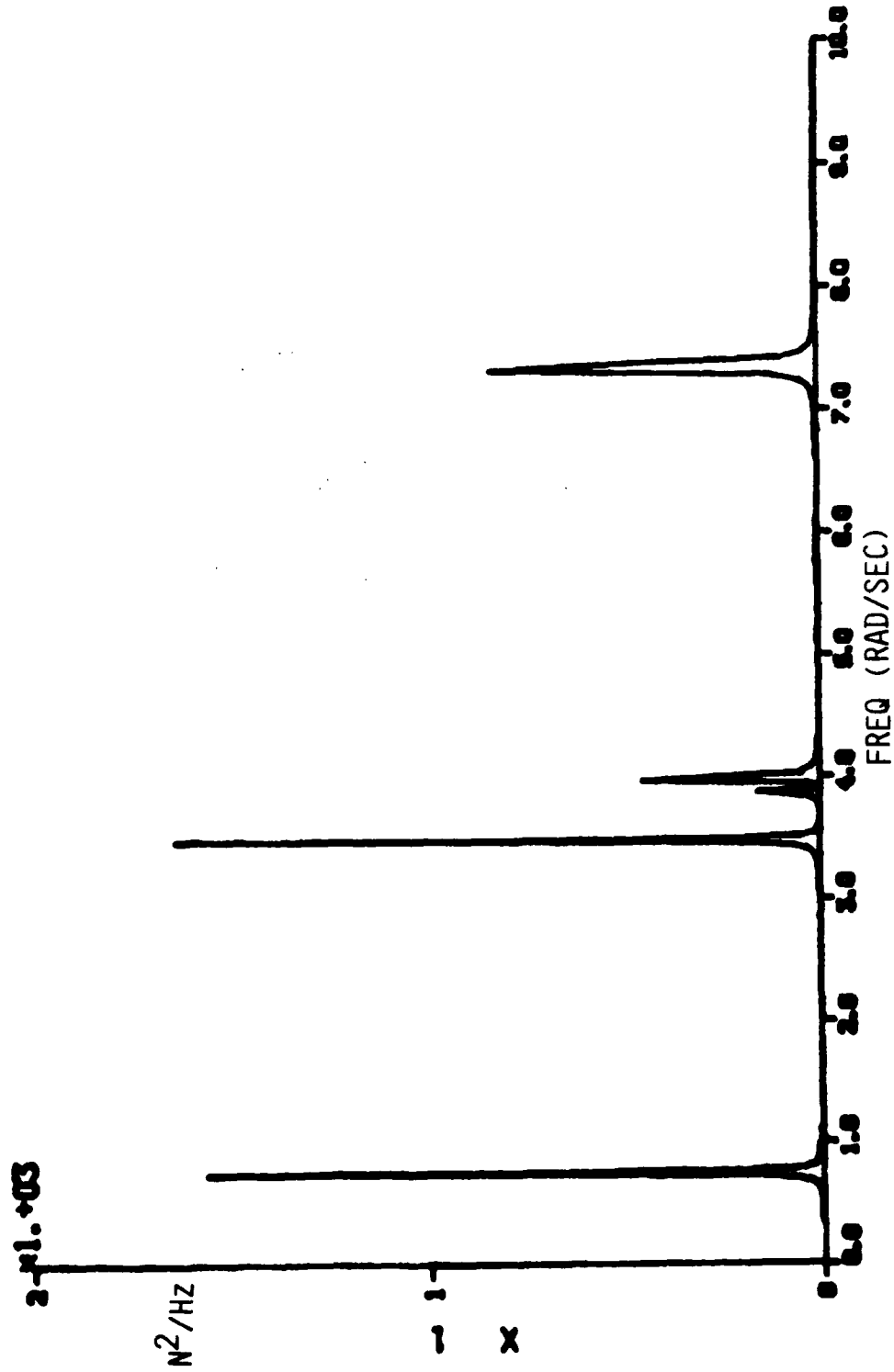


Figure 46. VCOSS/PPM Actuator Power Requirements

ACTUATOR 5 PSD

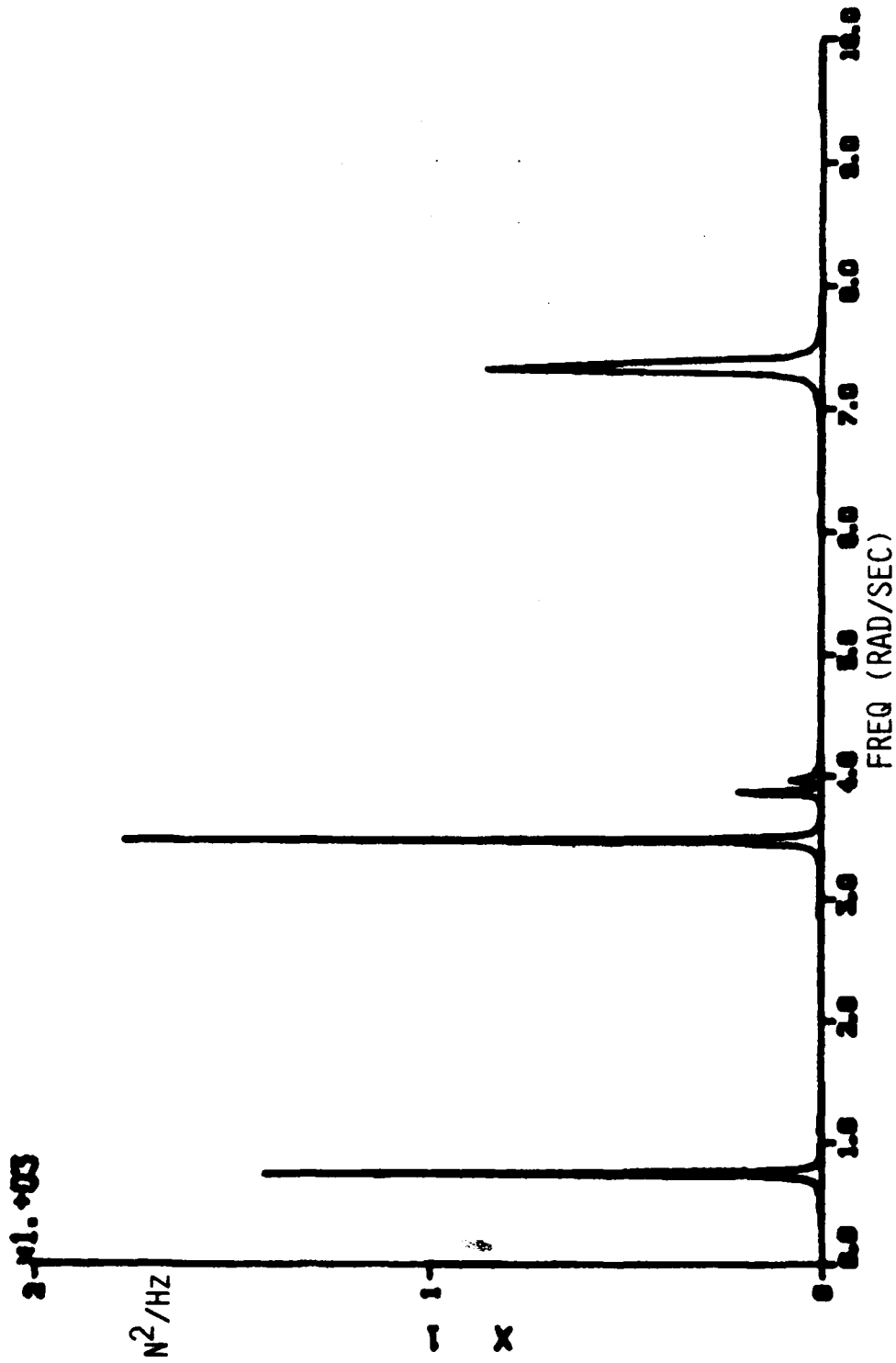


Figure 47. VCOSS/PPM Actuator Power Requirements

ACTUATOR 8

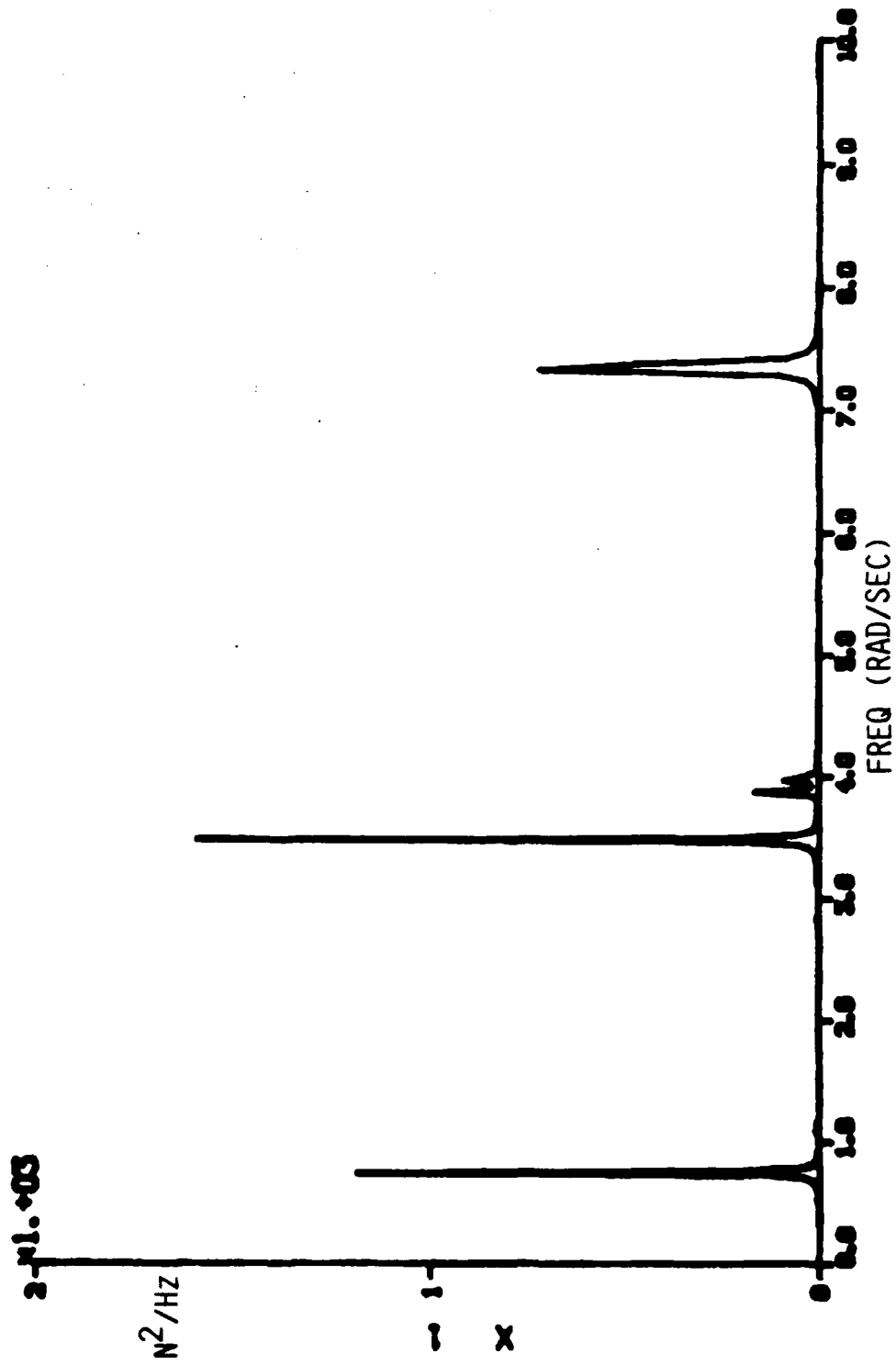


Figure 48. VCOSS/PPM Actuator Power Requirements

ACTUATOR 3 PSD

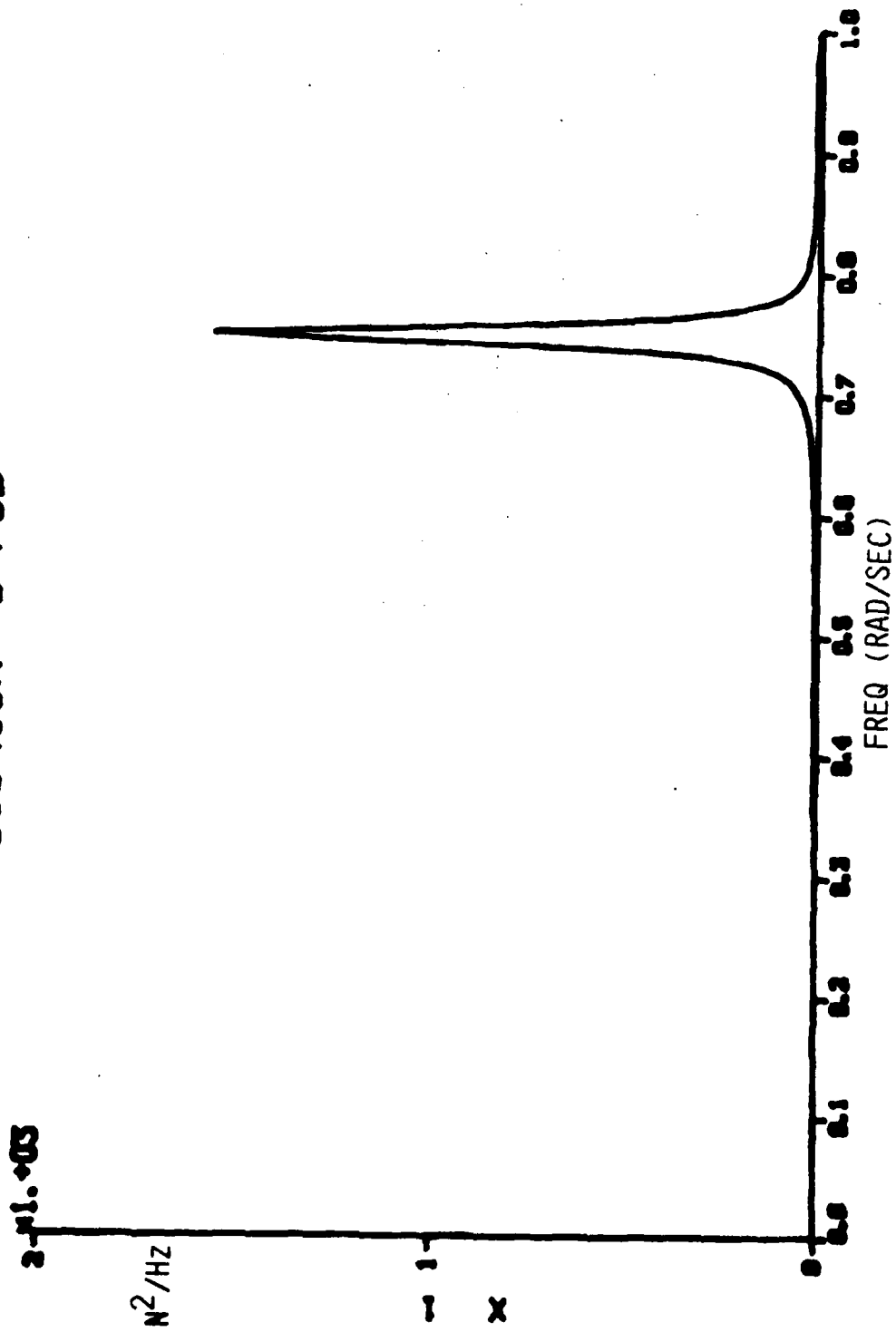


Figure 49. VCOSS/PPM Actuator Power Requirements

Table 27

ACTUATOR SIZING

WORST CASE LEVEL OF EFFORT (RMS)

<u>CONTROL FREQUENCY</u>	<u>BANDWIDTH</u>	<u>FORCE</u>	<u>ACTUATOR</u>
(RAD/S)	(RAD/SEC)	(N)	
0.75	0.035	3.	3
3.5	0.033	3.1	5
3.86	0.03	1.2	5
3.97	0.032	1.5	3
7.33	0.086	5.1	5

which the RMS value was computed is displayed, with the corresponding actuator number. For instance at 3.5 rad/sec, actuator 5 requires the most force, an average of 3.1 N in a bandwidth of 0.033 rad/sec. As can be seen, force levels are relatively small, around or below 5 N.

b. Proof-Mass Actuator Sizing

In proof-mass actuators in general, where m is the mass of the proof-mass and x its displacement, the force delivered is in first approximation given by:

$$f = m\ddot{x}$$

Thus, if f occurs about the frequency ω , the corresponding amplitude of the displacement is given by:

$$x_0 = \frac{f_0}{m\omega^2}$$

For a given force level, the displacement will thus depend upon the choice of m , and upon the frequency. Since, in proof-mass actuators, the displacement is limited, the mass m must become large when the frequency is low. Table 28 shows the displacements required at the various frequencies studied earlier, for three values of the mass. As expected, the strong dependence upon the frequency makes the 0.75 rad/sec case the worst one.

Even with a 30 kg mass, the displacement needed is 18 cm. Although such mass is still very small compared to the total mass of the spacecraft, it drives the design of the actuator toward larger dimensions. In Fig. 50 are shown two pivoted proof-mass actuator designs, one based on the 0.75 rad/sec frequency, one

Table 28

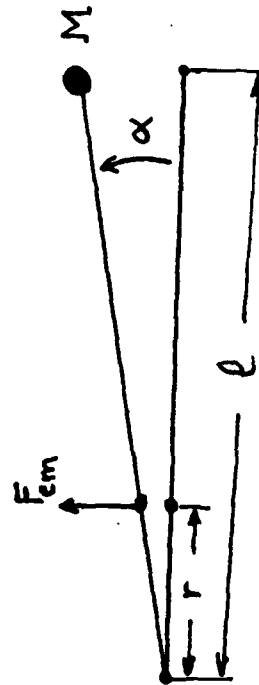
ACTUATOR SIZING

PROOF - MASS ACTUATORS

<u>FREQUENCY</u> (RAD/S)	<u>FORCE</u> (N)	<u>DISPLACEMENT (M)</u>		
		M = 1 KG	10 KG	30 KG
0.75	3.	5.300	0.530	0.018
3.5	3.1	0.250	0.025	0.008
3.86	1.2	0.081	0.008	0.003
3.97	1.5	0.095	0.010	0.003
7.33	5.1	0.094	0.009	0.003

PROOF-MASS ACTUATORS

	"LOW" FREQUENCY DESIGN	"HIGH" FREQUENCY DESIGN
ω_{min}	MINIMUM FREQUENCY (RAD/S)	
M	MASS (KG)	3.5
ℓ	LENGTH (CM)	10.
ρ	LEVER RATIO	25.
F_{em}	MOTOR FORCE (N)	1/10
α	ANGULAR TRAVEL	50
		± 60



$$\rho = r / \ell$$

Figure 50. Actuator Sizing

based on the next frequency (3.5 rad/sec), the so called "high" frequency design. Both designs utilize a 50 N electrodynamic motor, but different masses, length and angular travel. As can be seen, the "high" frequency design is more compact and lighter and will be easier to make than the "low" one. However, the latter is still feasible, with a lever arm below 1 meter. A conceptual arrangement for this actuator is shown in Fig. 51.

c. Conclusions

The preceding results show that a pivoted proof-mass (PPM) actuator could be designed to cover the whole range of frequencies required to control the LOS. The design of such actuators is entirely driven by the lowest frequency to be controlled, because of the $1/\omega^2$ effect. Considering that the lowest frequency in this case was 0.75 rad/sec, i.e., about a 1/10th of a Hertz, it appears that it falls within the range of a static alignment system. Such a system must be implemented anyway to correct for structural deformations due to launch or thermal effects, and will be more appropriate to use than a PPM. The alignment system will generally use position actuators to move the mirror surfaces with respect to the structure and will have enough bandwidth to include the 0.1 Hz mode. The higher modes, however, can be taken care of with small size PPM actuators. The reader should review the initial design guidelines stated earlier to place these conclusions in perspective.

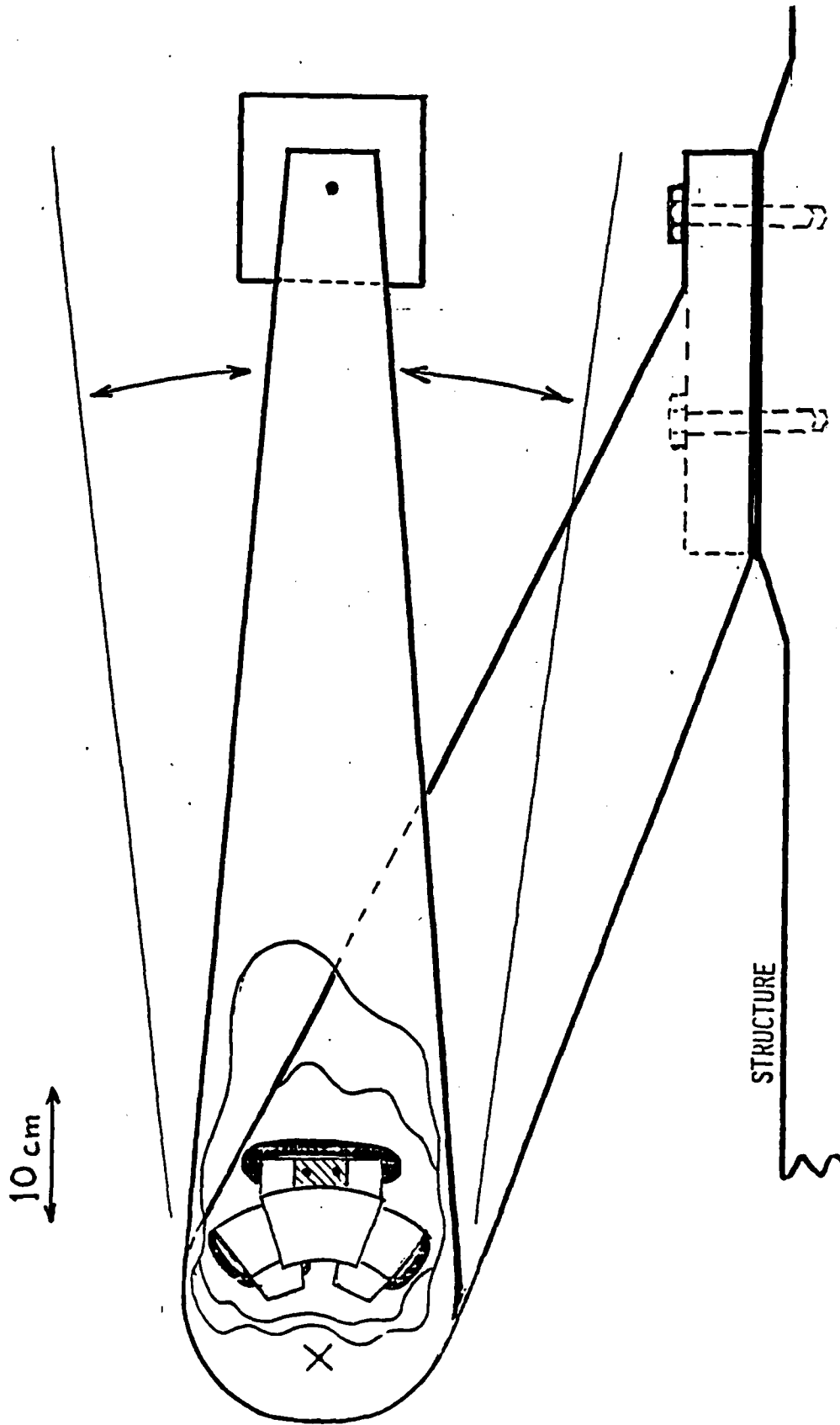


Figure 51. Low Frequency PPM Design

7. EFFECTS OF ACTUATOR DYNAMICS

Having demonstrated a procedure for high-performance control design (HAC) and stability augmentation (LAC) assuming infinite actuator bandwidth, we turn now to the problems imposed by realistic actuators upon HAC/LAC design, stability, and performance. It has been shown [6] that the transfer functions of LAC with a pivoted-proof-mass (PPM) actuator are described by

$$f(s)/x(s) = \frac{cs}{(1 + \tau_1 s)(1 + \tau_2 s)} \quad (c > 0) \quad (37)$$

where $f(s)$ is the force on the structure, $\tau_1 \gg \tau_2$, c is the active control gain, and $x(s)$ is the structural displacement at the actuator location. For frequencies smaller than $(1/2\pi)\tau_1^{-1}$, the system behaves like a damper, then more like a spring, and a final roll-off occurs after $(1/2\pi)\tau_2^{-1}$ with the response going to zero with a -1 slope, as shown in Fig. 52. Since the "idealized" LAC transfer function is

$$f(s)/x(s) = cs,$$

the dynamic effect of a PPM upon a commanded force f_c is given by:

$$\frac{f(s)}{f_c(s)} = \frac{1}{(1 + \tau_1 s)(1 + \tau_2 s)} \quad (38)$$

Thus, the dynamics impose a first-order rolloff on the control effort at frequency $(2\pi \tau_1)^{-1}$, and above $(2\pi \tau_2)^{-1}$ exhibit second-order behavior.

To investigate the impact of these actuators upon HAC/LAC controls, the following assumptions are made:

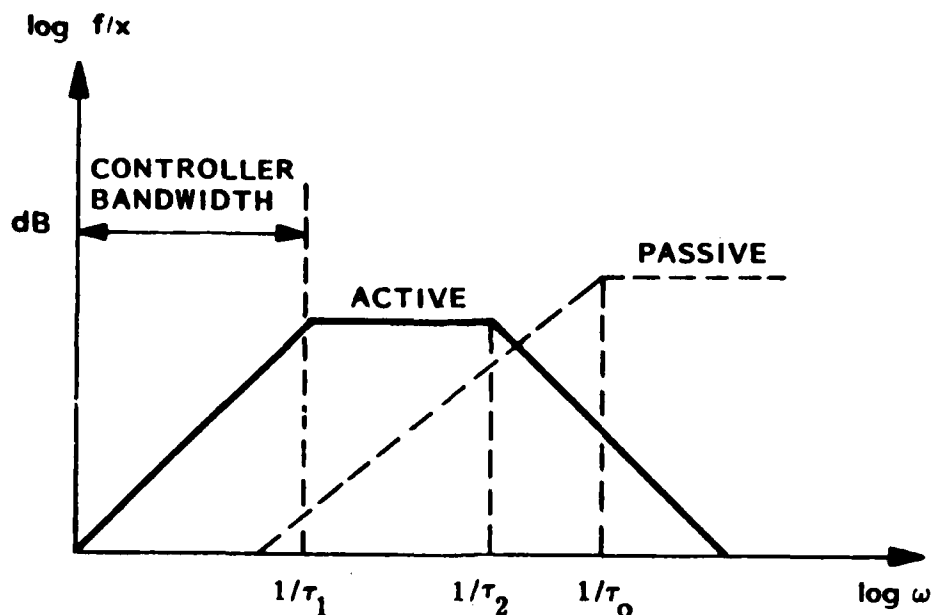


Figure 52. Frequency Response of Active and Passive Dampers

- (1) τ_1 and τ_2 are known quantities. They are readily determined experimentally.
- (2) $(2\pi \tau_1)^{-1}$ is much larger than the highest known (accurately modeled) frequency in the structural model. Otherwise, the actuator dynamics can (and should) be included in the control design model explicitly.

The degree of impact upon controlled performance depends upon the presence of unknown, unmodeled structural modes with which the actuator might interact. An analysis using a class of "evaluation models" containing different truncated modes would show the effects, but the lack of a common reference would make comparisons difficult. Therefore, a different approach is taken here: A single "ideal" controller is designed and evaluated using a representative structural model, with HAC and LAC gains chosen

to reflect a "worst case" pathology; namely, destabilizing HAC spillover in the highest mode compensated by the LAC. Parameter studies are conducted by evaluating stability and performance degradation as a function of actuator rolloff characteristics using this baseline design. The results give a clear picture of actuator effects; although in reality the unknowns are high frequency structural modes rather than actuator dynamics.

a. Idealized Baseline Design Example

A baseline structural HAC/LAC control design is produced using a 34-mode evaluation model and two colocated actuator/sensor pairs. Referring to Fig. 28, 34 modes give a credible representation of "known" and "unknown" structural modes provided the known bandwidth is defined as 0-2 Hz. Actuator/sensor locations 2 and 3 (see Fig. 20) are selected based upon the performance controllability rankings given in Figs. 29 through 31. These plots show that the actuator/sensor complements on each mirror have almost identical authority to the total complement (compare with ACT/LOS in Fig. 28), and further that this authority is dominated by the actuators on the mirror corners. The disturbance model used is the two-disturbance PSD described in [5].

Figure 53 shows the open-loop modal rankings obtained using this model. As in the full design, mode selections for a control design model are made using these rankings; however, the range of model certainty is presumed to be 0-2 Hz. The selected modes are shown in Fig. 54, and the design model spectrum is given in Table 29.

Using this 10-mode design model, an LQG controller is computed with control and measurement weights selected such that

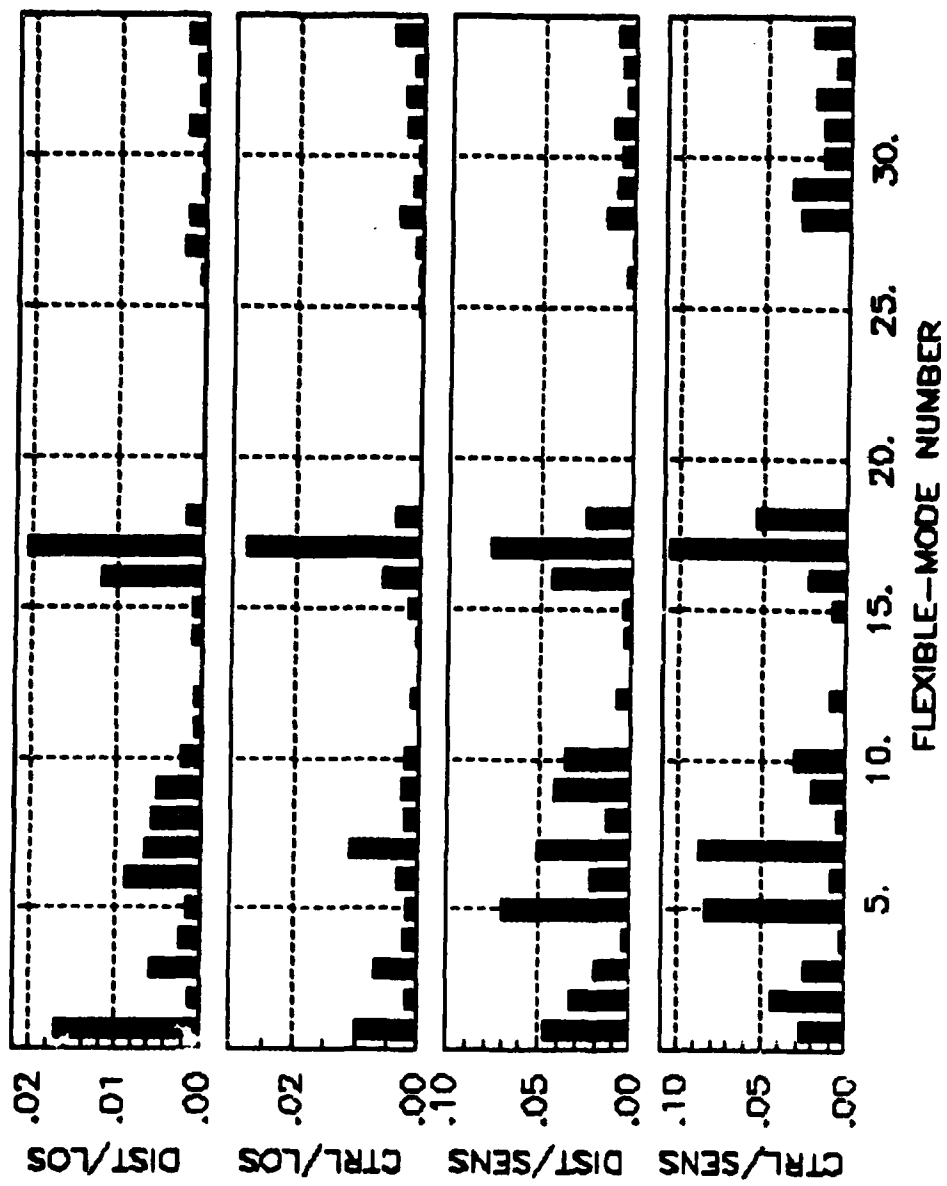


Figure 53. Open-Loop Modal Analysis of 34-Mode Model

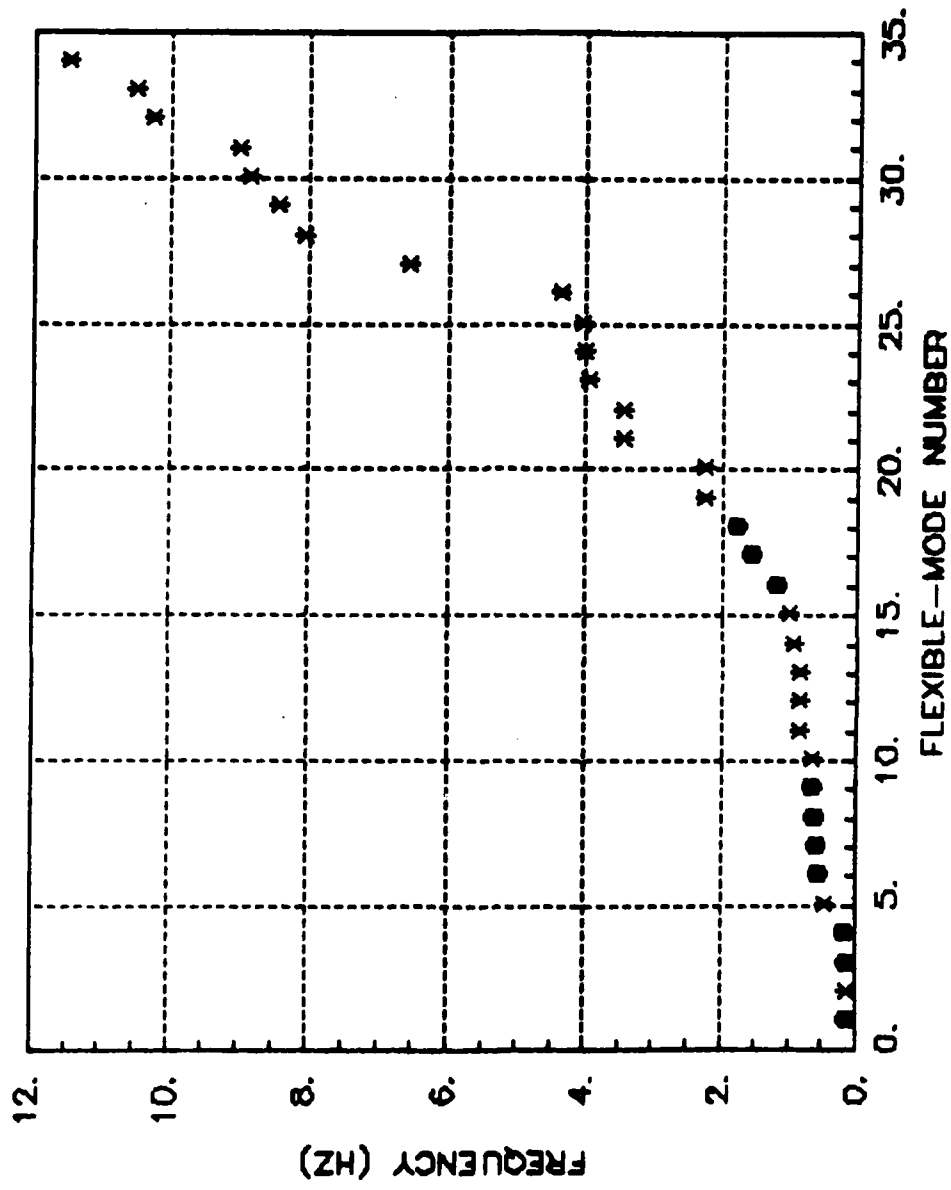


Figure 54. Open-Loop Frequencies of 34-Mode Evaluation Model and Design Model

Table 29

FREQUENCIES OF 10-MODE DESIGN MODEL

REAL PART	IMAG. PART	FREQ. (Hz)	DAMPING RATIO
-0.0014	0.7105	0.1131	0.0020
-0.0019	0.9359	0.1490	0.0020
-0.0022	1.0939	0.1741	0.0020
-0.0070	3.4984	0.5568	0.0020
-0.0075	3.7404	0.5953	0.0020
-0.0077	3.8519	0.6131	0.0020
-0.0080	3.9904	0.6351	0.0020
-0.0146	7.2774	1.1582	0.0020
-0.0195	9.7442	1.5508	0.0020
-0.0223	11.1387	1.7728	0.0020

the closed-loop design spectrum of the controller goes to 3 Hz. The control design and filter design spectra are given in Tables 30 and 31, respectively. This choice of gains represents an "optimistic" high-gain HAC controller since the closed-loop bandwidth exceeds that of the design model; and indeed the resulting spillover destabilizes the full closed-loop system. A LAC of the form

$$u = \begin{bmatrix} -1000 & 0 \\ 0 & -1000 \end{bmatrix} y \quad (39)$$

is used to compensate for this spillover.

Thus, the desired pathological baseline is achieved. The HAC alone causes a right-shift in the unmodeled modes, actually destabilizing mode 34, and the LAC is required for system stability. The HAC and HAC/LAC spectra are shown in Figs. 55 and 56. A closed-loop stochastic analysis is given in Table 32. Note that the total vibration reduction is only a factor of 7, owing to the limited control authority of the two actuator/sensor pairs. This is further reflected in the component-cost comparison of Figs. 57 and 58, which show a higher-than-usual contribution from the in-band modes.

b. First-Order Actuator Effects

The first parameter study is performed assuming $\tau_2 = 0$ in equation (38), representing a case where actuator/controller interaction is dominated by the first-order rolloff. After appending the first-order actuator model to the closed-loop evaluation model, the closed-loop HAC/LAC spectrum and stochastic performance are evaluated for a range of τ_1 given by:

$$(2\pi \tau_1)^{-1} = 20, 18, \dots, 6, 4, 2, 1 \quad (\text{Hz}) \quad (40)$$

Table 30

CONTROL DESIGN SPECTRUM

REAL PART	IMAG. PART	FREQ. (Hz)	DAMPING RATIO
-4.9711	10.8675	1.9020	0.4160
-4.9711	-10.8675	1.9020	0.4160
-0.0237	11.1670	1.7773	0.0021
-0.0237	-11.1670	1.7773	0.0021
-0.0282	7.3414	1.1684	0.0038
-0.0282	-7.3414	1.1684	0.0038
-0.3346	3.7635	0.6013	0.0886
-0.3346	-3.7635	0.6013	0.0886
-0.0117	3.4855	0.5547	0.0034
-0.0117	-3.4855	0.5547	0.0034
-0.0106	3.9813	0.6336	0.0027
-0.0106	-3.9813	0.6336	0.0027
-0.0087	3.8578	0.6140	0.0023
-0.0087	-3.8578	0.6140	0.0023
-0.0201	0.7348	0.1170	0.0274
-0.0201	-0.7348	0.1170	0.0274
-0.0297	0.9422	0.1500	0.0315
-0.0297	-0.9422	0.1500	0.0315
-0.0027	1.0954	0.1743	0.0024
-0.0027	-1.0954	0.1743	0.0024
-94.2478	0.0000	15.0000	1.0000
-94.2478	0.0000	15.0000	1.0000

Table 31

FILTER DESIGN SPECTRUM

REAL PART	IMAG. PART	FREQ. (Hz)	DAMPING RATIO
-94.2566	0.0000	15.0014	1.0000
-94.2478	0.0000	15.0000	1.0000
-5.4517	11.1664	1.9777	0.4387
-5.4517	-11.1664	1.9777	0.4387
-0.0228	11.1495	1.7745	0.0020
-0.0228	-11.1495	1.7745	0.0020
-0.5161	7.3096	1.1663	0.0704
-0.5161	-7.3096	1.1663	0.0704
-0.2895	3.5397	0.5652	0.0815
-0.2895	-3.5397	0.5652	0.0815
-0.1776	4.0071	0.6384	0.0443
-0.1776	-4.0071	0.6384	0.0443
-0.0401	3.9039	0.6214	0.0103
-0.0401	-3.9039	0.6214	0.0103
-0.0528	3.6795	0.5857	0.0144
-0.0528	-3.6795	0.5857	0.0144
-0.1486	0.7955	0.1288	0.1836
-0.1486	-0.7955	0.1288	0.1836
-0.0308	0.9365	0.1491	0.0329
-0.0308	-0.9365	0.1491	0.0329
-0.0053	1.0973	0.1746	0.0049
-0.0053	-1.0973	0.1746	0.0049

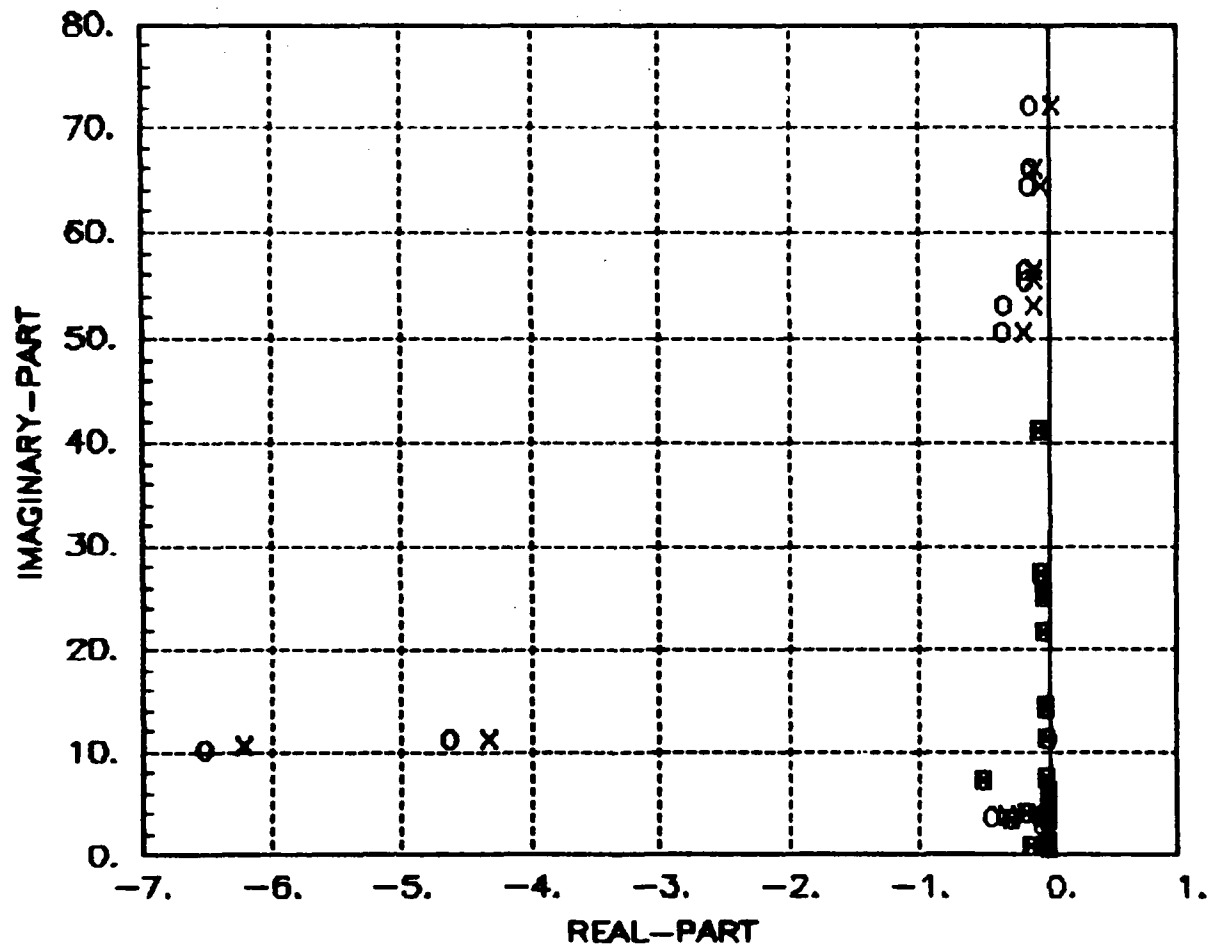


Figure 55. Full Closed-Loop Spectrum (X=Hac, O=Hac/Lac)

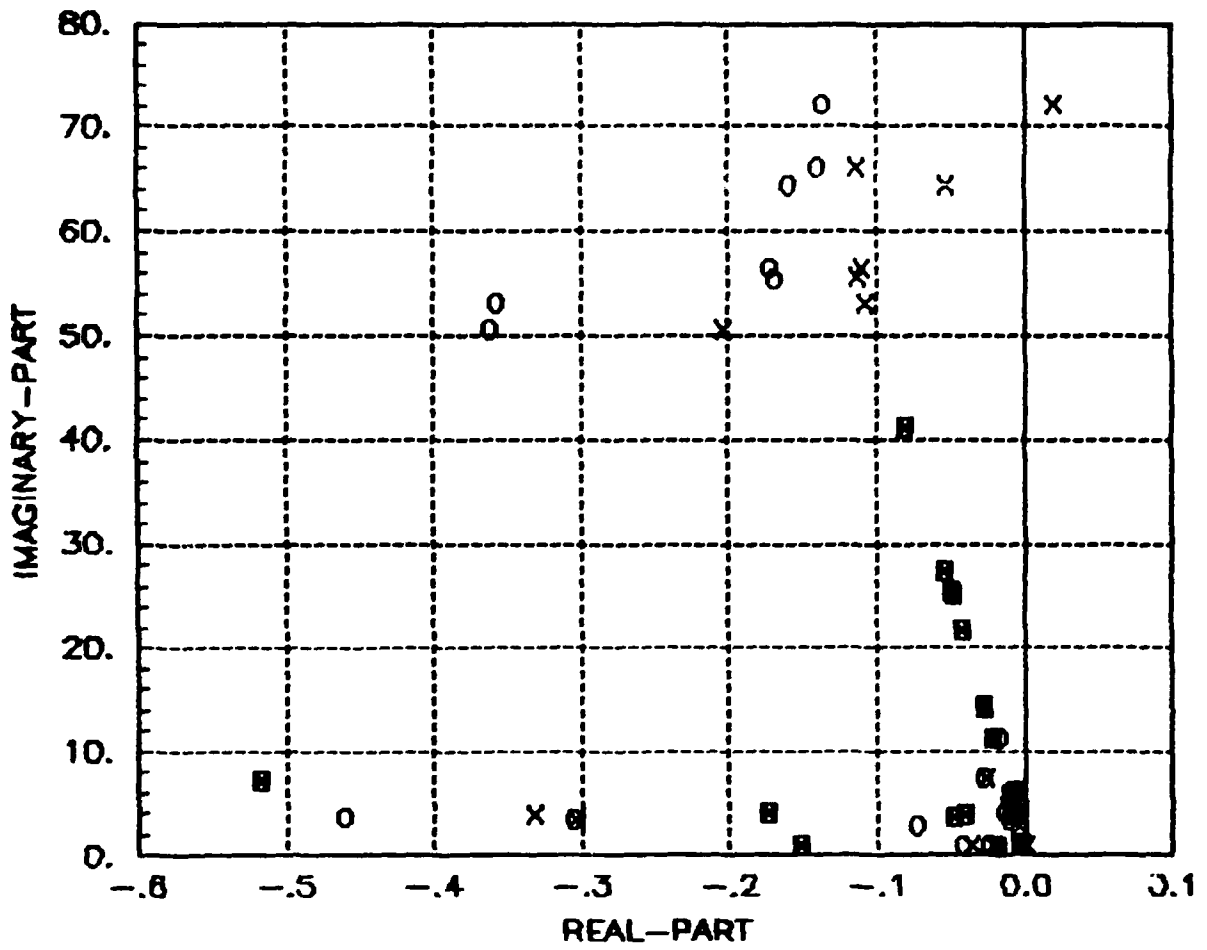


Figure 56. Full Closed-Loop System: X=HAC, O=HAC/LAC (Expanded Scale)

Table 32

34-MODE PERFORMANCE EVALUATION

	OPEN LOOP	HAC/LAC	HAC/LAC WITH RATE SENSOR NOISE OF INTENSITY $5 \times 10^{-7} \frac{M^2}{SEC}$
RSS LOS x (μ RAD)	75.35	33.00	33.55
RSS LOS y (μ RAD)	967.79	128.76	130.33
TOTAL RSS LOS (μ RAD)	970.72	132.93	134.58

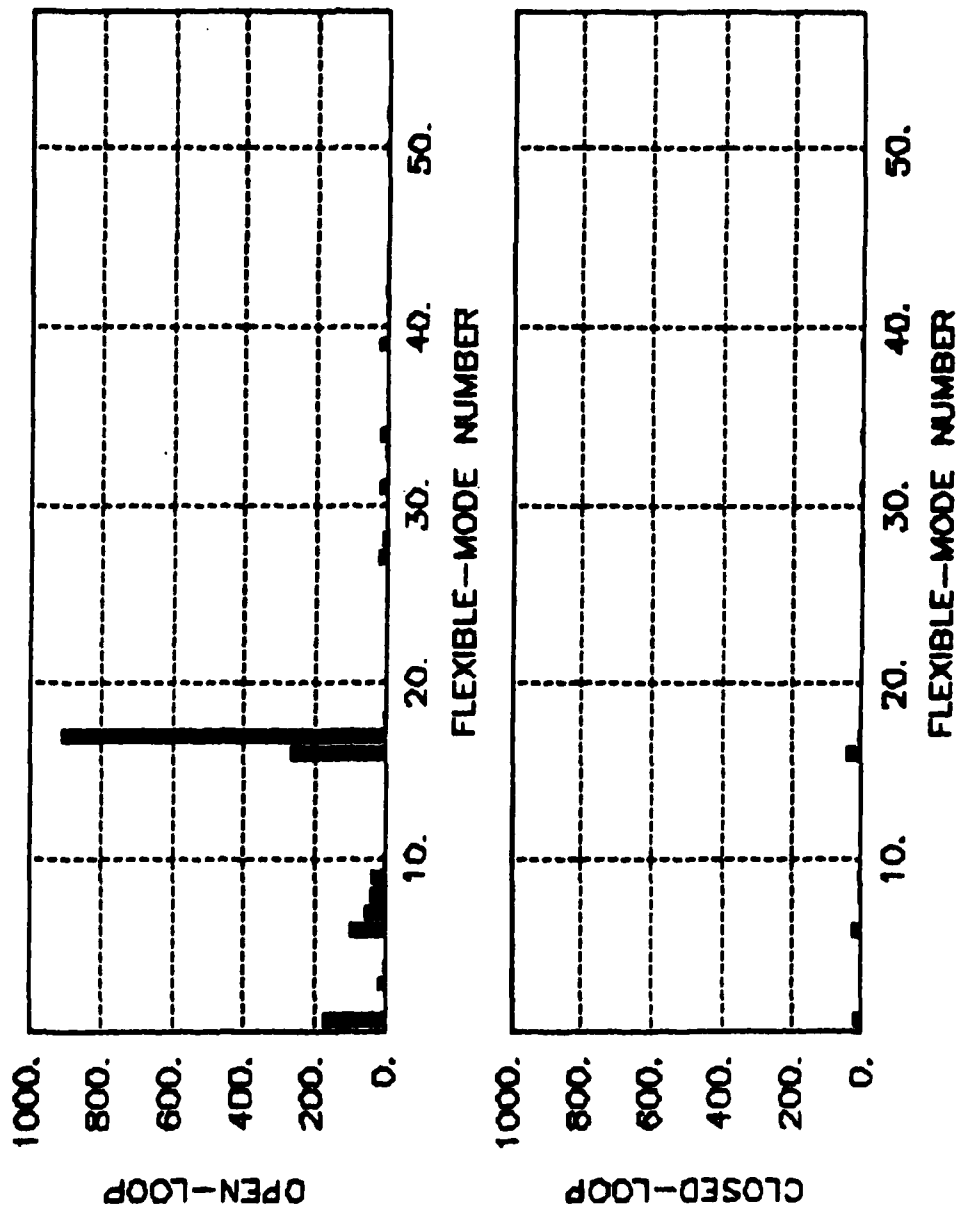


Figure 57. Open-Loop Modal Coordinate "Component Costs" with Corrected Disturbance

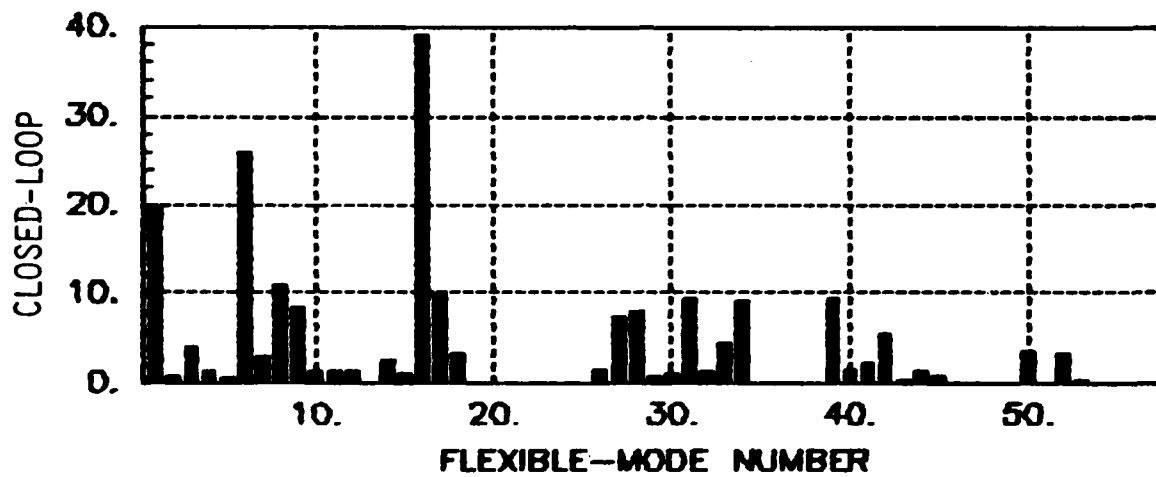


Figure 58. Open-Loop Modal Coordinate "Component-Costs" with Corrected Disturbance - Expanded Scale

Figure 59 shows that the high-frequency closed-loop poles move to their open-loop values as rolloff frequency decreases, which is intuitive since the actuator dynamics are attenuating the high-frequency control signals. The next four figures zoom in on the high-frequency locus to show how these poles move.

Figure 60 shows the first-order actuator effects on mode 31. Since the HAC action upon mode 31 is negligible, this figure shows the effect of the first-order rolloff on the LAC alone. There is no destabilization at all; the locus moves uniformly to the open-loop value without "overshoot." It will be shown analytically in the next section that the first-order rolloff cannot destabilize a LAC.

The effects on modes 32 and 33 are shown in Figs. 61 and 62. Here LAC is compensating for pole-shifts to the right due to HAC spillover. Notice that the locus crosses 0.2% open-loop damping line before reaching the open-loop pole. This effect is even more pronounced for mode 34, shown in Fig. 63. Since mode 34 is unstable by design under HAC alone, and stabilized by LAC to less than the open-loop damping value, the entire locus lies to the right of the 0.2% damping line. Therefore, instabilities can result whenever the first-order rolloff frequency is near to the potential spillover region.

It is clear from these results that the first order term "turns-off" any controller action beyond its bandwidth. This applies to LAC action as well as HAC spillover effects. However, in doing so the actuator can permit spillover to become problematic where LAC action is critical. There are two ways to alleviate this problem:

- (1) Select actuators such that $(2\pi \tau_1)^{-1}$ is sufficiently above the controller bandwidth, so that HAC spillover cannot be present.

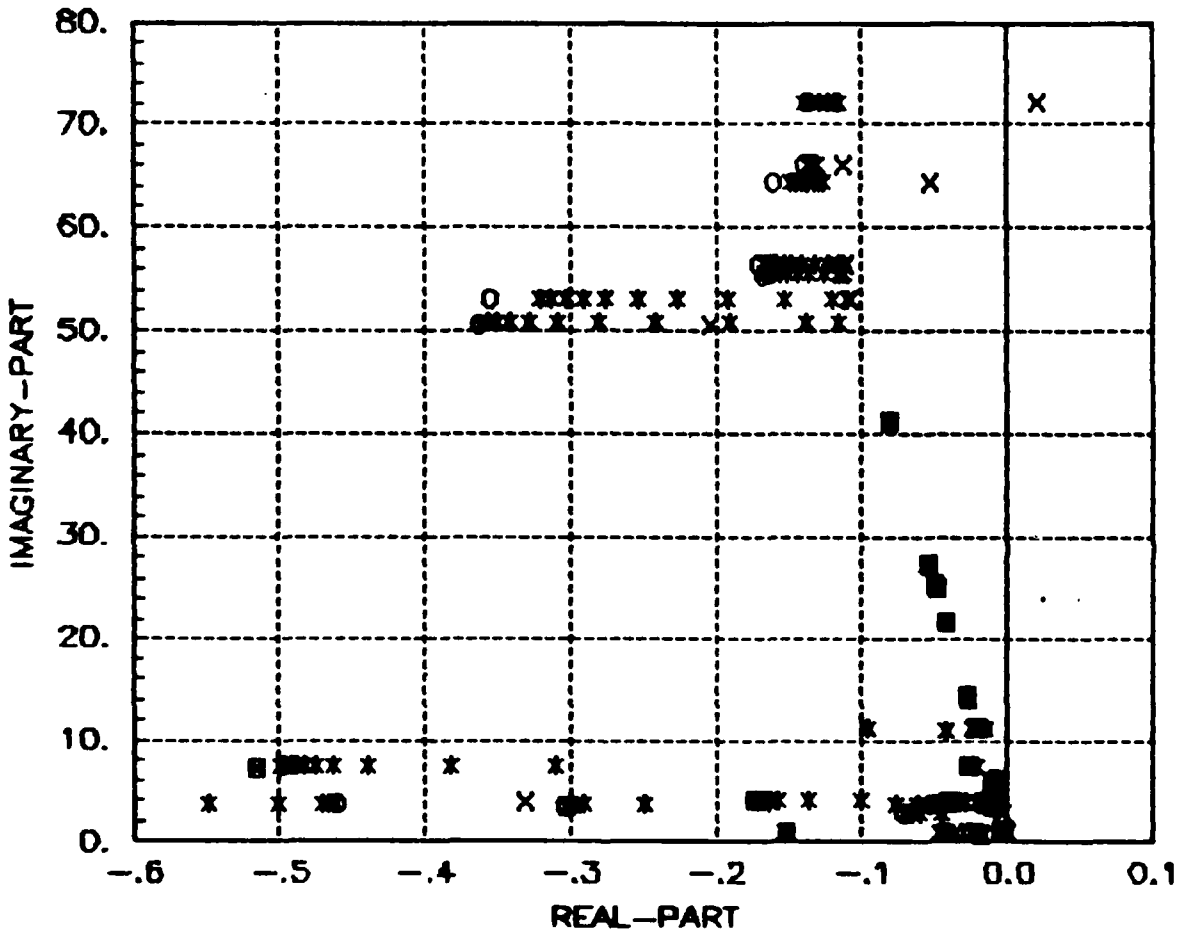


Figure 59. Full Closed-Loop Spectrum: X=HAC, O=HAC/LAC, *=Locus as First-Order Rolloff Decreases

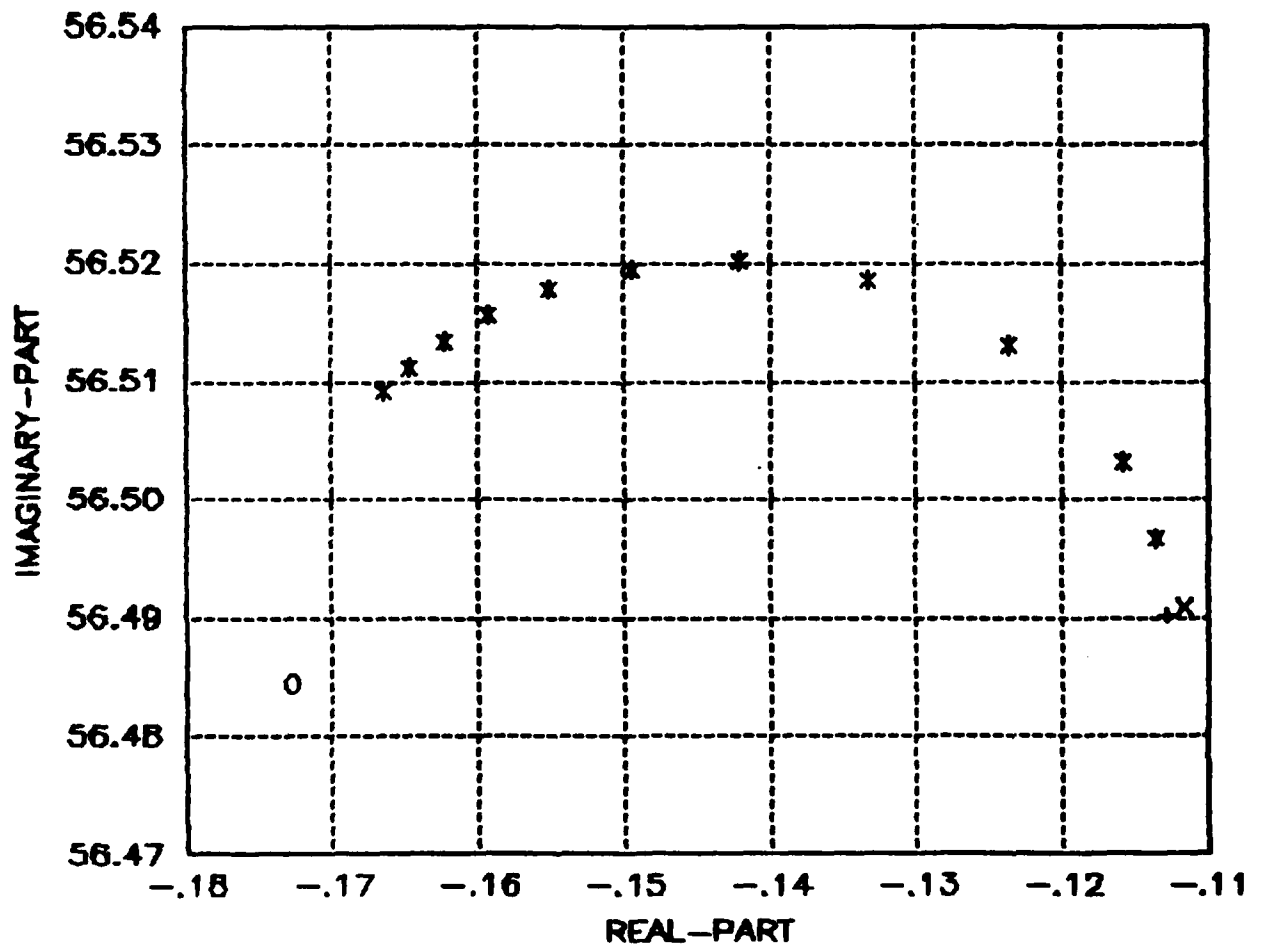


Figure 60. Effect of First-Order Actuator Rolloff Upon Mode 31

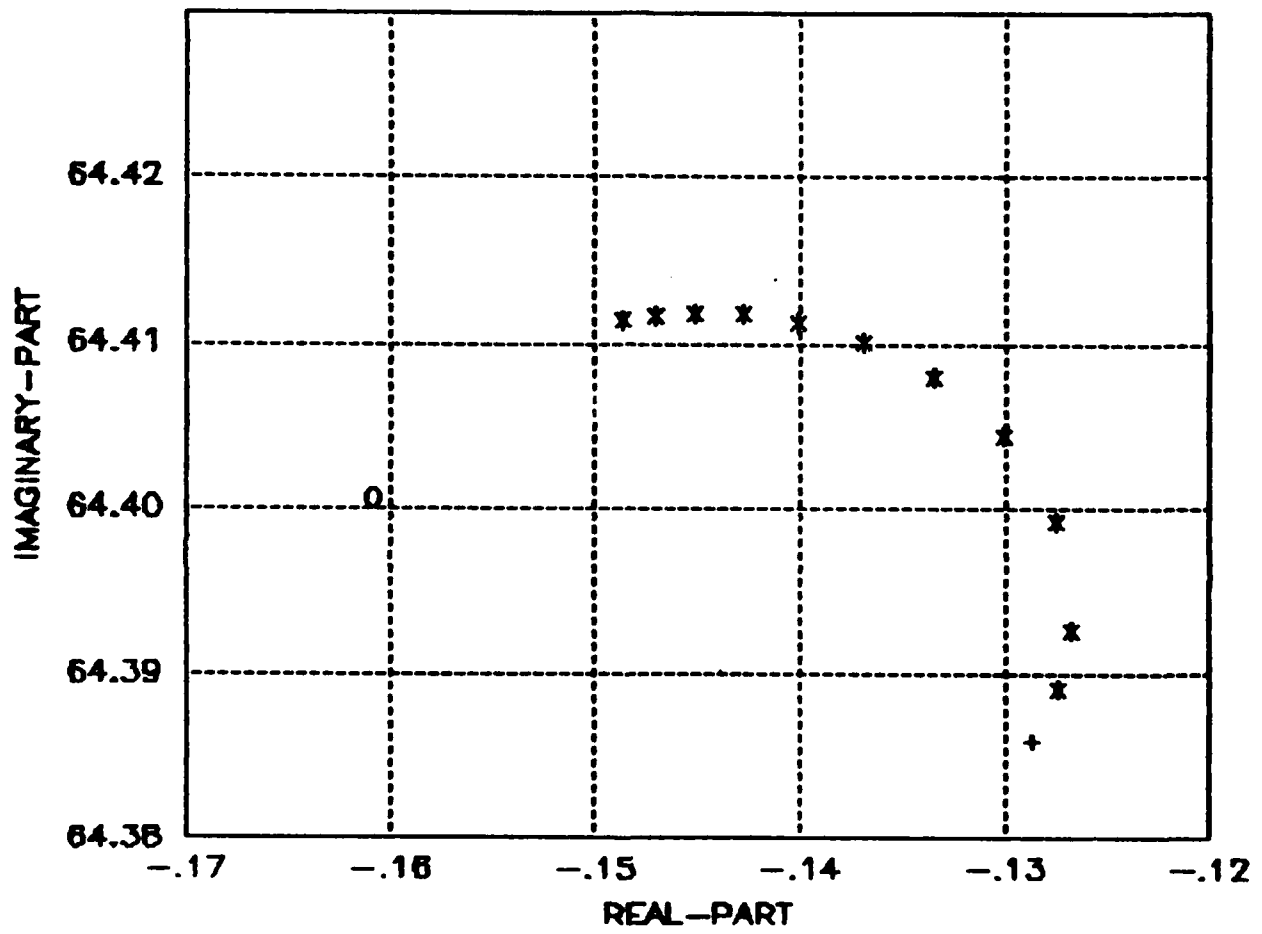


Figure 61. Effect of First-Order Actuator Rolloff Upon Mode 32

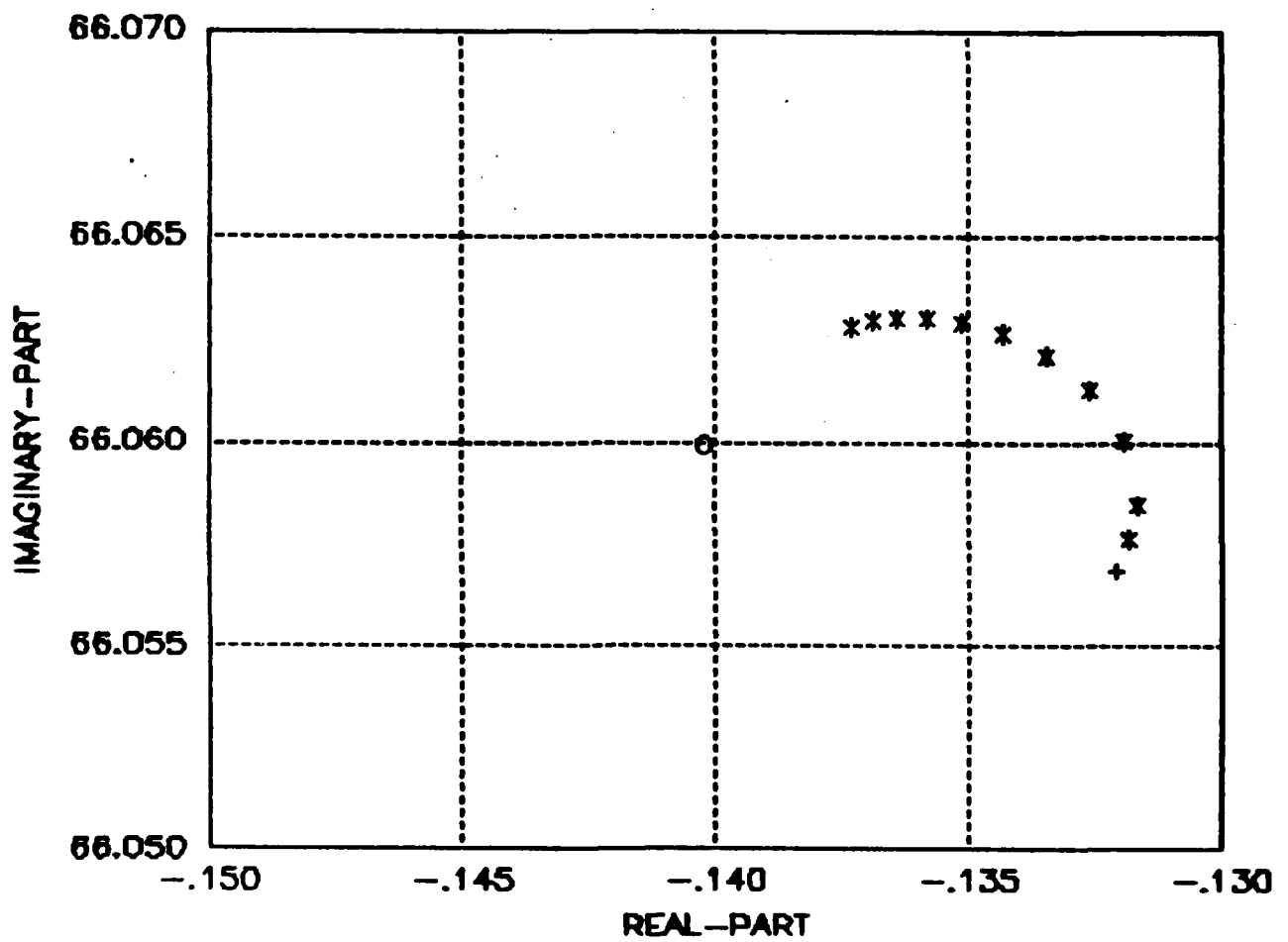


Figure 62. Effect of First-Order Rolloff Upon Mode 33

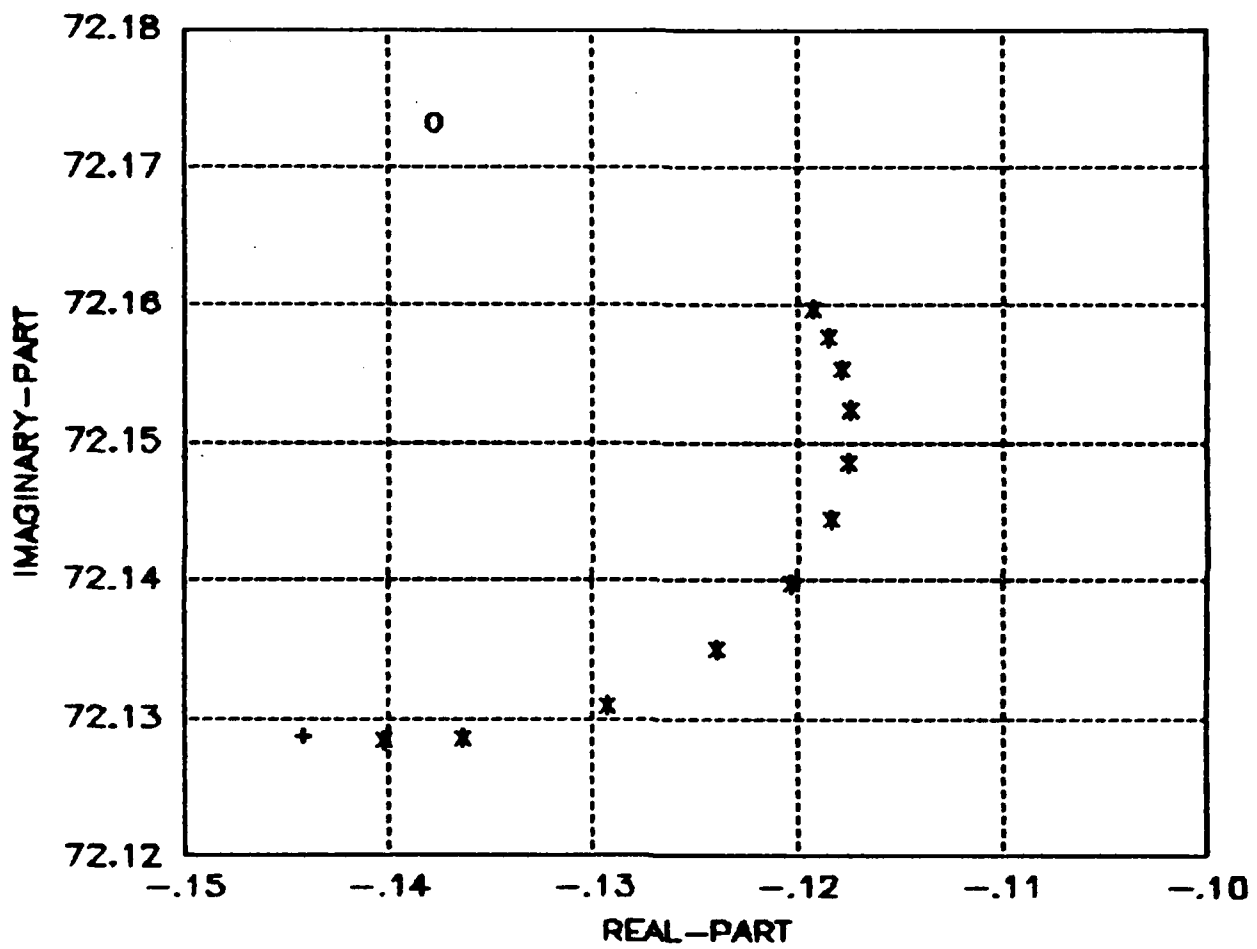


Figure 63. Effect of First-Order Actuator Rolloff Upon Mode 34:
 O=HAC/LAC, +=Open Loop

- (2) Impose a separate rolloff on the HAC control signal to suppress spillover effects at the actuator rolloff frequency.

Either way, the actuator effect will not be destabilizing.

The effect of the first-order actuator rolloff on closed-loop stochastic performance is shown in Fig. 64. Clearly the degradation is negligible (less than 7% at 6 Hz) for any realistically high actuator bandwidth.

c. Second-Order Actuator Effects

This is the more realistic case, where $\tau_1 \geq \tau_2 > 0$. It has been shown [6] that the LAC root-shift using a second-order actuator is

$$\mathcal{R}e(d\lambda_n) \equiv -\zeta_{cn} \omega_n \approx - \frac{1 - \tau_1 \tau_2 \omega_n^2}{2(1 + \tau_1^2 \omega_n^2)(1 + \tau_2^2 \omega_n^2)} \sum_a c_a \phi_{an}^2 \quad (41)$$

and thus that in the absence of passive damping, a LAC will always destabilize structural modes whose frequencies are beyond $(2\pi\sqrt{\tau_1\tau_2})^{-1}$. (Note that when $\tau_2 = 0$ the sign of $\mathcal{R}e(d\lambda_n)$ cannot change; a condition suggested in the previous section.) For LAC alone, stability can be guaranteed if sufficient passive damping is present. If the natural structural damping is too small, additional passive damping can be achieved by means of a passive device mounted in parallel with the actuator. Equation (41) then takes the following form:

$$f(s)/x(s) = \frac{cs}{(1 + \tau_1 s)(1 + \tau_2 s)} + \frac{ps}{1 + \tau_0 s} \quad (42)$$

where p is the passive gain of the damping actuator, and the LAC root shift equation becomes:

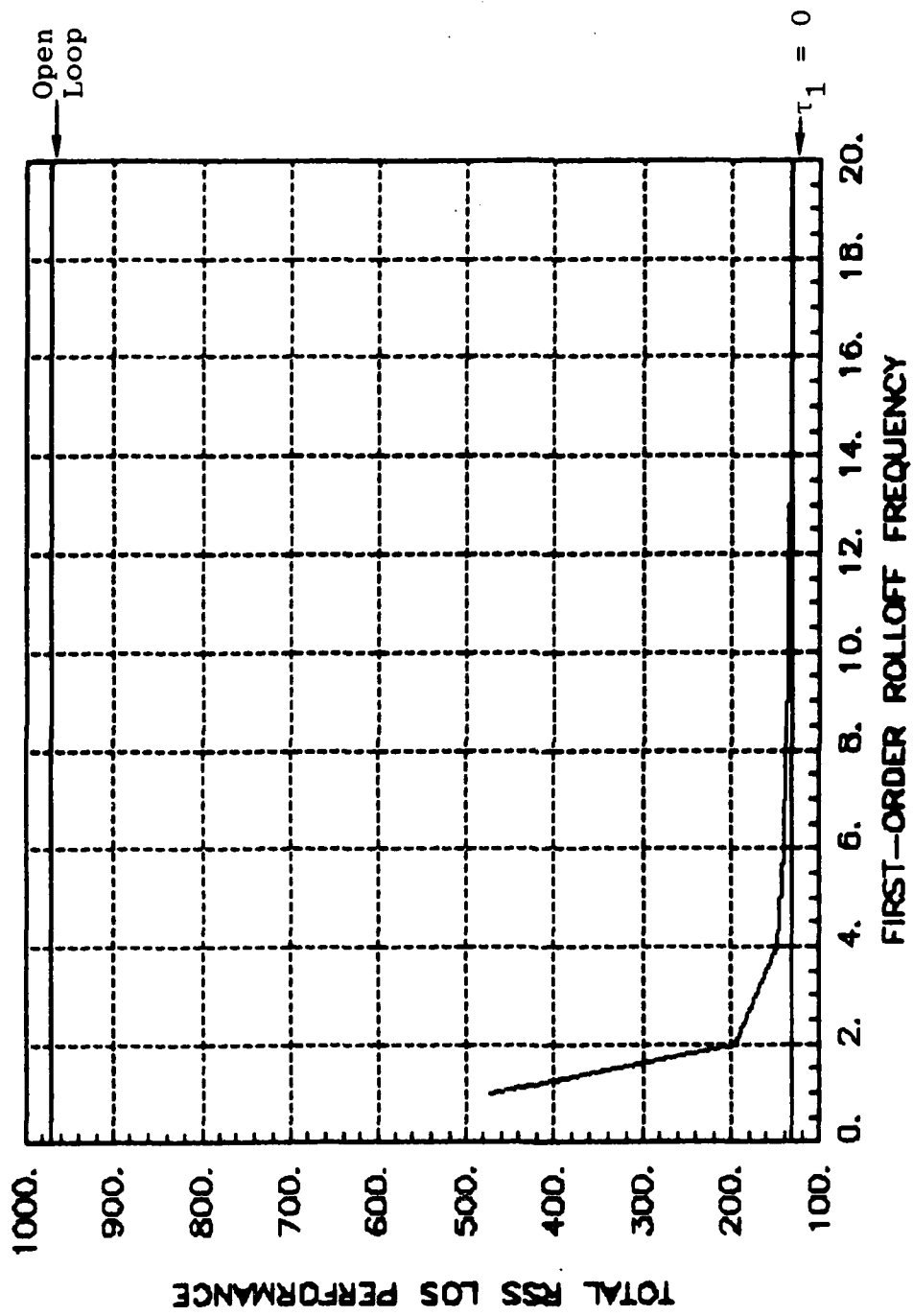


Figure 64. Performance Degradation Due to First-Order Actuator Rolloff

$$\begin{aligned}
2 \zeta_n \omega_n &= 2 \zeta_{on} \omega_n + \sum_a \left[\frac{p_a}{(1 + \tau_o^2 \omega_n^2)} + \frac{1 - \tau_1 \tau_2 \omega_n^2 c_a}{(1 + \tau_1^2 \omega_n^2)(1 + \tau_2^2 \omega_n^2)} \right] \phi_{an}^2 \\
&= 2 \zeta_{on} \omega_n + \frac{p'}{(1 + \tau_o^2 \omega_n^2)} + \frac{(1 - \tau_1 \tau_2 \omega_n^2) c'}{(1 + \tau_1^2 \omega_n^2)(1 + \tau_2^2 \omega_n^2)}
\end{aligned}$$

where

$$p' = \sum_a p_a \phi_{an}^2 = p \sum_a \phi_{an}^2 \cong 2 \zeta_{pn} \omega_n$$

$$c' = \sum_a c_a \phi_{an}^2 = c \sum_a \phi_{an}^2 \cong 2 \zeta_{cn} \omega_n$$

(43)

and ζ_{on} is the natural structural damping. A necessary and sufficient condition is given by the following theorem:

LAC Stability Theorem (Aubrun): Unconditional stability of a LAC system is guaranteed if and only if, for each mode n , the active damping ratio ζ_{cn} is less than a certain maximum ζ_{cn}^* . This maximum active damping ratio in any of the modes within the bandwidth of an active LAC controller is proportional to the sum of the natural structural damping ζ_{on} and the damping ζ_{pn} introduced by a passive damper mounted in parallel with the actuator. Specifically,

$$\zeta_{cn} \leq \zeta_{cn}^* = R_{\max} (\zeta_{on} + \zeta_{pn}) \quad (44)$$

where the value of the proportionality constant R_{\max} is given by:

$$R_{\max} \cong \min \left[K + 2 \sqrt{K}, \tau_1 \tau_2 / \tau_o^2 \right] \quad (45)$$

where

$$K \equiv \tau_1/\tau_2 + \tau_2/\tau_1 + 2 \quad (46)$$

and where $1/\tau_1$, $1/\tau_2$ are the poles of the active damper, and $1/\tau_0$ is the pole of the passive damper.

The proof, along with a detailed exposition on LAC design and implementation, may be found in [6].

It is assumed for the present study that no passive damper is present ($\zeta_{pn} = 0$), and that $\tau_1 = \tau_2$. This is the "worst case" of second-order actuator since ζ_{cn}^* is minimized.

(1) Second-Order Effects on LAC Alone

To fully understand the impact of second-order actuator dynamics upon HAC/LAC controllers, it is illuminating to look at the effects upon LAC alone. The closed-loop LAC-controlled 34-mode spectrum is shown in Table 33. For the "worst case" of $\tau_1 = \tau_2 = \tau$, closed-loop spectra are computed using the second-order actuator model and the following range of rolloff frequencies:

$$(2\pi\tau)^{-1} = 20, 18, \dots, 6, 4, 2, 1 \quad (\text{Hz}) \quad (47)$$

The resulting locus is shown in Fig. 65. As the rolloff frequency decreases, the high-frequency closed-loop poles move to the right of the open-loop 0.2% damping line before reaching their open-loop values. Figs. 66 through 68 show this motion more clearly.

There are two points to be made from these figures. Since the active term in the root-shift equation (Table 33) is zero

Table 33

FULL CLOSED-LOOP LAC SPECTRUM

REAL PART	IMAG. PART	FREQ. (HZ)	DAMPING RATIO	REAL PART	IMAG. PART	FREQ. (HZ)	DAMPING RATIO
-0.3001	72.1209	11.4785	0.0042	-0.4631	9.7649	1.9559	0.0474
-0.1584	66.0546	10.5129	0.0024	-0.0285	7.2798	1.1586	0.0039
-0.2409	64.3848	10.2472	0.0037	-0.0139	6.0966	0.9703	0.0023
-0.1741	56.4843	8.9898	0.0031	-0.0115	5.7505	0.9152	0.0020
-0.1700	55.5418	8.8398	0.0031	-0.0103	5.1741	0.8235	0.0020
-0.3547	52.9903	8.4339	0.0067	-0.0120	5.1271	0.8160	0.0024
-0.2656	50.6233	8.0571	0.0052	-0.0102	5.1213	0.8151	0.0020
-0.0825	41.1564	6.5503	0.0020	-0.0232	4.0238	0.6404	0.0058
-0.0545	27.2484	4.3367	0.0020	-0.0128	3.9877	0.6347	0.0032
-0.0509	25.4552	4.0513	0.0020	-0.0082	3.8520	0.6131	0.0021
-0.0501	25.0456	3.9861	0.0020	-0.1206	3.7285	0.5937	0.0323
-0.0497	24.8634	3.9571	0.0020	-0.0079	3.4985	0.5568	0.0023
-0.0434	21.6906	3.4522	0.0020	-0.0858	2.8655	0.4563	0.0299
-0.0431	21.5732	3.4335	0.0020	-0.0022	1.0939	0.1741	0.0020
-0.0283	14.1629	2.2541	0.0020	-0.0037	0.9349	0.1488	0.0039
-0.0283	14.1368	2.2499	0.0020	-0.0052	0.9241	0.1471	0.0100
-0.1383	11.0868	1.7663	0.0125	-0.0034	0.7105	0.1131	0.0048

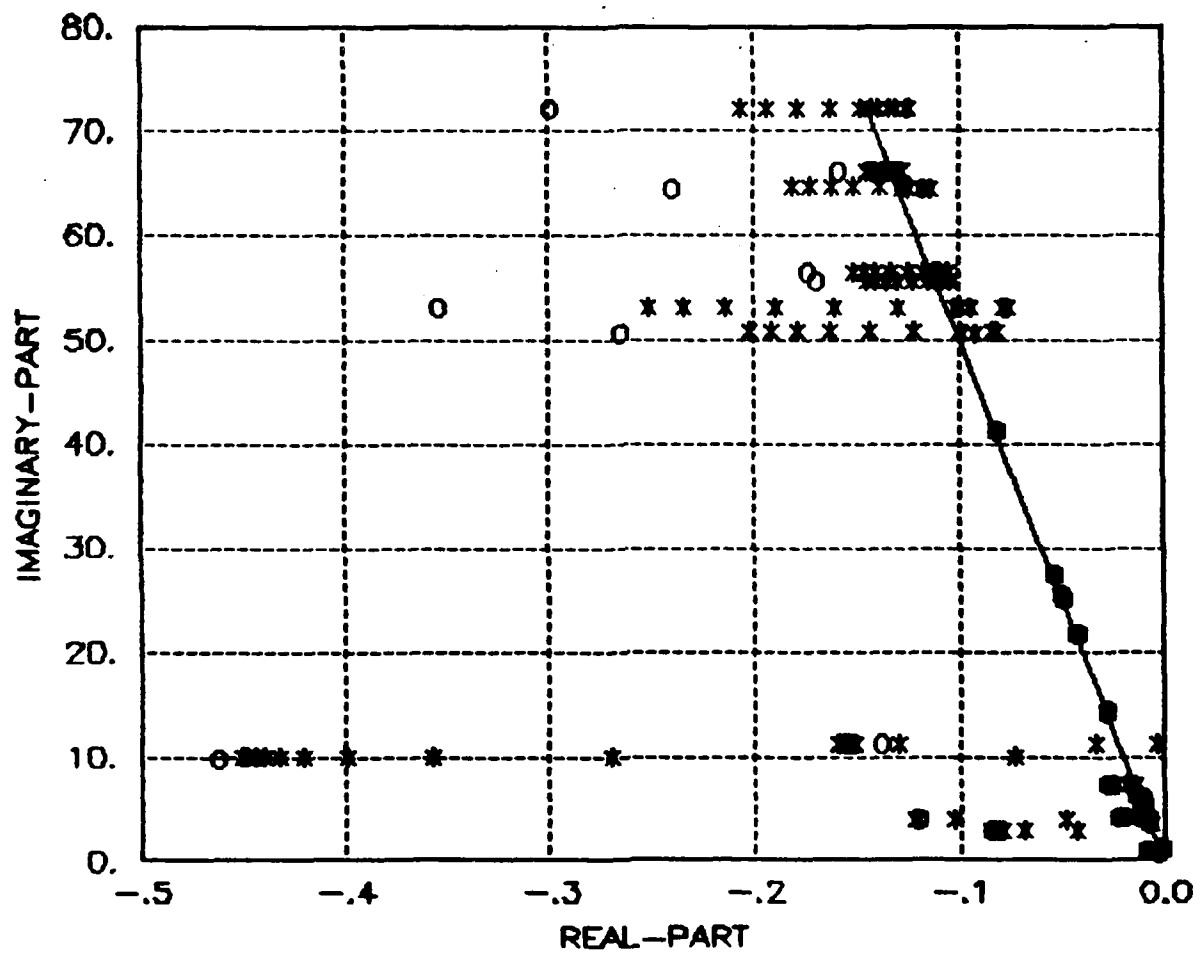


Figure 65. Effect of 2nd-Order Actuator Dynamics Upon LAC

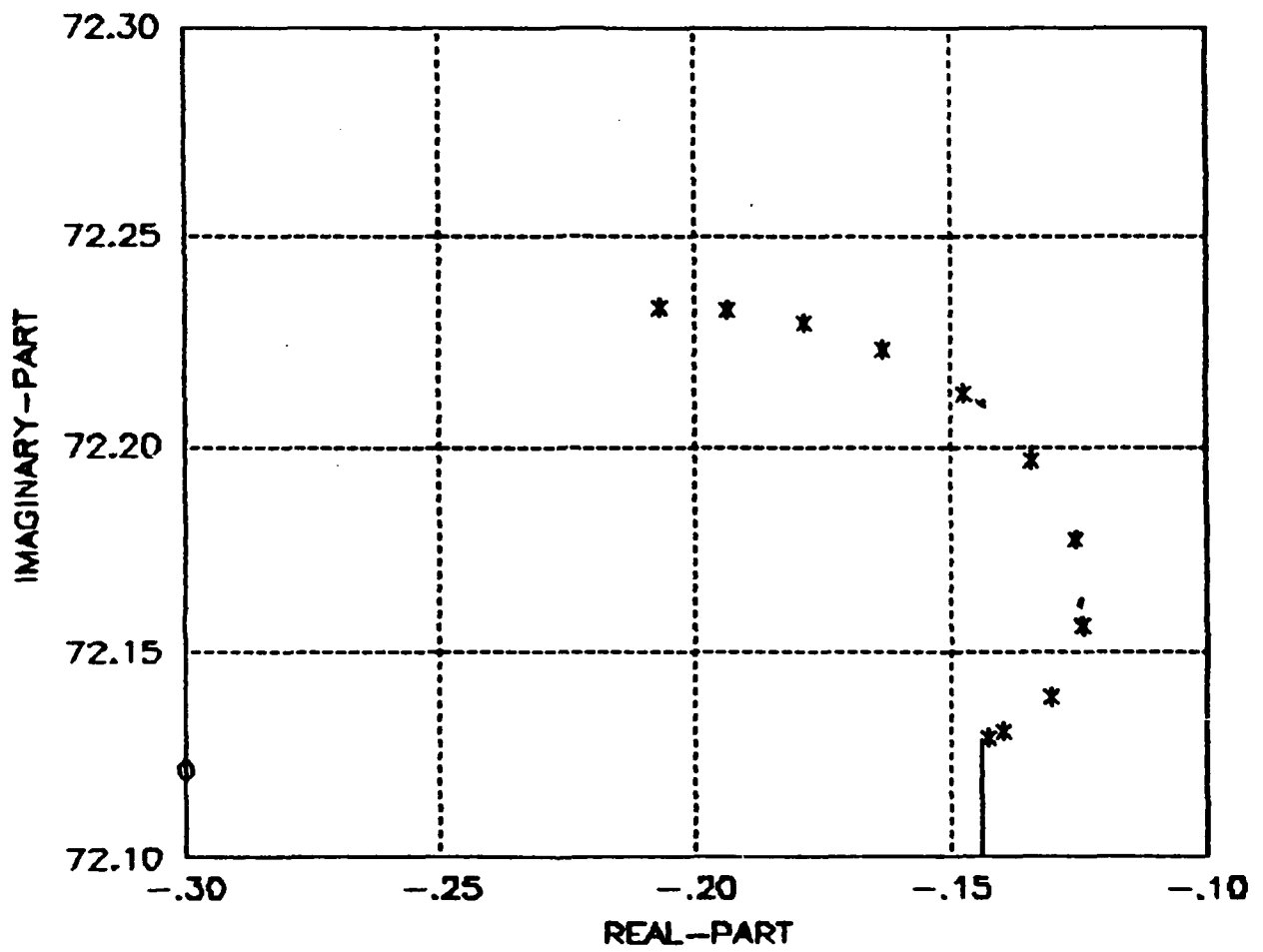


Figure 66. Effect of 2nd-Order Actuator Dynamics Upon Mode 34

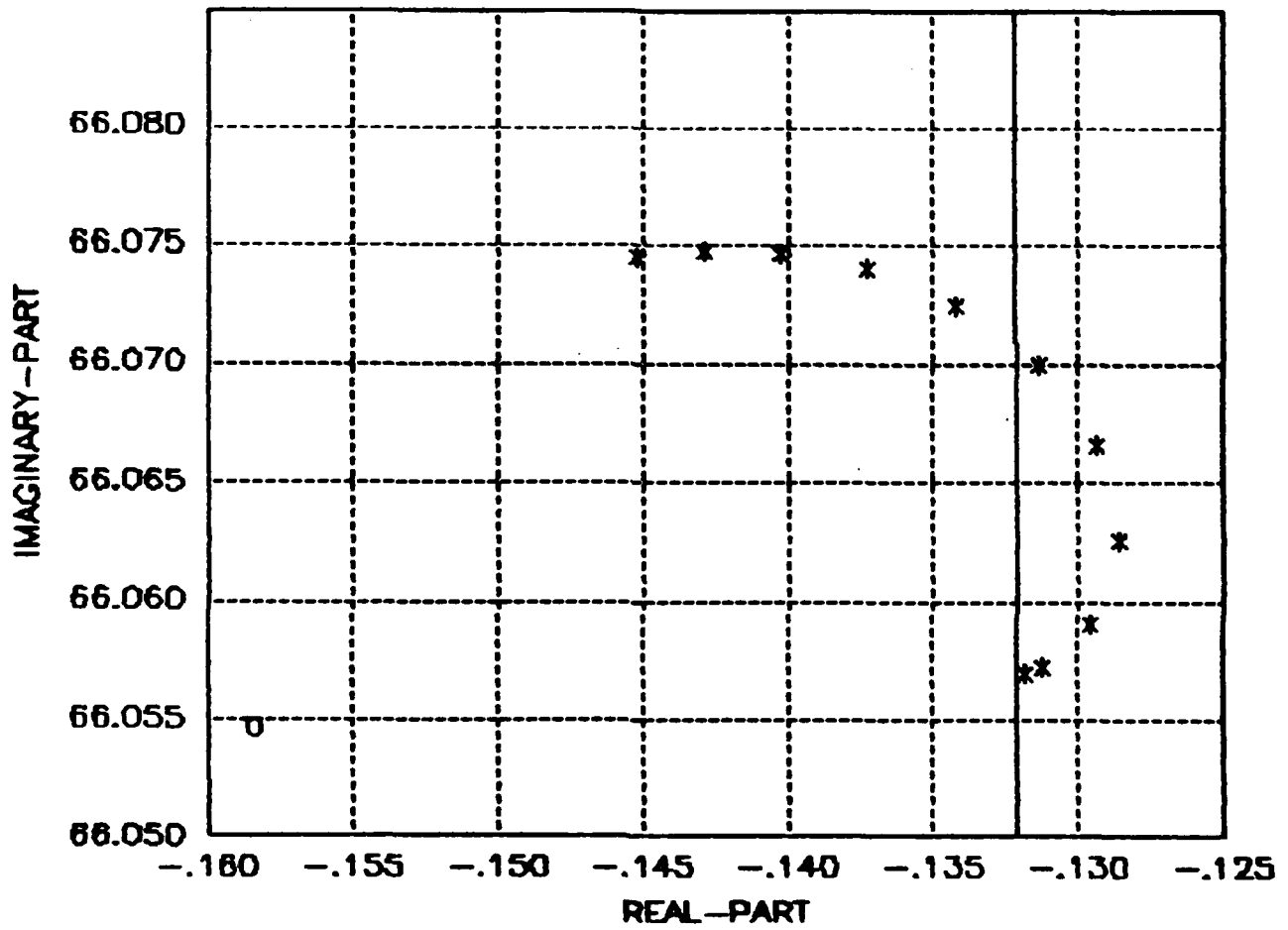


Figure 67. Effect of 2nd-Order Actuator Dynamics Upon Mode 33

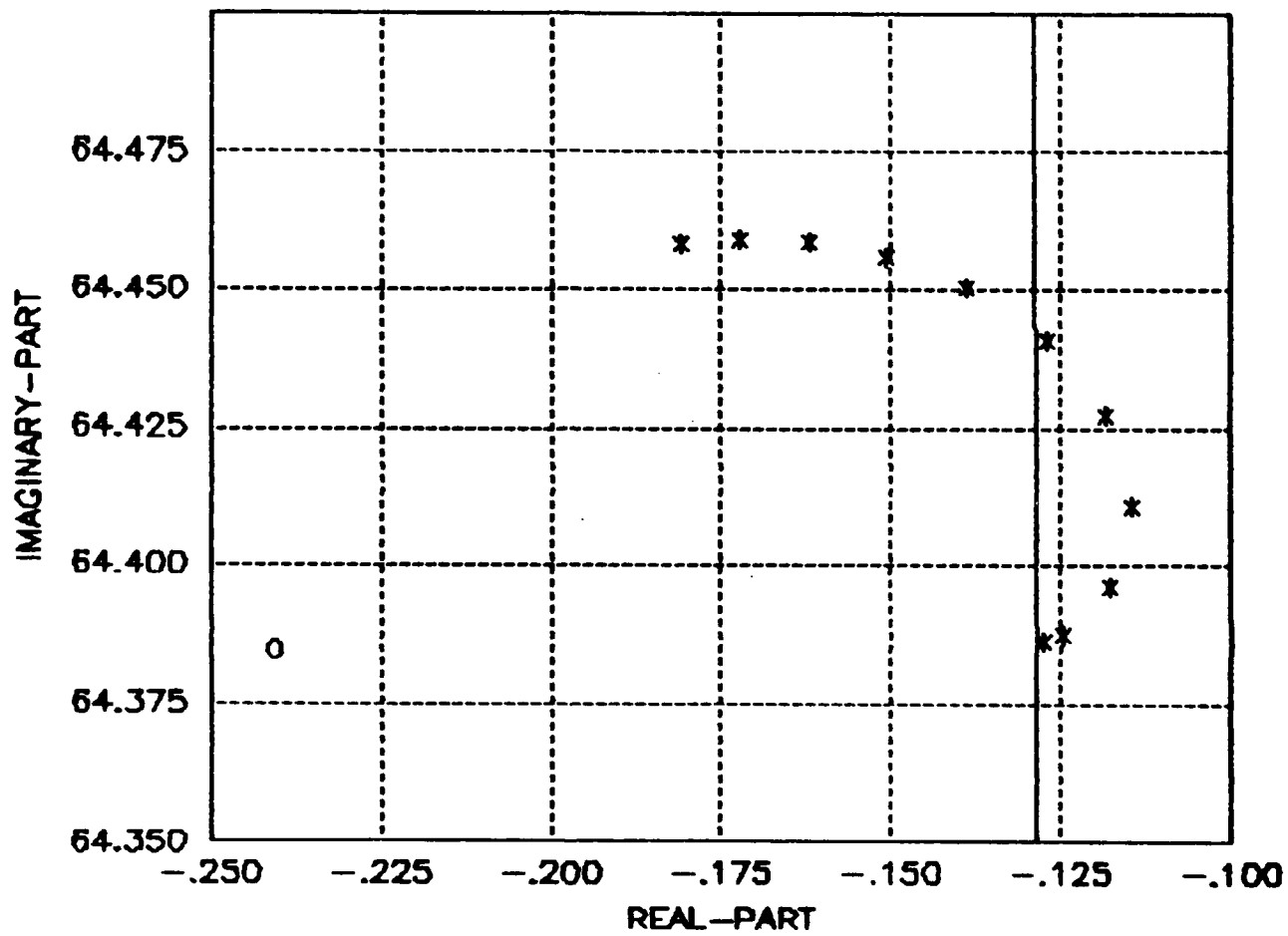


Figure 68. Effect of 2nd-Order Actuator Dynamics Upon Mode 32

when $\tau\omega_n = 1$, the closed-loop damping and open-loop damping in mode n should be equal when the rolloff frequency equals the modal frequency. By inspection of the figures, this is indeed the case. Secondly, it is straightforward to show that equation (35) achieves its minimum when $\tau\omega_n = \sqrt{3}$, and this minimum is evident in the figures. For example, the 11 Hz mode 33 has a predicted minimum when the rolloff frequency is 6.4 Hz; and this agrees with Fig. 67.

(2) Second-Order Effects Upon HAC/LAC Controller

Using the "worst case" second-order actuator model, the closed-loop spectrum and stochastic performance of the baseline HAC/LAC controller are computed for each of the following rolloff frequencies:

$$(2\pi\tau)^{-1} = 30, 28, 26, \dots, 6, 4, 2, 1 \text{ (Hz)} \quad (43)$$

The locus of closed-loop poles is shown in Fig. 69, and the high-frequency loci are shown in expanded scale in Figs. 70 through 73.

The movement of mode 31 (Fig. 70) is essentially the actuator/LAC interaction effect, since the HAC does nothing to this mode. In fact, the 0.2% damping crossing and the minimum damping occur at $\tau\omega_n = 1$ and $\tau\omega_n = \sqrt{3}$, respectively. However, the degree of right-shift in the higher-frequency modes is much more pronounced than for the LAC alone. The most dramatic effect is upon mode 34, shown in Fig. 73. Recall that the first-order rolloff caused a right-shift in this mode because the destabilizing HAC overpowered the LAC compensation (see Fig. 63). The second-order actuator/LAC interaction compounds this effect, producing a more severe reduction in damping.

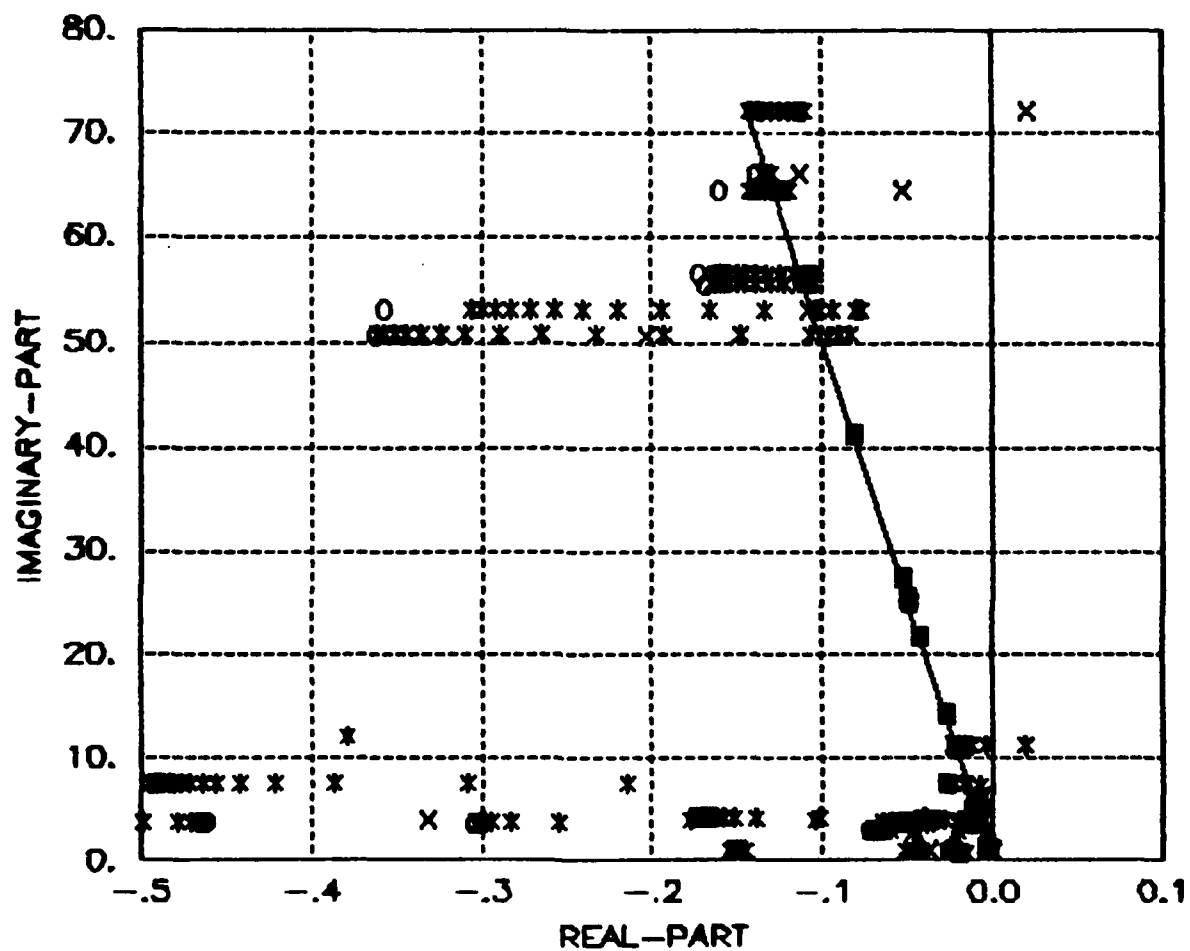


Figure 69. Effect of 2nd-Order Rolloff Upon HAC/LAC:
 X=HAC, O=HAC/LAC, *=Locus as Rolloff
 Frequency Decreases

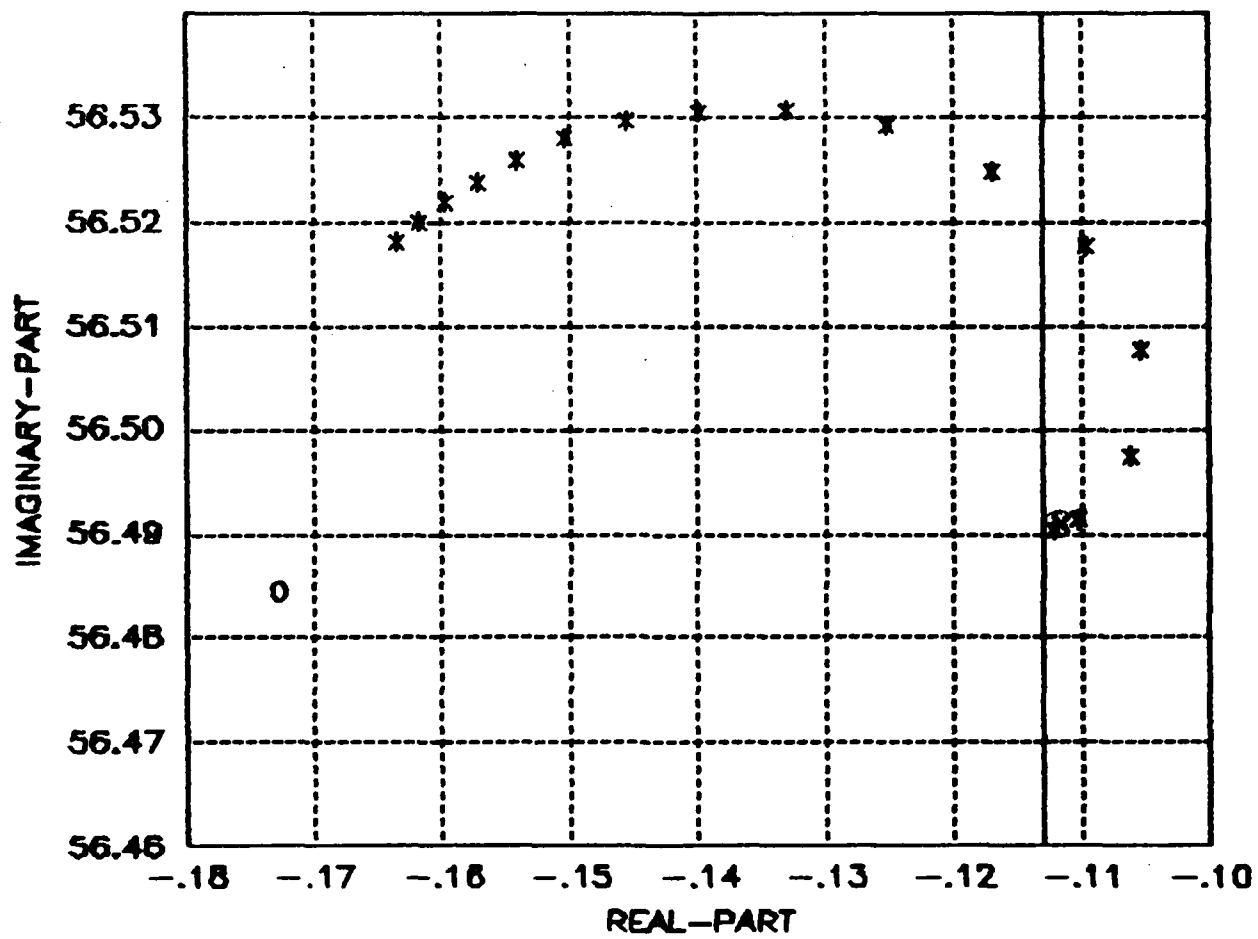


Figure 70. Effect of 2nd-Order Rolloff Upon HAC/LAC: MODE 31

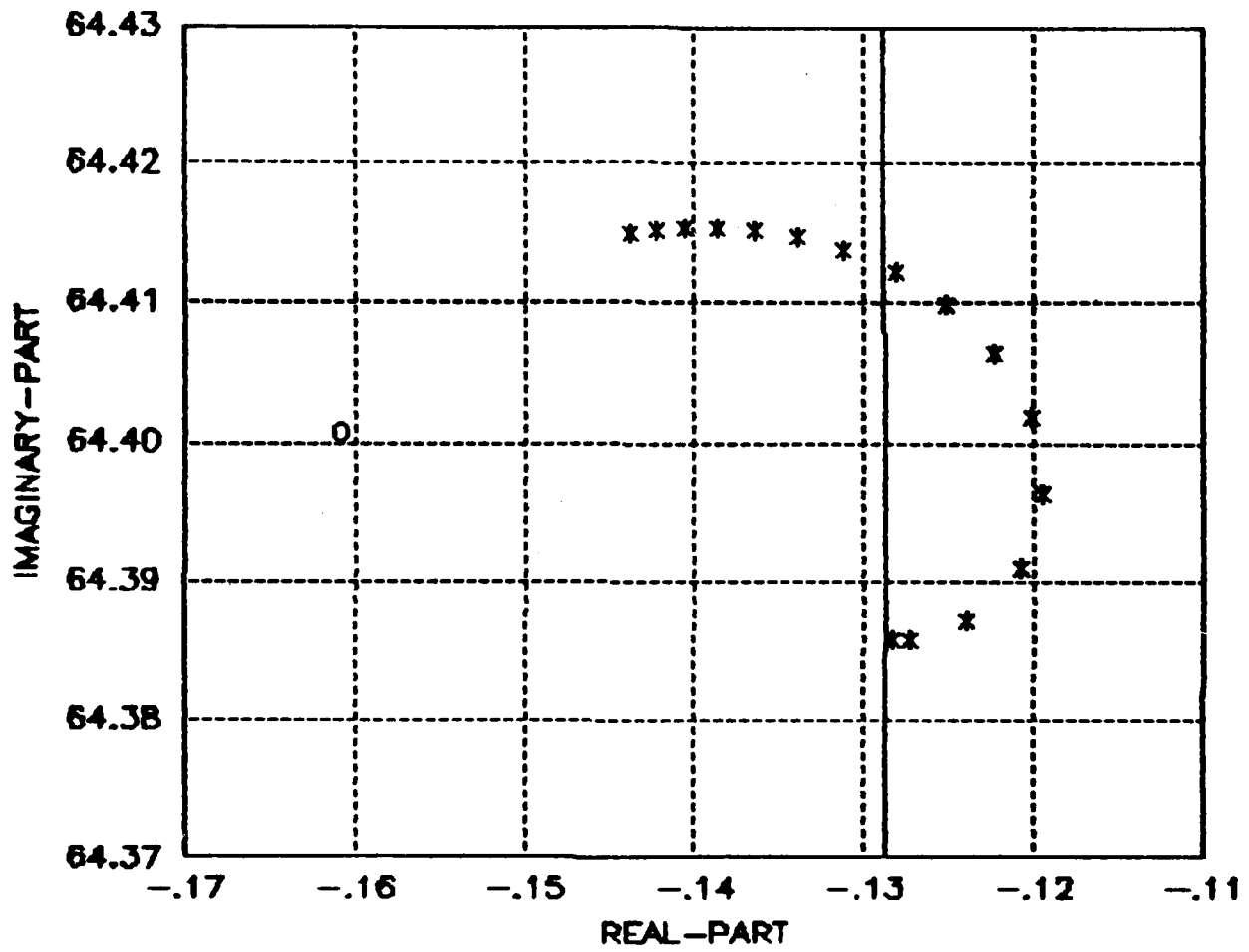


Figure 71. Effect of 2nd-Order Rolloff Upon HAC/LAC: Mode 32

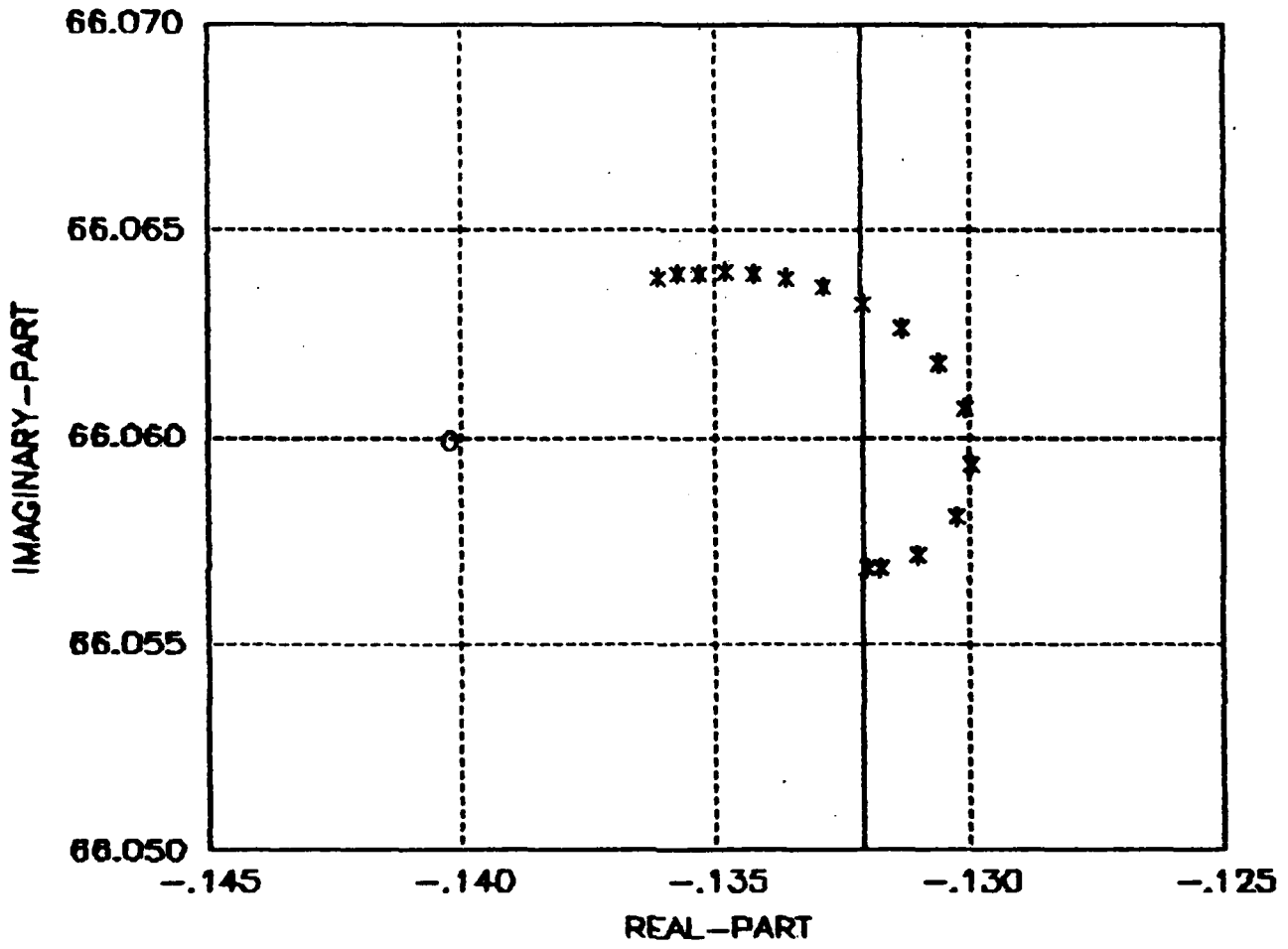


Figure 72. Effect of 2nd-Order Rolloff Upon HAC/LAC: Mode 33

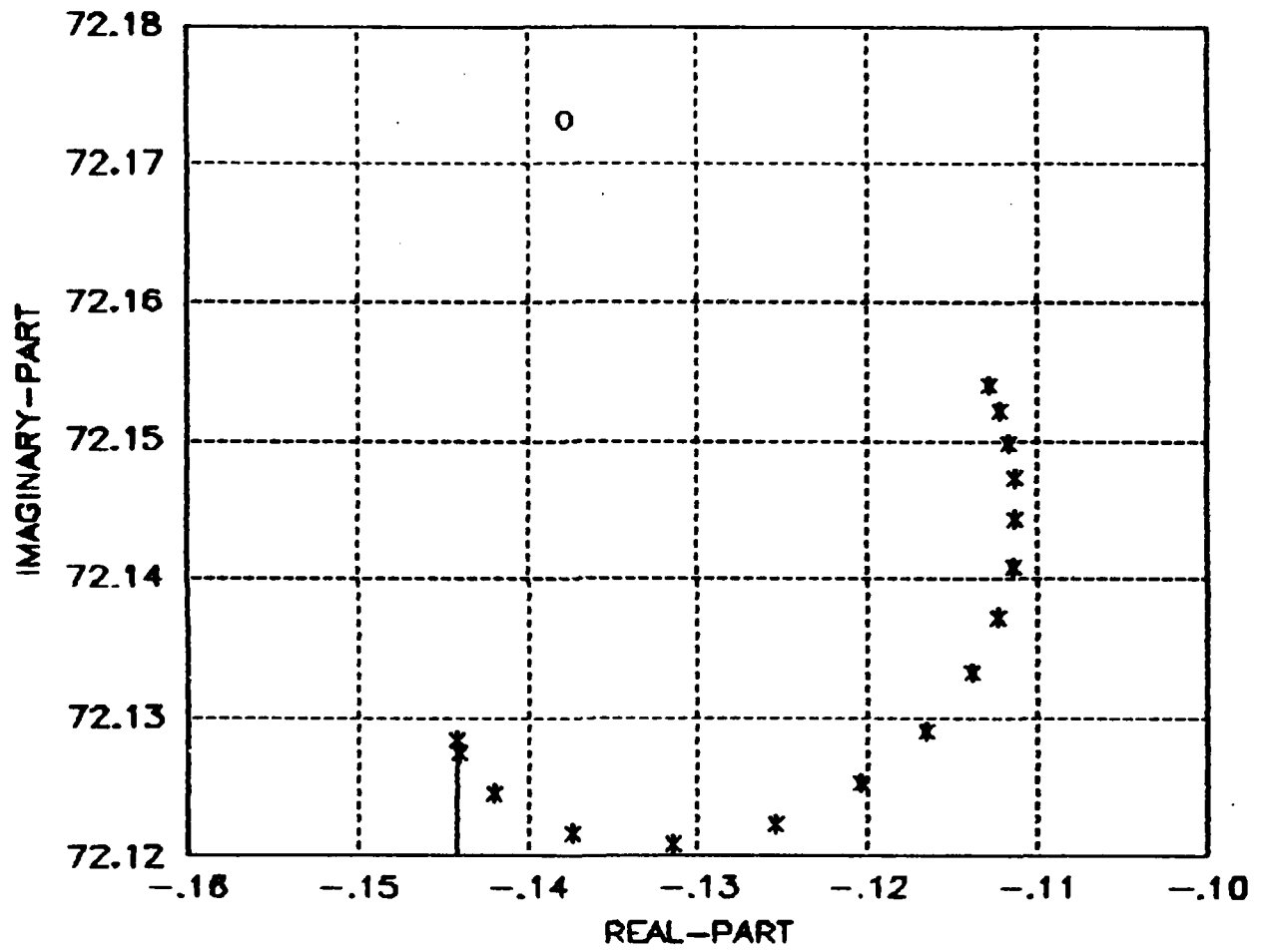


Figure 73. Effect of 2nd-Order Rolloff Upon HAC/LAC: Mode 34

Thus, the LAC stability issue exacerbates the loss of stability robustness when spillover compensation occurs near the actuator rolloff frequency.

As with the first-order case, this problem is solved if $(2\pi\tau)^{-1}$ is sufficiently above the controller bandwidth, or if the HAC is rolled-off artificially well below the actuator frequency. In either case, however, LAC destabilization is possible. Sufficient passive damping should be added to the actuator such that if an unmodeled mode were present at the frequency where the root-shift (equation 41) is minimum, the closed-loop damping would be acceptable.

The impact of second-order actuator dynamics upon HAC/LAC performance for this example is shown in Fig. 74. Although the degradation is slightly higher than for the first order case, it is still minimal for any reasonable actuator rolloff.

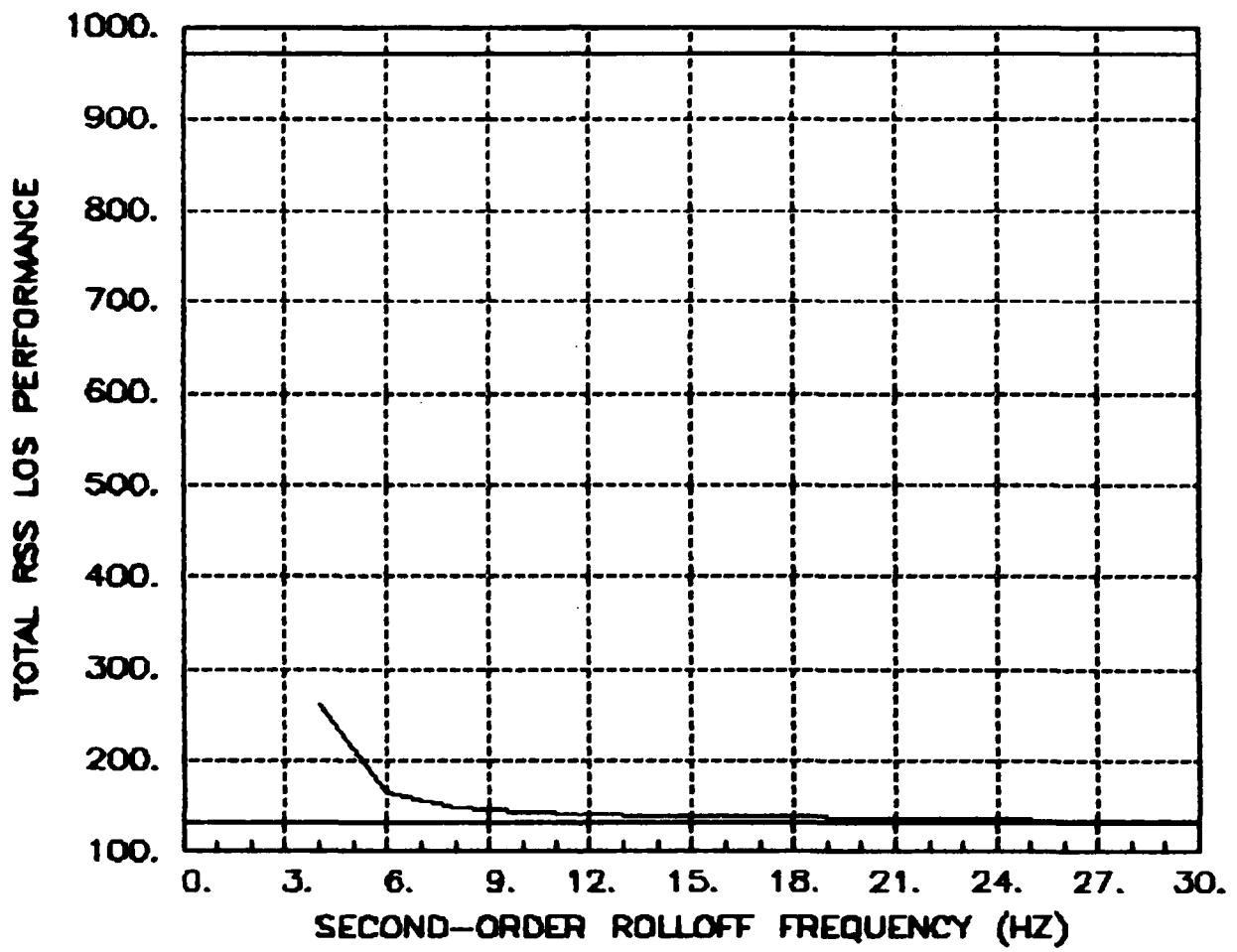
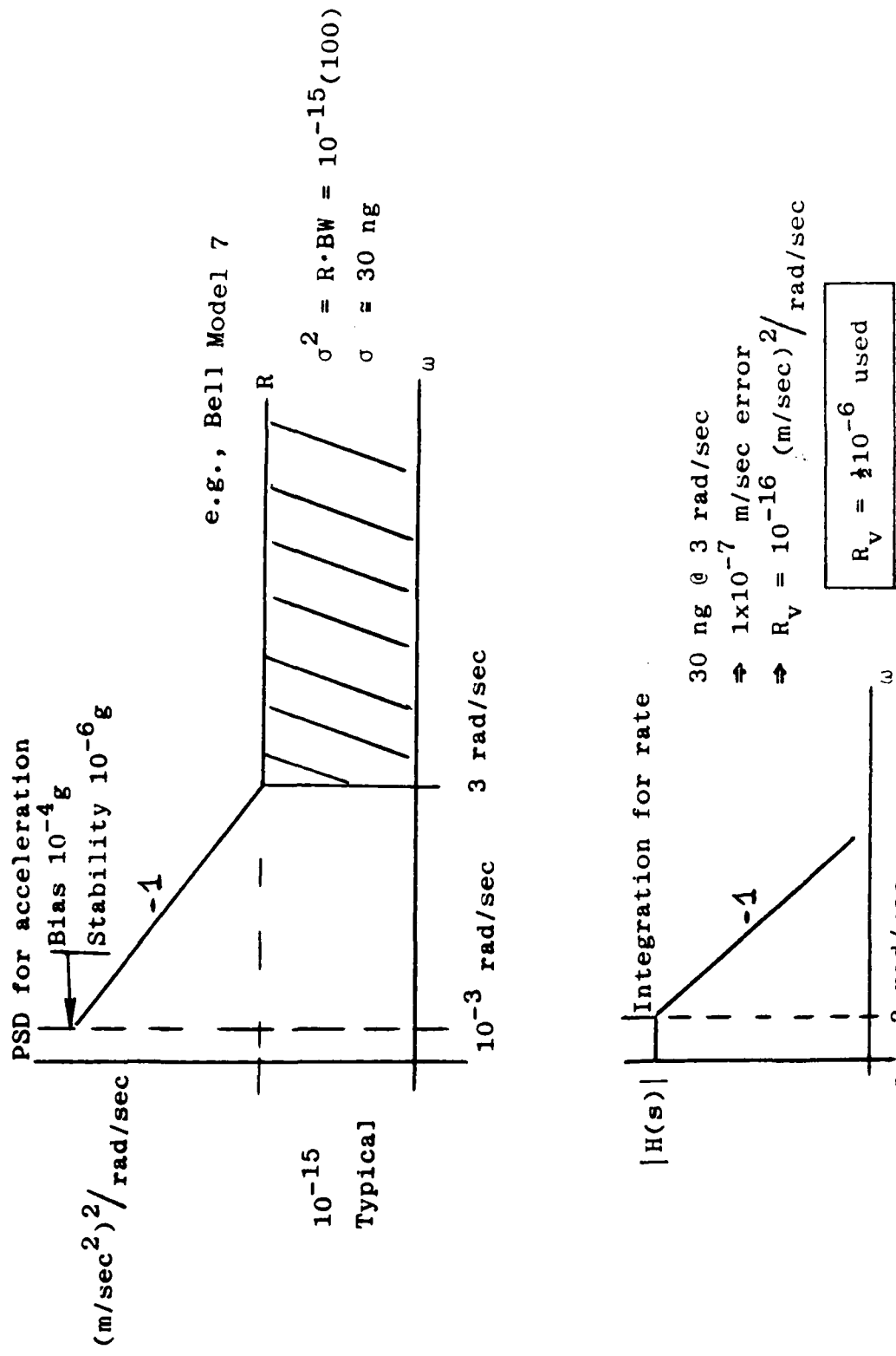


Figure 74. Performance Degradation Due to Second-Order Actuator Rolloff

8. SENSOR MODELING EFFECTS

The principal terms of sensor modeling errors will be bias, scale factor, and misalignment errors and these errors will create LSS control mechanization difficulties at low frequency. Since rigid-body controls are being put aside for the present study, only the high-frequency effects for accelerometer mechanizations will be examined here. Optical sensing, used extensively in large space structures (LSS) control, generally exhibits high signal-to-noise performance. These systems are prone, however, to measurement matrix errors. This is a more general type of error which is discussed (in broad context) in subsection 9.

For high-performance accelerometers used above 0.5 Hz or so, broadband noise is the principal hardware characteristic which may be important for control performance evaluation. Typical noise power spectra for such instruments are shown in Fig. 75. The equivalent rate noise is also estimated in the figure. Integrated noise figures of 30 ng (1σ) are currently attainable at modest cost for units like the Bell model 7. For distributed sensing, the accelerometer noise figure (at high frequency) does not cause significant performance degradation as shown in Table 34. Here the equivalent white rate noise is propagated through the system using the 34 mode evaluation and the two actuator/four sensor "reduced set" described in subsection 7. To see an effect, however, the white rate intensity was increased by about 9 orders-of-magnitude as shown. Thus, it can be concluded that accelerometer usage for LSS control will not be limited by broadband accelerometer noise.



Accelerometer noise above 0.5 Hz not significant.

Figure 75. Accelerometer Noise Models

Table 34

34-MODE PERFORMANCE EVALUATION

	OPEN LOOP	HAC/LAC	HAC/LAC WITH RATE SENSOR NOISE OF INTENSITY $5 \times 10^{-7} \frac{M^2}{SEC}$
RSS LOS x (μ RAD)	75.35	33.00	33.55
RSS LOS y (μ RAD)	967.79	128.76	130.33
TOTAL RSS LOS (μ RAD)	970.72	132.93	134.58

9. EFFECTS OF GENERAL ACTUATOR/SENSOR MODELING ERRORS

a. Robustness of Control Design

Since the spacecraft model is a baseline representation of the actual system, the control design must be able to accommodate errors in the model. Typical sources of model error in spacecraft systems include:

- numerical errors due to approximate modeling techniques, e.g., high order NASTRAN models.
- actual parameter changes in the LSS, e.g., thermal effects, gravity, spacecraft and antenna dimensions, mass distributions, etc.
- unmodeled dynamics, e.g., effect of reduced order modeling, neglected residual modes ("spillover"), neglected actuator/sensor dynamics, non-linearities,, etc.
- incomplete data obtained from on-earth testing, e.g., partially assembled structures in simulated zero-g.

Therefore, uncertainty in the baseline model arises from both actual causes and intentional approximations of complicated phenomena. In many cases, these are indistinguishable.

b. Modeling and Model Uses

In a broad sense, model error refers to measurable differences between two systems. Normally, one of these is the actual system, and the other is a "model" of the actual system. However, since models are developed for different uses, there can be several models of an actual system; consequently, model error can also refer to measurable differences between two models of the same system. For example, the model used in the evaluation phase of a control design is a high fidelity representation of the spacecraft; this model is usually referred to as the baseline

model. The model used for control design, however, is considerably simpler; it is usually obtained from the baseline model by any number of methods, e.g., modal truncation, linearization, etc.

Thus, there are several models for any system--different models are used for control design, analysis, and evaluation. In fact, there is no unique model of a system, because models are determined by their use. But model use, in turn, is determined by performance requirements. In other words, the limitations or errors associated with a particular model are intimately connected with the performance demands of control system design based on the model.

c. Model Error

To obtain a quantitative bound on model error, the source of the error must be determined, and then a suitable test procedure devised. Consider a controlled spacecraft, as depicted in Fig. 76, with the following model:

Sensor Model

$$z = y + n$$

Dynamic Model

$$y = M(s)u + d$$

Controller

$$u = C(s)e, \quad e = r - z \quad . \quad r = \text{reference}$$

where $M(s)$ is a finite dimensional transfer function matrix model representing the dynamics of the actuators and spacecraft; $C(s)$ is the transfer function matrix of the controller; d is

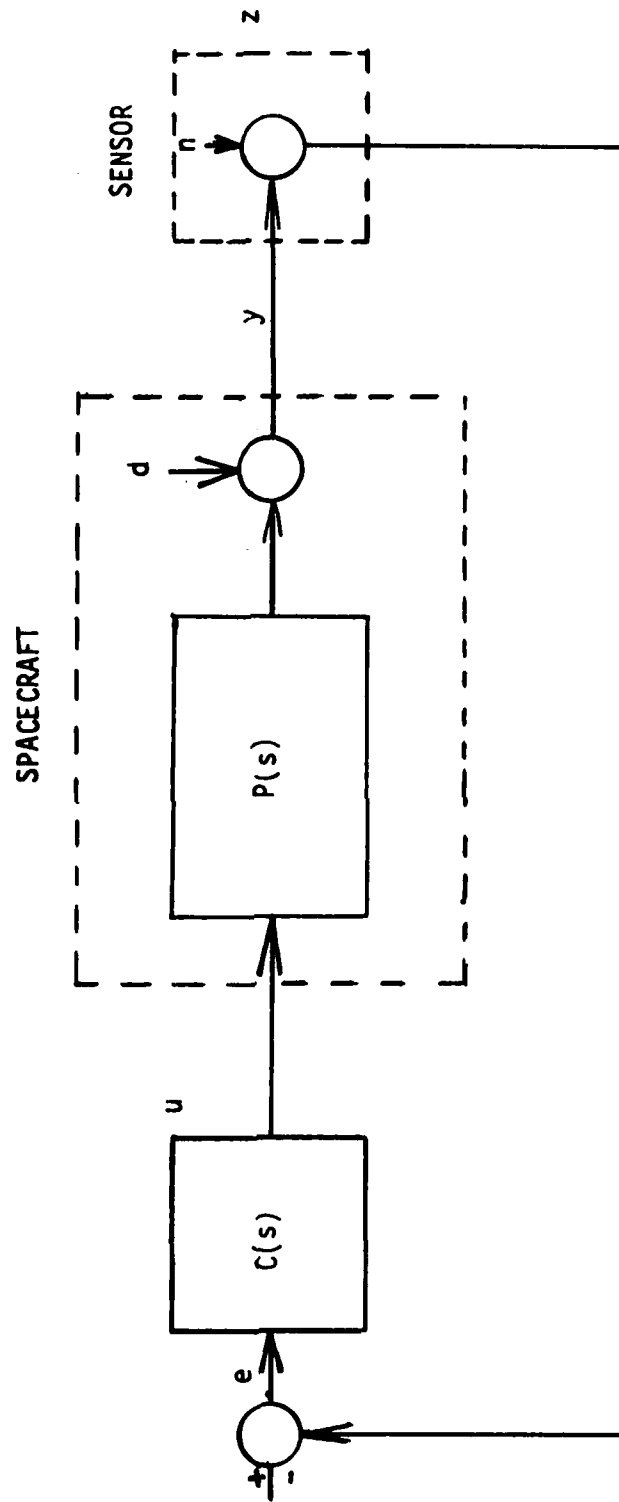


Figure 76. Block Diagram of Controlled Spacecraft

the effect of external disturbance forces on the sensed outputs; and n the sensor noise. Let the actual dynamics be

$$y = P(s)u + d \quad (44)$$

where $P(s)$ is not necessarily finite dimensional. For example, $P(s)$ can be either a high order NASTRAN model or represent data from the actual system, whereas $M(s)$ is the reduced order control design model. Thus, the controlled output is:

$$\begin{aligned} y &= (I + PC)^{-1} d + (I + PC)^{-1} PC (r-n) \\ &= H_{yd} d + H_{yr} (r-n) \end{aligned} \quad (45)$$

(The complex variable 's' has been suppressed for brevity of notation, unless needed for clarification.) Note that

$$H_{yd} + H_{yr} = I \quad (46)$$

Since M is a reduced order model of P , let

$$P = M + \Delta_r \quad (47)$$

where Δ_r represents the effect of neglected residual modes.

Thus:

$$\begin{aligned} H_{yd} &= \bar{H}_{yd} - (I + MC)^{-1} [I + \Delta_r C (I + MC)^{-1}]^{-1} \Delta_r C (I + MC)^{-1} \\ \bar{H}_{yd} &= (I + MC)^{-1} \end{aligned} \quad (48)$$

where \bar{H}_{yd} is the nominal transfer function with no model error, i.e., $\Delta_r = 0$.

A bound on the size of Δ_r can be obtained from the simple input/output test:

$$\delta_r(\omega) = \frac{\text{RMS}(y - Mu)}{\text{RMS}(u)} \bigg|_{u = u_0 \sin \omega t} \quad (49)$$

where $\text{RMS}(x)$ is the root-mean-square (RMS) value of x . Thus, injecting sinusoidal signals into the actual system and the model and comparing the outputs gives a bound on Δ_r . In fact, it can be shown that

$$\bar{\sigma}[\Delta_r(j\omega)] \leq \delta_r(\omega) \quad (50)$$

where $\bar{\sigma}(A)$ is the maximum singular value of the complex matrix A , i.e., the square root of the maximum eigenvalue of A^*A .

Similarly, we can examine the way in which other kinds of model error enter into the closed-loop dynamics. The spacecraft model, for example, may not include actuator dynamics. This omission can be represented by the model error form,

$$P = M(I + \Delta_a) \quad (51)$$

where Δ_a represents the deviation from the dynamics of an actuator with infinite bandwidth. In this case, the model error test is:

$$\bar{\sigma}[\Delta_a(j\omega)] \leq \delta_a(\omega) = \frac{\text{RMS}(y - Mu)}{\text{RMS}(Mu)} \bigg|_{u = u_0 \sin \omega t} \quad (52)$$

The effect on closed-loop response is:

$$H_{yd} = \bar{H}_{yd} - (I + MC)^{-1} M[I + \Delta_a(I + CM)^{-1}CM]^{-1} \Delta_a C(I + MC)^{-1} \quad (53)$$

d. Stability Robustness

The model error bounds can be used to quantitatively determine the robustness of stability, i.e., stability margins. If the nominal spacecraft model M is stabilized by the controller C , then the actual spacecraft is stable if:

(2) For reduced order model errors Δ_r ,

$$\delta_r(\omega) \bar{\sigma}\{C(j\omega)[I+M(j\omega)C(j\omega)]^{-1}\} < 1, \quad \omega \geq 0 \quad (54)$$

or (1) For actuator model errors Δ_a ,

$$\delta_a(\omega) \bar{\sigma}\{[I+C(j\omega)M(j\omega)]^{-1}C(j\omega)M(j\omega)\} < 1, \quad \omega \geq 0 \quad (55)$$

Table 35 summarizes these robustness tests for generic model errors bounded by

$$\bar{\sigma}[\Delta(j\omega)] \leq \delta(\omega), \quad \omega \geq 0 \quad (56)$$

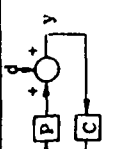
where $\delta(\omega)$ is determined from input/output tests, e.g., RMS tests. Table 35 shows the stability margins, denoted by δ_{sm} , defined as the maximum bound on model error, which (at the specified location, e.g., actuator, sensor, etc.) insures stability. Thus,

$$\delta(\omega) < \delta_{sm}(\omega), \quad \omega \geq 0. \quad (57)$$

e. Performance Robustness

Once having determined frequency dependent bounds on the model, a similar procedure can be used to bound the effect of model error on performance, i.e., performance robustness. For example, define the frequency dependent performance measure $\rho(\omega)$ as,

Table 35. STABILITY AND PERFORMANCE ROBUSTNESS MARGINS

GENERIC FORM OF MODEL ERROR	SOURCE OF MODEL ERROR IN SPACECRAFT SYSTEM	STABILITY MARGIN		PERFORMANCE MARGIN
<p>P := actual plant M := model Δ := model error</p>		<p>Guaranteed stability if $\bar{\sigma}(\Delta) < \delta_{SM}$</p>	<p>Controlled Spacecraft</p> 	<p>Nominal ($\Delta = 0$): $\bar{H}_{yd} = (I + MC)^{-1}$ Guaranteed performance $\bar{\sigma}[H_{yd} - \bar{H}_{yd}] \leq \bar{\sigma}[\bar{H}_{yd}]$ if $\bar{\sigma}(\Delta) \leq \delta_{PM}$</p>
<p><u>Additive</u> $P = M + \Delta$</p>	<ul style="list-style-type: none"> neglected residual modes, e.g. <ul style="list-style-type: none"> spillover reduced order modeling uncertain interacting structural modes 	<p>$\delta_{SM} = 1/\bar{\sigma}[(I + MC)^{-1}]$</p>		<p>$\delta_{PM} = \delta_{SM} \rho(\rho + 1)^{-1}$</p>
<p><u>Output Multiplicative</u> $P = (I + \Delta)M$</p>	<ul style="list-style-type: none"> sensor errors <ul style="list-style-type: none"> misalignments bandwidth scale factors neglected high frequency phenomena, e.g., <ul style="list-style-type: none"> model approximations friction stiction 	<p>$\delta_{SM} = 1/\bar{\sigma}[(I + MC)^{-1}MC]$</p>		<p>$\delta_{PM} = \delta_{SM} \rho(\rho + 1)^{-1}$</p>
<p><u>Input Multiplicative</u> $P = M(I + \Delta)$</p>	<ul style="list-style-type: none"> actuator errors <ul style="list-style-type: none"> bandwidth nonlinearities parasitics quantization 	<p>$\delta_{SM} = 1/\bar{\sigma}[(I + CM)^{-1}CM]$</p>		<p>$\delta_{PM} = \delta_{SM} \rho \left\{ \rho + \delta_{SM} \bar{\sigma}[C(I + MC)^{-1}] \cdot \bar{\sigma}[(I + MC)^{-1}M] / \bar{\sigma}[(I + MC)^{-1}] \right\}^{-1}$</p>
<p><u>Output Multiplicative</u> $P = (I + \Delta)^{-1}M$</p>	<ul style="list-style-type: none"> low frequency parameter errors, e.g., <ul style="list-style-type: none"> uncertain mode shapes variations in mass distribution thermal effects uncertain right half plane poles 	<p>$\delta_{SM} = 1/\bar{\sigma}[(I + MC)^{-1}]$</p>		<p>$\delta_{PM} = \delta_{SM} \rho(\rho + 1)^{-1}$</p>
<p><u>Input Multiplicative</u> $P = M(I + \Delta)^{-1}$</p>		<p>$\delta_{SM} = 1/\bar{\sigma}[(I + CM)^{-1}]$</p>		<p>$\delta_{PM} = \delta_{SM} \rho \left\{ \rho + \delta_{SM} \bar{\sigma}[C(I + MC)^{-1}] \cdot \bar{\sigma}[(I + MC)^{-1}M] / \bar{\sigma}[(I + MC)^{-1}] \right\}^{-1}$</p>

$$\rho(\omega) := \bar{\sigma}\{H_{yd}(j\omega) - \bar{H}_{yd}(j\omega)\} / \bar{\sigma}\{\bar{H}_{yd}(j\omega)\} \quad (58)$$

This gives a relative measure of the deviations of H_{yd} about the nominal \bar{H}_{yd} . In the face of reduced order model error Δ_r a specified level of performance robustness $\rho(\omega)$ is achievable if

$$\frac{\delta_r(\omega) \bar{\sigma}\{C(j\omega)\} \bar{\sigma}\{[I+M(j\omega)C(j\omega)]^{-1}\}}{1 - \delta_r(\omega) \bar{\sigma}\{C(j\omega)[I+M(j\omega)C(j\omega)]^{-1}\}} \leq \rho(\omega), \quad \omega \geq 0 \quad (59)$$

Similar expressions for performance robustness can be obtained as a result of other sources of model error, e.g., sensor model error. Table 35 summarizes these performance robustness tests for generic model error. The table shows the performance margins, denoted by δ_{pm} , defined as the maximum bound on model error (at the specified location) which insures the specified performance tolerance. Thus,

$$\delta(\omega) \leq \delta_{pm}(\omega), \quad \omega \geq 0 \quad (60)$$

guarantees performance robustness. This also guarantees stability, since,

$$\delta_{pm}(\omega) < \delta_{sm}(\omega), \quad \omega \geq 0. \quad (61)$$

f. Example: Actuator Uncertainty

In this section we present an example which illustrates the use of the robustness analysis techniques just described. The problem considered is to determine the effect of actuator bandwidth on performance and stability of the baseline control design for the CSDL-II (rev. 3) model. The control system uses 2 actuators and 4 sensors located as shown in Fig. 20. The control design (see subsection 7) is based on a model with no actuator

dynamics, i.e., the actuators are assumed to have infinite bandwidth. For the purposes of analysis, both of the actuators are modeled identically by,

$$u_{ai} = H_a(s)u_i, \quad i = 1, 2 \quad (62)$$

where u_a is the force out of the actuator; u is the force command (control signal); and $H_a(s)$ is the transfer function of each actuator given by

$$H_a(s) = \frac{\omega_a^2}{s^2 + 2\xi_a\omega_a s + \omega_a^2}, \quad \omega_a = 2\pi f_a \quad (63)$$

where f_a is the bandwidth and ξ_a is the damping ratio, which is assumed to be fixed at $\xi_a = 1$. The bandwidth is then varied until instability ensues. From subsection 7c it is determined that performance is degraded by no more than 10% for $f_a \geq 12$ hz, and stability is guaranteed for $f_a \geq 4$ hz. We will now compare these exact results with the approximate results obtained using the formulae in Table 35. The relevant stability and performance margins (from the Table) are,

$$\delta_{sm} = 1/\bar{\sigma}[(I+CM)^{-1}CM] \quad (64)$$

$$\delta_{pm} = \delta_{sm} \rho \left\{ \rho + \delta_{sm} \bar{\sigma}[C(I+MC)^{-1}] \bar{\sigma}[(I+MC)^{-1}M] / \bar{\sigma}[(I+MC)^{-1}] \right\}^{-1}$$

The model error is taken to be

$$\Delta_a(s) := I - H_a(s)I \quad (65)$$

Thus, $\Delta_a(s)$ represents the error between the ideal infinite bandwidth actuators and the actual ones. As a result,

$$\delta_a(\omega) := \bar{\sigma}[\Lambda_a(j\omega)] = \frac{\omega(\omega^2 + 4f_a^2)^{\frac{1}{2}}}{[(\omega^2 - \omega_a^2)^2 + 4\xi_a^2\omega_a^2\omega^2]^{\frac{1}{2}}} \quad (66)$$

Figure 77 shows the effect of actuator bandwidth on the stability margins, i.e., plots of δ_{sm} vs. ω and δ_a vs. ω with actuator bandwidth $f_a = 3.7$ Hz. This corresponds to the lowest actuator bandwidth that ensures stability, i.e., $\delta_a(f_a) = \delta_{sm}(f_a)$. Compare this to 3 Hz which was obtained from an eigenvalue analysis with the actuator dynamics included. The small discrepancy is due to the inherent conservatism in the robustness analysis.

Similarly, Fig. 78 shows the effect of actuator bandwidth on the performance margin, i.e., plots of δ_{pm} vs. ω and δ_a vs. ω with actuator bandwidth $f_a = 160$ Hz. This corresponds to the lowest actuator bandwidth which ensures a 10% performance degradation ($\rho = 0.1$) where $\delta_a(f_a) = \delta_{pm}(f_a)$. Compare this to 20 Hz obtained from the full system eigen-analysis. The discrepancy here is large, principally due to the difference in performance measures. Further basic research is required to alleviate this conservatism.

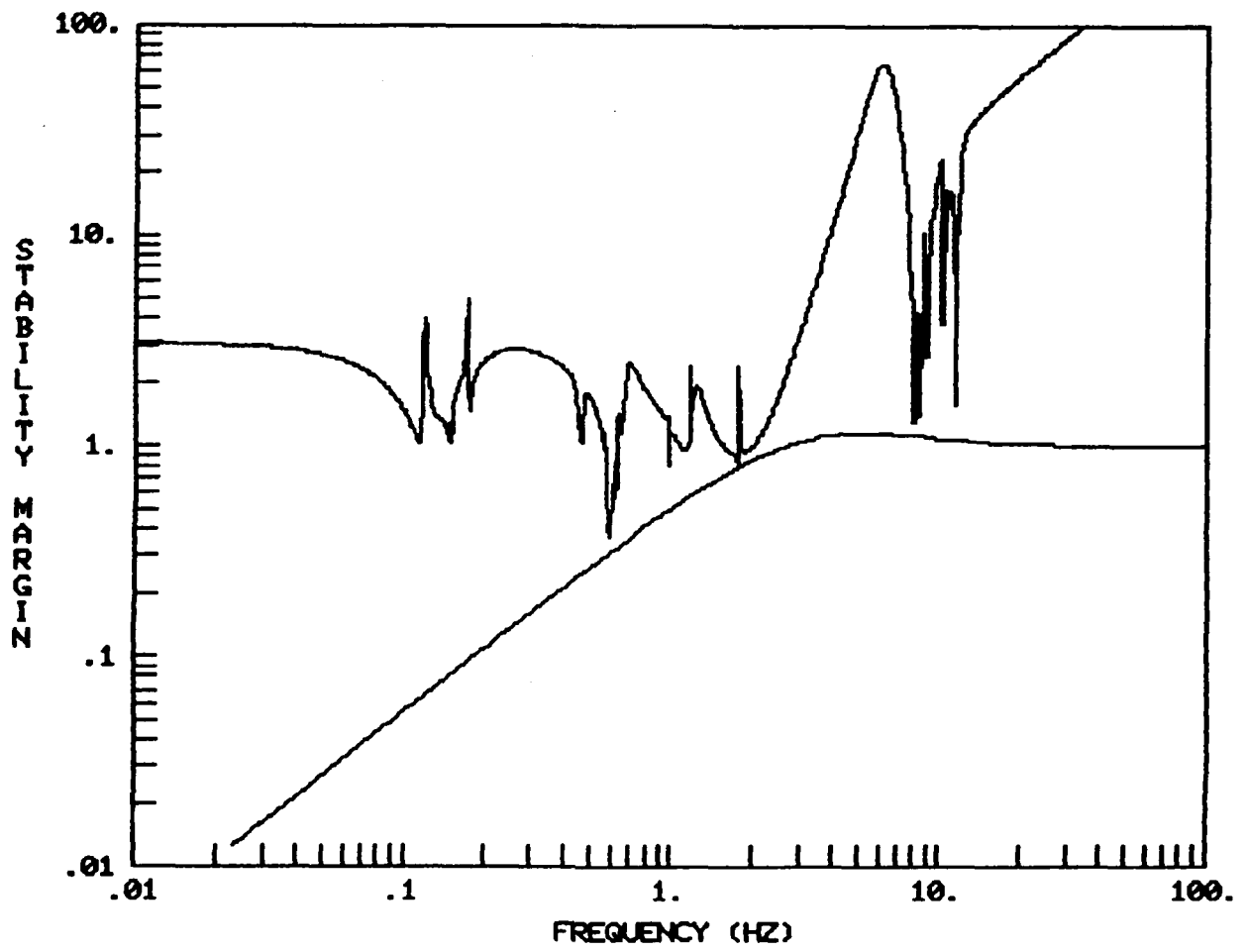


Figure 77. Stability Margin (Actuator Bandwidth 3.7 Hz)

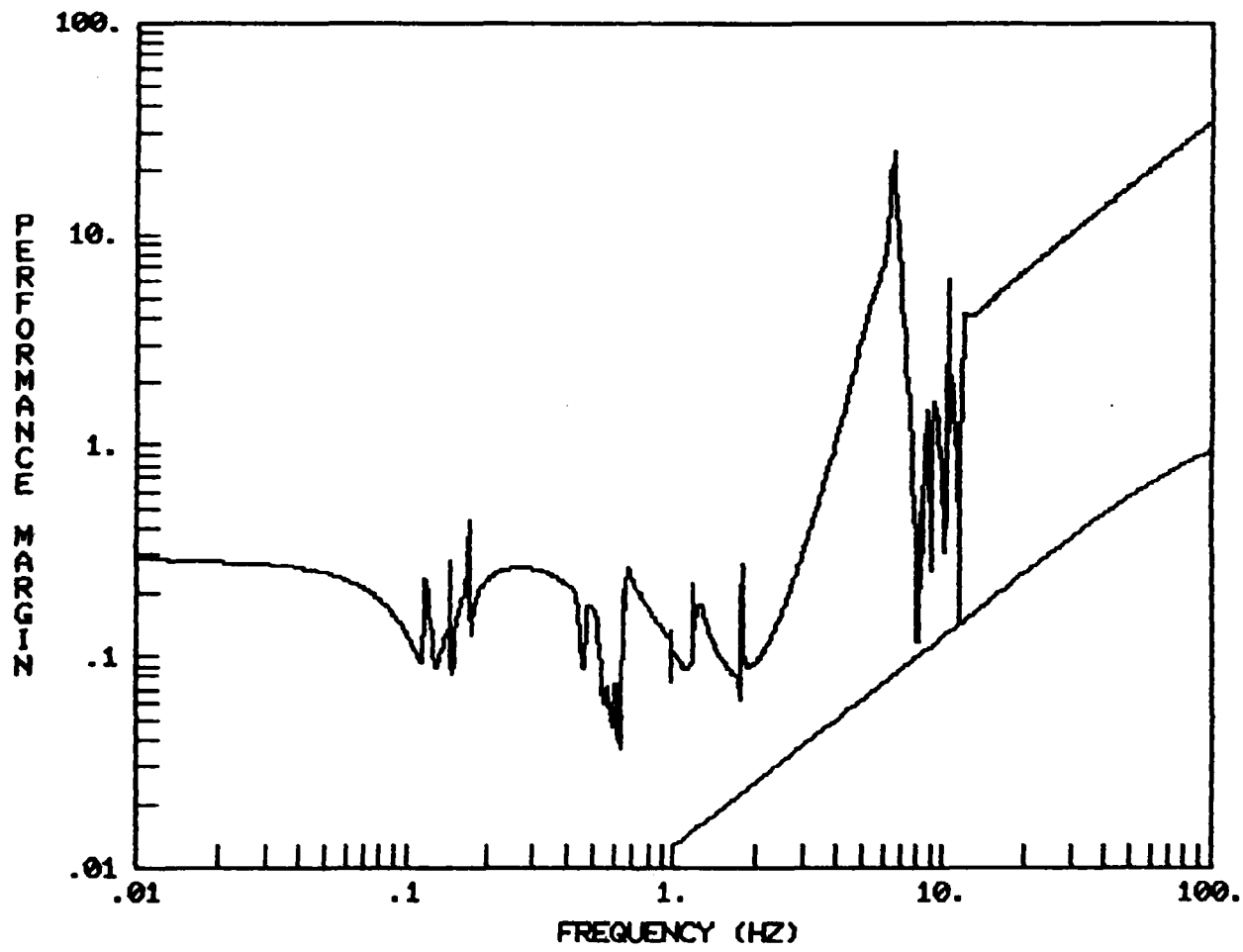


Figure 78. Performance Margin 10 Percent Degradation
(Actuator Bandwidth 160 Hz)

10. RESULTS COMPARISON FOR STIFFNESS DESIGNS

One of the VCOSS program objectives is to compare performance results for a "soft" actively controlled structure with those of a passive "stiff" structure. Such comparisons are difficult to interpret, however, if each structure is not optimized to enhance either a passive or active controls approach. Notwithstanding these difficulties, the comparisons can now be examined. For the passive structural performance, the results are given in Table 36, due to CSDL, for the combined broadband and discrete power spectra. Three models are shown for both the six independent disturbance sources and the two source "equivalent" input (cf. subsection 5). Some disagreement still remains over the open-loop response for two sources, so discussion here will be restricted to the six source results. Rev 00 is the original ACOSS model while Rev 03, the VCOSS model, is a softened version of Rev 00. Open-loop response degrades by about a factor of 3 for the "soft" model. A stiffer version, Rev 04, produces about a 4 to 1 performance spread between Rev 04 and Rev 03. Thus, it is reasonable to expect these kinds of improvements through structural stiffening exercises.

The closed-loop comparison is recapitulated in Table 37. The open-loop values have shifted slightly since the discrete power spectra are not included. The reduction factor in closed-loop is now about 14, using 6 effective actuators. More actuators can boost this value to about 80. The principal observation is that much larger reduction is achievable through simple active controls than via simple structural stiffening. Performance sensitivity to model uncertainty will also be better for the closed-loop systems. In either case here, sufficient reduction factors to meet the specification are not obtainable without resorting to integrated controls including isolation and low-frequency alignment systems--all considered out-of-scope for this study. Nevertheless, the simple actuators used in this study, coupled with low-frequency alignment

to handle 0.1 Hz modes, can produce significant performance improvements without major impacts on structural redesign and without complex modeling changes to synthesize the controls.

Table 36. PASSIVE SYSTEM RESPONSE TO COMPLETE PSD

	2 INPUTS				6 INPUTS			
	LOSX	LOS Y	LOS	DEF	LOSX	LOS Y	LOS	DEF
REV00	161.38	602.71	623.94	18.37	91.88	364.11	375.52	15.18
REV03	161.61	1949.25	1955.94	171.61	135.88	1116.37	1124.61	129.22
REV04	73.77	485.71	491.28	10.54	83.82	264.90	277.84	6.69

Table 37. REV 03 CLOSED-LOOP PERFORMANCE WITHOUT DISCRETE FREQUENCY POWER SPECTRA

	LOSX	LOS Y	LOS	
Rev 03	131.7	1109.5	1117.3	Open-loop
	26.4	75.6	80.1	Closed-loop

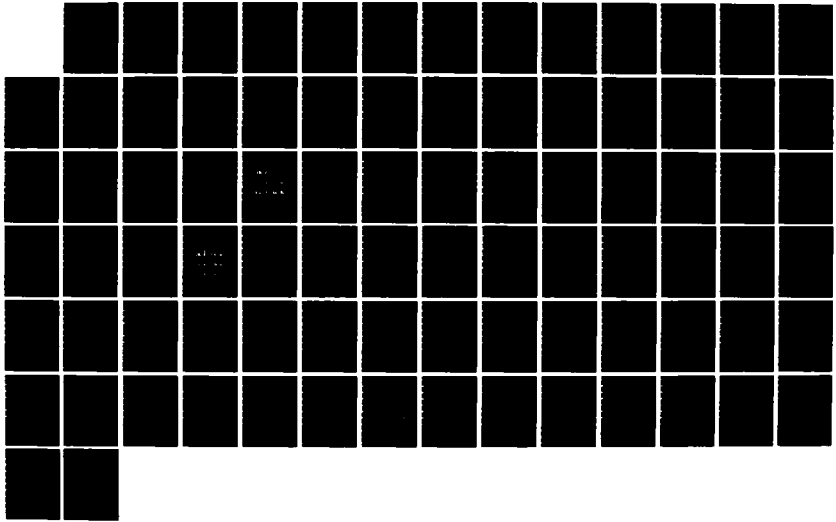
AD-A139 931

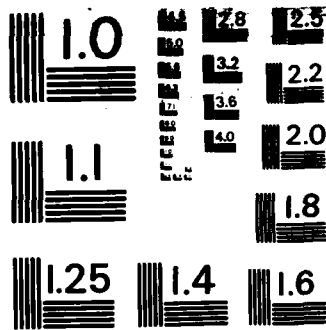
VIBRATION CONTROL OF SPACE STRUCTURES VCOSS A: HIGH AND
LOW-AUTHORITY HAR. (U) LOCKHEED MISSILES AND SPACE CO
INC SUNNYVALE CA J N AUBRUN ET AL. JUL 83 LMSC-D883019
AFWAL-TR-83-3074 F33615-81-C-3220 F/G 20/11

3/3

UNCLASSIFIED

NL





MICROCOPY RESOLUTION TEST CHART
NATIONAL BUREAU OF STANDARDS-1963-A

11. CONCLUSIONS

This first VCOSS study focused on the system performance limitations imposed by actuator, sensor, and signal processing hardware. To provide some depth to the study, restrictive assumptions were made at the outset to bound the investigation. The most significant of these assumptions is the removal of the rigid-body control problem. It is in this region that sensor modeling is most important; attitude, alignment, and modal control systems' authority also must be resolved at very low frequency. These complex issues have not as yet been adequately addressed and, thus, results shown here must be properly interpreted. A system design methodology which includes hardware constraints has been shown to be effective in producing implementable control system designs. The process may be highly iterative to meet system design constraints. A preliminary hardware selection for the VCOSS studies includes: (1) proof-mass dampers, (2) accelerometers, and (3) a candidate digital processor architecture. The main conclusions of VCOSS to date deal with high-frequency actuator dynamics, and this report makes a significant contribution in this area.

Realistic actuation adds a significant twist to the HAC/LAC stability robustness issue due to the combined effects of spillover/compensation rolloff and LAC/actuator interaction; however, this can be handled in a straightforward manner. It is shown, in fact, that any desired high-frequency stability margin can be guaranteed via HAC frequency shaping and passive damping actuator augmentation for any realistic (PPM) actuator. The impact of realistic actuators upon performance robustness is shown to be minimal, requiring no design modification at all.

The effects of actuator/sensor modeling errors and the juxtaposition of these errors with spacecraft modeling uncertainty

appears to be a solvable problem using frequency-domain error criteria like singular value decomposition of the system return difference. Combinations of appropriate frequency shaping, hardware selection, and realistic assessment of model error can allow LSS control hardware realizations to produce predictable performance. It remains to test the validity of these statements through appropriate ground and flight experiments.

REFERENCES

1. B. C. Moore, "Principal Component Analysis in Linear Systems: Controllability, Observability, and Model Reduction," IEEE Trans. Auto. Control, Vol. AC-26, No. 1, February 1981.
2. R. E. Skelton, "Cost Decomposition of Linear Systems with Application to Model Reduction," International J. of Control, Dec. 1980.
3. ACOSS 5, Phase 1A Final Report, LMSC D811889, November 1981.
4. ACOSS Phase 1 Proposal, LMSC/DARPA, 1978.
5. R. Strunce, "ACOSS PSD Disturbance Model (Revised July 8, 1982)," CSDL Memo, June 11, 1982.
6. J. -N. Aubrun and G. Margulies, "Low-Authority Control Synthesis for Large Space Structures," NASA Contractor Report under Contract NAS1-14887-TASK 11, May 1982.
7. T. Henderson, "Active Control of Space Structures (ACOSS) Model 1", The Charles Stark Draper Laboratory, Inc., Report C-5437, September 1981.
8. T. Henderson, "VCOSS Design Model and Disturbances", CSDL Memo, November 13, 1981.

APPENDIX A

Reduction of Large Flexible Spacecraft
Models Using Internal Balancing
Theory

**Reduction of Large Flexible Spacecraft Models
Using Internal Balancing Theory**

C. Z. Gregory, Jr.*

Integrated Systems, Inc., Palo Alto, California

Abstract

A new and computationally simple method for flexible spacecraft model reduction is presented. Using an internal balancing approximation shown to be valid when natural damping is small, the method provides quantitative modal rankings with respect to disturbance environment, actuator authority, sensor observability, and performance objective. These rankings are used to select a reduced set of structural modes for controller design, and also to anticipate potential closed-loop performance and stability problems resulting from modal truncation. The method is demonstrated using a 54-mode spacecraft example.

*Research Scientist. Member AIAA.

List of Figures

- Fig. 1. Approximation Error for Two-Mode Subsystem
- Fig. 2. Open-Loop Modal Analysis
- Fig. 3. Closed-Loop Spectrum with 10-Mode Controller
- Fig. 4. Closed-Loop Spectrum with 10-Mode Controller (Expanded Scale)
- Fig. 5. Closed-Loop Modal Costs for 10-Mode Controller
- Fig. 6. Closed-Loop Spectrum with 14-Mode Controller
- Fig. 7. Closed-Loop Spectrum with 14-Mode Controller (Expanded Scale)
- Fig. 8. Closed-Loop Modal Costs for Three Controllers
- Fig. 9. Closed-Loop Spectrum for 14-Mode Controller with LAC
- Fig. 10. Closed-Loop Spectrum for 14-Mode Controller with LAC (Expanded Scale)

I. Introduction

The deployment of large space structures will require feedback control to meet stringent vibration, line-of-sight, jitter, and surface quality performance criteria. Flexible spacecraft control design requires mathematical models of plant dynamics, actuator/sensor locations, and disturbance environment, all defined with respect to performance objectives. These "evaluation models", obtained by finite-element analysis, can contain hundreds of structural modes known with varying degrees of accuracy. This paper addresses open-loop reduction of these models for the purpose of feedback control design.

Model reduction for control design is motivated by practical issues: hardware limitations, reduced computation power on-line, and robustness. In principle, an "optimal" control can be generated for a large model using modern control techniques, but this control is at least as complex as the model itself. When the "reduced controller-order" constraint is formally imposed, optimal control methods lose their attractive closed-form solutions. Therefore, a reduced-order "control design" model is selected using the same criteria as for the evaluation model: namely, to represent the system accurately with respect to the performance objectives.

The typical approach to structural model reduction is mode selection. The simplest, dominant-frequency selection¹, ignores the fact that actuator and sensor placement, disturbances, and performance requirements also affect modal dominance. Modal-cost

analysis^{2,3} addresses the latter two issues by prescribing modal rankings based upon relative contributions to a stochastic cost functional. It is shown² that the modal-costs decouple asymptotically as damping approaches zero. The influence of actuator/sensor placement upon modal dominance is not treated, however, and the problem remains that feedback control can couple the disturbance into open-loop "undisturbed" modes.

Recently a general model-reduction approach based upon state selection from a gramian-balanced ("internally-balanced") coordinate representation has been proposed^{4,5,6}. For a given input/output configuration, this approach produces a "balanced approximation" to the large model by defining and retaining the "most controllable/observable" states. Open-loop application of this reduction method to problems involving two sets of inputs (disturbances and actuators) and outputs (regulated variables and sensors) is in general not possible, because a different coordinate basis is required for each input/output pair. However, results for lightly-damped single-input single-output flexible systems⁷ have shown that modal truncation and balanced approximation are equivalent, asymptotically, as damping approaches zero. The implied asymptotic equivalence of modal and balanced coordinates extends to the multi-input multi-output case, and is fundamental to the present work.

This paper gives a systematic mode-selection procedure for large lightly-damped structural models, based upon the theory of "internal balancing"⁴. The model-reduction/control-design problem is described in Section II. Section III briefly reviews internal

balancing theory , develops an approximation for multi-input multi-output lightly-damped structures, and investigates the approximation accuracy for practical problems. Similarities with recent, independently obtained single-input single-output results⁸ are noted. Section IV attempts a physical interpretation of the results with respect to the control design issues, and proposes a new mode-selection methodology for lightly-damped structures. A complete design example is given in Section V.

II. Problem Statement

Consider an evaluation model containing structural dynamics in modal form:

$$\begin{aligned}
 \ddot{\eta} + 2Z\Omega\dot{\eta} + \Omega^2\eta &= \mathcal{B}u + \mathcal{D}w \\
 z &= \mathcal{M}_1\dot{\eta} + \mathcal{M}_2\eta \quad (\text{measurements}) \\
 y &= \mathcal{C}_1\dot{\eta} + \mathcal{C}_2\eta \quad (\text{regulated variables}) \\
 J &= \lim_{t \rightarrow \infty} E\{y^T y\} \quad (\text{performance measure})
 \end{aligned} \tag{1}$$

where $\eta \in \mathbb{R}^n$, $Z = \text{diag}\{\zeta_i\}$, $\Omega = \text{diag}\{\omega_i\}$, u is the control vector, and w is the disturbance vector. Defining

$$b_i \triangleq \text{i'th row of } \mathcal{B}$$

$$d_i \triangleq \text{i'th row of } \mathcal{D}$$

$$m_{ji} \triangleq \text{i'th column of } \mathcal{M}_j$$

$$c_{ji} \triangleq \text{i'th column of } \mathcal{C}_j$$

an equivalent state-space representation of (1) is:

$$\dot{x} = Ax + Bu + Dw$$

$$z = Mx$$

$$y = Cx$$

$$J = \lim_{t \rightarrow \infty} E(y^T y)$$

} (2)

where

$$x = [\dot{\eta}_1 \ \eta_1 \ \dot{\eta}_2 \ \eta_2 \ \dots \ \dot{\eta}_n \ \eta_n]^T$$

$$A = \begin{bmatrix} A_1 & & & 0 \\ & A_2 & & \\ & & \ddots & \\ 0 & & & A_n \end{bmatrix}$$

$$A_i = \begin{bmatrix} -2\zeta_i \omega_i & \omega_i^2 \\ 1 & 0 \end{bmatrix}$$

$$B = [b_1^T \ 0 \ b_2^T \ 0 \ \dots \ b_n^T \ 0]^T$$

$$D = [d_1^T \ 0 \ d_2^T \ 0 \ \dots \ d_n^T \ 0]^T$$

$$M = [m_{11} \ m_{21} \ m_{12} \ m_{22} \ \dots \ m_{1n} \ m_{2n}]$$

$$C = [c_{11} \ c_{21} \ c_{12} \ c_{22} \ \dots \ c_{1n} \ c_{2n}]$$

Mode-selection for control design requires evaluation of the relative importance of each mode to the control problem. The specific issues which influence this evaluation are:

- modal fidelity
- controllability
- observability
- disturbance environment
- performance objective

None of these criteria stands alone. For example, it makes little sense to retain the most accurately modeled mode if it is neither controllable nor observable in the measurements. Similarly, a highly controllable mode adds little to the controller performance if it is (strictly) unobservable in the sensors and in the performance. The problem is to find a reduced-order model which addresses each of these design issues such that controls designed for the reduced model perform well on the evaluation model.

III. Internal Balancing of Lightly-Damped Structures

In general, balanced model reduction is state selection in a special coordinate system. Before proceeding with mode-selection, this theory is reviewed.

Balanced Model Reduction

Consider a linear, time-invariant, asymptotically stable state-space system:

$$\left. \begin{aligned} \dot{x} &= Ax + Bu \\ y &= Cx \end{aligned} \right\} \quad (3)$$

having controllability grammian W_c^2 and observability grammian W_o^2 given by

$$W_c^2 = \int_0^{\infty} e^{At} BB^T e^{A^T t} dt \quad \text{or} \quad AW_c^2 + W_c^2 A^T + BB^T = 0 \quad (4)$$

$$W_o^2 = \int_0^{\infty} e^{A^T t} C^T C e^{At} dt \quad \text{or} \quad A^T W_o^2 + W_o^2 A + C^T C = 0 \quad (5)$$

The model (3) is internally balanced if

$$W_c^2 = W_o^2 = \Sigma^2$$

where $\Sigma^2 = \text{diag} [\sigma_1^2, \sigma_2^2, \dots, \sigma_n^2]$

and $i < j \Rightarrow \sigma_i^2 > \sigma_j^2$.

The σ_i^2 's are termed the "second-order modes" of (3). It has been shown⁴ that any model of this form (3) can be taken to internally balanced form using similarity transformations.

Next consider the balanced model partitioned as:

$$\begin{bmatrix} \dot{x}_1 \\ \dot{x}_2 \end{bmatrix} = \begin{bmatrix} A_{11} & A_{12} \\ A_{21} & A_{22} \end{bmatrix} \begin{bmatrix} x_1 \\ x_2 \end{bmatrix} + \begin{bmatrix} B_1 \\ B_2 \end{bmatrix} u$$

$$y = [C_1 \quad C_2] x$$

$$\Sigma^2 = \begin{bmatrix} \Sigma_1^2 & 0 \\ 0 & \Sigma_2^2 \end{bmatrix}$$

with $\Sigma_1^2 = \text{diag} \{ \sigma_1^2, \dots, \sigma_k^2 \}$ and $\Sigma_2^2 = \{ \sigma_{k+1}^2, \dots, \sigma_n^2 \}$. The essence of balanced model reduction^{4,6} is that if $\sigma_k^2 \gg \sigma_{k+1}^2$, then the input affects x_2 much less than it affects x_1 , and the output is affected by x_2 much less than by x_1 .

The internally balanced coordinate representation has a number of desirable properties with respect to model reduction. It is unique (to within a sign change on the basis vectors) provided the σ_i^2 's are distinct. The σ_i^2 's are similarity invariants of (A,B,C). Most remarkably, any arbitrary subsystem is

guaranteed to be asymptotically stable (subject to an additional restriction on the basis vectors in the nondistinct case⁶).

Application of balanced reduction to very large models is no easy task. Indeed, "transformation methods" are generally undesirable for large structural models because of computational problems and loss of a physically meaningful state vector. In the following it is shown that the balanced coordinates are a special case of modal coordinates, and thus that no explicit change of basis is necessary, provided the damping is very small and the frequencies are sufficiently distinct.

Application to Lightly-Damped Structural Models

Consider the state-space representation of a structural dynamics model in modal form:

$$\left. \begin{aligned} \begin{bmatrix} \ddot{\eta}_i \\ \dot{\eta}_i \end{bmatrix} &= \begin{bmatrix} -2\zeta_i \omega_i & -\omega_i^2 \\ 1 & 0 \end{bmatrix} \begin{bmatrix} \dot{\eta}_i \\ \eta_i \end{bmatrix} + \begin{bmatrix} b_i \\ 0 \end{bmatrix} u \quad ; \quad i=1, \dots, n \\ \\ y &= \sum_{i=1}^n [c_{1i} \quad c_{2i}] \begin{bmatrix} \dot{\eta}_i \\ \eta_i \end{bmatrix} \end{aligned} \right\} \quad (6)$$

Theorem: For any modal subsystem of (6), the transformation

$$\begin{bmatrix} \dot{\eta}_i \\ \eta_i \end{bmatrix} = \left\{ \frac{b_i b_i^T}{4\zeta_i \omega_i} \right\}^{1/2} \begin{bmatrix} 1 & 0 \\ 0 & \omega_i^{-1} \end{bmatrix} V_i \begin{bmatrix} \sigma_{1i}^{-1} & 0 \\ 0 & \sigma_{2i}^{-1} \end{bmatrix} q_i$$

where

$$\sigma_{1i}^2 \triangleq \left\{ \frac{(b_i b_i^T)^{1/2}}{4\zeta_i \omega_i} \right\} \left[c_{1i}^T c_{1i} + \omega_i^{-2} c_{2i}^T c_{2i} [1 - 2\zeta_i \gamma_i + 2\zeta_i (1 + \gamma_i^2)^{1/2}] \right]^{1/2}$$

$$\sigma_{2i}^2 \triangleq \left\{ \frac{(b_i b_i^T)^{1/2}}{4\zeta_i \omega_i} \right\} \left[c_{1i}^T c_{1i} + \omega_i^{-2} c_{2i}^T c_{2i} [1 - 2\zeta_i \gamma_i - 2\zeta_i (1 + \gamma_i^2)^{1/2}] \right]^{1/2}$$

$$V_i \triangleq \begin{bmatrix} v_{1i} & -v_{2i} \\ v_{2i} & v_{1i} \end{bmatrix} \quad , \quad \begin{aligned} v_{1i} &\triangleq [(1+v_i)/2]^{1/2} \\ v_{2i} &\triangleq [(1-v_i)/2]^{1/2} \end{aligned}$$

$$v_i \triangleq \text{sgn}(\gamma_i) [1 + \gamma_i^{-2}]^{-1/2} \quad \gamma_i \triangleq \omega_i c_{2i}^T c_{1i} / (c_{2i}^T c_{2i}) - \zeta_i$$

produces the following internally balanced modal subsystem:

$$\dot{q}_i = \omega_i \begin{bmatrix} -2\zeta_i v_{1i}^2 & -(1 - 2\zeta_i v_{1i} v_{2i}) (\sigma_{1i} / \sigma_{2i}) \\ (1 + 2\zeta_i v_{1i} v_{2i}) (\sigma_{2i} / \sigma_{1i}) & -2\zeta_i v_{2i}^2 \end{bmatrix} q_i$$

$$+ \left\{ \frac{4\zeta_i \omega_i}{b_i b_i^T} \right\}^{1/2} \begin{bmatrix} \sigma_{1i} v_{1i} b_i \\ -\sigma_{2i} v_{2i} b_i \end{bmatrix} u$$

$$y_i = \begin{pmatrix} b_i b_i^T \\ 4\zeta_i \omega_i \end{pmatrix}^{1/2} \begin{bmatrix} \sigma_{1i}^{-1} [c_{1i} v_{1i} + \omega_i^{-1} c_{2i} v_{2i}]^T \\ \sigma_{2i}^{-1} [-c_{1i} v_{2i} + \omega_i^{-1} c_{2i} v_{1i}]^T \end{bmatrix}^T q_i$$

$$\Sigma_i^2 = \begin{bmatrix} \sigma_{1i}^2 & 0 \\ 0 & \sigma_{2i}^2 \end{bmatrix}$$

Proof: The proof follows from direct substitution of Σ_i^2 into (4) and (5).

Noting that $\sigma_{1i}^2 \approx \sigma_{2i}^2$ when $\zeta_i \ll 1$, define the block-diagonal transformation:

$$\begin{bmatrix} \tilde{\eta}_i \\ \eta_i \end{bmatrix} = \begin{bmatrix} \alpha_i & 0 \\ 0 & \alpha_i / \omega_i \end{bmatrix} V_i q_i \quad (7)$$

where

$$\alpha_i \triangleq \left[b_i b_i^T / (c_{1i}^T c_{1i} + \omega_i^{-2} c_{2i}^T c_{2i}) \right]^{1/4} \quad (8)$$

and V_i , v_i , and γ_i are as defined above. Applying (7) to (6), the following model is obtained:

$$\dot{q}_i = \tilde{A}_i q_i + \tilde{B}_i u, \quad i=1, \dots, n \quad ; \quad y = \sum_{i=1}^n \tilde{C}_i q_i \quad (9)$$

where

$$\tilde{A}_i = \omega_i \begin{bmatrix} -2\zeta_i v_{1i}^2 & -(1-2\zeta_i v_{1i} v_{2i}) \\ (1+2\zeta_i v_{1i} v_{2i}) & -2\zeta_i v_{2i}^2 \end{bmatrix} ; \quad \tilde{B}_i = \alpha_i^{-1} \begin{bmatrix} v_{1i} b_i \\ -v_{2i} b_i \end{bmatrix}$$

$$\tilde{C}_i = \alpha_i \begin{bmatrix} (c_{1i} v_{1i} + \omega_i^{-1} c_{2i} v_{2i}) & (-c_{1i} v_{2i} + \omega_i^{-1} c_{2i} v_{1i}) \end{bmatrix}$$

Main Result

(i) If $\zeta_i \ll 1$, $i = 1, \dots, n$, then each modal subsystem of (9) is approximately internally balanced with

$$\Sigma_i^2 \approx \tilde{\Sigma}_i^2 = \sigma_i^2 I$$

$$\sigma_i^2 = (4\zeta_i \omega_i)^{-1} \left[b_i b_i^T (c_{1i}^T c_{1i} + \omega_i^{-2} c_{2i}^T c_{2i}) \right]^{1/2} \quad (10)$$

(ii) If $\max(\zeta_i, \zeta_j) \max(\omega_i, \omega_j) / |\omega_i - \omega_j| \ll 1$, $i \neq j$, then the entire model (9) is approximately internally balanced with

$$\Sigma^2 \approx \tilde{\Sigma}^2 = \begin{bmatrix} \sigma_1^2 I & & 0 \\ & \ddots & \\ 0 & & \sigma_n^2 I \end{bmatrix} \quad (11)$$

Proof

(i) The error in the balancing approximation for each modal subsystem is:

$$\frac{\left\| \begin{array}{c} \Sigma_i^2 - \tilde{\Sigma}_i^2 \\ \tilde{\Sigma}_i^2 \end{array} \right\|}{\left\| \tilde{\Sigma}_i^2 \right\|} = \left\| \left[\begin{array}{cc} \sigma_{1i}^2 - \sigma_i^2 & 0 \\ 0 & \sigma_{2i}^2 - \sigma_i^2 \end{array} \right] \right\| / \sigma_i^2$$

$$\leq \left| 1 - \left[1 - \frac{2\zeta_i c_{2i}^T c_{2i} [\gamma_i + (1+\gamma_i^2)^{1/2}]}{\omega_i^2 c_{1i}^T c_{1i} + c_{2i}^T c_{2i}} \right]^{1/2} \right|$$

$$\leq \left| 1 - \left[1 - \frac{2 \zeta_i [|\gamma_i| + (1+\gamma_i^2)^{1/2}]}{1 + (|\gamma_i| + \zeta_i)^2} \right]^{1/2} \right|$$

$$\leq 1 - (1 - 3\zeta_i)^{1/2} \quad \text{provided } \zeta_i < 1/3$$

(ii) Consider any two-mode subsystem of the transformed model. The controllability gramian for this subsystem is approximated by:

$$W_{c_{ij}} = \begin{bmatrix} \tilde{\Sigma}_i^2 & P_{ji}^T \\ P_{ji} & \tilde{\Sigma}_j^2 \end{bmatrix}$$

where P_{ji} satisfies

$$\tilde{A}_j P_{ji} + P_{ji} \tilde{A}_i^T + \tilde{B}_j \tilde{B}_i^T = 0$$

Solving for P_{ji} and taking the L_2 -norm leads to

$$\| P_{ji} \| \leq 2\sigma_j \sigma_i (1/\rho_1 + 1/\rho_2) \left[\zeta_j \omega_j \zeta_i \omega_i / ((1-\zeta_j)(1-\zeta_i)) \right]^{1/2}$$

$$\rho_1, \rho_2 = \left[\omega_j^2 + \omega_i^2 + 2\zeta_j \omega_j \zeta_i \omega_i \pm 2\omega_j \omega_i ((1-\zeta_j^2)(1-\zeta_i^2))^{1/2} \right]^{1/2}$$

Removing the subscripts to denote the maximum, we obtain

$$\| P_{ji} \| / \sigma^2 \leq 2\zeta(\omega/\Delta\omega + 1) / (1-\zeta) \approx 2(\zeta\omega/\Delta\omega + \zeta) \text{ if } \zeta \ll 1$$

from which it follows that

$$\frac{\| \| W_{c_{ij}} - \tilde{\Sigma}_{ij}^2 \| \|}{\| \| \tilde{\Sigma}_{ij}^2 \| \|} = \frac{\| P_{ji} \|}{\sigma^2} \ll 1 \text{ provided } (\zeta\omega/\Delta\omega) \ll 1$$

Similar results can be obtained for the observability gramian.

Rate Output Case

When $c_{2i} = 0$, $i=1, \dots, n$, the approximation (10) is exact and each modal subsystem of (6) is balanced regardless of its damping ratio. To illustrate the approximation error in (11), consider the two-mode subsystem obtained from (6) assuming $\zeta_1 = \zeta_2 = \zeta$ and normalizing the first frequency to unity:

$$\begin{bmatrix} \dot{q}_1 \\ \dot{q}_2 \end{bmatrix} = \begin{bmatrix} -2\zeta & -1 & 0 & 0 \\ 1 & 0 & 0 & 0 \\ 0 & 0 & -2\zeta(1+\Delta\omega/\omega) & -(1+\Delta\omega/\omega)^2 \\ 0 & 0 & 1 & 0 \end{bmatrix} \begin{bmatrix} q_1 \\ q_1 \end{bmatrix} + \begin{bmatrix} b_1 \\ 0 \\ b_2 \\ 0 \end{bmatrix} u$$

$$y_{12} = [c_{11} \quad c_{21} \quad c_{12} \quad c_{22}] \begin{bmatrix} q_1 \\ q_1 \end{bmatrix} \quad (12)$$

where $\dot{q} = dq/d\tau$ and $\tau = t\omega$. Choosing $b_1 = b_2 = c_{11} = c_{12} = 1$ the true (Σ) and approximate ($\tilde{\Sigma}$) balanced grammians are computed for several values of ζ and a range of $\Delta\omega$. The plot of approximation error in Fig. 1 shows the improvement in modal decoupling as damping ratio decreases. At $\zeta = 0.001$, for example, a 1% frequency difference results in only 5% approximation error.

Displacement Output Case

When $c_{1i} = 0, i=1, \dots, n$, the modal balancing error bound is

$$\frac{\left\| \Sigma_i^2 - \tilde{\Sigma}_i^2 \right\|}{\left\| \tilde{\Sigma}_i^2 \right\|} \leq \left| 1 - [1 - 2\zeta_i(1 + \zeta_i^2)^{1/2} - 2\zeta_i^2]^{1/2} \right| \leq \zeta_i(2 + 2\zeta_i + \zeta_i^2)$$

When $\zeta_i < .1$ this bound is comparable to that given in Ref. 8 for the SISO case:

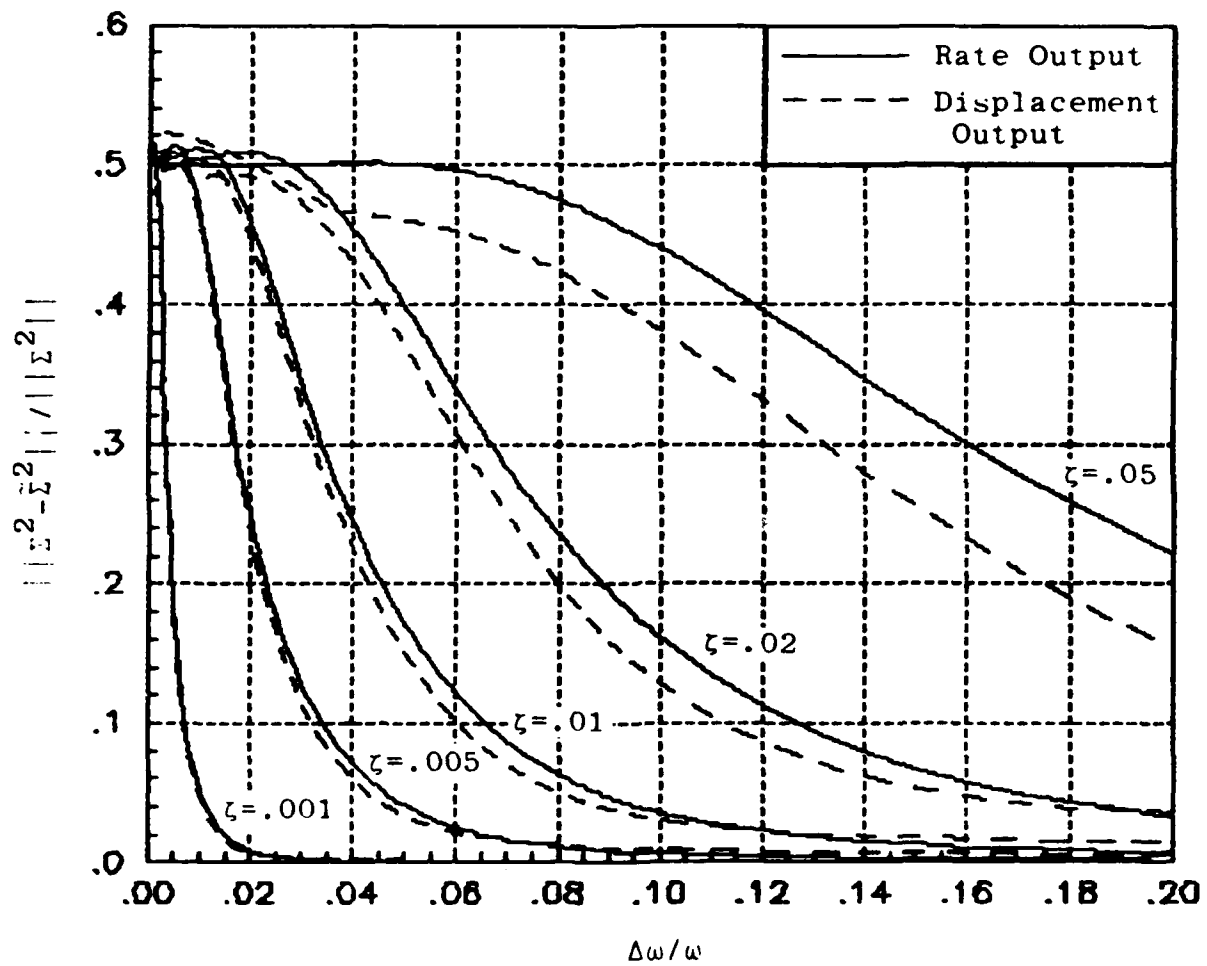


Figure 1. Approximation Error for Two-Mode Subsystem

$$4\zeta_1(1+2\zeta_1^2)^{1/2}(1+2\zeta_1)^{-1}(2+2\zeta_1^2)^{-1/2}$$

Choosing $b_1 = b_2 = c_{21} = c_{22}$ in (12), the displacement output balancing error is computed and plotted in Fig. 1.

IV. Mode Selection Methodology

The approximate modal balancing result enables quantitative modal analysis of the evaluation model with respect to physically meaningful design issues. Four modal rankings are discussed, followed by a suggested mode-selection procedure.

Disturbance to Regulated Variables: Σ_{DC}^2

The $\{\sigma_{DC_i}^2\}$ give a modal ranking in terms of open-loop performance. Large values indicate high disturbance propagation to the output, while small values imply low open-loop performance contribution. If the goal were simply to match open-loop performance, mode selection would be based on these rankings. Observe that the $\{\sigma_{DC_i}^2\}$ are equal to the balanced steady-state covariance when the model is forced with unit-intensity white noise. An interesting relationship exists between the $\{\sigma_{DC_i}^2\}$ and the modal costs ³ of the model (2). Assuming a zero-mean unit-intensity white noise disturbance and light damping, the open-loop modal costs are approximated by

$$\mu_i = (4\zeta_i \omega_i^3)^{-1} [d_i d_i^T (\omega_i^2 c_{1i}^T c_{1i} + c_{2i}^T c_{2i})]$$

Using (10), the following relationship is obtained:

$$\mu_i = 4\zeta_i \omega_i \sigma_i^4$$

Thus, modal-cost and internal-balancing criteria can differ. For example, if two modes have $\sigma_i = \sigma_j$ and $\omega_i > \omega_j$, then modal-cost favors the higher frequency while balancing ranks them equally.

Actuators to Regulated Variables: Σ_{BC}^2

These rankings show modal controllability of the performance. A small value of $\sigma_{BC_i}^2$ indicates that the given actuator configuration has little direct effect upon the contribution of mode i to the performance, regardless of its open-loop performance contribution. In particular, if $\sigma_{BC_i}^2 / \|\Sigma_{BC}^2\|$ is small and $\sigma_{DC_i}^2 / \|\Sigma_{DC}^2\|$ is large, a redesign of the actuator configuration is suggested.

Disturbances to Sensors: Σ_{DM}^2

The $\{\sigma_{DM_i}^2\}$ show modal observability of the disturbance in the sensors. A mode having a small relative $\sigma_{DM_i}^2$ may be impossible to estimate on-line. If the corresponding $\sigma_{DC_i}^2$ is large, the selection of sensor locations or types is inappropriate.

Actuators to Sensors: Σ_{BM}^2

The $\{\sigma_{BM_i}^2\}$ provide a modal analysis of potential controller authority for the given the actuator and sensor configuration.

Ideally the modes with large $\sigma_{BM_i}^2$ should align with those having large $\sigma_{DC_i}^2$ so that controller authority matches the performance objective. A Mode with large $\sigma_{BM_i}^2$ should be included in the design model even if $\sigma_{DC_i}^2$ is low, particularly if it is in the controller bandwidth, to prevent spillover problems.

Mode-Selection Procedure

Using the four modal rankings, the mode-selection process is performed as follows:

1. Select the modes having the largest $\sigma_{DC_i}^2$. These modes contribute most to the performance objectives, and assuming reasonable actuator and sensor placements, it should be possible to control each of the modes to some extent.
2. Examine the $\{\sigma_{BM_i}^2\}$. Include in the design model any highly controllable/measurable modes not selected in (1), especially if they are close in frequency to selected modes. Omission of these modes can cause spillover, which can destabilize the system.
3. Examine the $\{\sigma_{DM_i}^2\}$ and the $\{\sigma_{BC_i}^2\}$. Unselected modes having large values in either of these rankings indicate actuator/sensor configuration pathologies. A large $\sigma_{DM_i}^2$ indicates an unmodeled mode in the measurements, which will inhibit state estimation. An unmodeled mode with

large $\sigma_{BC_i}^2$ may be driven unpredictably by the controller to the detriment of performance. In either case, the modes should be included.

V. A Design Example

This application is performed on the Charles Stark Draper Laboratory model #2 (revision #3)⁹ which has 54 flexible modes, each with 0.2% open-loop damping. Six disturbance inputs are modeled as independent colored-noise sources, each having a 15 Hz. rolloff and a mean-squared value of $600\pi N^2$. There are nine collocated force-actuator/rate-sensor pairs and an additional measurement of line-of-sight (LOS) pointing error. Open-loop modal frequencies are given in Table 1. The linear evaluation model has 114 states (108 structural and 6 disturbance).

This example follows the two-level "high-authority/low-authority" control design approach described in Ref. 10. The balanced mode-selection methodology is applied for control of LOS pointing performance (HAC), and "low-authority control" (LAC)¹¹ using collocated actuators and rate-sensors is appended to the control law to prevent high-frequency "spillover"¹².

Modal Analysis

Using the approximate internal balancing relation (10), the following modal rankings are obtained:

● Disturbances - LOS

● Actuators - LOS

Table 1 Open-loop evaluation model frequencies

Mode Frequency		Mode Frequency		Mode Frequency	
No.	(Hz)	No.	(Hz)	No.	(Hz)
1	0.1131	19	2.2499	37	11.6523
2	0.1469	20	2.2541	38	11.6606
3	0.1490	21	3.4335	39	11.7353
4	0.1741	22	3.4522	40	13.3386
5	0.4549	23	3.9571	41	14.0969
6	0.5568	24	3.9861	42	14.8900
7	0.5953	25	4.0513	43	16.5092
8	0.6131	26	4.3367	44	17.1423
9	0.6351	27	6.5503	45	17.5072
10	0.6403	28	8.0570	46	17.7673
11	0.8151	29	8.4335	47	17.7682
12	0.8160	30	8.8400	48	17.7686
13	0.8235	31	8.9907	49	17.7767
14	0.9152	32	10.2474	50	21.0746
15	0.9703	33	10.5133	51	21.6642
16	1.1582	34	11.4797	52	22.0228
17	1.5508	35	11.6510	53	23.4744
18	1.7728	36	11.6522	54	23.8904

● Actuators - Rate Sensors

Absolute values of the open-loop modal costs³ are computed for comparison using the colored-noise disturbance. The RMS second-order modes and modal costs are plotted versus mode number in Fig. 2. Immediately evident is the clustering of these modal phenomena. The disturbance effect as seen through the line-of-sight is constrained to clusters of modes as is the ability to measure and control the model. Alignment of the "controllable clusters" and "disturbable clusters" indicates a favorable actuator/sensor configuration for the problem. Table 2 gives the quantitative modal ranking prescribed by each method.

Control Designs

Three controllers are designed and analyzed for the model. The first uses 10 low-frequency modes from the model and relatively low gains, i.e., a cautious design. Based upon closed-loop analysis of this controller and re-evaluation of Fig. 2, a second controller is designed. The bandwidth of this controller is allowed to expand into an adjacent "dead zone" of the model under the assumption that insensitive modes cannot cause spillover. A low authority control¹¹ is designed and added to the high-gain controller to give the third design. Full closed-loop modal and stochastic analyses are presented.

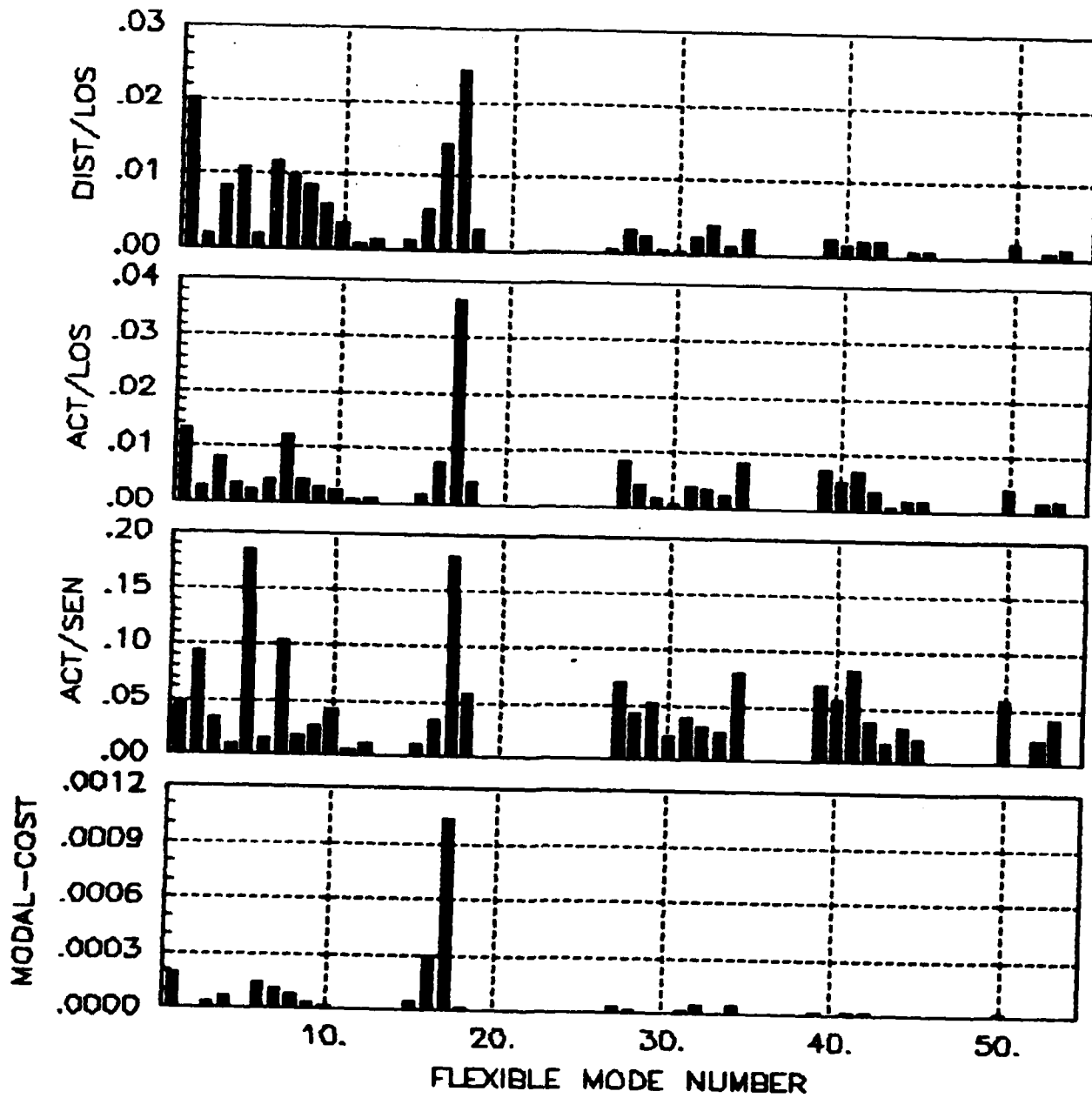


Figure 2. Open-Loop Modal Analysis

Cautious Controller

Mode Selection

Using the modal analyses of Fig. 2, modes 1, 3, 4, 6, 7, 8, 9, 15, 16 and 17 are selected. These are the first ten most disturbable modes with respect to LOS. Inspection of the second column of Table 2 shows that several controllable modes in the design model bandwidth have been omitted, and it is reasonable to expect that any undesirable in-band controller effects will be related to these modes.

Control Design

The ten selected modes and six disturbance states transform to a 26th order linear design model. Using standard LQG techniques, a state-feedback control is found which minimizes

$$J = \lim_{t \rightarrow \infty} E\{z_R^T z_R + b u_R^T u_R\} \quad (13)$$

where z_R is the LOS output of the reduced model and b is a tuning parameter. A reasonable closed-loop design spectrum, shown in Table 3, is obtained using $b = 10^{-11}$. The significant effect of this control is on modes 7 and 17. Mode 7 damping increases by nearly a factor of 30, but its frequency increases by less than one percent. Mode 17 experiences a damping increase of a factor of 200 and a frequency increase of 21%, placing it between the frequencies of unmodeled modes 18 and 19. Referring again to

Table 2 Modal rankings suggested by the analysis

DIST/LOS		ACT/LOS		ACT/SEN		MODAL COST	
Mode	σ_i	Mode	σ_i	Mode	σ_i	Mode	$\mu_i^{1/2}$
17	0.0242	17	0.0366	5	0.1836	17	0.0010
1	0.0202	1	0.0130	17	0.1813	16	0.0003
16	0.0141	7	0.0119	7	0.1037	1	0.0002
6	0.0116	34	0.0081	2	0.0941	6	0.0001
4	0.0110	27	0.0080	41	0.0831	7	0.0001
7	0.0099	3	0.0078	34	0.0786	8	0.0001
8	0.0085	16	0.0074	27	0.0702	4	0.0001
3	0.0084	39	0.0072	39	0.0700	32	0.0001
9	0.0059	41	0.0066	18	0.0582	15	0.0000
15	0.0056	40	0.0051	50	0.0570	34	0.0000
32	0.0038	6	0.0042	40	0.0564	9	0.0000
34	0.0034	28	0.0042	29	0.0510	3	0.0000
10	0.0033	50	0.0041	1	0.0466	27	0.0000
27	0.0032	18	0.0039	28	0.0426	39	0.0000
18	0.0028	8	0.0038	10	0.0417	31	0.0000
31	0.0025	31	0.0038	53	0.0401	28	0.0000
39	0.0024	32	0.0034	31	0.0379	42	0.0000
28	0.0024	42	0.0034	42	0.0367	41	0.0000

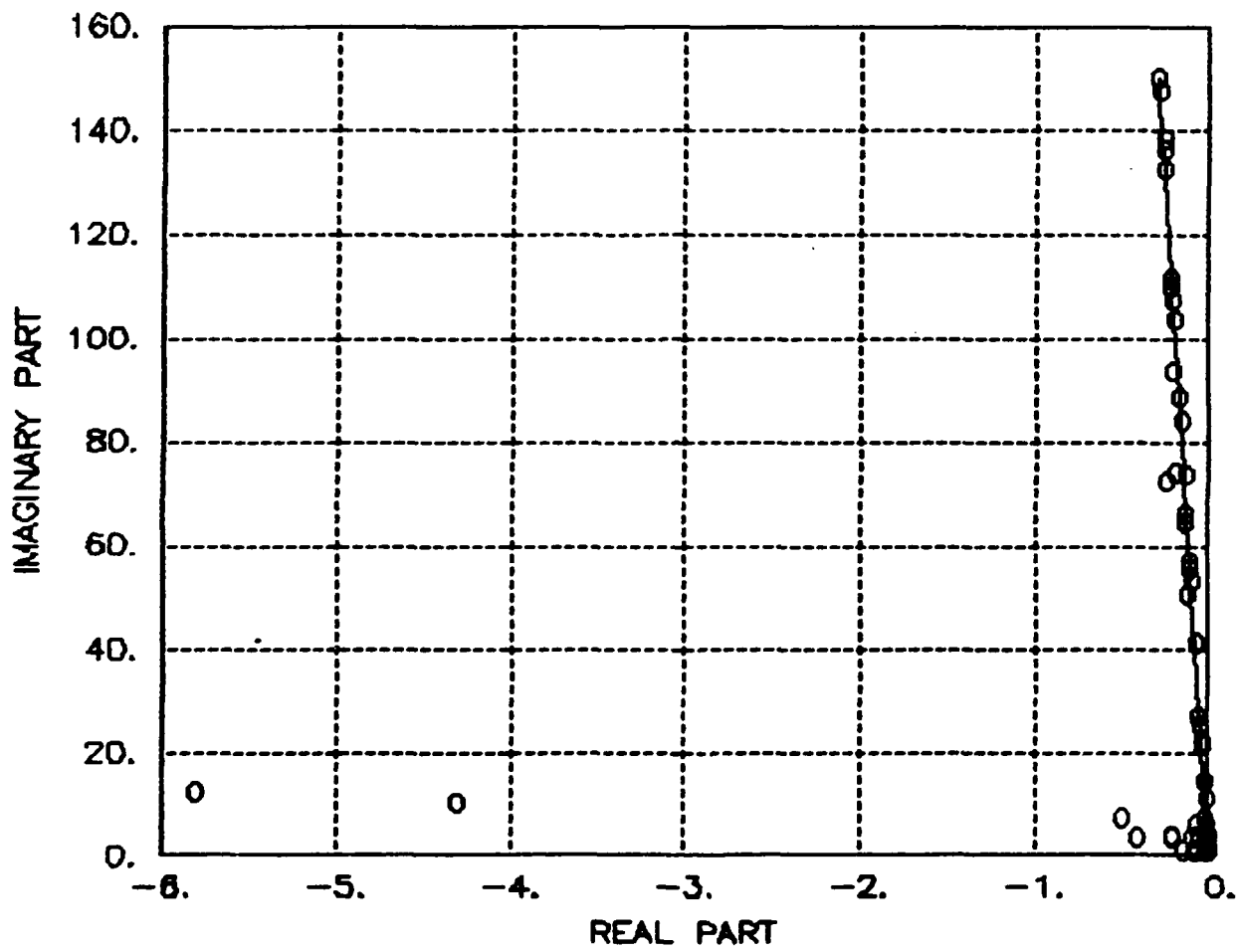


Figure 3. Closed-Loop Spectrum with 10-Mode Controller

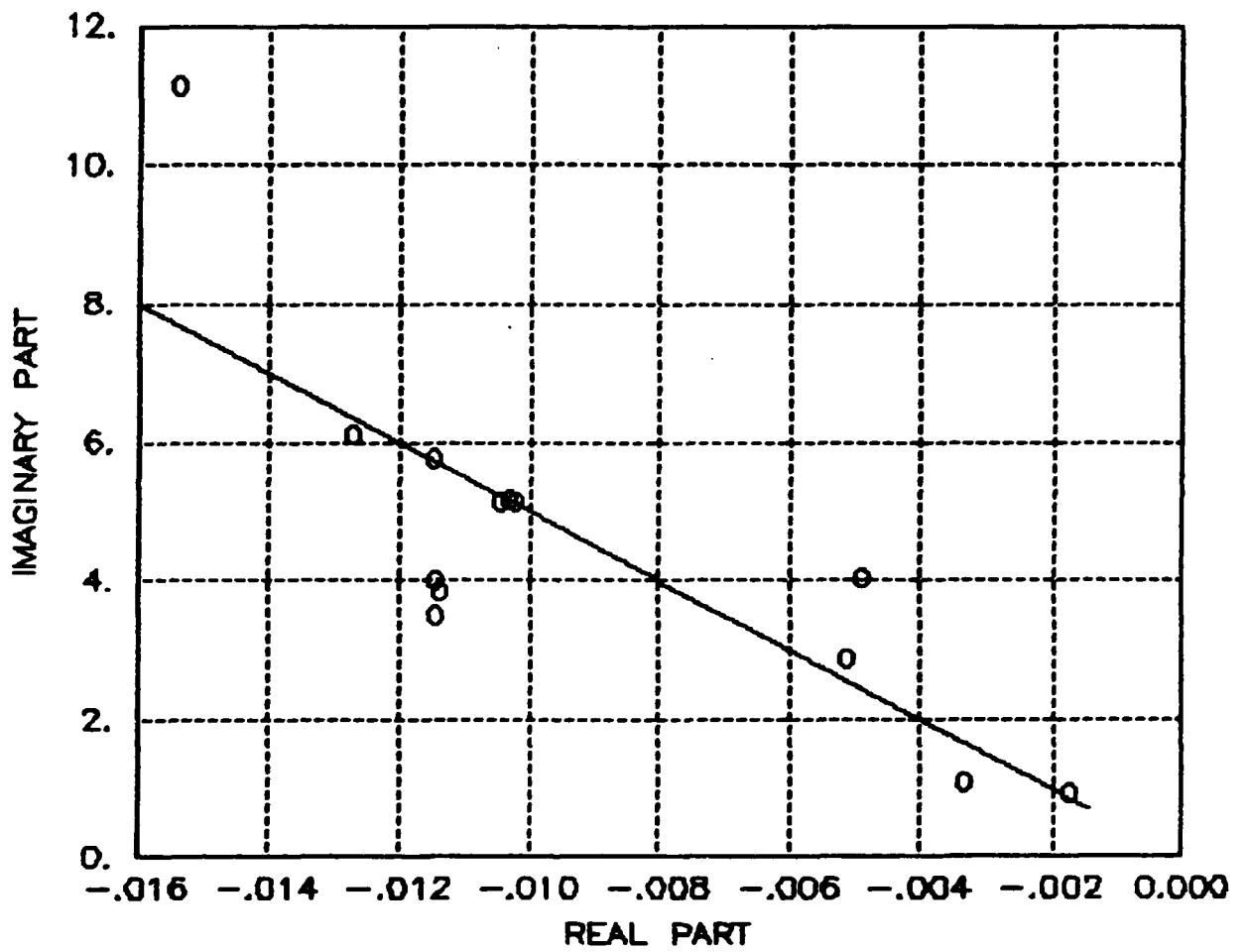


Figure 4. Closed-Loop Spectrum with 10-Mode Controller
(Expanded Scale)

Table 3 Closed-loop control spectrum of 10-mode model

Real part	Imaginary part	Frequency (Hz)	Damping ratio
-4.8001	10.8240	1.8845	.4054
-0.0270	7.3328	1.1671	.0037
-0.0127	6.0956	0.9701	.0021
-0.0115	3.9841	0.6341	.0029
-0.0114	3.8621	0.6147	.0030
-0.2178	3.7528	0.5983	.0579
-0.0114	3.4864	0.5549	.0033
-0.0033	1.0962	0.1745	.0030
-0.0222	0.9388	0.1495	.0237
-0.0203	0.7341	0.1169	.0276

Table 4 Closed-loop filter spectrum of 10-mode model

Real part	Imaginary part	Frequency (Hz)	Damping ratio
-5.5453	11.2239	1.9925	.4430
-0.5170	7.3093	1.1662	.0706
-0.0829	6.0898	0.9693	.0136
-0.0654	3.9831	0.6340	.0164
-0.2152	3.9445	0.6287	.0545
-0.4231	3.6162	0.5795	.1162
-0.0944	3.6258	0.5773	.0260
-0.0877	1.0982	0.1753	.0796
-0.0699	0.9299	0.1484	.0750
-0.1559	0.7796	0.1265	.1961

Fig. 2, modes 19, 20 and 21 are apparently uncontrollable with respect to both line-of-sight and sensor placement. Mode 18, however, has some controllability (it ranks 15th out of 54). The control bandwidth is therefore likely to influence mode 18.

A standard Kalman filter is found for the design model using the actual disturbance PSD and LOS "measurement noise" of intensity 5×10^{-10} , which gives a filter bandwidth roughly equivalent to the control bandwidth. The filter spectrum is shown in Table 4. Here also, the frequency increase in mode 17 is sufficient to encompass unmodeled mode 18.

Evaluation

The 10-mode controller is implemented with the full 114th order model. Fig. 3 shows that the closed-loop spectrum is stable, and also that the dominant control effects are limited to a few poles. The expanded scale in Fig. 4 shows the anticipated spillover in mode 18. Notice also the decreased damping in unmodeled modes 2, 5, and 10, which are well within the controller bandwidth. This "in-band spillover" occurs despite the relatively low controller authority over these three modes (see Fig. 2).

The stochastic performance with this controller is shown in Table 5. Using a total RSS control effort of 12.2N, the RSS LOS error is reduced to 16% of its open-loop value. Fig. 5 shows the absolute RMS modal costs with and without this controller. Significant cost-level reductions occur in modes 17, 16 and 1, which are the largest open-loop contributors. Notice that the

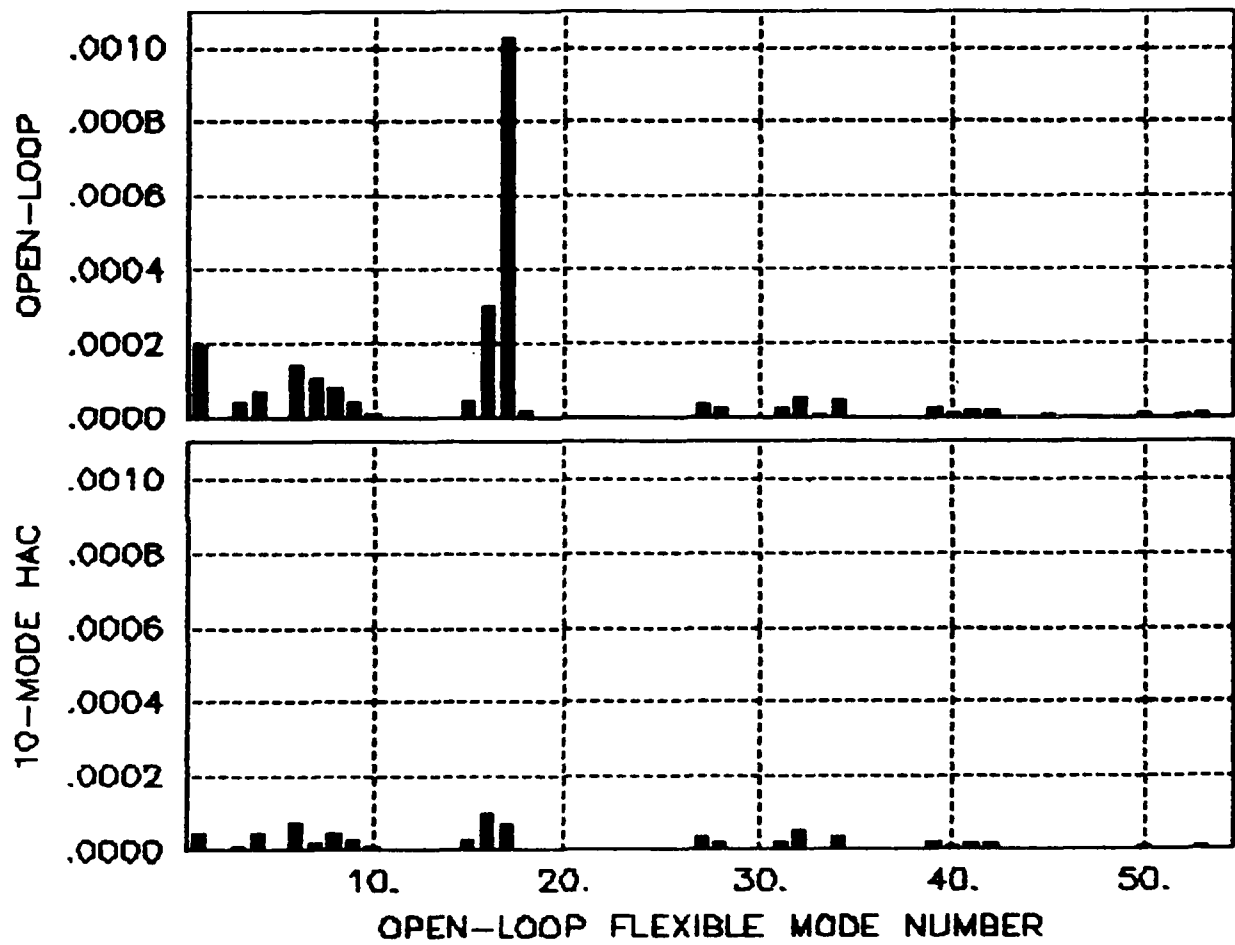


Figure 5. Closed-Loop Modal Costs for 10-Mode Controller

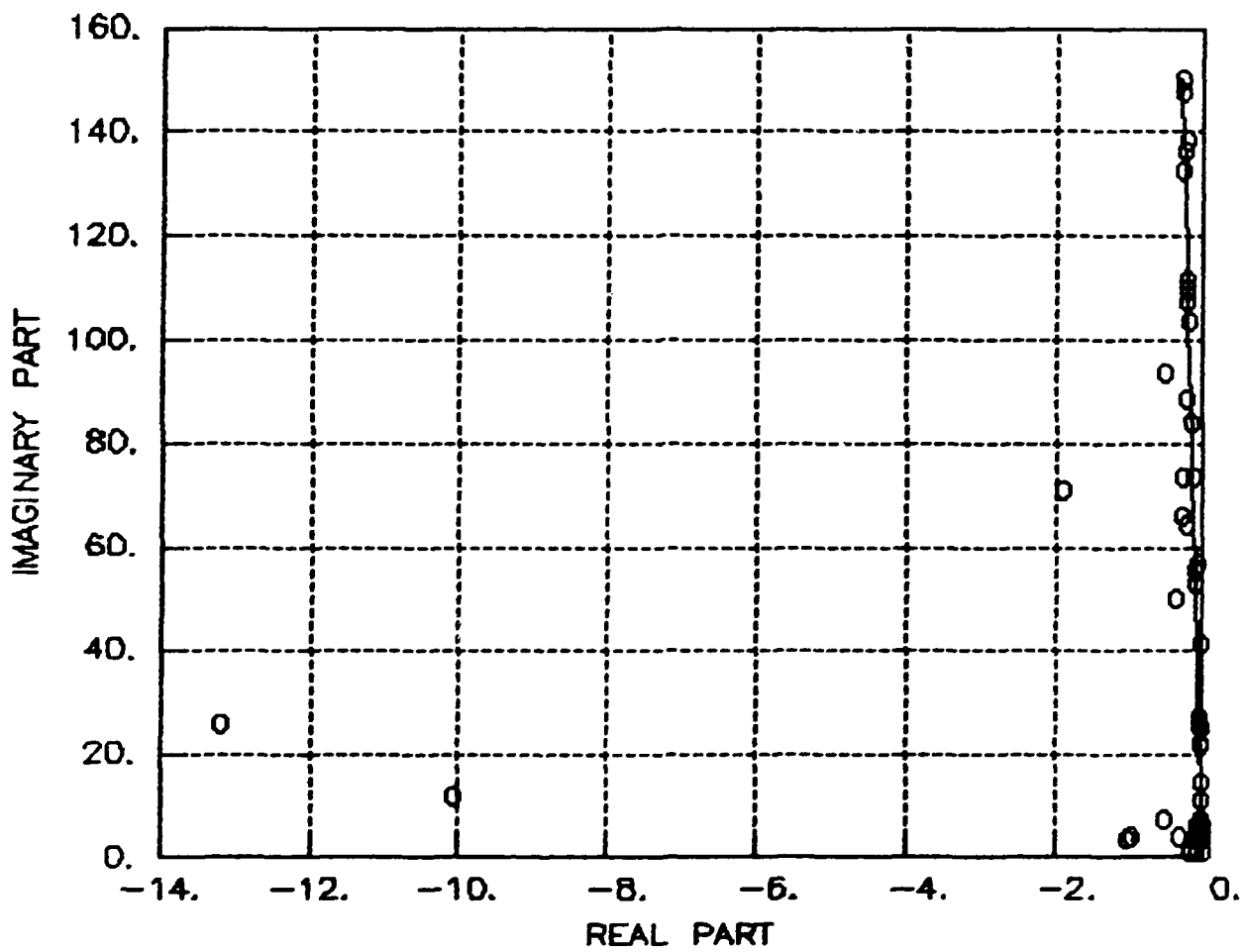


Figure 6. Closed-Loop Spectrum with 14-Mode Controller

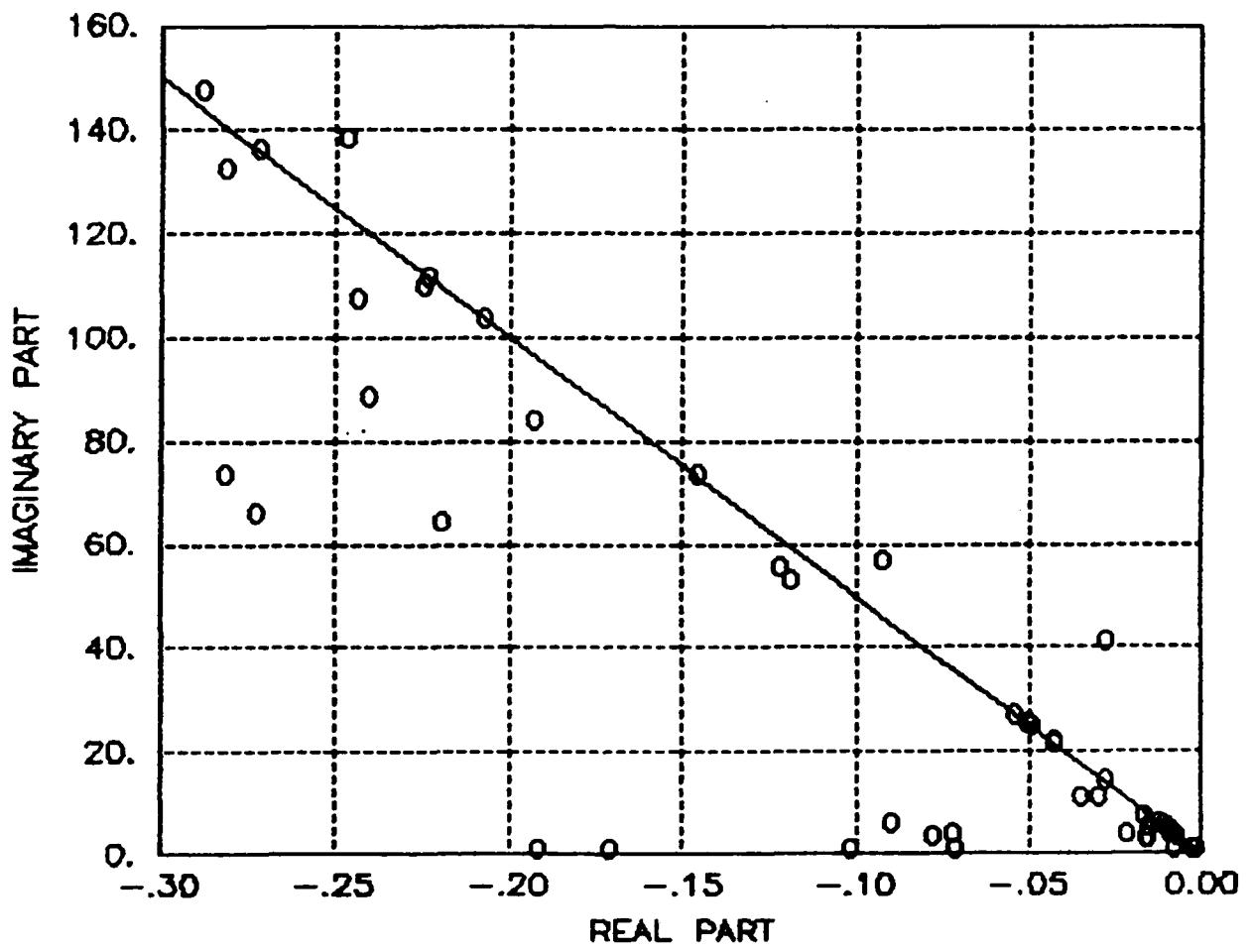


Figure 7. Closed-Loop Spectrum with 14-Mode Controller (Expanded Scale)

cost contributions of "spillover modes" 2, 5, 10, and 18 do not increase.

High-Gain Controller

Mode Selection

To account for the observed spillover effects and improve closed-loop performance, modes 2, 5 and 10, and high frequency mode 18 are added to the control design model. The fact that modes 19 through 26 are highly insensitive to control and disturbance inputs (see Fig. 2) is used to justify a closed-loop controller bandwidth extending into this dead zone.

Control Design

As before, a standard linear LOS regulator and Kalman filter is designed. For a control penalty of $5 \times 10^{-12} I$ and "measurement noise" of $5 \times 10^{-11} I$, the controller has bandwidth to 3.5 Hz which is well into the dead zone.

Evaluation

The closed-loop spectrum resulting from the high-gain control is shown in Fig. 6. As before, the dominant control effects are limited to a few modes. The expanded scale in Fig. 7 shows that the inclusion of modes 2, 5, and 10 in the design model eliminates

their in-band spillover. The expected high-frequency spillover is present; particularly in mode 27, which is the closest unmodeled mode to the controller bandwidth having significant controllability (see Fig. 2). Notice that as expected no problems occur in the dead zone modes. Higher frequency spillover effects are evident in modes 53, 52 and 31, which are well above the bandwidth of model certainty and cannot be handled explicitly. Fig. 8 shows the modal-costs of the 14-mode control compared with the 10-mode control. Notice the overall improvement in performance, with the exception of a spillover-induced cost increase in mode 27. The total RSS LOS error with this controller is 1% of the open-loop value (see Table 5).

High-Gain Controller with Low-Authority Control

The purpose of low-authority control (LAC) is to add damping to structural modes in the high-frequency uncertainty region. This method is described fully in Ref. 11. The actuator to rate sensor rankings in Fig. 2 indicate potential LAC modal authority. For this example, an LAC is designed to add 4 percent damping to the structural modes.

Evaluation

Fig. 9 shows the characteristic damping increase in the closed-loop spectrum. The expanded scale in Fig. 10 and the modal-costs in Fig. 8 show that all spillover effects, including

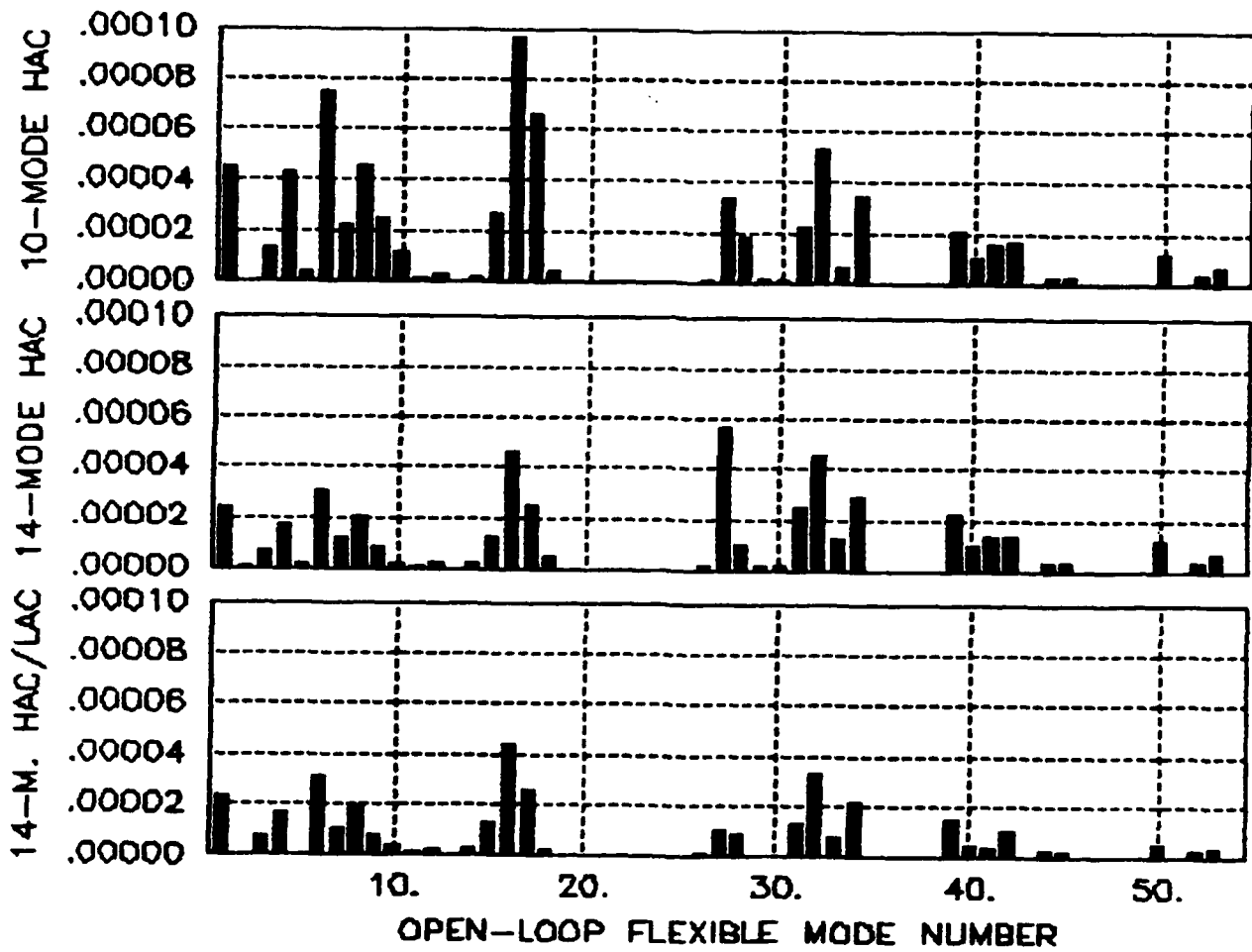


Figure 8. Closed-Loop Modal Costs for Three Controllers

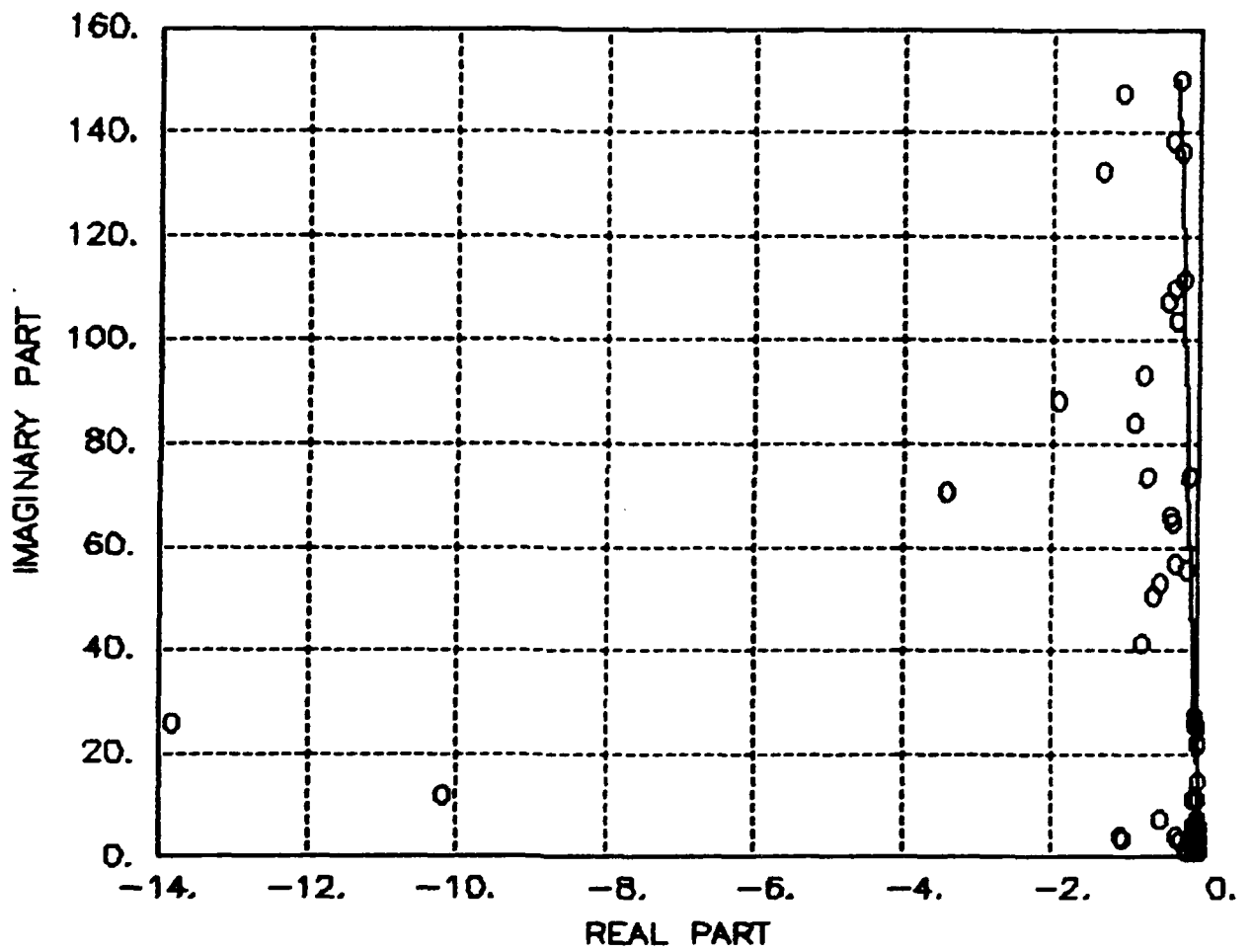


Figure 9. Closed-Loop Spectrum for 14-Mode Controller with LAC

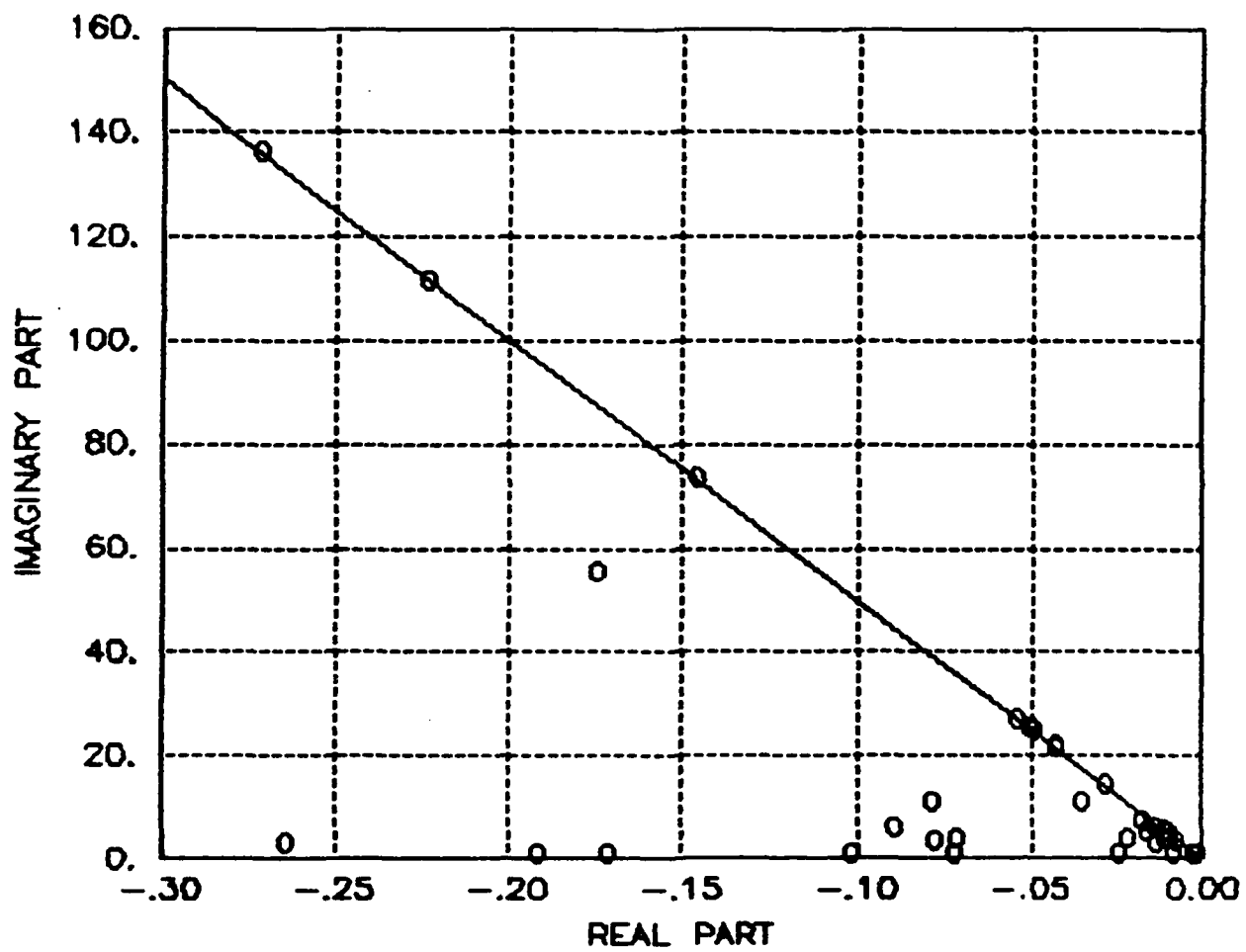


Figure 10. Closed-Loop Spectrum for 14-Mode Controller with LAC (Expanded Scale)

mode 27, are suppressed. The stochastic performance is included in Table 5.

Table 5 Stochastic performance analysis of controllers

	Open Loop	10-Mode Control	14-Mode Control	14-Mode Control with LAC
RSS LOS x (μ Rad)	131.7	62.4	69.0	26.4
RSS LOS y (μ Rad)	1109.5	175.9	87.5	75.6
Total RSS LOS(μ Rad)	1117.3	186.6	111.4	80.1
RSS Control Effort (N)	0	12.2	28.6	25.3

VI. Summary and Conclusions

An approximation to the internally-balanced coordinate representation for lightly-damped structural modes is derived. It is shown that the balancing transformation preserves the block-modal structure of the model, enabling detailed quantitative modal analyses with respect to controllability, observability, disturbability, and performance, without a change of coordinates. Using these analyses, a methodology for mode selection is proposed and successfully applied to a large spacecraft model.

Acknowledgements

The author is indebted to Prof. A. J. Laub for recognizing similarities between this work and that of Dr. E. A. Jonckheere; and to the latter for furnishing his (then unpublished) results⁸ for comparison. The helpful suggestions of Mr. M. G. Lyons, Dr. N. K. Gupta, and Dr. R. L. Kosut, as well as those of several anonymous reviewers, are greatly appreciated.

REFERENCES

1. Aoki, M., "Control of Large Scale Dynamic Systems by Aggregation," IEEE Transactions on Automatic Control, Vol. AC-13, No. 3, June 1968.
2. Skelton, R. E., and Hughes, P. C., "Modal Cost Analysis for Linear Matrix Second Order Systems," Journal of Dynamic Systems Measurement Control, Vol. 102, Sept. 1980, pp.151-163.
3. Skelton, R. E., Hughes, P. C., and Hablani, H. B., "Order Reduction for Models of Space Structures Using Modal Cost Analysis," Journal of Guidance, Control and Dynamics, Vol. 5, No. 4, July-August 1982, pp. 351-357.
4. Moore, B. C., "Principal Component Analysis of Linear Systems: Controllability, Observability and Model Reduction," IEEE Transactions on Automatic Control, Vol. AC-26, No. 1, February 1981, pp. 17-32.
5. Verriest, E. I., "On Balanced Realizations for Time Variant Linear Systems," Ph.D. dissertation, Stanford University, June 1980.
6. Jonckheere, E. A., and Silverman, L. M., "Singular Value Analysis of Deformable Systems," IEEE Conference on Decision

and Control, San Diego, Dec. 1981, pp. 660-668: see also Journal on Circuits, Systems, and Signal Processing, Special Issue on Rational Approximation for Systems, Vol. 1, No. 3-4, 1983.

7. Pernebo, L. and Silverman, L. M., "Model Reduction via Balanced State Space Representations," IEEE Transactions on Automatic Control, Vol. AC-27, No. 2, April 1982, pp. 382-387.
8. Jonckheere, E. A., "Principal Component Analysis of Flexible Systems - Open-Loop Case," to appear in International Symposium of the Mathematical Theory of Network and Systems, MTNS '83, Beer Sheva, Israel, June 1983; also submitted to IEEE Transactions on Automatic Control.
9. Henderson, T., "Active Control of Space Structures (ACOSS) Model 2," CSDL Report C-5437, September 1981.
10. Gupta, N. K., Lyons, M. G., Aubrun, J.-N., and Margulies, G., "Modeling, Control and System Identification Methods for Flexible Structures," AGARD-AG-260: Spacecraft Pointing and Position Control, Nov. 1981, paper no. 12.
11. Aubrun, J. N., "Theory of the Control of Structure by Low Authority Controllers," AIAA J, Guidance and Control, Vol. 3, No. 5, pp. 444-451, 1980.

12. Balas, M., "Modal Control of Certain Flexible Dynamic Systems," SIAM Journal of Control and Optimization, Vol. 16, 1978, pp. 450-462.

APPENDIX B

Charles Stark Draper Laboratory
Reference Data

SURVEY: TRANSLATIONAL POSITION SENSORS FOR SPACE

MODEL & MANUFACTURER	TYPE	SIZE	PERF (1-100Hz) (μ m)	COMMENT
MODIFIED BELL MODEL XI	FLEX RESTRAINT PROOF MASS	1" DIAM	0.001 (MEASURED)	
UNHOLTZ-DICKIE PA 1000 + 2216 ELECTRONICS	PIEZOELECTRIC		25	
CSDL				
SIX AXIS SPACE SENSOR	NON FLOATED, CYLINDRICAL PROOF MASS. 3 TRANS & 3 ANG. OUTPUTS	1-1 3/4 DIAM	0.0004- 0.001 (PROJECTED)	PROJECTION SUPPORTED BY TEST DATA
PENDULOUS ACCELEROMETER	FLOATED PENDULOUS DEVICE. 2 UNITS GIVE 6 AXES	1-1 3/4 DIAM	0.0004-0.0001 (PROJECTED)	

(CSDL.)

SURVEY: ANGULAR POSITION SENSORS FOR SPACE

MODEL & MANUFACTURER	TYPE	SIZE	PERF. (1-100Hz) (μ rad)	COMMENT
CSDL TAARA	FLOATED MAGNETIC SUSPENSION 3 AXIS	1-1 3/4 DIAM	0.01 (PROJECTED)	SUPPORTED BY TEST DATA
SYSTRON DONNER 8301	FLUID PROOF MASS. SINGLE AXIS	2" DIAM	1 (MEASURED) .01 (PROJECTED)	
GENERAL ELECTRIC ADA	SINGLE AXIS, WIRE SUSPEN- SION VELOCITY PICK OFF		UNKNOWN	HAS BEEN UN- WILLING TO SELL TO P&T COMPET- ITORS. DC CAL. DIFFICULT
HONEYWELL ESAA	ELECTROSTATIC			NO INFO.

(CSDL)

SURVEY: INERTIALLY STABILIZED MIRRORS

MODEL & MANUFACTURER	TYPE	PERF (1-100Hz)	COMMENT
CSDL	SOFT TRANSLATION CENTER OF PERCUSSION ACTIVE ROTATION	.01	NICE INTERFACE WITH OPTICAL SENSORS

(CSDL)

NEW TECHNOLOGY – TAARA, SASS vs. 10 PIGA TGG

- TGG, 10 PIGA CONCENTRATE ON VERY PRECISE dc PERFORMANCE IN 1 TO 20 g ENVIRONMENT WITH LARGE DYNAMIC RANGE IN DC TO 0.0003 HZ RANGE
- TAARA, SASS CONCENTRATE ON 0.1, 1 HZ AND ABOVE SIZE AND COSTS LEAD TO MULTI-AXIS APPROACH
- PRESENT TECHNOLOGY
 - PIGA USES SDM AND RESOLVER TO ACHIEVE LOW FREQUENCY ACCURACY, DYNAMIC RANGE, AND NULLING OF TORQUE SOMMING MEMBER
 - TGG USES PULSE TORQUING WITH INHERENT QUANTIZATION NOISE AT HIGH FREQUENCY
 - PERFORMANCE REQUIREMENTS RESULTED IN SINGLE AXIS INSTRUMENTS
- TAARA/SASS
 - UTILIZE ANALOG TORQUING OR PULSE INTERPOLATION TO REDUCE ac NOISE
 - LOWER DAMPING, RESTRAINTS TO INCREASE SENSITIVITY AT HIGHER FREQUENCY
 - USE LOW g TO ADVANTAGE IN ENHANCING SENSITIVITY, MULTI-AXIS DEVELOPMENT
 - CAPABLE OF 1-g TESTING FOR LOW-g UNIT

(CSDL)

THREE AXIS ANGULAR ACCELEROMETER (TAARA)

- DESCRIPTION
 - ONE Inch DIAMETER - 3 AXES OF ANGULAR RATE
 - FLOATED NON-PENDULOUS FLOAT
 - NEUTRAL BOUYANCY LEADS TO IDEAL CANDIDATE FOR 1g TESTING
 - ONE EXCELLENT AXIS 0.1 μ rad RESOLUTION IN 0.1 Hz UP BANDWIDTH CAN MEASURE DC ANGULAR ACCELERATION
 - TWO GOOD CHANNELS 1 μ rad RESOLUTION
 - 0.08 AND 0.2 μ RAD RESOLUTION IN 1 3/4 IN DIAM. UNIT
- UNIQUENESS
 - 3 AXES IN SMALL PACKAGE
 - RUGGEDNESS OF NEUTRAL BOUYANCY
 - EXCELLENT PERFORMANCE
 - MUCH LOWER COST THAN GYROS
 - CAPABLE OF EARTH FIXED ALL AXIS TESTING
- APPLICATION
 - VIBRATION SENSING IN 0.1 Hz AND ABOVE FOR SPACE AND AIRCRAFT VIBRATION CONTROL
 - APPLICABLE TO HALO, TALON GOLD, ACROSS STABILIZATION

(CSDL)

SIX AXIS SPACE SENSOR (SASS)

- DESCRIPTION
- UNFLOATED, BALANCED (NONPENDULOUS FLOAT)
- ONE INCH DIAMETER GIVES 3 ANGULAR AND 3 LINEAR POSITIONS
- ACCELERATION READING AT DC
- POSITION RESOLUTION
0.001 to 0.1 μ m (0.1 to 100 Hz)
- ANGULAR RESOLUTION
.1 to 1 μ rad
Improves on TAARA because of low damping possible
with all fills
- MAGNETIC SUSPENSIONS
 - HIGHLY EXCITED AND/OR ACTIVE SUSPENSIONS MAY PERMIT 1g TESTING
 - TWO MODE OPERATIONS TO HANDLE RIGID BODY TRANSIENTS

(CSDL)

SIX AXIS SPACE SENSOR (SASS)

- UNIQUENESS
 - 3 ROTATIONAL AND 3 TRANSLATIONAL OUTPUTS
 - SIMILAR TO CONVENTIONAL CSDL FLOATED CYROS
 - FLUID (OR GAS) DETERMINES DYNAMIC RANGE
 - LOW COST/CHANNEL
 - GOOD PERFORMANCE
- APPLICATION
 - COMPATIBLE WITH OPTICAL SENSING TECHNIQUES
 - VIBRATION SENSING OF 6 DOF - 3 LINEAR AND 3 ROTATIONAL POSITION
 - SUITABLE FOR ACROSS, POINTING AND TRACKING, AND OTHER SPACE MISSIONS
- STATUS
 - PRELIMINARY ANALYSIS AND DESIGN COMPLETE
 - FURTHER SUSPENSION TESTING REQUIRED

(CSDL)

LOW g-PIP

- DESCRIPTION
- NEUTRALLY BUOYANT PENDULOUS FLOAT ENHANCES EARTH BOUND 1g TESTING (LOW RISK)
- ONE OR TWO AXES OF LINEAR POSITION OR ACCELERATION
- ANALOG TORQUE REBALANCE
- 0.01 to 0.1 μm STABILIZATION (0.1 to 100 Hz)
- 2 UNITS GIVE 6 AXES OF INFO
- UNIQUENESS
- SIMILAR TO PRESENT PIPs
- FULLY FLOATED DESIGN ENHANCES 1g TESTING
- APPLICATION
- LINEAR POSITION AND ACCELERATION SIMILAR TO SASS

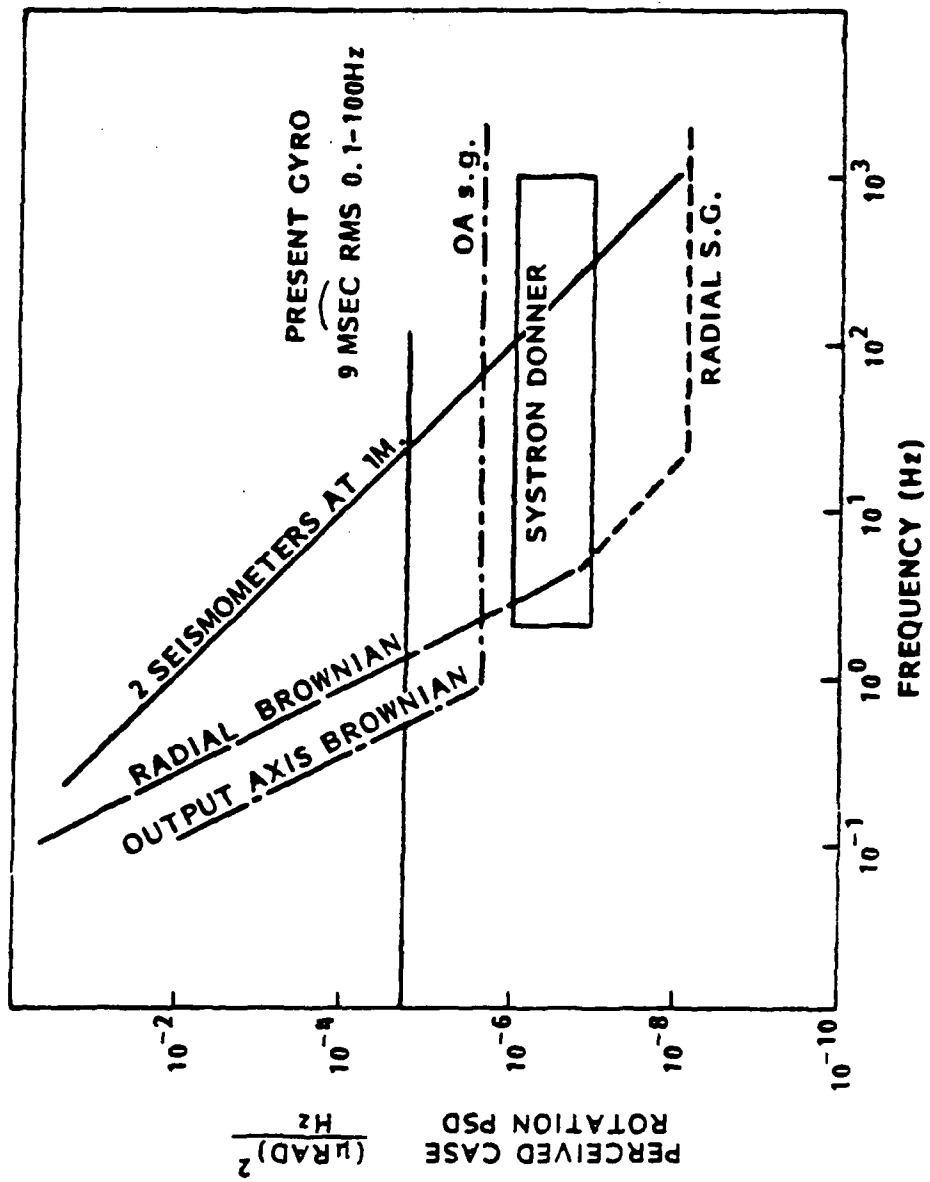
(CSDL)

DATA SUPPORTING PROJECTIONS

- S.G. DATA - MICROSYN
- 10 PIG VS EXCITATION
- TGC'S
- RADIAL SUSPENSION
- 2 DOF FLOATED GYRO
- BROWNIAN MOTION APPROACHED IN
 - CSDL GRADIOMETER
 - THIRD GENERATION GYROSCOPE (MPMJ)
- MULTI AXIS EXPERIENCE
 - FLOATED 2 DOF GYRO
 - MULTISENSOR (ACCEL. & GYRO)

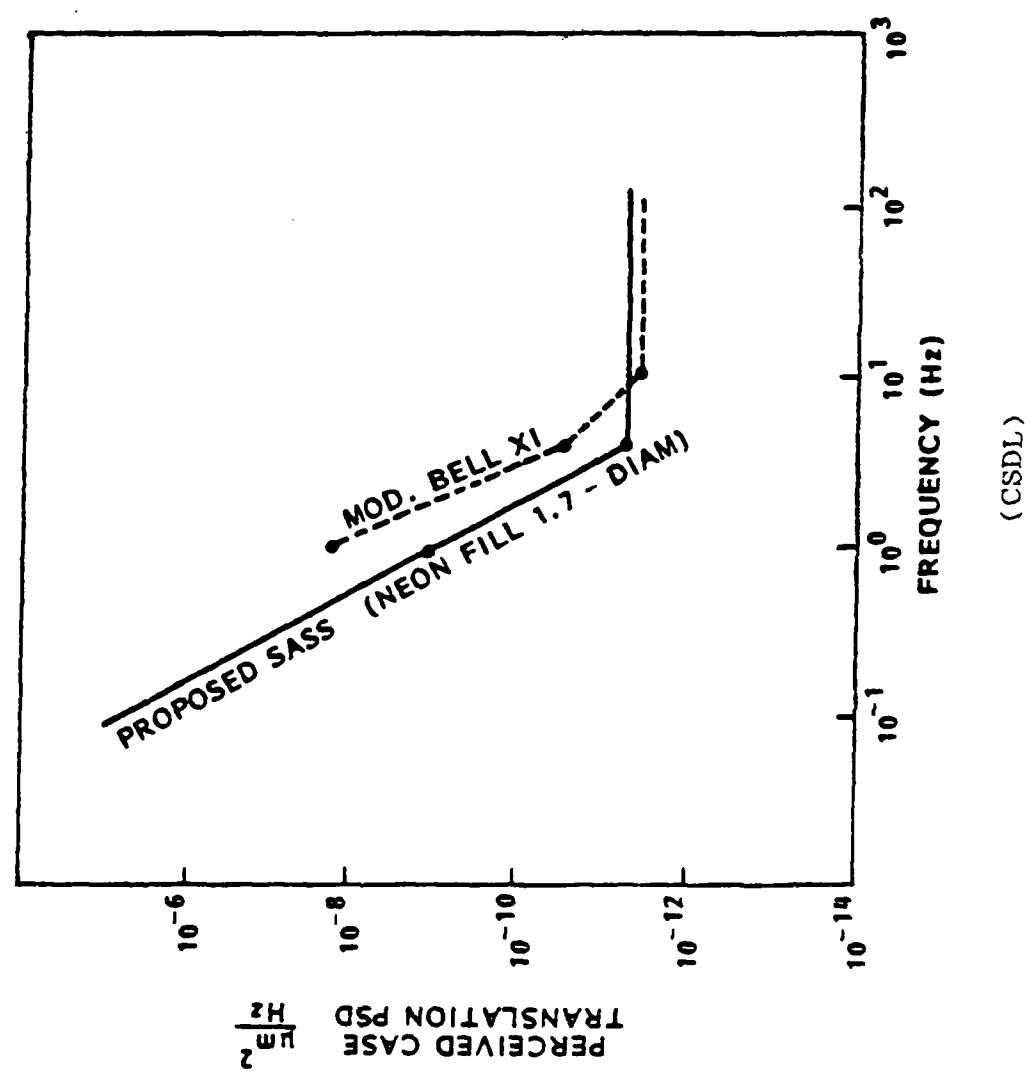
(CSDL)

1.7 INCH DIAM (ITGG SIZE)
 PROJECTED ANGULAR RESOLUTION
 (BASED ON 2 cp, 10^{-4} g DESIGN)



(CSDL)

1.7 INCH DIAM (ITGC SIZE)
 PROJECTED TRANSLATIONAL RESOLUTION
 (BASED ON 0.03 cp, 10⁻³ g DESIGNS)



TAARA/SASS PERFORMANCE SUMMARY - 1 IN DIAMETER UNIT

PARAMETERS	PARTIALLY FLOATED 2 cP FILL VISCOSITY	NEON FILL 0.03 cP VISCOSITY
FLOAT MASS	20 gm	20 gm
UNFLOATED MASS	10 gm	20 gm
TRANSVERSE INERTIA	20 gm-cm ²	20 gm-cm ²
AXIAL INERTIA	12 gm-cm ²	12 gm-cm ²
TRANSVERSE SPRING k	8.8 X 10 ³ (F _n = 3.3 Hz, 0.001 g)	1.8 X 10 ⁴ (F _n = 4.8 Hz, 0.001 g)
TRANSVERSE ROTATION k	3.5 X 10 ⁴ (F _n = 6.7 Hz)	7.2 X 10 ⁴ (F _n = 9.5 Hz)
AXIAL k	8.8 X 10 ³ (F _n = 3.3 Hz, 0.001 g)	1.8 X 10 ⁴ (F _n = 4.7 Hz, 0.001 g)
OA k	473 (F _n = 1.0 Hz)	473 (F _n = 1.0 Hz)
TRANSVERSE DAMPING	2 X 10 ⁴ (ξ = 23.8)	1400 (ξ = 1.2)
TRANSVERSE ROTATION DAMPING	1 X 10 ⁴ (ξ = 6.0)	720 (ξ = 0.3)
AXIAL DAMPING	5 X 10 ⁴ (ξ = 59.5)	3500 (ξ = 3.0)
OA DAMPING	30 (ξ = 0.2)	0.3 UNCONTROLLED - 30 WITH 30 WITH FEEDBACK ξ = 0.2
RESOLUTION OF INPUTS (0.1 to 100 Hz)	BROWNIAN SG NOISE	BROWNIAN SG NOISE
TRANSVERSE POSITION (X)	0.051 μm	0.007
TRANSVERSE ACCELERATION	0.062 μg	0.008
ANGULAR POSITION (θ)	1.8 μrad	0.48
ANGULAR ACC ACCELERATION	21 μrad/s ²	5.7
AXIAL POSITION (X)	0.081 μm	0.011
AXIAL ACCELERATION	0.098 μg	0.013
OA ANGLE (sg)	0.16 μrad	0.16
OA ANGLE ACCELERATION	1.9 μrad/s ²	1.9
ψ _X = 4.3 X 10 ⁻¹¹ $\frac{cm^2}{rad/s}$	ψ _{sg} = 1.8 X 10 ⁻¹⁹ $\frac{rad^2}{rad/s}$	ψ _{sg} = 1.8 X 10 ⁻¹⁹ $\frac{rad^2}{rad/s}$
ψ _θ = 6.8 X 10 ⁻¹² $\frac{rad^2}{rad/s}$		

(CSDL)

SOLID STATE ACCELEROMETER:
EXISTING DEVELOPMENT DEVICE

- DEVELOPED FOR TACTIC MISSILE GUIDANCE/AFWAL.
- FLEXIBLE SUBSTRATE WITH GOLD PROOF-MASS/PIEZOELECTRIC SENSING
- MEASURED CHIP NOISE $10 \text{ MG}/\sqrt{\text{HZ}}$ 0.1 HZ TO 1 HZ
- \$600K DEVELOPMENT TO DATE BY DOD/SIGNETICS

SSA DEVELOPMENT FOR LARGE SPACE STRUCTURES

- SCALING: REDUCTION OF MEMBRANE THICKNESS (1/2)
REDUCTION OF MEMBRANE WIDTH (1/5)

10/1 IMPROVEMENT IN SENSITIVITY

$1 \text{ MG}/\sqrt{\text{HZ}}$ NOISE LEVEL

- CAPACITANCE/RELUCTANCE SENSING:

0.1 TO $0.01 \text{ MG}/\sqrt{\text{HZ}}$
DEPENDING ON SCALING

-- SIMPLIFIES SEMICONDUCTOR PROCESSING

-- MORE COMPLEX PACKAGING

- SCALED PROTOTYPES INITIAL COST \$100K

- NEW SENSOR PROTOTYPES--\$500K

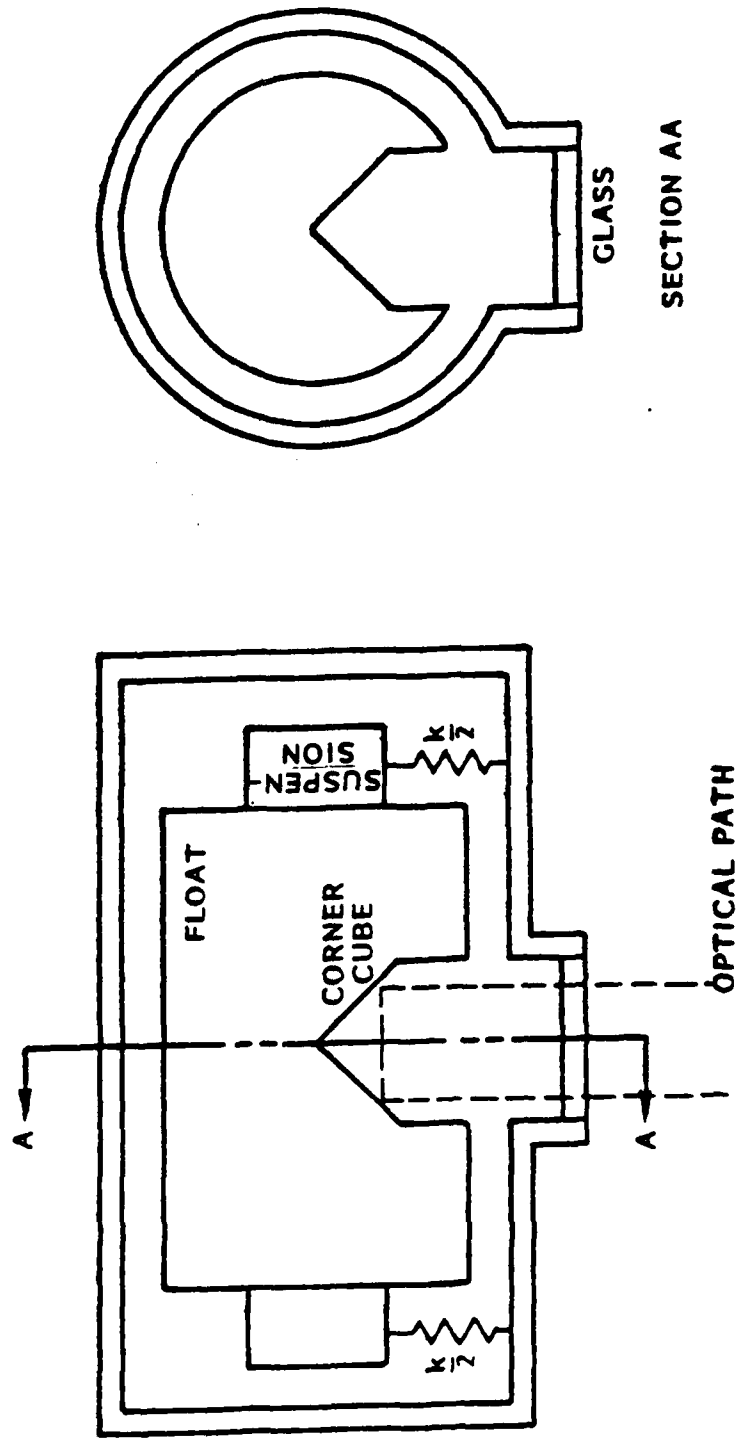
INERTIALLY STABILIZED REFLECTORS

- DESCRIPTION
 - GAS FILLED FOR OPTICS
 - AT BANDWIDTHS ABOVE 0.1 Hz. DECOUPLE REFLECTOR FROM STRUCTURE
- UNIQUENESS
 - OPTICS INERTIALLY STABILIZED
 - NOVEL DESIGNS
- APPLICATION
 - SPACE STRUCTURE DAMPING. INERTIAL REFERENCE FOR OPTICAL SYSTEMS PROGRAMS
- SUPPORTING DATA
 - OPTICAL REFERENCE GYRO
 - SASS/TAARA DATA BASE
- STATUS
 - PRELIMINARY ANALYSIS COMPLETE
 - QUESTIONS ABOUT SOFT SUSPENSIONS AND LOW FREQUENCY INPUTS (ONE G, RIGID BODY) MUST BE RESOLVED.

(CSDL)

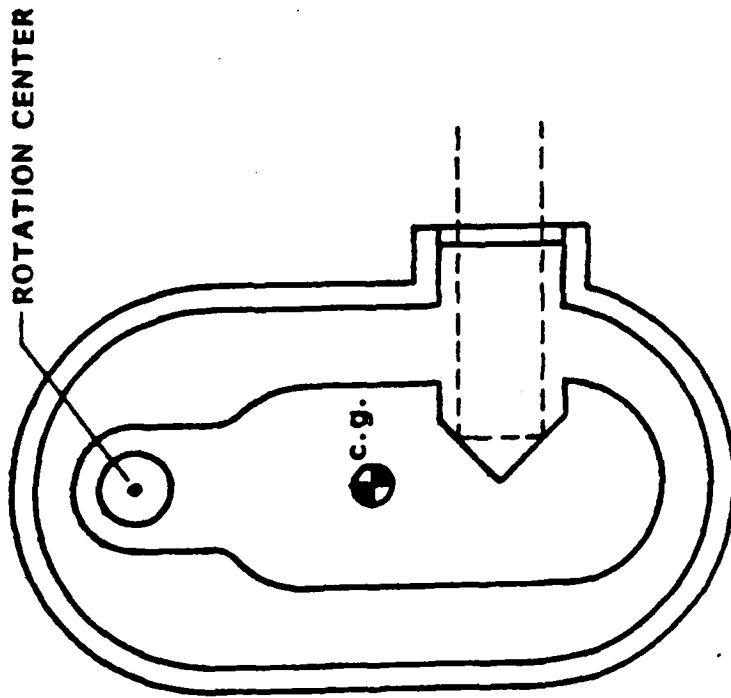
INERTIALLY STABILIZED REFLECTORS

1. DIRECT APPROACH SOFT (PROBABLY ACTIVE) SUSPENSION



(CSDL)

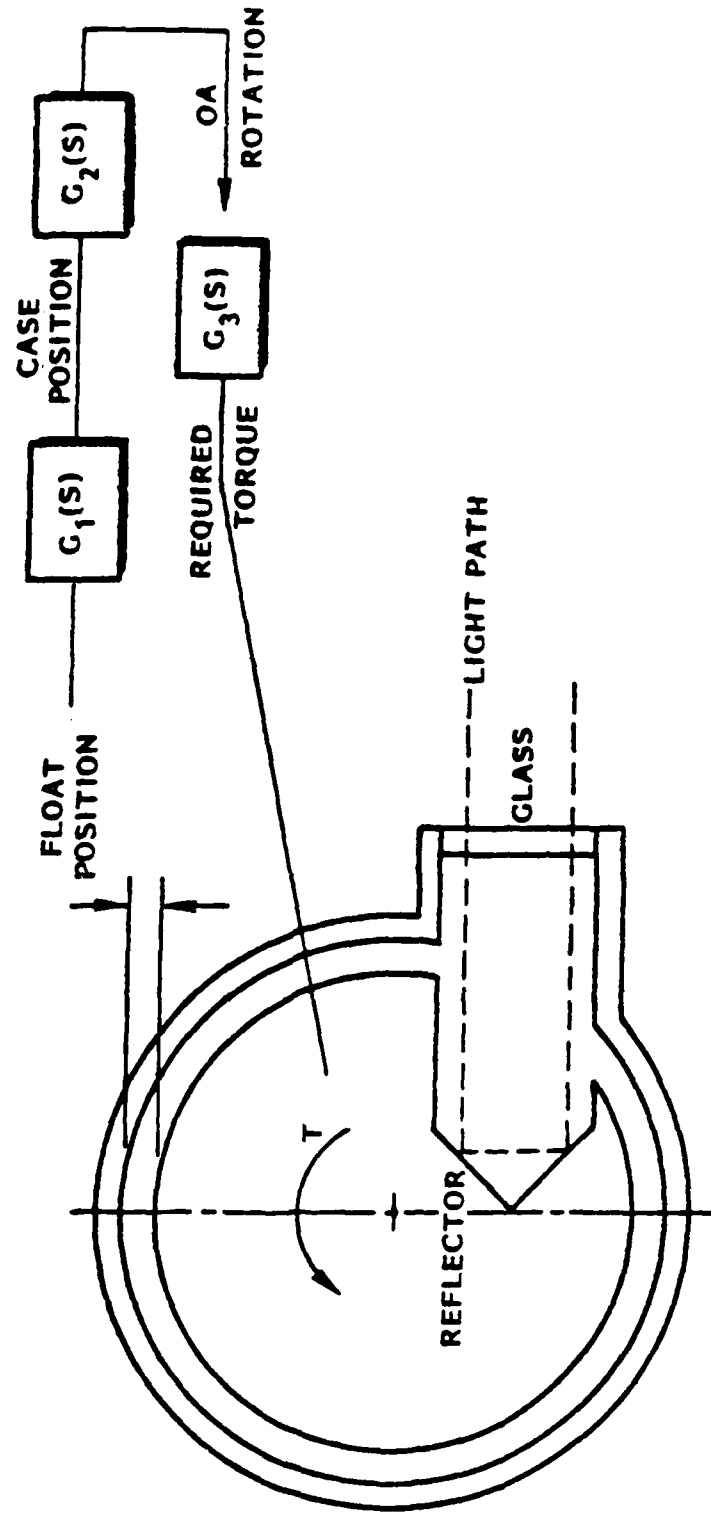
2. CENTER OF PERCUSSION



- ROTATION, c.g., MIRROR POSITION SELECTED SO THAT ROTATION COUNTERS LOS TRANSLATION. TUNING AND SOFT OA LOOP KEEPS CASE ROTATION FROM TRANSLATING MIRROR IN PERFORMANCE BANDWIDTH.
- STIFF RADIAL SUSPENSION
- SOFT LOOP REQUIRED ONLY ALONG OA WHERE GOOD TORQUER AND s.g. HAS TRADITIONALLY BEEN LOCATED.

(CSDL)

3. ROTATION CONTROLLED BY RADIAL SIGNAL



(CSDL)

APPROACH

- BUILD TWO PENDULOUS FLOATED PROTOTYPES TO FURNISH INFO SO FUTURE DESIGNS CAN BE EXECUTED CONFIDENTLY WHEN SPECS DETERMINED
- TWO UNITS TO PERMIT RESOLUTION TESTING
- SPECIFIC VERIFICATIONS
 - LOW FREQ BROWNIAN LIMIT. NO OTHER OBSTACLES
 - LOW FREQ s.g. RESOLUTION LIMIT
 - OPTIMAL EXCITATION - BARKHAUSEN NOISE
 - MULTIAXIS DYNAMICS
 - SUSPENSION COUPLING
 - ONE g. (LOADED SUSPENSION)
 - ACTIVE VS PASSIVE LOOPS
- DESIGN FEATURES
 - LOW VISCOSITY AND ENLARGED GAPS FOR LOW DAMPING
 - DOUBLE WOUND CORES WITH MANY LEADS BROUGHT OUT FOR FLEXIBLE SUSPENSION TESTING
 - PENDULOSITY ALLOWS LOADED AND UNLOADED SUSPENSION TESTING

(CSDL)

LMSC OPTICAL VIBRATION SENSOR

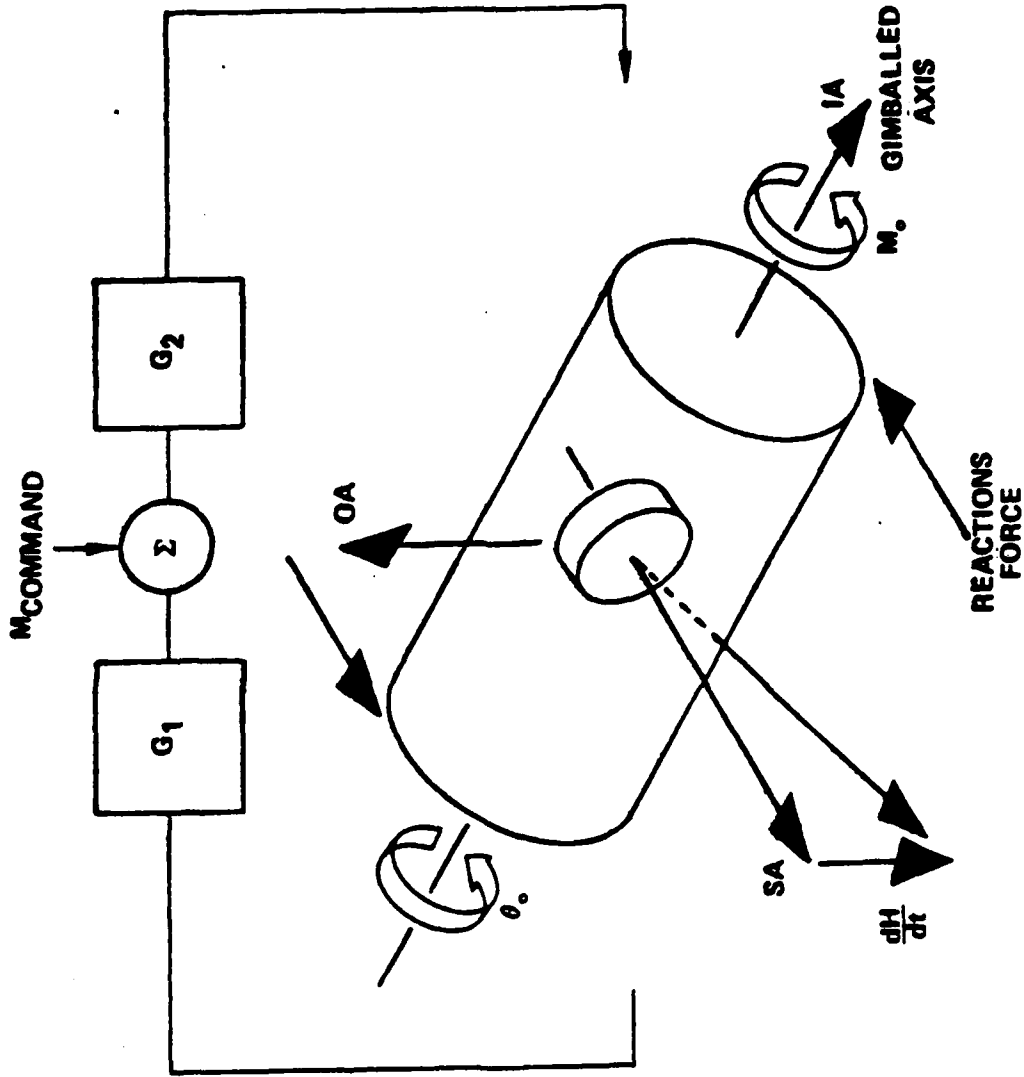
- MULTIPLE CHANNEL STARRING SYSTEM
- MICRO-PHASE MEASUREMENT (RELATIVE MOTION), DIGITAL MECHANIZATION
- CURRENT 2-CHANNEL BRASSBOARD RESOLVES 0.08 μ M
- 10 CHANNEL CAPABILITY DEMONSTRATION FOR ACROSS PHASE 1A.

CMG OVERVIEW

- PRINCIPLE OF OPERATION
- CMG ADVANTAGES
- DESIGN OBJECTIVES
 - JITTER versus BANDWIDTH
 - SC NOISE
- APPROACHES TO IMPROVED CMG
- PRELIMINARY DESIGN AND CONCERN AREAS
 - WHEEL BEARINGS
 - GIMBAL TORQUER
 - GIMBAL TACH.
- SUMMARY

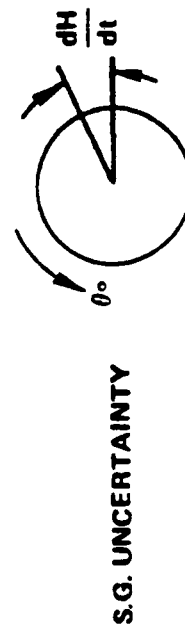
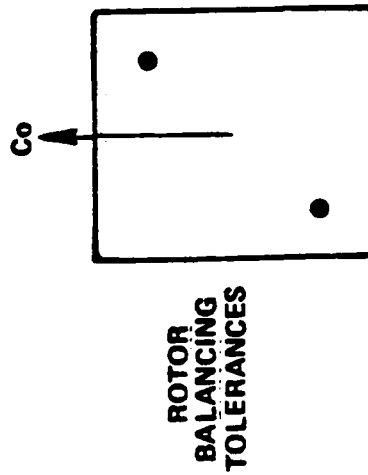
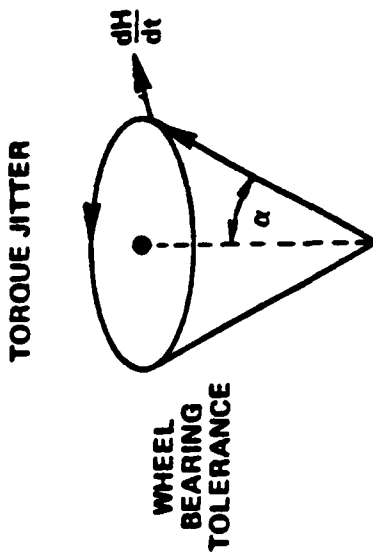
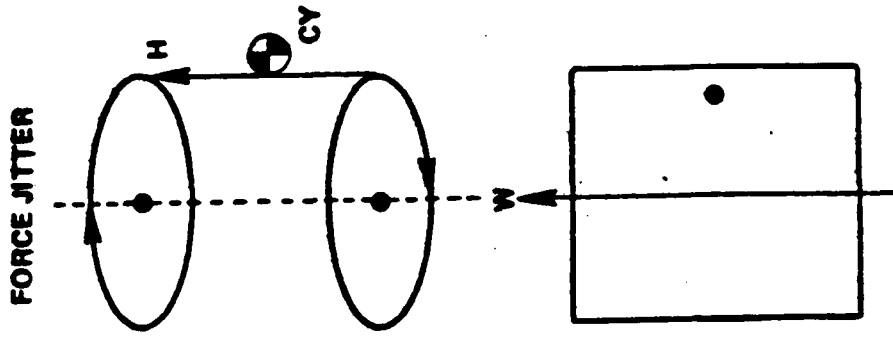
(CSDL)

PRINCIPLES OF CMG OPERATION

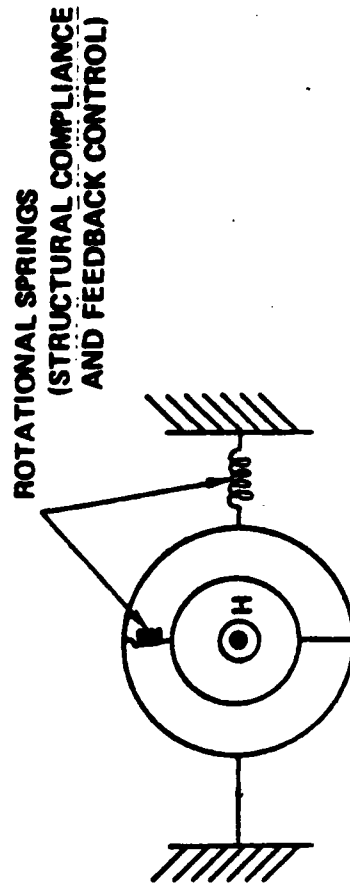


- θ_0 = ROTOR ROTATION ANGLE
- $M_{REACTION} = H\dot{\theta}_0$
- M_0 = INPUT TORQUE = $I_0 \ddot{\theta}_0 + \text{FRICTION}$
- S = LAPLACE TRANSFORM OF $\frac{d}{dt}$
- $M_{REACTION} = \frac{M_0 H}{I_0 S}$

JITTER SOURCES



TORQUER BANDWIDTH IS RELATED TO TRANSMITTED JITTER



- NON GIMBALLED AXIS, ALL JITTER TRANSMITTED.
- BELOW CMG BANDWIDTH, ALL WHEEL JITTER TORQUE IS TRANSMITTED TO CMG.
- ABOVE CMG BANDWIDTH, JITTER TORQUE IS ATTENUATED FOR GIMBALLED AXIS.

PERCEIVED REQUIREMENTS & OBJECTIVES

	H (ft/lb/s)	BANDWIDTH M_0/M_c (Hz)	JITTER (WHEEL SPEED AND HARMONICS)		COMMENT
			FORCE (lbs)	TORQUE (lb-in.)	
SLEWING CMG EXISTING	1000	5	0.5	5	BEFORE LMSC MAG ISOLATION TO ATTENUATE JITTER
CSDL PROJECTED	1000	5	0.05	0.5	
POINTING AND STABILITY CMG	20-100	100	-	-	
DEMONSTRATOR	10	200	0.01	0.005	CSDL ABILITY TO BALANCE BALL BEARING OR GAS AND RETAINER - LESS BEARING

(CSDL)

NEW TECHNOLOGY IN PROPOSED CMG's

- **WIDE BANDWIDTH - 200 Hz versus PRESENT 50 Hz**
- **RIGID GIMBAL AND TWO TORQUERS TO MINIMIZE GIMBAL TWISTING**
- **HIGH BAND SERIES MOTOR GIMBAL TORQUER**
- **TORQUER MOUNTED DIRECTLY TO RIGID STRUCTURE**
- **MAGNETIC SUSPENSION FOR GIMBAL TORQUERS**
- **ISOLATE HIGH FREQUENCY JITTER**
- **DEVELOPMENT REQUIRED**
- **ALTERNATIVE TO BALL BEARING GIMBAL AXIS**
- **IMPROVED BALL BEARING FOR SPIN AXIS**
- **RETAINERLESS BEARING AND BALL MATCHING REDUCE BALL ORBIT SPEED NOISE**
- **STATE OF ART DYNAMIC BALANCING REDUCES DME SPEED cycle/rev**
- **GAS BEARING FOR SPIN AXIS**
- **SERIES DC TORQUER FOR TORQUE MAGNITUDE AND BANDWIDTH**
- **CAPACITIVE WIDE ANGLE RESOLVER**

APPROACHES TO "QUALITY" CMG

- APPROACH #1
 - ELIMINATE JITTER
 - SMOOTH WHEEL BEARING
 - GAS, IMPROVED BALL - CSDL EXPERIENCE
 - PRECISELY STATICALLY AND DYNAMICALLY BALANCED WHEEL
 - SYMMETRIC DESIGN
 - CSDL CYRO AND RW EXPERIENCE
 - BANDWIDTH REQUIRES
 - STIFF STRUCTURE - CSDL CYRO EXPERIENCE
 - WIDE BAND TORQUER LSMC DESIGN
 - SINGLE GIMBAL ENHANCES STRUCTURAL RIGIDITY
- APPROACH #2
 - MOVE JITTER TO HIGH FREQUENCY
 - HIGH SPEED WHEEL
 - SUSPENSION/GIMBAL FOR HIGH FREQUENCY ISOLATION
 - MAGNETIC, GAS, FLUID, GIMBAL SUSPENSIONS
 - CHOICE FOR SLEWING CMG

(LEDS) ELECTRODYNAMIC SUSPENSION SYSTEM

OBJECTIVE:

DEVELOP A HIGH PERFORMANCE MAGNETIC VIBRATION ISOLATION SUSPENSION SYSTEM WHICH WILL ISOLATE VIBRATIONS ORIGINATING IN CONTROL MOMENT GYROSCOPES AND MOMENTUM WHEEL ASSEMBLIES FROM THE SPACECRAFT STRUCTURES WHILE ALLOWING THE HIGH FORCES FOR ATTITUDE CONTROL TO TRAVERSE THE GAP.

APPROACH:

USE THE LMSC ELECTRODYNAMIC ACTUATOR CONCEPTS IN A CONFIGURATION SURROUNDING THE VIBRATION SOURCE ASSEMBLIES WHICH CAN PROVIDE HIGHER BANDWIDTHS, LOWER OVERALL WEIGHTS, LOWER POWER REQUIREMENTS AND SIMPLIFIED SUPPORT ELECTRONICS.

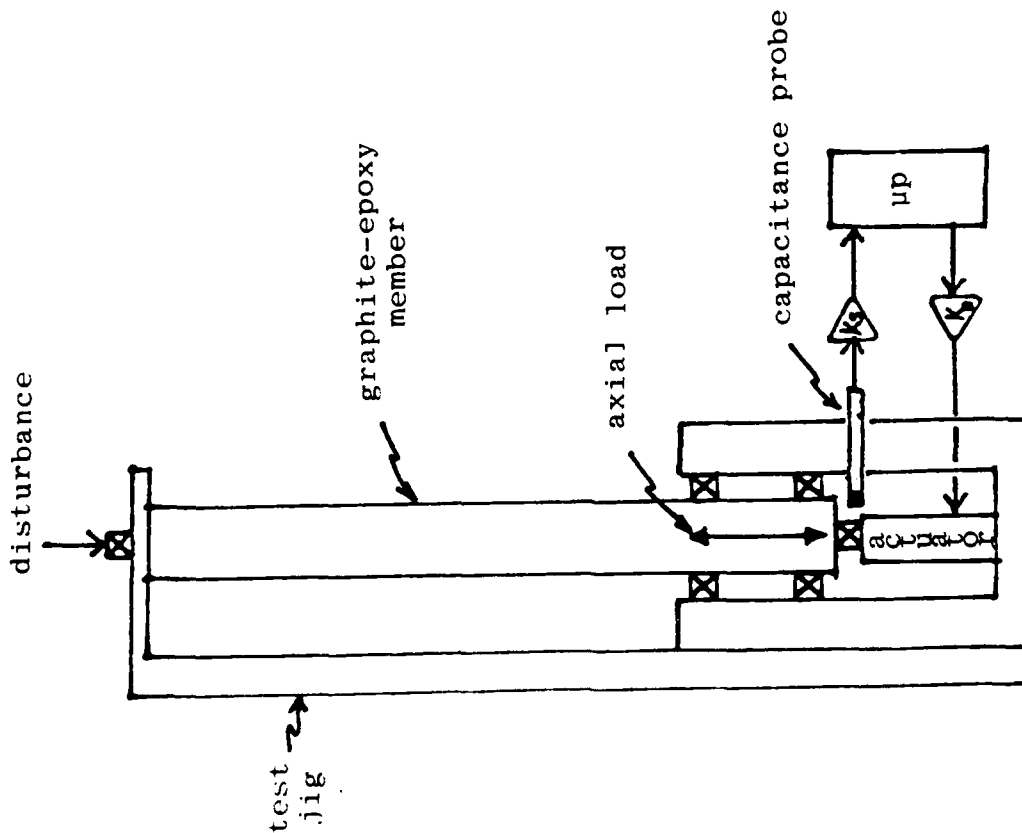
MEMBER DAMPER ACTUATOR (1, 2)

FORCE EFFECTOR

- 1) BURLEIG PIEZOELECTRIC PUSHER PZ-30
 - 0-5 μM
 - .0055 $\mu\text{M/VOLT}$
- 2) LMSC MA2-F/T
 - 20 LBS FORCE
 - $\pm 40 \mu\text{M MAX}$
 - 1 NANO-M SENSITIVITY

SENSOR

- 1) ADE MICROSENSE GAGE 2120
 - 1 NANO-M
- 2) OTHERS



[1] A. GREENLEAF, "RESEARCH AND DEVELOPMENT REPORT, ACTIVE DAMPING", PROJECT 5903, ITEK, DECEMBER 1977

[2] ROBERT L. FORWARD, "ELECTRONIC DAMPING OF VIBRATIONS IN OPTICAL STRUCTURES", APPLIED OPTICS, VOL. 18, NO. 5, MARCH 1979

MEMBER DAMPER ACTUATOR (CONT.)

TASKS

- 1) DEVELOP A TEST SET-UP SUCH THAT VARIOUS SENSOR/
FORCE EFFECTOR COMPLIMENTS CAN BE EVALUATED
- 2) DEVELOP ANALYTICAL MODEL FOR AN ACTUATOR IN SERIES
WITH A STRUT MEMBER
- 3) DESIGN ANALOG/DIGITAL HYBRID CONTROL LAW
- 4) COMPARE PIEZOELECTRIC PUSHER WITH MA2-F/T
- 5) DEMONSTRATE MICROVIBRATIONAL CONTROL OF AXIAL FORCE
LOADS ON STRUT MEMBER

(CSDI.)

END

FILMED

5-84

DTIC